

Miniaturized bioreactor for bioprocessing: design
and optimisation of a three-phase fluidized bed

by

Yi Zhang

A thesis submitted for the degree of

Doctor of Philosophy



School of Engineering,
Newcastle University, UK

November 2021

Abstract

The fluidized bed reactor (FBR) is a processing platform relying on the fluidization of solids by liquid/gas flows, thus achieving the excellent multi-phases contact, minimum diffusional resistance, good heat and mass transfer. Recently, the miniaturization of fluidized bed has received much attention due to its fast screening and process intensification. However, the application of miniaturized fluidized bed in bioprocessing and bioproduction is still not explored, although FBR enables higher mass transfer, lower shear force and less energy consumption compared with flask, stirred-tank reactor and photobioreactor, respectively.

To broaden the applicability of fluidized bed reactor in bioprocessing, this thesis combined the miniaturized fluidized bed reactor with *Nidula niveo-tomentosa* fungi to investigate the performance of FBR on fungal fermentation and raspberry ketone bioproduction. Thus, four main research themes were subsequently formulated and explored: (I). Design and fabrication of the micro-fluidized bed through 3D-printing technique; (II). Development of deeper understanding of the micro-fluidized bed based on liquid-gas and liquid-solid-gas hydrodynamic characteristics; (III). Investigation the cultivation parameters and different bioreactors for fungal fermentation and production; (IV). Development and investigation of a bench-scale fluidized bed reactor for fungal fermentation and raspberry ketone production.

The preliminary study of pellet fluidization provided an experimental basis for the fungal fermentation using fluidized bed reactor, as fungal pellets in the micro-fluidized bed could be well fluidized by both liquid and gas flows, while the gas flow can not only improve the mixing but also decrease pellet agglomeration. Then, the following study demonstrated that the optimal cultivation conditions including 75g/l glucose concentration, 2.5 g/l of phenylalanine, 3-week-old of 40% seed culture can largely improve raspberry ketone (RK) production in flask culture. Besides, the homogenization which breaks the pellets into free mycelia can further promote

RK production. Finally, the combination of these optimal parameters with the bench-scale fluidized bed bioreactor yielded raspberry ketone (up to 5 times compared to the control study by flask culture) and raspberry compounds (up to 3 times compared to the control study by flask culture), improving the overall bioproduction of *Nidula niveo-tomentosa* fungi.

Therefore, this thesis successfully proved the novel use of fluidized bed bioreactor for fungal fermentation, as the gas/liquid flows can fluidize the pellets which provide sufficient mass transfer and gas supply. Besides, the gas flow can decrease the pellet agglomeration thus mitigating the dead zone. Such a combination of fluidized bed bioreactor with fungal pellets opens up opportunities to develop a suitable and efficient bioprocessing technique in fungal fermentation.

Acknowledgements

I would like to express my sincere gratitude to my supervisors, Dr Vladimir Zivkovic, Dr Yuen Ling Ng, Dr Kheng-Lim Goh and Dr Yvonne Chow, for their invaluable guidance, unstinting supports and patience throughout my PhD study. I am grateful to Newcastle University and Agency for Science, Technology and Research (A*STAR), Singapore for funding my PhD programme over the past years.

I would like to acknowledge all the Process Intensification (PI) group members and Merz Court staff for their academic and technical help. I am always grateful to my friends, Lu, Yuqing, Yueyue, Hao, Ge, Shuolei, Zhiming, Lan, Huagui, Baohua, Steven, Guanqi, Wenchuan, Tobechi, Orlando, Abdul, Aumber, etc., in UK and China for the happy and unforgettable time. My thanks also go to the staff in SIFBI, particularly Eric, Xin Hui, Nui, Dennis, Mitch, Vita, Simon, Xi Xian, Wee Suan, Geraldine, Pnelope, Megan, Hanizah, Prashant, Raymund, etc., for their help and friendship during my attachment in A*star, Singapore.

Last, but never least, I would like to thank my parents and parents-in-law for their endless love and trust in my life. I am also indebted to my beautiful wife, Ming Wan, for her taking care, support and understanding, for always standing by my side without doubt, for accompanying me all the time and filling every day of my life.

Thank you all.

Table of Contents

Abstract	i
Acknowledgements	iv
List of publications and conferences	viii
Publications	viii
Conferences	viii
List of Figures	ix
List of Tables	xiii
Nomenclature	xiv
Chapter 1 Introduction	1
1.1 Background	1
1.1.1 Micro-fluidized bed bioreactor	1
1.1.2 Fungal fermentation for raspberry ketone production	1
1.2 Significance and innovation	2
1.3 Aims and objectives	3
Chapter 2 Literature review	6
2.1 Introduction	6
2.2 Micro-fluidized bed	6
2.2.1 Characteristics of MFB	8
2.2.2 Applications	23
2.2.3 Conclusions and Prospect	38
2.3 Fungal fermentation	40
2.3.1 Pellet formation and growth	40
2.3.2 Factors on pellet growth	41
2.3.3 Fungal fermentation in different reactors	43
2.4 Raspberry ketone production	46
2.5 Summaries	48
Chapter 3 Approaches and methodologies	51
3.1 Introduction	51
3.2 Micro-fluidized bed techniques	51
3.2.1 Micro-fluidized bed design and fabrication.....	51
3.2.2 Image capture and processing.....	54
3.2.3 Hydrodynamics investigation of the micro-fluidized bed	54

3.3 Fungal fermentation	58
3.3.1 Microorganisms	59
3.3.2 Strain and Chemicals	59
3.3.3 Cultivation medium preparation and characterization.....	59
3.3.4 Preparation of seed culture and flask culture.....	62
3.3.5 Investigation of fungal pellets	63
3.3.6 Cultivation parameters for flask culture	65
3.3.7 Liquid sampling	66
3.3.8 Experimental setup	71
Chapter 4 Micro-fluidized bed design and hydrodynamics	75
4.1 Introduction	75
4.2 Results and discussions	75
4.2.1 Micro-fluidized bed design and fabrication.....	75
4.2.2 Hydrodynamics investigation of the miniaturized fluidized bed.....	81
4.3 Conclusions	111
4.3.1 Fluidized bed design and fabrication.....	111
4.3.2 Hydrodynamics investigation of the miniaturized fluidized bed.....	111
Chapter 5 Investigation of cultivation parameters for fungal fermentation	114
5.1 Introduction	114
5.2 Results and discussions	116
5.2.1 Glucose concentration	116
5.2.2 Freezer stock VS agar plate	118
5.2.3 Seed culture age.....	120
5.2.4 Inoculum concentration	121
5.2.5 UV radiation time	123
5.2.6 Phenylalanine concentration.....	125
5.2.7 Pellet morphology.....	127
5.2.8 Optimized conditions.....	130
5.3 Conclusions	132
Chapter 6 Comparison of RK production in different bench-scale bioreactors	133
6.1 Introduction	133
6.2 Results and discussions	133
6.2.1 Pellet morphology.....	133
6.2.2 Pellet biomass	136

6.2.3 Production of RK and RA	137
6.2.4 Effects of pellet morphology and suspension stages	138
6.2.5 Selectivity: Raspberry Ketone vs. Raspberry Alcohol	139
6.2.6 Challenges and prospects.....	140
6.3 Conclusions	142
Chapter 7 Fungal fermentation using bench-scale fluidized bed reactor.....	143
7.1 Introduction	143
7.2 Results & discussions	144
7.2.1 Gas flowrates	144
7.2.2 Gas sparger size	147
7.2.3 Minimum fluidization operation using increasing gas flowrate	149
7.2.4 Optimized conditions.....	153
7.3 Conclusion.....	156
Chapter 8 Conclusions and future work.....	158
8.1 Conclusions	158
8.1.1 Micro-fluidized bed techniques	158
8.1.2 Fungal fermentation study	160
8.2 Future work	162
Appendices.....	164
Appendix A: Micro-fluidized bed geometry with dimensions	164
A.1. Upper part	164
A.2. Lower part.....	167
Appendix B: Experimental calibration	168
B.1 OMEGA-FL3635G gas flowmeter calibration	168
B.2 WASTON MARLOW 530U Peristaltic Pump	168
B.3 Liquid viscosity measurement by ATAGO VISCO TM -985 viscometer	169
References.....	170

List of publications and conferences

Publications

Zhang, Y., Ng, Y.L., Goh, K.-L., Chow, Y., Wang, S., Zivkovic, V., 2021. 'Fluidization of fungal pellets in a 3D-printed micro-fluidized bed', *Chemical Engineering Science* 236, 116466

Zhang, Y., Goh, K.-L., Ng, Y.L., Chow, Y., Wang, S., Zivkovic, V. 2021. 'Process intensification in micro-fluidized bed systems: a review', *Chemical Engineering and Processing-Process Intensification* 164: 108397

Zhang, Y., Goh, K.-L., Ng, Y.L., Chow, Y., Zivkovic, V. 2021. 'Design and investigation of a 3D-printed micro-fluidized bed', *Chemengineering*, 2021. 5(3): p. 62.

Zhang, Y., Peterson, E.C., Ng, Y.L., Goh, K.-L., Zivkovic, V., Chow, Y., 2021. 'Comparison of fungal morphology and raspberry ketone production using different bench-scale bioreactors', *Bioresource Technology*, to be submitted.

Zhang, Y., Ng, Y.L., Goh, K.-L., Zivkovic, V., Chow, Y. 2021. 'Investigation of cultivation parameters for raspberry ketone production by flask culture of *Nidula Niveo-tomentosa*', *Biotechnology and Bioengineering*, to be submitted.

Zhang, Y., Ng, Y.L., Goh, K.-L., Zivkovic, V., Chow, Y. 2021. 'Study of fungal fermentation using a bench-scale fluidized bed reactor', *Powder Technology*, to be submitted.

Conferences

Dial-a-Molecule Enabling Technologies Summer School (funded by EPSRC), Loughborough University, UK, 30 July – 3 August 2018

Oral presentation titled 'Fluidization of fungal pellets using miniaturized 3D-printed fluidized bed' at Fluidization XVI conference, Guilin, China, 26 – 31 May 2019

Poster & Oral presentation titled 'Pellet fluidization using a 3D-printed micro-fluidized bed' at 17th Annual BioProcessUK Conference, Online, 1 – 2 December 2020

Oral presentation titled 'Investigation of fungal fermentation in a miniaturized liquid-solid-gas fluidized bed reactor' at 7th International Conference on Micro and Nano Flows (MNF 2021), Online, 24 – 26 May 2021

List of Figures

Fig. 2.1. Bibliographic co-occurrences of MFB based on the Scopus database [24].	7
Fig. 2.2. Graph of the number of MFB-related publications versus publication year. Indicated on the curve is an outline of the key development of MFB.	9
Fig. 2.3. Examples of MFB systems: (a) the MFBs with $400 \times 175 \mu\text{m}^2$ cross-section were fabricated in a polydimethylsiloxane (PDMS) chip by standard soft lithography techniques [15], (b) micro-circulating fluidised bed design was made by milling 1×1 mm cross-section channels into Perspex, (c) a 3D-printed MFB with cross-sectional area of 15×15 mm [45], (d) a micro-fluidized bed whose bed column is made up of a quartz capillary of 0.8 mm inner diameter, 6 mm outer diameter and 60 mm length, (e-f) a MFB reaction analyzer (MFBRA) developed by the Institute of Process Engineering (IPE), Chinese Academy of Sciences [46].	11
Fig. 2.4. Schematics of determining U_{mf} in liquid-solid and liquid-gas MFB: (a) bed expansion curve (bed ratio versus superficial liquid velocity) to extrapolate U_{mf} , (b) typical pressure drops profile (fluidization and defluidization) generated by comparing the pressure drops at various superficial gas velocities.	12
Fig. 2.5. Comparison of mixing in the particle-free channel and micro-fluidized bed at different liquid flowrates: (a) $190 \mu\text{m/s}$, (b) $286 \mu\text{m/s}$, (c) $361 \mu\text{m/s}$, respectively [64], Simulation snapshots of the scalar concentration fields in the exit plane for (d) fixed bed and (e) fluidized bed [69].	17
Fig. 2.6. Schematic of the bed regime transitions (from packed bed to turbulent bed) in the gas-solid micro-fluidized bed with the inert of Geldart type A, B, C, and D powders, respectively.	18
Fig. 2.7. Schematics of gas spargers with different design: (a) sieve plate sparger, (b) multiple ring spargers, (c) spider-shape sparger, (d) multiple pipe sparger	19
Fig. 2.8. (a) fluidized bed consists of purely benzoic acid particles, (b) fluidized bed is composed of benzoic acid pellets and inert particles, (c) simplified model of circulating fluidized bed, (1) riser column, (2) outlet, (3) top particles return pipe, (4) settler and calming column, (5) bottom particles return pipe, (6) inlet.	21
Fig. 2.9. Diagram of the high-pressure fluidized bed for particle coating process using the rapid expansion of supercritical fluid solutions (RESS): (a) fluidized bed, (b) & (c) buffer autoclaves, (d) compressor [110].	24
Fig. 2.10. 2D schematics and 3D models of the main component of the micro interconnected fluidized bed for oxygen carrier evaluation [156]. T_i and P_i (with $i = 1$ to 4) indicate temperature and pressure measuring points.	31
Fig. 2.11. Images of main components of different bioreactor systems: (a) flask culture, (b) stirred-tank reactor, (c) panel bioreactor, (d) fluidized bed reactor.	32
Fig. 2.12. Schematic of fungal growth and pelletization in different stages. Stage 1: Micro-morphological growth based on coagulative and non-coagulative mode, Stage 2: Macro-morphological growth with branching and extension of hyphae for pellet formation, Stage 3: fungal cell autolysis into fragmented species for next round pelletization.	41
Fig. 2.13. Biosynthetic approach for raspberry ketone and anthocyanins. The biosynthesis of raspberry compounds starts from the coupling of p -coumaric acid to CoA by the 4CL enzyme. Afterwards, the coumaroyl-CoA is converted into raspberry ketone with the supply of malonyl-CoA.	48
Fig. 3.1. Images of cross section of fluidized bed with different dimensions: (a) $7.5 \text{ mm} \times 20 \text{ mm}$, (b) $10 \text{ mm} \times 10 \text{ mm}$, (c) $15 \text{ mm} \times 15 \text{ mm}$.	52
Fig. 3.2. Fluidized bed printing and post-printing process: (a) the fluid bed is printing by the Form 2 SLA printer, (b) post-washing process is to clean the surface of printed parts, (c) post-curing process is used to strengthen the inner bonds of the parts.	53

Fig. 3.3. Schematic diagram of the experimental setup for fungal pellets fluidization.	55
Fig. 3.4. (a) Image of fungal pellets after 4-week flask culture in 90 mm petri dish, (b) Corresponding size distribution obtained from 600 pellet samples.	58
Fig. 3.5. Density measurement for cultivation media: (a) preparation of the clean and autoclaved volumetric flask, (b) weighing of the empty flask, (c) filling cultivation medium to the scale line and weighting the weight again.	60
Fig. 3.6. Viscosity measurement for cultivation medium: (a) image of the VISCO TM -895 digital viscometer, (b) A1 spindle with 100 ml calibrating liquid inside the L beaker for viscosity calibration, (c) digital screen on the top of viscometer shows the process of liquid viscosity measurement.	62
Fig. 3.7. Procedures for pellet size characterization: (a) take the flask culture from incubator, (b) transfer the pellets-media mixture from flask into petri dish for photograph using Scan 2000, (c) use ImageJ to process the photograph for size measurement, (c) use the function of Analyse Particles to get the results of each pellet's diameter.	64
Fig. 3.8. (a) Agar plate for fungal strains storage, (b) Samples of freezer stocks kept in -70 °C fridge, (c) Images of well-prepared flask culture, (d) Schematic shows the procedure to prepare flask culture with inoculum concentration of 10%, 20% and 40%, respectively.	66
Fig. 3.9. (a) Configuration of the 1260 Infinity II HPLC, (b) Liquid samples are kept in HPLC glass vials in -20°C for long-term storage, (c) Image of ZORBAX Eclipse Plus C18 HPLC column for raspberry compounds detection.	68
Fig. 3.10. (a) Configuration of the YSI 2900 Biochemistry Analysers, (b) 96-well sample pate for loading samples, (c) The analysed results can be checked and displayed on the screen.	70
Fig. 3.11. Schematic diagram of the experimental setup: (a) panel bioreactor (PBR), (b) fluidized bed reactor (FBR).	72
Fig. 4.1. Images of three different types of distributors: (a) bar-shape distributor, (b) perforated plate distributor, (c) mesh-particles distributor. Simple schematics of distributors are given below the actual images.	76
Fig. 4.2. Bubble morphologies in different distributors: (a) single bubbles of >5mm in diameter in bar-shape distributor, (b) multiple bubble flows in perforated plate distributor, (c) single bubble flow goes through the left side of the mesh-particles distributor.	77
Fig. 4.3. Models of the fluidized bed: (a) top view of the lower part, (b) front view of the lower part showing the liquid inlet and gas inlet located at the left side and bottom, respectively, (c) CAD model of the main column, (d) image of the assembled 3D-printed fluidized bed.	80
Fig. 4.4. Representative pictures of bubble flow regimes with the increase of gas flowrate but a static liquid flow. $d_G = 100 \mu\text{m}$. (a). $Q_G = 3.7 \text{ ml/min}$, (b). $Q_G = 5.4 \text{ ml/min}$, (c). $Q_G = 9.9 \text{ ml/min}$, (d). $Q_G = 15.5 \text{ ml/min}$, (e). $Q_G = 22.9 \text{ ml/min}$, (f). $Q_G = 32.7 \text{ ml/min}$. $d_B = 15 \text{ mm}$	83
Fig. 4.5. The mean bubbles' size for different capillary sizes of (a) $d_G = 50 \mu\text{m}$, (b) $d_G = 100 \mu\text{m}$, (c) $d_G = 150 \mu\text{m}$ as a function of liquid velocity, U_L and gas flowrates, Q_G	84
Fig. 4.6. Bubbles' velocity as a function of liquid velocity, U_L for the different gas flowrates, Q_G . Subfigures corresponds to the 3 different orifice sizes of (a) $d_G = 50 \mu\text{m}$, (b) $d_G = 100 \mu\text{m}$ and (c) $d_G = 150 \mu\text{m}$	86
Fig. 4.7. Characterization of gas volume fraction, ϵ_G as a function of gas flowrate, Q_G and liquid velocity, U_L with different gas sparger sizes: (a) $d_G = 50 \mu\text{m}$, (b) $d_G = 100 \mu\text{m}$, (c) $d_G = 150 \mu\text{m}$	88
Fig. 4.8. Bed expansion with the increase of liquid velocity in medium culture using 1 g of pellets. $d_B = 15 \text{ mm}$	91
Fig. 4.9. Graph of the ratio of experimental $U_{mf, ex}$, to theoretical, $U_{mf, th}$, minimum fluidization velocity versus pellets mass in cultivation medium (squares) and ultrapure water (circles).	93
Fig. 4.10. Snapshots of pellets defluidization of 1 g pellets in cultivation medium. $d_B = 15 \text{ mm}$	94
Fig. 4.11. Bed expansion studies of the fungal pellets in both cultivation medium and ultrapure water: (a) 0.5 g pellets, (b) 1.0 g pellets, (c) 1.5 g pellets.	96

Fig. 4.12. Bed expansion characteristics with the parameters of liquid velocity and bed voidage: (a) 0.5 g pellets, (b) 1.0 g pellets, (c) 1.5 g pellets.	98
Fig. 4.13. Dependency of n' based on static bed voidage.....	100
Fig. 4.14. Representative snapshots of different flow regimes with different gas flowrate and pellet biomass in ultrapure water. $d_B = 15$ mm.	102
Fig. 4.15. Representative snapshots of different flow regimes with different gas flowrate and pellet biomass in medium. $d_B = 15$ mm.	104
Fig. 4.16. Fluidization regime maps of fungi in both cultivation medium and ultrapure water: (a) 0.5 g pellets, (b) 1.0 g pellet, (c) 1.5 g pellets.	106
Fig. 4.17. Representative example of PIVlab analysis for 1 g pellets in medium: (a) mean velocity displays the pellet minimum fluidization by liquid flow, (b) mean velocity displays the pellet minimum fluidization by gas flow, (c) scatter plot showing the velocity distribution of 1 g pellets by liquid flow in medium, (d) scatter plot showing the velocity distribution of 1 g pellets by gas flow in medium, (e) display of the vortex locators with corresponding intensity for 1 g pellets by gas flow in medium.	108
Fig. 4.18. (a) mean radial velocity of pellet fluidization at different conditions, (b) mean axial velocity of pellet fluidization at different conditions.	109
Fig. 5.1. Study of glucose concentrations on fungal growth and bioproduction: (a) time-course profiles of biomass dry weight, (b) RK curves during 5-weeks fermentation, (c) RA production during fermentation, (d) RC accumulation during the fermentation. Other cultivation parameters: 2 weeks old of preculture, 10% of inoculum concentration, 10h/d of UV-A exposition, 1.5 g/l of phenylalanine.	116
Fig. 5.2. Comparison of the seed culture type on fungal growth and bioproduction: (a) Time-course profiles of biomass dry weight, (b) RK curves during 4-week fermentation, (c) RA production during fermentation, (d) RC accumulation during the fermentation. Other cultivation parameters: 75g/l of glucose concentration, 2 weeks old of preculture, 10% of inoculum concentration, 10h/d of UV-A exposition, 1.5 g/l of phenylalanine concentration.	119
Fig. 5.3. Effects of the seed culture age on fungal growth and bioproduction: (a) biomass growth curves, (b) RK curves during 5-week fermentation, (c) RC accumulation during flask culture, (d) specific productivities for RA and RC. Other cultivation parameters: 75g/l of glucose concentration, 10% of inoculum concentration, 10h/d of UV-A exposition, 1.5 g/l of phenylalanine concentration.	120
Fig. 5.4. Study of seed culture concentration on 5-week fungal growth and bioproduction: (a) biomass concentration profiles, (b) RK curves, (c) RA curves, (d) RC accumulation during flask culture, (e) glucose consumption during fungal fermentation, (f) average yield coefficients Y_{XS} (gram dry weight per gram substrate), Y_{PS} (gram product per gram substrate) and Y_{PX} (gram product per gram dry weight) during batch fermentations. Other cultivation parameters: 75g/l of glucose concentration, 2 weeks old of preculture, 10h/d of UV-A exposition, 1.5 g/l of phenylalanine concentration.	122
Fig. 5.5. Effects of UV-A exposition time on fungal growth and bioproduction: (a) biomass growth curves, (b) RK curves during 5-week fermentation, (c) RA curves during flask culture, (d) RC accumulation during 5-week fermentation. Other cultivation parameters: 75g/l of glucose concentration, 2 weeks old of preculture, 10% of inoculum concentration, 1.5 g/l of phenylalanine concentration.	124
Fig. 5.6. Study of phenylalanine concentration on fungal fermentation: (a) Biomass concentration curves, (b) RK curves during 5-week fermentation, (c) RA curves in 5-week fermentation, (d) RC accumulation during flask culture, (e) phenylalanine consumption during fungal fermentation, (f) average yield coefficients Y_{PS} (gram compounds produced per gram phenylalanine consumed). Other cultivation parameters: 75g/l of glucose concentration, 2 weeks old of preculture, 10% of inoculum concentration, 10h/d of UV-A exposition.	126

Fig. 5.7. Images of Fungal samples after 5-week flask fermentation: (a) no homogenization during flask culture, (b) homogenization of the flask at week-2 (Homogenization-2), (3) homogenization of the flask content at week-3 (Homogenization-3). Other cultivation parameters: 75g/l of glucose concentration, 2 weeks old of preculture, 10% of inoculum concentration, 10h/d of UV-A exposition, 1.5 g/l of phenylalanine concentration.	128
Fig. 5.8. Effects of fungal morphology on fungal growth and bioproduction: (a) biomass concentrations, (b) RK curves during 5-week fermentation, (c) RA curves during flask culture, (d) RC accumulation during 5-week fermentation.	129
Fig. 5.9. Fungal fermentation under optimized conditions: (a) biomass growth and glucose consumption, (b) bioproduction.	131
Fig. 6.1. Images of pellet samples after 5-weeks fermentations in (a) flask culture, (b) stirred-tank reactor (STR), (c) panel bioreactor (PBR) and (d) fluidized bed reactor (FBR), (e) pellet size and sphericity after 5-week fermentation from different bioreactors, (f) biomass concentrations of fungal cells after 5-weeks fermentation in different bioreactors.	134
Fig. 6.2. Schematic diagram of pellet morphology changes in different bioreactors. STR: stirred-tank reactor, PBR: panel bioreactor, FBR: fluidized bed reactor.	135
Fig. 6.3. Bioproduction and substrate consumption during 4 weeks of fungal fermentation. (a) Graph of raspberry ketone concentration versus time, (b) Graph of raspberry alcohol versus time, (c) Graph of total raspberry compounds concentration versus time, (d) Graph of glucose consumption concentration versus time to illustrate glucose consumption. STR: stirred-tank reactor, PBR: panel bioreactor, FBR: fluidized bed reactor.	136
Fig. 6.4. Selectivity of RK and RA in RK-to-RA transition: (a) graph of RK distribution versus time, (b) graph of RA distribution versus time. STR: stirred-tank reactor, PBR: photobioreactor, FBR: fluidized bed reactor.	140
Fig. 7.1. Fluidization regimes showing the change of pellet fluidization during 4-week of fermentation. $Q_G = 0.15$ v.v.m, $d_G = 0.15$ mm. $d_B = 50$ mm.	144
Fig. 7.2. Study of gas flowrates on fungal growth and bioproduction: (a) final biomass dry weights under different gas flowrates, (b) raspberry ketone curves during 4-weeks fermentation, (c) raspberry alcohol production during fermentation, (d) raspberry compounds accumulation during the fermentation.	146
Fig. 7.3. Effects of gas sparger size on fungal growth and bioproduction: (a) final biomass dry weights under different gas orifice sizes, (b) raspberry ketone curves during 4-weeks fermentation, (c) raspberry alcohol production during fermentation, (d) raspberry compounds accumulation during the fermentation.	148
Fig. 7.4. Snapshots of fungal fermentation in last week under minimum fluidization regime by increased gas flowrate with different gas orifice size. (a). 0.15 mm gas sparger; (b). 0.8 mm gas sparger; (c). 1.2 mm gas sparger. $d_B = 50$ mm.	151
Fig. 7.5. Study of the minimum fluidization state operations with different gas orifice sizes on fungal fermentation: (a) Profiles of minimum gas flowrates to fluidize pellets during the fermentations, (b) final biomass dry weights for each gas sparger size under minimum fluidization condition, (c) RK concentration profiles for each gas sparger size under minimum fluidization condition, (d) RA conversions for each gas sparger size under minimum fluidization condition, (e) RC accumulation for each gas sparger size under minimum fluidization condition, (f) average specific productivities for RK, RA and compounds under minimum fluidization state.	151
Fig. 7.6. Snapshots show fungal fluidization regimes changes under optimized cultivation conditions during fungal fermentation: (a) Day 1, (b) Day 3, (c) Day 5, (d) Day 7, (e) Day 10, (f) Day 13, (g) Day 15, (h) Day 17. $d_B = 50$ mm.	155
Fig. 7.7. Bioproduction of RK, RA and compounds in FBR under optimized cultivation parameters.	155

List of Tables

Table 2.1 Summary of the influences of different parameters on U_{mf} in MFBs.....	14
Table 2.2 Summary of wastewater treatment using different micro-fluidized bed reactor systems in recent years.	34
Table 3.1 Base culture media formulation for fungal cultivation.	57
Table. 3.2 Cultivation parameters and their corresponding levels.	67
Table 4.1 Calculated and extrapolated parameters of Richardson-Zaki equation.	99
Table 5.1 Optimal parameters for improving RK synthesis in flask culture.	130
Table 6.1 Various yield values at endpoint in different bioreactors using glucose as substrate.	137
Table 7.1 Details of the optimal cultivation parameter adopted in fluidized bed reactor system.	153

Nomenclature

A	Cross-sectional area of bed column (mm^2)
d_b	Diameter of each bubble diameter (mm)
d_B	Diameter of internal bed (mm)
d_P	Particle diameter (mm)
g	Acceleration of gravity (m/s^2)
H	Bed height (mm)
H_0	Initial bed height (mm)
k	Proportional coefficient of Richardson-Zaki equation
K_C	Mass transfer coefficient
n	Exponent of Richardson-Zaki equation
n'	Extrapolated exponent of Richardson-Zaki equation
Q_G	Volumetric gas flowrate (ml/s)
Q_G^*	Dimensionless volumetric gas flowrate
Q_L	Volumetric liquid flowrate (ml/s)
Q_L^*	Dimensionless volumetric liquid flowrate
Q_P	Specific productivity (mg/g/day)
R^2	Coefficient of determination
Re	Reynolds number
Sc	Schmidt number
Sh	Sherwood number
U_F	Superficial velocity of fluid (mm/s)
U_G	Gas velocity (mm/s)
U_G^*	Dimensionless gas velocity
U_L	Superficial liquid velocity (mm/s)

$U_{L, min}$	Minimum liquid velocity (mm/s)
$U_{L, max}$	Maximum liquid velocity (mm/s)
U_L^*	Dimensionless liquid velocity
U_{mf}	Minimum fluidization velocity (mm/s)
$U_{mf, ex}$	Experimental minimum fluidization velocity (mm/s)
$U_{mf, th}$	Theoretical minimum fluidization velocity (mm/s)
U_t	Terminal velocity (mm/s)
U_t'	Extrapolated terminal velocity (mm/s)
V_b	Volume of each bubble (mm ³)
V_C	Volume of bed column (mm ³)
Y_{PX}	Yield of product from biomass (mg/g)
Y_{PS}	Yield of product from substrate (mg/g)
Y_{XS}	Biomass yield (g/g)
ΔV	Pellet volumes drop due to funnel filtration (mm ³)

Greek letter

ε	Bed voidage
ε_G	Gas volume fraction
ε_0	Initial/static bed voidage
ε_0'	Revised initial/static bed voidage
ρ_G	Gas density (kg/m ³)
ρ_L	Liquid density (kg/m ³)
ρ_P	Pellet/particle density (kg/m ³)
$\Delta\rho$	Density difference between fluid and solids (kg/m ³)
\emptyset_P	Pellet/particle sphericity
μ_G	Gas viscosity (Pa·s)
μ_L	Liquid viscosity (Pa·s)

Abbreviations

CCS	Carbon capture and storage
-----	----------------------------

COD	Chemical oxygen demand
DO	Dissolved oxygen
FBR	Fluidized bed reactor
FPS	Frame per second
HRT	Hydraulic retention times
ID	Inner diameter
MFB	Micro-fluidized bed
MEA	Monoethanolamine
PBR	Photobioreactor
PI	Process intensification
RA	Raspberry alcohol
RC	Raspberry compounds
RESS	Rapid expansion of supercritical solutions
RK	Raspberry ketone
STR	Stirred-tank reactor
TGA	Thermogravimetric analyser

Chapter 1 Introduction

1.1 Background

1.1.1 Micro-fluidized bed bioreactor

Fluidized bed has been commonly used as one type of reactors in chemical and process industries. The fluidized particles are suspended and recirculated by the upward liquid/gas flow along the fluidic chamber to generate the extremely turbulent nature of the liquid-solid phase, thus ensuring its excellent multi-phases contact, minimum diffusional resistance, good heat and mass transfer [1]. In recent years, the micro-fluidized bed technique, initially proposed by Potic et al. [2], has attracted more attention as good tool for fast screening of solid process and bioprocesses, but also due to further process intensification. In the field of bioprocessing and bioproduction, the demand for high throughput with controllable and quantitative operating conditions gave rise to the development of bioreactor systems, such as stirred tank reactor (STR), photobioreactor and fluidized bed bioreactor. Compared to the low mass transfer in flask, high shear force from agitated impeller of STR, high capital cost of PBR, the fluidized bed bioreactor relies on the liquid/gas flows for solid fluidization to achieve a high mass/heat transfer with low mechanical stress. Therefore, the micro-fluidized bed bioreactor with the advantages of fast screening, low capital cost and minimum shear stress on cells/strains, stimulates its huge potentials for the first stage of bioprocessing and bioproduction, and will provide fundamental knowledge for the scale-up industrial application in future.

1.1.2 Fungal fermentation for raspberry ketone production

Fungal fermentation is an economic and manageable bioprocessing, relying on the fermentation of different yeasts, bacteria and other microbial in bioreactors to produce various raw materials and food (i.e., yogurt, beer, meads, etc.). For lab-scale research, using miniaturized bioreactors for small-size cell culture is more controllable to obtain the desired biological products, thus benefitting for parallelization, automation and cost reduction.

Particularly, the fungal fermentation of *Nidula niveo-tomentosa* was reported and used for the bioproduction of 4-(4-hydroxyphenyl)-butan-2-one (commonly known as raspberry ketone) [3]. Raspberry ketone (RK) is an important component of raspberry flavour and widely used in food industry [4, 5]. Recently, RK has also been reported to enhance lipid metabolism and prevent obesity, thus stimulating its high demand and significant value in health care [6, 7]. It is known that RK can be produced either from natural plants/fruits such as raspberries, blackberries, grapes and rhubarb [7], or from chemical synthesis [8, 9]. Compared to the synthetic products whose price varies from 8 to 10 \$/kg, the price of natural raspberry ketone can be up to \$20000/kg [10]. According to the EC Flavour Directive, RK production via fungal fermentation is regarded as natural product, indicating the great values of fungal fermentation of *Nidula niveo-tomentosa*.

1.2 Significance and innovation

Cell cultivation in the micro-fluidized bed bioreactor is achieved in the form of cells fluidization by liquid/gas flow, thus having the advantages of fast screening, sufficient mass transfer rate but low shear stress compared to other types of bioreactors. To fluidize the microorganisms with micro-scale size and much less density than water, the cell immobilization technologies (i.e., attachment, entrapment, self-aggregation, containment) were developed to enhance cell stability in continuous fluidization condition [11, 12]. However, the long-term cell cultivation through the immobilized cell fluidization currently suffers from the cell detachment from carriers or cell leakage from encapsulation. In contrast, the fungus of *Nidula niveo-tomentosa* grow from free mycelia to mature pellets with up to centimetres-scale size and higher density than water, which means the fungal pellets can be directly fluidized and cultivated in the micro-fluidized bed bioreactor without the use of cell immobilization.

Regarding the production of natural raspberry ketone, the typical methods of microbial or enzymatic processes have been attempted to promote the yields [3, 13, 14], but these methods

involve the submerged cultivation of the cells/fungi in the flask due to its simple and convenient operations. However, the low mass transfer and limited dissolved oxygen by flask culture would hinder the cells growth and consequent yield. More importantly, limited volume of the flask means the production is unscalable for industrial application.

In this project, the fungal fermentation using the micro-fluidized bed bioreactor for RK production is a novel attempt, which not only provides the sufficient oxygen and nutrients by the continues and liquid flows, but also mitigates the cell damage/death mainly resulted from the moving parts in other bioreactors. Most importantly, this work is used as the early-stage screening for RK production, which will be fundamental basis for the following scale-up industrial application in future.

1.3 Aims and objectives

This project overall aim is to investigate the hydrodynamics of the miniaturized fluidized bed reactor in general and use 3-phase fluidized bed bioreactor for screening and optimization fungi cultivation and raspberry ketone bioproduction. The specific objectives of the project are:

1. Design, fabrication and optimization of miniaturized 3-phase fluidized bed.
2. Study of hydrodynamics of optimized fluidized bed reactor.
3. Optimization and screening of 3-phase fluidized bed bioreactor for fungi fermentation.

First year research mainly focused on the fabrication and optimization of the fluidized bed. The miniaturized fluidized bed was designed via Google SketchUp and then fabricated using 3D printing techniques. The final cross-section area of the bed was decided to be 15×15 mm after many fluidization tests using fluidized beds with different dimensions, to balance the wall effect and the requirement of minimizing solids (fungal cells) quantity to be used in testing. The maximum bed height is 15 cm due to the limited building volume of Form2 printer ($145 \times 145 \times 165$ mm), although this can be overcome by printing in parts if necessary.

Because the fluidized bed is used for cell cultivation, the bubbles inside the chamber must be smaller (less than 3mm) to avoid bubbles rapture which could result in cell damage or death. Therefore, in this research the capillary tubing embedded within 3D printed liquid distributor are used for gas sparger, which enables to limit bubble size and avoid bubble rapture. The 3D-printed liquid distributor is made up with uniformly placed tubes (1 mm × 1 mm in cross section) among the rectangular plates (15mm × 15 mm), is designed and selected for liquid distributor due to its good performance in distributing liquids while keeping the solids above the distributor plate.

Second year research is made up of hydrodynamics characterization of miniaturized fluidized bed and the preparation of fungal fermentation using fluidized bed bioreactor. Hydrodynamics study of the fluidized bed is mainly divided into two parts: liquid-gas bubble column and liquid-solid fluidization. In liquid-gas bubble column, the effects of gas velocity, liquid velocity, diameter of gas orifice on bubble size, bubble velocity, bubble volume fraction have been characterized. The study of bubbles generation and movement is a fundamental but significant part for the bubbles control in aerobic fungal fermentation. While in liquid-solid system, the mature fungal pellets of 2-3 mm in diameter and $\sim 1.1 \text{ g/cm}^3$ in density were used to study the effects of liquid and gas flowrates on pellet fluidization.

The final part of PhD project is the investigation of fungal fermentation using fluidized bed bioreactor. This part of research is collaborated with Singapore Institute of Food and Biotechnology Innovation (SIFBI), Singapore, where the student is trained and supervised by Dr Yvonne Chow. The fungal fermentation is aimed to produce the target product of raspberry ketone by the fungi cells *Nidula niveo-tomentosa*, which will be inoculated and cultured in the miniaturized fluidized bed bioreactor, to characterize pellets morphology and RK production rate during fermentation. Meanwhile, the operating parameters including glucose concentration, seed culture age, inoculant concentration and UV exposure time were characterized using flask

culture, to explore the fungal growth and related production. To differentiate the fluidized bed bioreactor performance on fungal fermentation, other types of bioreactor systems including flask culture (48 ml), stirred tank reactor (750 ml), panel bioreactor (400 ml) were used to compare their effects on the fungus growth and raspberry compounds production. The fungal fermentation using bench-scale fluidized bed bioreactor provides the fundamental knowledge for bioreactor screening and scale-up fermentation in future.

Chapter 2 Literature review

2.1 Introduction

This chapter consists of the review of micro-fluidized bed (MFB) and fungal fermentation. In MFB part, the fundamental research of MFB and its applications have been reported. In the fungal fermentation part, the fungal growth and pellet formation process are briefly reviewed. Besides, the cultivation parameters that affect the process of pelletization and subsequent bioproduction are also summarized. Finally, the raspberry ketone production via fungal fermentation in different bioreactors have been introduced.

2.2 Micro-fluidized bed

The micro-fluidized bed reactor (MFBR) is a novel technology for engineering processing and screening application. The MFBR has exhibited good mixing, high mass/heat transfer, reduced reaction time and cost, but issues that remain unsolved are the low fluidization quality and scalability. In this section, fundamental studies are reviewed to explain and reveal the benefits of the miniaturized reactor for rapid processing and screening. Subsequently, recent progress of the MFBR applications were evaluated and compared with other types of reactors from the perspective of process intensification (PI). Finally, the challenges and prospects for this technology for PI are also briefly discussed.

Since its re-introduction by Potic et al. [2] in mid 2000s, the MFB was either defined by the principle of small hydraulic diameter, or as general small-scale fluidized beds in conventional engineering context showing apparent changes in hydrodynamics properties. Definitions of MFB based on hydraulic diameter of the bed vary from sub-500 μm [15] to several centimetres [2, 16], although the widely asserted boundary between macro- and micro-fluidization is 1 mm [15, 17]. From the degree of gas back-mixing, Xu et al. [18] defined the MFB with the inner diameter of 21 mm and the static bed height in the range of 20–50 mm. Besides, Xu et al. also

[Fig. 2.1](#) summarizes the bibliographic network of MFB studies from the Scopus database. According to the bibliographic network, it is obvious that MFB techniques have been intensively studied in terms of the fundamental characteristics (illustrated by green and orange clusters), as well as applications including chemical conversions (indicated from yellow and blue clusters) and bioprocessing (presented by red clusters). Based on the bibliographic network, this chapter aims to review the fundamental characteristics of MFB, as well as the recent progress of MFB applications from the perspective of process intensification. Finally, the current bottlenecks and potential future work regarding the micro-fluidized bed systems are also addressed.

2.2.1 Characteristics of MFB

In this section, the fundamental research on the minimum fluidized velocity, mixing performance and mass transfer of micro-fluidized beds are discussed with regard to the hydrodynamics performance from micro-fluidized bed to macro-fluidized bed, but also principally addresses the significance to process intensification.

2.2.1.1 Brief history of micro-fluidization

A brief history of micro-fluidization development is illustrated in [Fig. 2.2](#). The study of MFB can be traced back to the 1980s when Scott & Piskorz [25, 26] used a fluidized bed reactor of 20 mm ID for flash pyrolysis of coal and wood samples. Although Scott & Piskorz built this fluidized bed and initiated the research in 1982, Funazukuri et al. [27] explicitly called it “micro-fluidized bed” when using the same fluidized bed reactor for pyrolysis of cellulose in 1986. However, the study of micro-fluidized bed seemed to be suspended afterwards. From the beginning of this century, the size of fluidized beds has been further reduced. Effendi et al. [28, 29] characterized carbon deposits in the quartz fluidized bed with the column ID less than 10 mm. Afterwards, Potic et al. [2] in 2005 re-introduced the concept of MFBs with an internal diameter of only a few millimetres (i.e. 1-3 mm), followed by Xu et al. [19] who investigated

the wall effect and operability of the MFB. This time the research into micro-fluidized bed did not vanish again as it was supported by co-current research interest in microfluidics. This can be considered as the starting point on micro-fluidization research and indeed the study from Potic et al. is commonly regarded as the initial study in the field [19, 23, 30].

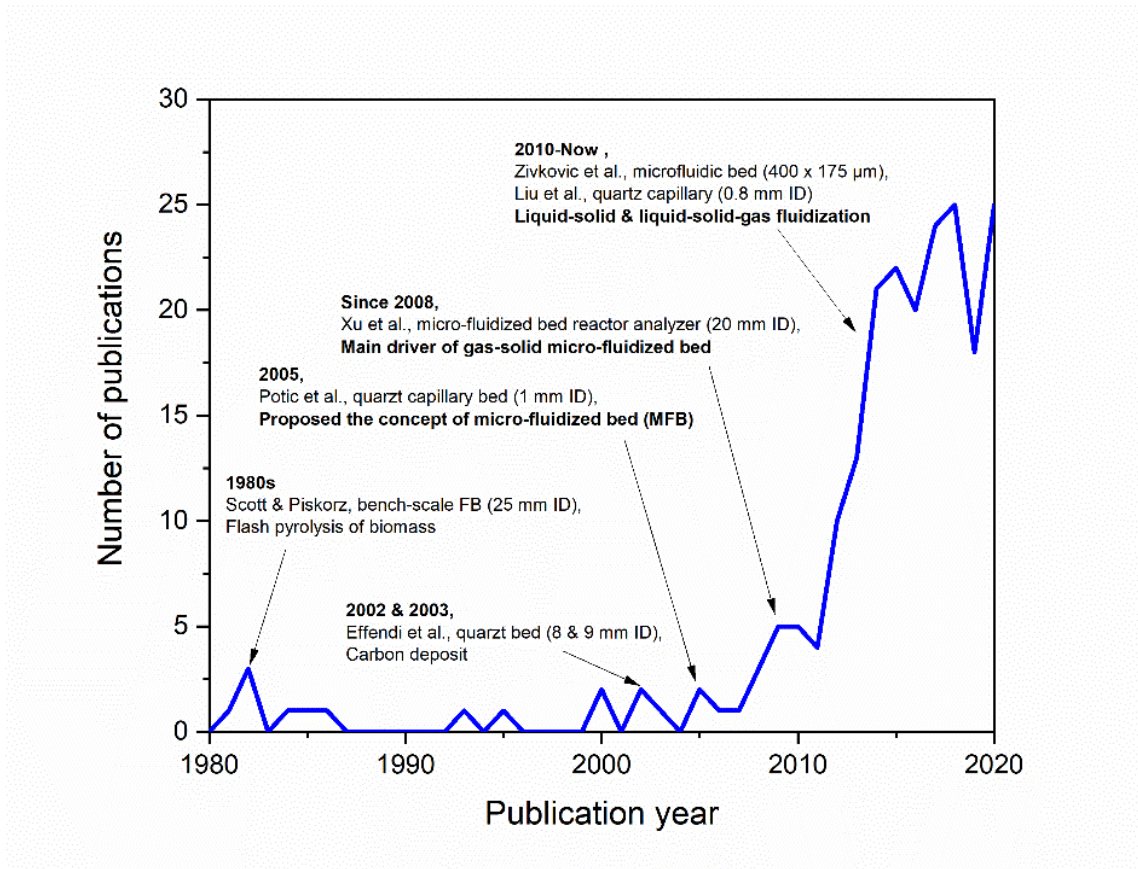


Fig. 2.2. Graph of the number of MFB-related publications versus publication year. Indicated on the curve is an outline of the key development of MFB.

Although the reports of MFB by Xu’s group came after Potic et al. [2], Xu and his colleagues actually kick-started the field by not only characterizing the hydrodynamic parameters (i.e. particle size, column size, fluidization velocities) but also broadening the application of gas-solid MFB in areas such as gasification, pyrolysis and combustion. One note is that the work started in 2005 [31] but the first reports came a bit later. Furthermore, Zivkovic et al. [15, 32] and Liu et al.[33, 34] promoted the development of MFBs which were based on the liquid-solid and liquid-solid-gas micro-fluidization. Meanwhile, Pereiro et al. proposed a magnetic micro-

fluidized bed for bacteria extraction [35, 36] and DNA analysis [37], thus broadening the use of micro-fluidized bed system in biological area.

2.2.1.2 MFB design and fabrication

To date, different types of MFBs have been reported with a variety of fabrication approaches such as soft lithography techniques, additive manufacturing, micro-machining, and capillary systems, shown in Fig. 2.3. The rectangular or cylindrical bed column with different hydraulic diameters strongly affect the fluidization performance, thus investigating the hydrodynamic characteristics of MFB is essential for bed design and optimization. As shown in Fig. 2.3a, Zivkovic et al. [38] developed microfluidic beds with microchannels formed from a PDMS chip by a simple, cheap and fast method known as lithography [39]. do Nascimento et al. [22, 40] designed and fabricated a robust MFB by milling square cross section millimetre channels into a Perspex block fitted with a distributor (Fig. 2.3b). In recent years, 3D-printing techniques have enabled the fabrication of complicated MFB (Fig. 2.3c) which could be hard to design and manufacture by conventional mechanical tools, but the effect of surface roughness of the printed parts may alter fluidization performance [40, 41]. As shown in Fig. 2.3d, the quartz capillaries with various internal diameters are more commonly used as the bed column, as the transparent bed wall allows for the visualization analysis [33]. However, the MFBs mentioned above may not endure chemical reactions where high temperature is involved. Instead, the fluidized beds constructed from stainless steel have been proposed by other researchers [42]. To meet the requirements of complex gas-solid reactions, Xu et al. [43] proposed a micro-fluidized bed reaction analyzer (MFBRA) which enables on-line pulse feeding and rapid reaction in high-temperature conditions (Fig. 2.3e &f), leading to the development of multifunctional micro-fluidized bed with online monitoring and processing capacities. For instance, this MFBRA was reported to prepare Ni/AC catalysts, which were online characterized by the plasma-atomic emission spectroscopy (ICP-AES), transmission electron

microscope (TEM), temperature programmed desorption (TPD), Fourier transform infrared spectroscopy (FT-IR), and X-ray photoelectron spectroscopy (XPS) [44].

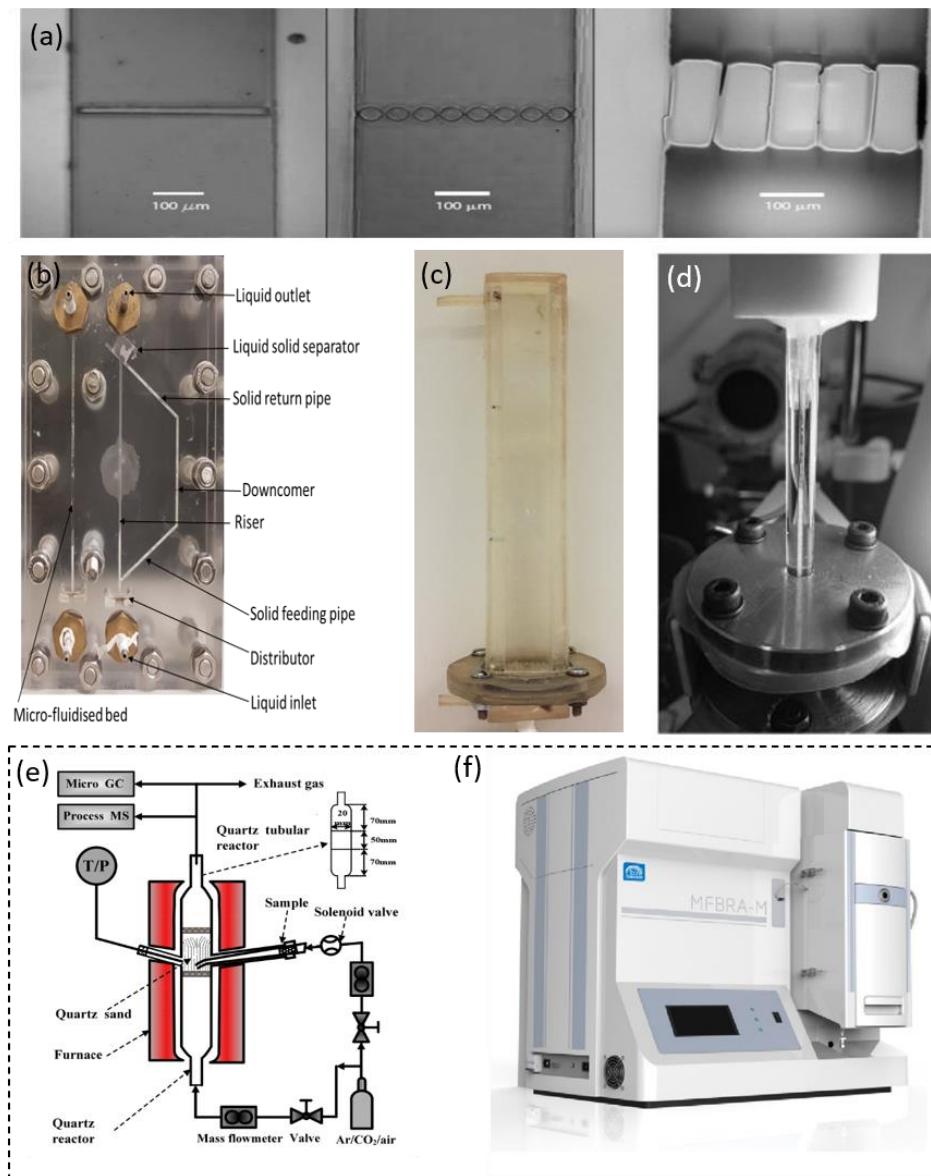


Fig. 2.3. Examples of MFB systems: (a) the MFBs with $400 \times 175 \mu\text{m}^2$ cross-section were fabricated in a polydimethylsiloxane (PDMS) chip by standard soft lithography techniques [15], (b) micro-circulating fluidised bed design was made by milling 1 x 1 mm cross-section channels into Perspex, (c) a 3D-printed MFB with cross-sectional area of $15 \times 15 \text{ mm}$ [45], (d) a micro-fluidized bed whose bed column is made up of a quartz capillary of 0.8 mm inner diameter, 6 mm outer diameter and 60 mm length, (e-f) a MFB reaction analyzer (MFBRA) developed by the Institute of Process Engineering (IPE), Chinese Academy of Sciences [46].

2.2.1.3 Minimum fluidization velocity

Minimum fluidized velocity U_{mf} is generally defined as the smallest velocity of the gas/liquid flow to make the packed bed into loosen bed. Knowledge of U_{mf} enables one to obtain a desired fluidization velocity and maintain good reactor operation. In the context of a gas-solid MFB

system operated at above U_{mf} , the gas flow completely supports the weight of bed and the pressure drop (ΔP) remains constant (Fig. 2.4a). Therefore, using a pressure transducer to compare pressure drop across the bed at different gas velocities is an effective method to determine the value of U_{mf} [19, 30]. It is noted that the pressure drop measured by methods of ascending is much higher than that by descending gas velocity. Han et al. explained this by the wall effects, as the downwards wall friction force during fluidization resists particles expansion [47]. Besides, they also argued that the bed voidage is relatively lower for fluidization process than for defluidization process, leading to much higher pressure drops. Alternatively, characterization of U_{mf} in gas-solid fluidization can be roughly assessed from the flow regimes, in which the minimum fluidization corresponds to slight bed expansion, followed by flow regimes of particulate, bubbling, slugging and turbulence bed with the increase of gas flowrate [23].

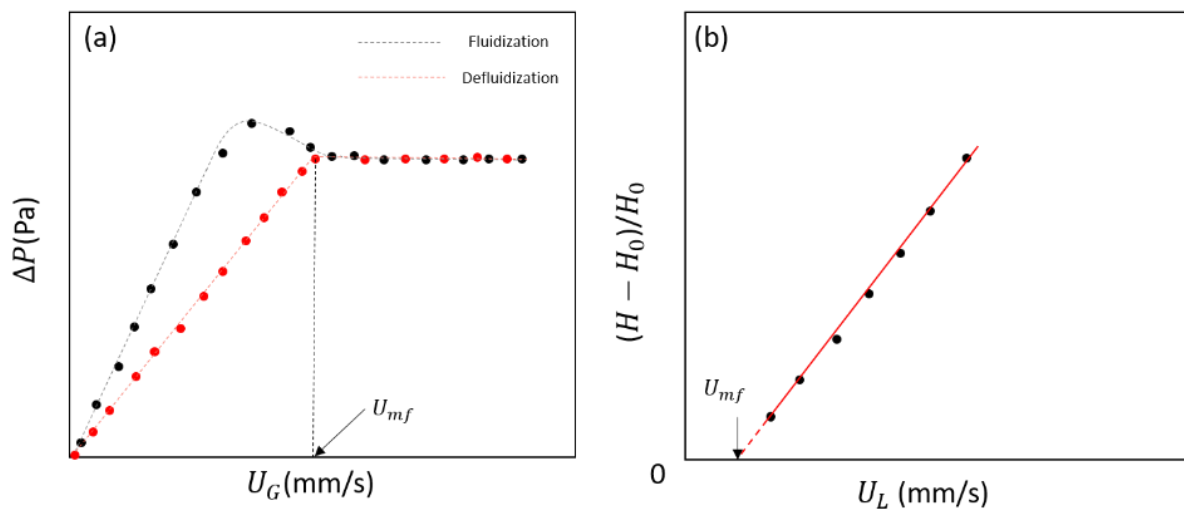


Fig. 2.4. Schematics of determining U_{mf} in liquid-solid and liquid-gas MFB: (a) bed expansion curve (bed ratio versus superficial liquid velocity) to extrapolate U_{mf} , (b) typical pressure drops profile (fluidization and defluidization) generated by comparing the pressure drops at various superficial gas velocities.

For liquid-solid systems, the method of pressure drop is also applicable although it may be difficult to measure U_{mf} in an industrial-scale fluidized bed system. Therefore, U_{mf} for the liquid-solid MFB is experimentally obtained through visual observations with the use of high-speed camera [22, 33, 38, 48]. In Fig. 2.4b, U_{mf} is determined by extrapolating the bed

expansion curve which is created by reading liquid velocity and corresponding bed expansion ratio. Besides the experimental methods, there are many mathematical models for predicting U_{mf} [49-53]. One of the most commonly utilized equation was proposed by Ergun [54]:

$$\frac{\Delta P}{H} = \frac{150\mu}{\phi_p^2 d_p^2} \frac{(1-\varepsilon)^2}{\varepsilon^3} U_F + \frac{1.75\rho_F}{\phi_p} \frac{(1-\varepsilon)}{\varepsilon^3} U_F^2 \quad (2.1)$$

where H is the bed height (not the column height), U_F , ϕ_p , ρ_F , d_p , ρ_p , g and μ refer to the superficial velocity of fluid, particle sphericity, density of fluid, particle diameter, particle density, acceleration due to gravity and dynamic fluid viscosity, respectively. On the right side of Eq. (1), the first term refers to the pressure loss due to viscous effect dominantly in the laminar flow region, while the second term is the pressure loss resulted from inertial forces with high Reynolds numbers [55]. The Ergun equation has been widely used to predict the pressure drop of the packed bed based on the relationship of pressure drop and fluid velocity, especially involving the regular-shaped spherical particles [56, 57].

However, in the micro-scale fluidic system, the parameters of surface force and wall effects must be considered. The importance of surface force and inevitable wall effect may become dominant over the volumetric forces such as gravity, thus affecting the performance of particles fluidization. In recent years, many researchers have identified the existence and influence of surface force and wall effect on U_{mf} , by characterizing the parameters such as bed-to-particle ratio d_B/d_P [16, 22, 33, 58, 59], initial bed height H_0 [19, 30, 60], particle properties [15, 61], wall roughness [23], etc. Studies of surface force and wall effects on MFBs are summarized and presented in Table 2.1. Many works focused on d_B/d_P and H_0 to conclude that U_{mf} increase with the increase of H_0 or the decrease of d_B/d_P . In fact, the decrease of d_B/d_P results in an intensified wall effect due to the increased contact area between bed wall and particles. The contact area varies linearly with d_B^2 while the bed volume varies linearly with d_B^3 . Thus, a reduction in d_B causes the relative magnitude of bed-wall friction exceeds the magnitude of

drag force between particles and fluid [23]. Similarly, larger static bed height H_0 results in bigger bed-wall contact area, namely a bigger wall friction. By comparing the deviations between the experimental minimum fluidization velocity $U_{mf,e}$ and the theoretical minimum fluidization velocity $U_{mf,t}$ calculated by conventional correlations such Ergun equation, this may enable one to predict and study the unavoidable wall effect and surface force in MFBs.

Table 2.1 Summary of the influences of different parameters on U_{mf} in MFBs.

Reference	Bed properties	Parameters	Results & Conclusions
Doroodchi et al. [58]	Liquid-solid bed; Bed sizes: 0.8, 1.2 17.1 mm; Particle size: 225 μm .	d_B/d_P ;	U_{mf} increased with the decrease of d_B/d_P
Zivkovic and Biggs [15]	Liquid-solid bed; Bed size: $400 \times 175 \mu\text{m}^2$; Particle size: 26.5, 30.5, 34.5 and 38.5 μm .	Liquid/particle properties	Glass micro-particles can be fluidized by Ethanol instead of water in the PMMA microchannels.
Liu et al. [19]	Gas-solid bed; Bed size: 0.8 mm; Particle sizes: 22, 37 and 58 μm .	d_B/d_P ; H_0	U_{mf} decreased obviously with decreasing d_P and increasing d_B ; Little relation with both d_P and H_0 when $d_B > 20\text{mm}$.
Wang and Fan [16]	Gas-solid bed; Bed size: varying from 700 μm to 5 mm; Particle size: 53 μm .	d_B/d_P	U_{mf} decreased with the increase of d_B when d_P kept the same.
do Nascimento et al. [22]	Liquid-solid bed; Bed sizes: 1, 2 mm; Particle size: 21 μm .	d_B/d_P	The increase in U_{mf} scales linearly with the decrease of d_B/d_P .
Guo et al. [60]	Gas-solid bed; Bed sizes: 4.3, 5.5, 10.5, 15.5, 20.5, 25.5 mm; Particle sizes: 30, 51, 53 μm .	d_B/d_P ; H_0	U_{mf} increased with decreasing d_P ; U_{mf} was increased linearly with H_0
Li et al. [48]	Liquid-solid bed; Bed sizes: 0.8, 1.45 and 2.3 mm; Particles sizes: ranging from 22 to 58 μm .	d_B/d_P	U_{mf} increased with the decrease of d_B/d_P
Rao et al. [30]	Gas-solid bed; Bed sizes: 1.6 and 2.4 cm; Particle sizes: ranging from 100 to 550 μm .	d_B/d_P ; H_0	U_{mf} increased as d_B was reduced, or H_0 was increased.
Tang et al. [59]	Liquid-solid bed; Bed sizes: 3.15 and 11.6 mm; Particle sizes: varying from 89 to 352 μm .	d_B/d_P	U_{mf} was 1.67 to 5.25 times higher than theoretical value when d_P/d_B varied from 0.017 to 0.091.
Li et al. [34]	Liquid-solid bed & Gas-liquid-solid bed; Bed size: 3 mm; Particle sizes: ranging from 50 to 300 μm .	d_B/d_P	U_{mf} increased with the decrease of d_B/d_P
Lu et al. [42]	Liquid-solid bed; Bed sizes: 35 mm; Particle size: 30 μm .	Temperature; Pressure	U_{mf} increased with increasing temperature but decreases with increasing pressure.
Vanni et al. [62]	Liquid-solid bed; Bed sizes: 2, 3, 3.2 and 5 cm; Particle sizes: 50, 70 and 105 μm .	d_B/d_P	U_{mf} increased with the decrease of d_B/d_P
Chen et al. [61]	Liquid-solid bed; Bed size: 46.25 mm; Particle size: 10.31 μm .	Particle surface hydrophobicity	U_{mf} decreased after the ultrafine particles (Al_2O_3) was treated with a surfactant.

Besides the study of d_B/d_P and H_0 , the properties of liquid and solid phase can also influence the fluidization performance. Zivkovic et al. [32] experimentally studied the micro-fluidization using a rectangular microchannel of $400 \times 174 \mu\text{m}^2$, in which the glass microspheres of $30.5 \mu\text{m}$ was unable to fluidize using deionized water due to the adhesive effects between glass particles and the PMMA bed wall, even though the non-ionic surfactant (Tween 80) was used. When changing the fluidizing medium of deionized water into ethanol, the particles were able to fluidize but the surface force and wall effect was still existed. Chen [61] explored the influence of surface hydrophobicity in fluidization. By using the surfactant-treated ultrafine particles (Al_2O_3), liquid-solid contact angle of ultrafine particles increased, which not only indicated the existence of surface force between particles and bed walls, but also provided a possibility to achieve a better fluidization. Actually, it is not uncommon to decrease the friction or attachment between solids and bed wall with the use of surfactant. For instance, Pluronic F-68 (PF-68) is a widely used surfactant to decrease cell-bubbles interaction and attachment in cell cultivation[63].

Currently, little is known about wall effects and surface force study in MFBs in terms of how to minimize these effects. One reason is the variety of particle properties (size, shape, density, material, etc.), fluidizing medium (density, viscosity, contents, etc.), bed geometry and material, makes it difficult in solving the problem of the bed-wall effects. Another reason is that the technique of MFBs is still in the early stage and not the mainstream reactors with little attention concentrated on these issues. Anyhow, for real utilization of MFBs, surface force and wall effect could significantly affect the fluidization performance in the MFB, which cannot be neglected.

2.2.1.4 Mixing studies

Effective mixing is aimed at achieving a thorough and rapid interaction physically and chemically between multiphase flows during the engineering processing, particularly in those

area where heat, mass transfer and reactions are involved [64]. According to the different mixing mechanisms on different spatial scales, mixing process is subdivided into: micro-mixing (relied on molecular diffusion), meso-mixing (e.g. formation and disintegration of flow eddies) and macro-mixing (e.g. flow folding and turbulent structures) [65, 66]. Different from the diffusive mixing in micro scale, the flow patterns in fluidized bed reactors are directly related to meso-mixing and macro-mixing [67]. From this point of view, micro-fluidized bed reactor has an excellent mixing property because: (1) the compact design of fluidic chamber increases the surface to volume ratio, thus enhancing the contact area; (2) the fully fluidized solids enhance the contact time between multiple phases.

Liquid mixing. Doroodchi et al.[68] compared the mixing performance of two miscible fluids between the MFB and particle-free capillary tube. In their study, fluidization of the borosilicate particles of $\sim 98 \mu\text{m}$ by sodium iodide solution in a 1.2 mm capillary tubing bed dramatically decreased the mixing time, which was reflected by using a dye dilution technique. Although their studies confirmed that the MFB enhanced mixing performance, it did not explain the relationship between bed voidage and mixing efficiency, which is important at the macroscopic level. Such a relationship between bed voidage and mixing efficiency was experimentally investigated by Zivkovic et al. [64], who confirmed that the superficial velocity and bed voidage strongly influenced the mixing performance. At low superficial fluid velocity, MFB was not affected as the bed voidage was close to a packed bed. However, the voidage began to enhance mixing when the bed was expanded. Additionally, they demonstrated that the mixing effect in the MFBs was about 3 times greater than those in particle-free channel (Fig. 2.5a-c), which was in good agreement with the findings from Doroodchi et al. [68]. Apart from the experimental studies, Derksen [69] characterized the enhancement of bed voidage on mixing performance by means of direct numerical simulation, which confirmed that the scalar mixing

in the fluidized bed yielded a more uniform distribution than that in the fixed bed (Fig. 2.5d & e).

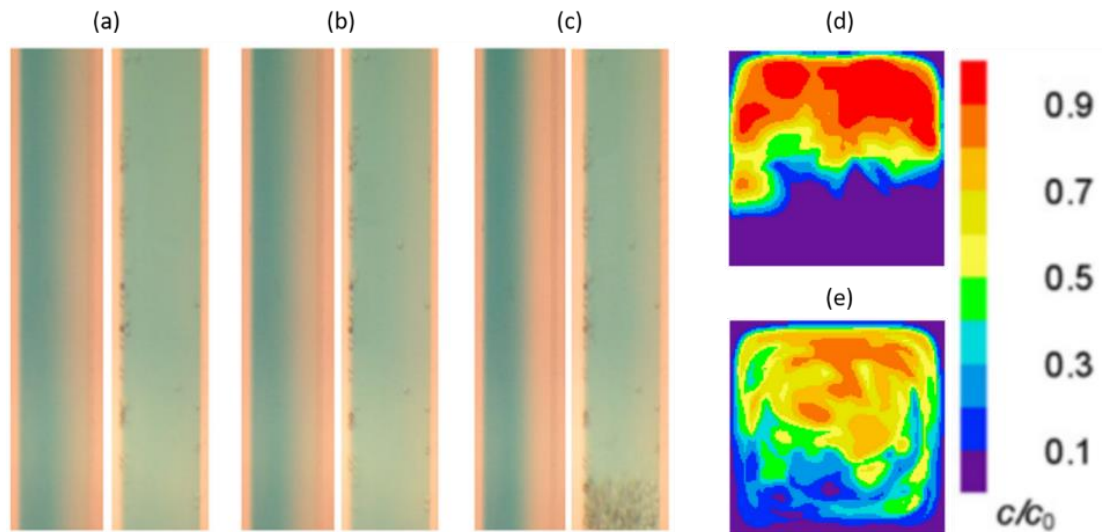


Fig. 2.5. Comparison of mixing in the particle-free channel and micro-fluidized bed at different liquid flowrates: (a) 190 $\mu\text{m/s}$, (b) 286 $\mu\text{m/s}$, (c) 361 $\mu\text{m/s}$, respectively [64], Simulation snapshots of the scalar concentration fields in the exit plane for (d) fixed bed and (e) fluidized bed [69].

Solid mixing in gas-fluidized bed. Compared with liquid-solid fluidization, gas-solid fluidized bed reactors are more widely applied in industrial process such as combustion, gasification, polymerization, catalytic cracking and oxidation [55, 70]. Fig. 2.6 presents a typical gas mixing profiles in the gas-solid micro-fluidized bed, where the transition of the bed regimes from packed bed to turbulent bed has occurred [71]. During the transition of bed regimes, the bed of Geldart A particles starts to expand at U_{mf} and becomes bubbling at the gas velocities of $2 \times U_{mf}$, while that of Geldart B directly transits from a static bed into a bubbling bed. The Geldart C and D beds experience the channelling and spouted bed regime, respectively, before reaching the turbulent bed regimes [72]. Alternatively, Han et al. [47] summarized the reported experimental data and identified the particulate, bubbling, slugging and turbulent fluidization regimes based on superficial gas velocity, ratios of d_B/d_P and H_0/d_B . However, the overall particle mixing in gas-solid fluidized bed is much less uniform both in axial and radial directions in comparison to liquid-solid or liquid-solid-gas fluidized beds [73]. Although

increasing the fluidization velocity is a simple and effective method to promote mixing effect, many researchers pointed out that increasing the gas velocity mainly improves the axial mixing effect [74, 75]. The non-uniform gas-solid mixing due to the inevitable accumulation of solids near the reactor wall was also reported by Wang et al. [76], who simulated the effect of injector structures and locations on the mixing characteristics of trace sample and bed material in MFB reaction analyser.

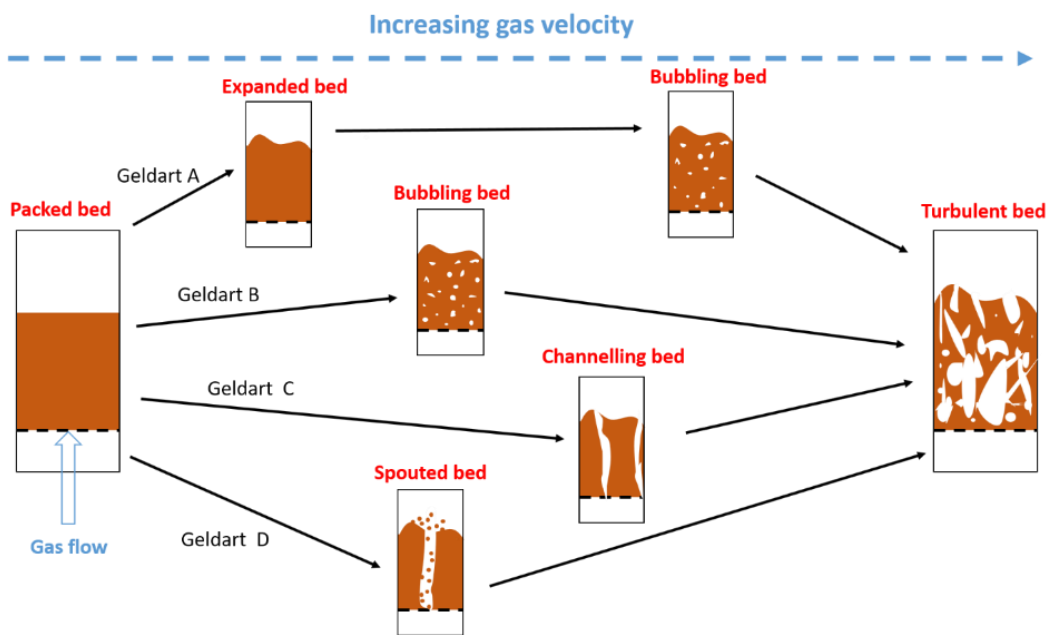


Fig. 2.6. Schematic of the bed regime transitions (from packed bed to turbulent bed) in the gas-solid micro-fluidized bed with the inert of Geldart type A, B, C, and D powders, respectively.

To improve the radial mixing, this may require the sparger design to be optimized in the following ways: (1) increasing the gas orifice number; (2) optimizing sparger design for uniform distribution of bubble flows; (3) minimizing the non-homogeneous radial solids distribution. Fig. 2.7 shows the typical sparger designs with evenly-placed gas orifices, which are effective at improving the mixing in radial direction, although some orifices near the gas entrance discharge more compared to the gas holes near the rear end with the effect of pressure drop among gas orifices [77]. To promote solid mixing in the small-scale fluidized bed, several novel distributor designs have been proposed recently. For instance, McDonough et al. [23]

used the additive manufacturing technique to fabricate the MFB which contained a planar distributor plate featuring 1-mm square holes, leading to the improvement in their gas-solid fluidization study. Odeley et al. [78] demonstrated that the particle radial velocity increased 5.2 times when performing swirling fluidization with the flow channels oriented at 45° (with respect to their vertical flow channel counterparts). Similarly, the swirling fluidization of the particle bed was reported to intensify the heat and mass transfer as well as the mixing rate in a 3D-printed toroidal fluidized bed (50 mm ID and 10 mm annular width) [79]. Apart from the optimized gas distributor designs, the application of external loads (e.g., magnetism, ultrasound, thermal, etc) to drive the flow and enhance mixing efficiency has also been reported [80-82]. For instance, Karimi et al. [83] introduced ferromagnetic particles in the magnetically assisted fluidized bed (28 mm ID and 800 mm height) to improve mixing, which relied on the magnetic solids to decrease the agglomeration of solids.

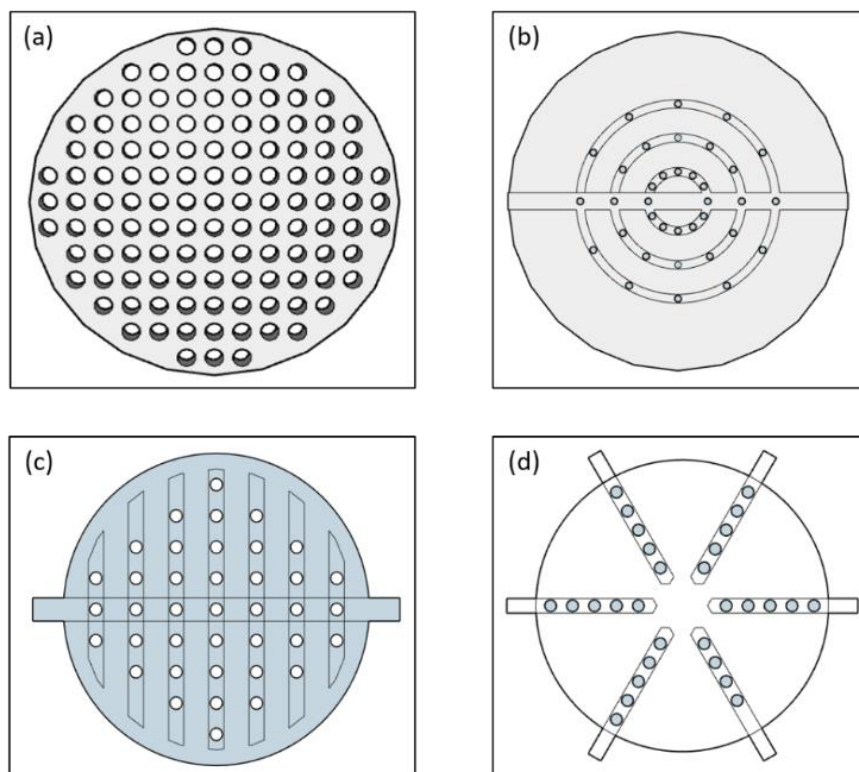
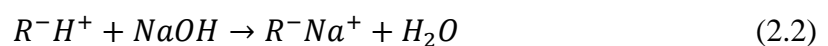


Fig. 2.7. Schematics of gas spargers with different design: (a) sieve plate sparger, (b) multiple ring spargers, (c) spider-shape sparger, (d) multiple pipe sparger

To date, many reports on the study of mixing efficiency cover liquid-solid and liquid-gas fluidized beds. Although the three-phase fluidized bed is more widely used in industry such as wastewater treatment and beer fermentation, only a few studies on the three-phase fluidization were introduced. Note, for solids with uneven density and size, high flow rate may result in the particle segregation, consequently this hinders the mixing in fluidized bed reactors [74, 84]. Thus, in real application, the non-uniformity of solid phase needs to be considered.

2.2.1.5 Mass transfer studies

The accurate prediction and analysis of mass transfer are essential for any reactor design and industrial processing. Most experimental studies of mass transfer have involved the dissolution of benzoic acid particles, which are easily pelleted from powders and exchange mass with fluid phase. The mass flow rate is generally determined in two ways: (1) by measuring the benzoic acid concentration in the inlet and outlet of the fluidization column; (2) by comparing the quantity of the particles before and after dissolution. The total interfacial area was obtained by multiplying the area of one particle, deduced from its shape and size, by the number of particles [85]. Based on the literature, the fluidized bed is composed entirely of the active particles (i.e., in fluid catalytic cracking) in Fig. 2.8a [86-88]. Another situation illustrated in Fig. 2.8b shows that the column consists of both the inert particles (i.e. sand or glass beads) and benzoic acid solids [89, 90], which corresponds to the practical situations such as the combustion of char particles in a fluidized bed boiler. Besides the utilization of active particles, ion exchange for determining mass transfer in fluidized bed has also been reported [91-93], which used a cationic resin initially in the H⁺ form and passed a dilute sodium hydroxide solution through the fluidized bed [92]. The reaction is described as follows:



Here, R^- represents the solid ion exchange matrix. The mass transfer was determined from the measurement of inlet and outlet concentration using probe needles for on-line productivity

analysis [93]. In terms of PI, the micro-circulating fluidized bed has also been proposed for mass transfer study [94], as the circulating fluidized bed can enlarge the active zone fraction to total bed by the continuous fluidization in column (Fig. 2.8c). So far, a lot of progress has been made on the intensification of mass transfer in fluidized bed based on the experimental studies. However, more advanced experimental techniques are still required to help achieve a comprehensive understanding of the mass transfer mechanisms as well as promote the measuring accuracy.

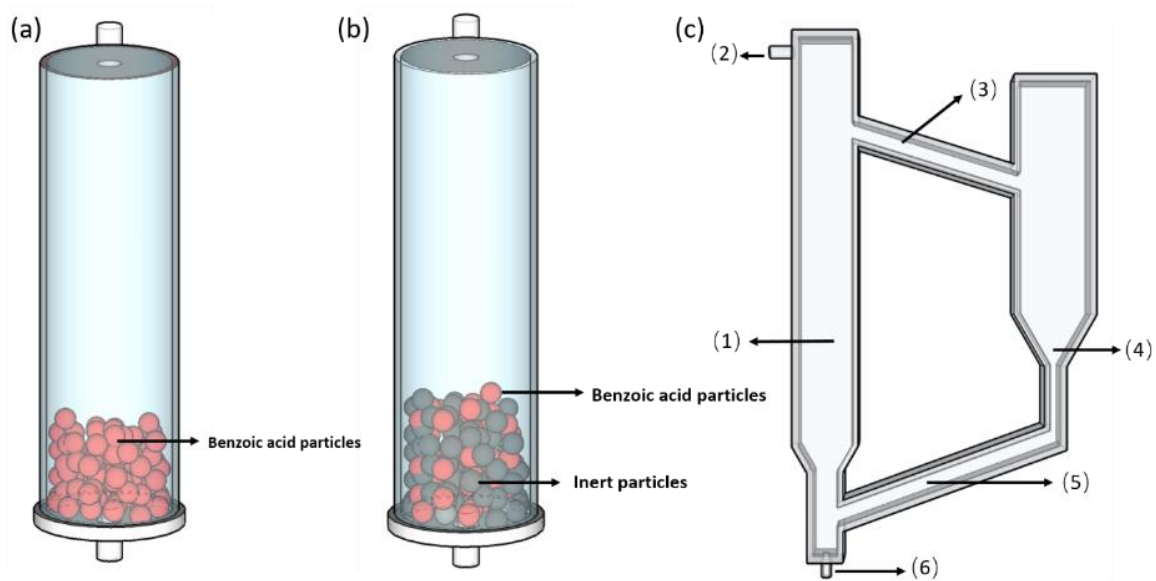


Fig. 2.8. (a) fluidized bed consists of purely benzoic acid particles, (b) fluidized bed is composed of benzoic acid pellets and inert particles, (c) simplified model of circulating fluidized bed, (1) riser column, (2) outlet, (3) top particles return pipe, (4) settler and calming column, (5) bottom particles return pipe, (6) inlet.

Theoretical analyses have also been conducted on the mass transfer studies in fluidized beds using empirical/semi-empirical correlations. Typically, these correlations involved the Sherwood number (Sh), a dimensionless number which is expressed as a function of Reynolds number (Re) and Schmidt number (Sc) through using the Frossling-type equation [95]:

$$Sh = k + b \times Re^c + Sc^d \quad (2.3)$$

where k , b , c and d refer to the parameters in each specific experiment. The first term on the right-hand side (k) represents mass transfer in diffusive conditions, while the second one refers

to the enhancement of mass transfer caused by the convective fluid flow around the solids [96]. Based on the Frossling-type equation, many authors have sought to relate Sh to Re based on particle size, superficial liquid velocity, terminal velocity, and liquid viscosity.

One of the fundamental investigations is the effect of particle properties on mass transfer coefficient K_C . Ballesteros et al. [85] demonstrated that K_C was independent of the solid particles diameter through the dissolution study of the angular particles in a liquid fluidized bed (50 mm ID), in which the particle shape remained unchanged during dissolution. The column diameter and initial bed height have been observed to have no influence on mass transfer rate [93, 97]. The effects of bed voidage on K_C were presented by Dwivedi and Upadhyay[98]. By comparing the liquid-solid mass transfer in fixed and fluidized beds, they concluded that K_C was inversely proportional to bed voidage. More specifically, Yang et al. [99] found that the largest mass transfer capacity in liquid-solid mini-fluidized bed reactor when the bed voidage was 0.7 in their photocatalytic degradation research. The application of miniaturized fluidized bed involving high mass transfer coefficient will be reviewed in next section.

These proposed and modified correlations can analyse mass transfer to some extent. However, several discrepancies exist among the results from the previous literatures, making it difficult to unify the analysis and evaluation. For instance, the column diameter was reported to have no influence on mass transfer rate [93]. However, Arters and Fan [100] pointed out that the mass transfer near the wall region of the gas-liquid-fluidized bed (40 mm ID and height) was much lower than in the radially centred region; they attributed this to the weak turbulences along the bed wall. Instead, Arters and Fan concluded mass transfer coefficient was independent of liquid flowrate [87], while Boskovic-Vragolovic et al. [89] demonstrated a slight decrease in mass transfer rate with increasing velocity in the liquid-solid fluidized beds with 40 mm ID and particle size ranging from 0.5 – 2.98 mm. These conclusions were

conflicting because of the limited range of parameters for correlations and different operating conditions, which implies that a single correlation is inadequate for describing the complete behaviour over the entire range of Reynolds number or Schmidt number. Thus, the segregated correlations may be a feasible approach to well-fit the experimental observations and describe the actual mass transfer mechanism under various fluidization systems.

2.2.2 Applications

The adoption of PI-based techniques has led to rapid advancement with the application of miniaturized fluidized bed reactors in conventional chemical processing, as well as in areas such as environmental issues and biological industrial. In this section, the miniaturized fluidized bed techniques are discussed from a PI perspective.

2.2.2.1 Solid processing

Granulation screening

High-energy ball milling, electro-deposition, liquid phase reduction are techniques capable of performing granular processing, but these methods require either high cost or complex operating conditions [101]. Recently, the high fluid-solid contact efficiency makes it attractive to employ the MFB for particle granulation. However, the particles agglomeration under ambient temperature conditions and more problematic sintering activity at high temperatures strongly limit the use of MFB [102, 103]. To minimize the defluidization situation and improve the fluidization quality, many methods have been proposed addressing the optimization the granular processing in MFBs.

Zhong et al. [104] investigated the defluidization behaviour of iron powders with different fluidization gases (Ar, N₂, CO, H₂) in the bubbling fluidized bed with 25 mm ID. They concluded that (1) the defluidization tendency decreased with increasing the viscosity and density of gases; (2) the sintering of iron powders (resulted from the adhesion force due to surface softening) increased with increasing temperature. The sintering problem has been

resolved by Li et al. [101], who presented a “two-stage reduction” process for the synthesis of high-purity ultrafine Ni particles in the MFB reactor (20 mm ID). In the first stage, the raw ultrafine NiO particles were fed into hydrogen-solids micro fluidized bed for initial reduction at low temperature (340-400°C) for 15 min, which enhanced the self-agglomeration and fluidization of Ni particle. In the second stage, further-reduction for the higher purity of the Ni powders was achieved at high temperature (500-600°C) for 2 minutes. Similarly, the concept of multistage reactions in MFBs has also been applied to reduce metal oxides [105-107], granulation of WS₂ nanoparticles [108] and Mg₂Si [109]. In summary, MFBs technique is feasible for use in the granulation process; with regard to PI, it also improves the processing performance and product quality.

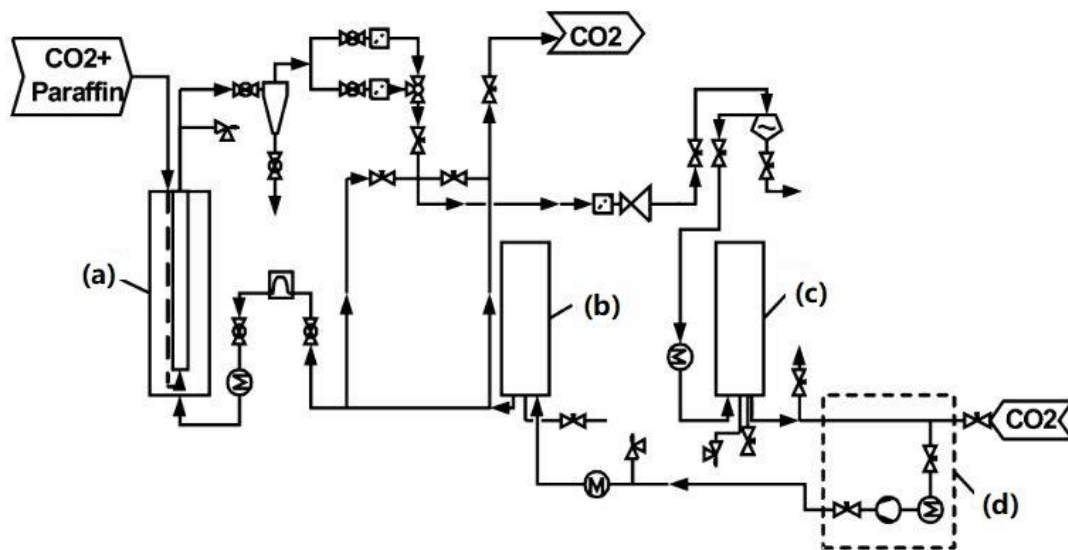


Fig. 2.9. Diagram of the high-pressure fluidized bed for particle coating process using the rapid expansion of supercritical fluid solutions (RESS): (a) fluidized bed, (b) & (c) buffer autoclaves, (d) compressor [110].

Encapsulation of particles

The encapsulation of particles to produce pills, pellets and tablets are widely used in the food and pharmacy industries. The encapsulation process inside a fluidized bed is achieved by spraying a coating solution into the fluidized solids, which contains several cycles of wetting-drying process to form a uniform coating on the particle surface [111, 112]. The coating

droplets are sprayed on the surface of particles through a coating-solution nozzle driven by centrifuge, air pressure, ultrasonics [113]. Simultaneously, the hot air is pumped into the bed to fluidize the particle bed and dry the wet surface.

The MFBs combined with the rapid expansion of supercritical solutions (RESS) has been intensively used for the particle encapsulation (Fig. 2.9). Tsutsumi et al. [114] initially employed RESS in a micro-fluidized bed (50 mm ID) to conduct the coating process, in which the supercritical carbon dioxide solutions of paraffin were sprayed through the nozzle into the bed that was fluidized by air. A big improvement in their work is no significant agglomeration, achieved by spraying the coating material directly on the particle surface without the presence of liquid droplets which acted as a binder for particles. Later, Schreiber et al. [115] used the molten paraffin mixed in supercritical carbon dioxide for the encapsulation of silica-particles and glass beads in a MFB at high pressures. The agglomeration of particles was mitigated by using a nozzle with an orifice diameter of 50 μm and a fluid velocity of 2.23 times the minimum fluidization velocity. Similarly, by applying the RESS process in a high-pressure MFB, Rodríguez-Rojo et al. [116] reported that good extraction yields could be achieved by setting the extraction flowrates for bottom-spray and top-spray methods to 2 kg/h and 4 kg/h, respectively. The better coating quality was observed in top-spray experiments at the equivalent operating conditions, which was explained by the low wet-particle concentration in the vicinity of the nozzle due to the bottom spray configuration. Besides, Rosenkranz et al. [110] proposed the encapsulation of two different irregular shaped proteins, namely a model protein (bovine serum albumin, BSA) and a pharmaceutical protein (insulin) in a high-pressure fluidized bed (39.2 mm ID and 550 mm height) with RESS techniques, which had the advantages of relatively low process temperature and the absence of any organic solvents. Although the paraffin coating of those bed mixtures in the high-pressure fluidized bed by means of RESS-process was feasible at low temperatures, particle rupture caused by the energy of the nozzle

jet meant a further optimization for protein coating was required. Leeke et al. [117] successfully coated the nanoparticles onto a micron-sized excipient for a range of nanoparticle actives without the need of liquids and high temperatures, but their method was limited by the low solubilities of actives in carbon dioxide.

To date, the main drawbacks of particle encapsulation are agglomeration, rupture and low yields. However, micro-fluidized beds, combined with RESS, has useful applications in the coating process, especially for coating nanoparticles. In future, the modification to RESS method and development of novel techniques are expected to improve particle encapsulation in MFBs.

Particle separation

In industrial applications, particle separation is a key step to collect the target solids with high content and uniform particle size, and to remove unexpected components from the mixture. For solid segregation in a fluidized bed, although particle shape [118], pressure drop [119, 120], distributor design [121], bed thickness [122] and height [123] were reported to influence particle separation, the main concerns are particle density and size [124, 125]. Magnetically stabilized fluidized beds have been reported to be able to separate solid phase, especially for the extraction of metal solids (e.g., Iron ore). However, there is no literature on the application of the micro-fluidized bed for solid separation. One reason could be that the industrial solids (i.e., metals and coals) contain larger sizes and require conventional-scale fluidized bed for separation. On that note, the use of MFB for nano-size particle separation would be an interesting topic for further investigation in future research.

2.2.2.2 Chemical conversions

The conversions of biomass to energy and fuels depend on various thermochemical or biochemical processing, such as combustion, gasification, pyrolysis and fermentation [126]. Owing to its ability to manipulate solids, intimate contact between the phases and excellent

mixing and heat-transfer characteristics, fluidized bed technology has been applied successfully to facilitate the thermochemical reactions [76, 127]. The advantages of using MFBs for thermochemical processes are faster reaction, higher reaction rate and lower capital costs as compared to conventional scaled-up fluidized bed reactors. In this section, the recent utilization of MFBs for such thermochemical processes are discussed. Drawbacks of using MFBs during the biomass conversions have also been addressed.

Catalytic cracking

Boffito et al. [128] proposed a one-step cracking/transesterification of vegetable oil for the production of biodiesel in a 7-mm ID quartz bed, which reported a highest biodiesel selectivity of 44% in optimal conditions. Unfortunately, this one-step method could only be operated continuously for 20 minutes, thus limiting its potential for a long-term utilization. Furthermore, the surface of the catalysts $\text{CaO}/\text{Al}_2\text{O}_3$ were deactivated with coke, and the fluidized bed was condensed and slumped by oil. Altogether these problems could be resolved by periodically regenerating the catalyst to clear the built-up of the coke with several oxygen-cycles of combustion. However, how to optimize the regenerated catalyst for biodiesel selectivity remained unclear. Utilizing the same size fluidized bed system, Edake et al. [129] reported the production of 1,3-propanediol from glycerol hydrogenolysis using catalysts $\text{Pt}/\text{WO}_3/\text{Al}_2\text{O}_3$ in a fluidized bed operating above 240 °C and at ambient pressure. Starting from the glycerol dehydration to acrolein, followed by rehydration to 3-hydroxypropanal and finally the hydrogenation to 1,3-PDO, it was observed that the yield of 1,3-PDO reached 14% after 2h at 260 °C. The by-products were 2-PrOH, propanal, methanol, ethylene glycol, acetone, CO and CO_2 , which were required for improving the selectivity of the proposed mechanism to achieve a higher yield of targeted products. In terms of PI, the MFB system required shorter reaction times and lower concentrations of catalyst to achieve substantial production rates, e.g. 10 t of catalyst for 80 kt/y of biodiesel production [130]. Furthermore, Guo et al. [131] developed a

two-stage MFB reactor for catalytic thermal decomposition of biomass tar, which broadened the application of MFB in liquid cracking area.

Pyrolysis

Pyrolysis is a thermochemical process that converts the solid or liquid fuels into gas, char and tar in the absence of oxygen. Jia et al. [132] compared the pyrolysis of two woody biomasses (Douglas and oak) by the respective micro-fluidized bed reactor (MFBR) and fixed bed reactor (FBR); each reaction connected a single photoionization (SPI) mass spectrometer for real-time and on-line analysis of the labile primary tars from biomass pyrolysis. Using this SPI mass spectrometer, they observed that biomass composition and temperature affected the volatile composition during the fast pyrolysis of biomass in their MFB [133]. From the point of view of experimental parameters on pyrolysis, Gao et al. [134] compared the pyrolysis of three Iranian waste oils, namely Ahwaz (AW), Gachsaran (GS) and Abiyan (AY), in MFB and concluded that the reaction temperature and reaction rate were important factors for reaching maximum conversion of fuel. Mao et al. [135] investigated the co-pyrolysis characteristic of biomass and lignite in the MFB analyser under isothermal conditions. They were able to calculate the kinetic parameters for each individual gas components of the co-pyrolysis using iso-conversional method. Yu et al.[136] found the micro fluidized bed reactor facilitated the rapid pyrolysis reactions with higher gas yield but lower amount of carbon residues compared to those derived from tests in fixed bed reactor. They concluded that this was the result of much higher heating rate and more efficient mass transfer in the micro-fluidized bed reactor. In terms of PI, as the micro-fluidized bed reactor enables fast pyrolysis, the biomass could be rapidly heated to predetermined temperature on order of seconds, thus speeding up the products of pyrolysis and maximizing bio-oil yield.

Gasification

Gasification is an effective method for converting biomass (such as coal and other carbon-involved fuels) into energy. This method begins with rapid pyrolysis and char gasification thereafter [137, 138]. Zeng et al. [139] investigated the MFB reactor for the isothermal gasification of *ex situ* char-CO₂ in a micro fluidized bed reaction analyser. The micro-fluidized bed reactor presented a much higher reaction rate than results derived from a thermogravimetric analyser (TGA). Alternatively, They also proposed a two-stage gasification technology involving a MFB pyrolyzer for biomass pyrolysis (the first stage) and a MFB gasifier for char gasification (the second stage), achieving the production of clean industrial fuel gas gasification [140]. Afterwards, Wang et al. [141] applied this MFB reaction analyser to evaluate the gasification of *in situ* and *ex situ* char, under isothermal condition, in the presence of CO₂ as a gasification agent. The authors concluded that the char gasification behaviour and kinetics could be affected by the pyrolysis atmosphere and annealing (cooling). Alternatively, by changing the gasification agent from CO₂ to H₂, Wang et al. [142] characterized the isothermal reaction of char gasification with steam at 0.1 MPa at low temperatures range (750–950 °C) and high temperature range (950– 1100 °C), from which they concluded the effects of the reaction temperature and steam partial pressure on the reaction rate of char–steam gasification. Furthermore, Zhang et al. [143] reported the use of 10 wt.% black liquor could decrease the completion time of petroleum coke steam gasification at 900 °C from 120 min to about 40 min, thus speeding up the gasification in MFB. The same group also reported the catalysts regeneration via coke-steam gasification to solve the problem of excessive heat generated via coke combustion [144]. On the other hand, by minimizing external mass transfer limitations in bed column, Cortazar et al. [145] developed a novel micro-fluidized bed (26 mm ID and 300 mm height) with thermogravimetric flow (that could precisely monitor the mass loss rate throughout the gasification process) by mitigating the external mass transfer limitations in the

bed column and relying on solid-gas contact between the reactive gaseous stream and the char samples.

In addition, the MFBs have also been applied in chemical processing, such as drying [146], oxidation [147] and reduction [148, 149]. Due to its rapid heat and mass transfer, the MFB can lower the temperature and concentration gradient but raise the reaction rate, thus presenting its huge potential in real chemical conversion. For instance, Latifi et al. [150] have fitted a MFB (alumina tube of 25 mm ID) with an induction heating system to heat the particles to the reaction temperature of 1500 °C in less than 5 s. However, the challenges are incomplete combustion due to high moisture content, pollutant emissions (i.e., SO_x, CO) existing in traditional combustion processes. Other issues affecting the performance of MFB reactor such as solids agglomeration and sintering have yet been well understood. Thus, it is important to consider these issues when designing and applying the MFBs in engineering applications.

2.2.2.3 CO₂ capture

Carbon capture and storage (CCS) refer to the removal and absorption of CO₂ from processes such as combustion or gasification, with the aim of mitigating greenhouse effects and climate change [151]. The utilization of MFBs for carbon capture have attracted much attention in recent years. Fang et al. [152] characterized the cyclic CO₂ capture and CaCO₃ regeneration properties in a high-temperature micro-fluidized bed reactor. They found that the carbon-capture MFB reactor exhibited a decreasing efficiency of CO₂ capture with increasing the cycles because of the loss of sorbent activity, but the efficiency was relatively stable when the sorbent became saturated. In the presence of limestone, other factors that could affect carbon-capture were coal ash, carbonation reaction stage (kinetically controlled stage and product layer diffusion-controlled stage) and particle size [153]. However, Fang and co-workers provided no description on the fluidization performance of solids during the carbonation/calcination process, although the different modes of solids circulation might be linked to the CO₂ capture rate.

Using the same micro-fluidized bed thermogravimetric analyzer (MFB-TGA), Li et al. [154] evaluated the reaction kinetics of CaO carbonation in calcium looping. When CO₂ concentration was within 50 vol% (1 bar), the reaction rate constant was observed to be $8.0 \times 10^{-10} \text{ m}^4/(\text{mol}\cdot\text{s})$ while the activation energy of the carbonation reaction was almost zero and the reaction was first order. By evaluating the direct reaction between CO₂ and Ca(OH)₂ in MFB, Yu et al. [155] identified the presence of Ca(HCO₃)₂, an unstable intermediate product whose activation energy was determined to be 40 KJ/mol. Recently, Shen et al.[156] developed a micro interconnected fluidized bed (30 mm ID and 100 mm height, endowed with interconnectivity to accommodate oxygen, Fig. 2.10), to promote CO₂ capture by oxy-fuel combustion [157]. Their system was found to yield the conversion efficiencies of 100%, 36.8% and 16%, for H₂, CO and CH₄ with hematite OCs, respectively, but the issues of carbon deposition and OC attrition limited the applicability of this system.

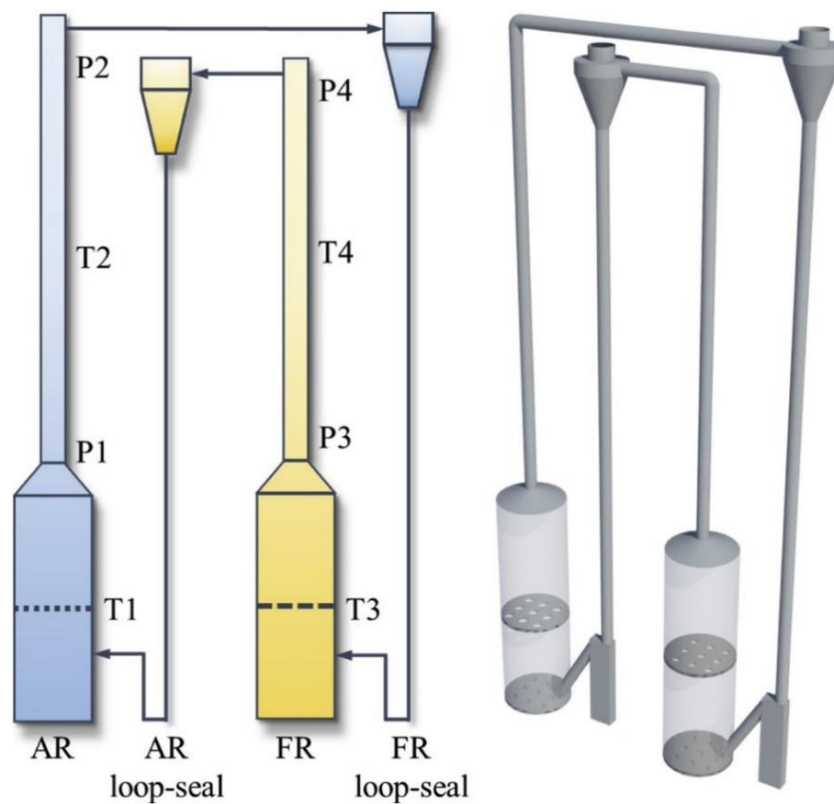


Fig. 2.10. 2D schematics and 3D models of the main component of the micro interconnected fluidized bed for oxygen carrier evaluation [156]. T_i and P_i (with i = 1 to 4) indicate temperature and pressure measuring points.

In recent years, more researchers have attempted to apply the external forces (e.g., sound field, magnetic) into MFBs to improve the CO₂ capture capacity. For instance, a sound-assisted CO₂ capture MFB (a Plexiglas column of 40 mm ID) filled with fine activated carbon has been developed by Raganati et al. [158]. The authors evaluated the different adsorbent materials and noticed that the sorbent of HKUST-1 yielded the highest CO₂ adsorption capacity [159, 160]. To enable larger-scale CO₂ capture, Li et al. [161] studied the CO₂ capture in HVAC (Heating, Ventilation and Air Conditioning) with the use of a novel Compact Micro Fluidized beds (CMFB), which contains 100 micro fluidized beds (10 mm in length and width, 42 mm in heights). Their novel design by combining numerous MFBs in parallel is a typical way to scale up the production rates but maintains the advantages of micro-fluidization. Other MFB systems have been developed endowed with sorbents such as magnetite loaded carbon fine particles [162], micro-encapsulated carbonate solution [163]. These newly developed absorbents largely promoted the CO₂ capture capacity, but the shortcomings including complex synthesis of the functional particles, low robustness and high cost require the further improvements in future.

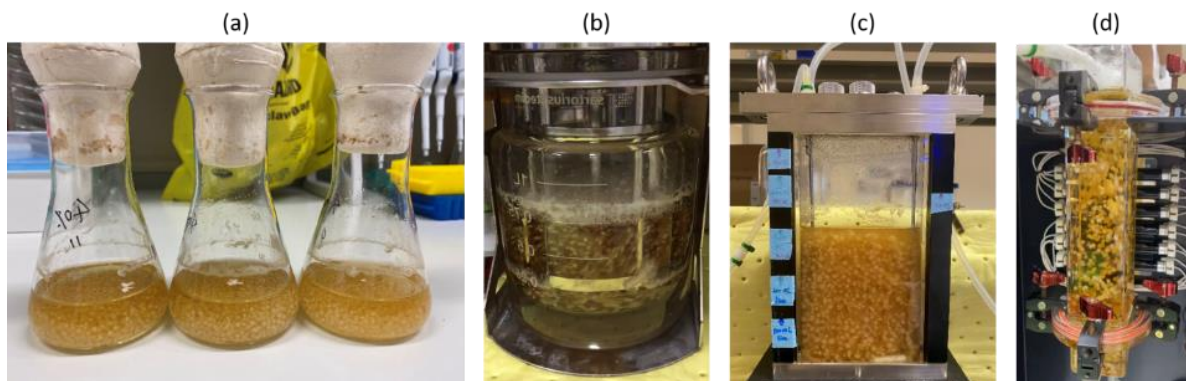


Fig. 2.11. Images of main components of different bioreactor systems: (a) flask culture, (b) stirred-tank reactor, (c) panel bioreactor, (d) fluidized bed reactor.

2.2.2.4 Bioprocessing and bioproduction

The demand for high throughput with controllable and quantitative operating conditions gave rise to the development of bioreactor systems, such as flask culture, stirred tank reactor (STR), panel bioreactor and fluidized bed reactor (Fig. 2.11). Compared to the low mass transfer in

flask, high shear force from agitated impeller of STR, high capital cost of PBR, fluidized bed bioreactors rely on the fluidization of solids to achieve a high mass/heat transfer with low mechanical stress, thus stimulating its potential in bioengineering and bioproduction. To fluidize the tiny microorganisms without being washed out, the cell immobilization technologies (i.e., attachment, entrapment, self-aggregation, containment) were developed to enhance cell stability in continuous fluidization condition [11, 12]. In the following subsections, the applications of MFB bioreactors in bioengineering such as wastewater treatment, biogas production and other bio-application have been reviewed.

Wastewater treatment

At present, the removal of recalcitrant pollutants from both domestic and industrial wastewater remains a big challenge for ecosystem and human life. One economical method is the biological treatment process such as the activated sludge process [164]. The combination of MFB with the cell immobilization technology is widely applied for wastewater treatment. For instance, Chowdhury et al. [165] compared the biological nutrient removal ability using a novel liquid-solid circulating fluidized-bed (LSCFB) bioreactor with and without the recirculation of particles (the Lava rock particles attached with biomass). The system without particles was able to remove 94, 80 and 65 % of organic (chemical oxygen demand, COD), nitrogen (N), and phosphorous (P), respectively. With the presence of these particles, the system removed excess phosphorus with overall removal efficiencies of 91, 78 and 85 % for C, N, and P, respectively. Kuyukina et al. [166] tested different immobilized biocatalysts on the hydrophobized carriers such as sawdust, poly (vinyl alcohol) cryogel (cryoPVA) and poly (acrylamide) cryogel (cryoPAAG) for the petroleum-contaminated water treatment in the fluidized bed reactor (14 mm ID, 120 mm length). They found the 70–100% removal of n-alkanes (C₁₀–C₁₉) and 66–70% removal of 2–3-ring PAHs, demonstrating the applicability of MFBs for biotreating petroleum-contaminated water. In addition, with co-immobilized

Rhodococcus ruber IEGM 615 and *Rhodococcus opacus* IEGM 249 strains on sawdust, Kuyukina and co-authors found that their approach could achieve 70% biodegradation efficiencies for alkanes and PAHs within two weeks compared to the corresponding 24 and 37% without the inoculations in the bed [167]. Similarly, another example of petroleum wastewater biodegradation was reported by Banerjee et al. [20], who used the immobilized hyper phenol-tolerant strains of *Bacillus cereus* (AKG1 MTCC9817 and AKG2 MTCC9818) in a fluidized bed bioreactor (50 mm ID) to reduce 95% of the initial phenolic compounds under the continuous mode of operation. To demonstrate the efficiency of MFB in wastewater treatment, Qiu et al. [168] compared the formaldehyde biodegradation by immobilized *Methylobacterium* sp. XJLW cells in both the three-phase MFB (36 mm ID, 460 mm height) and the shake flask. They found the immobilized cells from fluidized bed reactor could degrade 5 g/L formaldehyde with a maximal degradation rate of 464.5 mg /L/h after 20 batches recycling, while cells from flask culture showed a lower formaldehyde tolerance (1.2 g/L) in 8 h shake flask tests.

Table 2.2 Summary of wastewater treatment using different micro-fluidized bed reactor systems in recent years.

Reference	Column ID (mm)	Wastewater	Particle properties	Microorganisms	Results
Chowdhury et al. [165]	20, 76	Degritted municipal wastewater	Lava rock particles; $dp = 0.3\text{--}1.0$ mm	Return activated sludge of 3511 mg TSS/L and 2810 mg VSS/L	Removal of 91, 78 and 85 % for organic (chemical oxygen demand, COD), nitrogen (N), and phosphorous (P), respectively with particle recirculation.
Kuyukina et al. [166]	14	Petroleum-contaminated water	Hydrophobized carriers such as sawdust, poly (vinyl alcohol) cryogel (cryoPVA) and poly(acrylamide) cryogel (cryoPAAG) $dp = 1\text{--}3$ mm	Strains of <i>Rhodococcus ruber</i> IEGM 615 and <i>Rhodococcus opacus</i> IEGM 249	70–100% removal of n-alkanes (C10–C19) and 46–70% removal of 2–3-ring PAHs.
Kuyukina et al. [167]	14	Oilfield wastewater	Sawdust samples; $dp = 1\text{--}3$ mm	Strains of <i>Rhodococcus ruber</i> IEGM 615 and <i>Rhodococcus opacus</i> IEGM 249	70% biodegradation efficiencies for alkanes and PAHs within two weeks; 75–96% removal of heavy metals (Al, Cr, Cu, Fe, Hg, Zn, Mn).
Banerjee et al. [20]	50	Petroleum wastewater	Ca-alginate beads; $dp=3$ mm	Strains of <i>Bacillus cereus</i> (AKG1 MTCC9817 and AKG2 MTCC9818)	95 % or more reduction of COD and phenolic compounds.

Qiu et al. [168]	36	Formaldehyde (H-CHO)	Gel-entrapped beads; Dp = 4-5 mm	Strain of <i>Methylobacterium</i> sp. XJLW	Degradation of 5 g /L formaldehyde (with a maximal degradation rate of 464.5 mg/L/h under the optimum conditions)
Ballesteros et al. [169]	20, 40	Nickel-containing synthetic wastewater	nickel carbonate granule; dp = 0.50-0.15 mm	/	98.8% of nickel removal.
Chen et al. [170]	34.4, 50	Campus domestic wastewater	Natural zeolites; dp = 0.2 - 1 nm	Anaerobic digested sludge	Removal of COD, BOD and SS reached 84, 87, and 96%, respectively, with a HRT from 3 to 4 h.
Geng et al. [171]	31	Isopropanol	Calcium alginate, Polyvinyl alcohol, Activated carbon, SiO ₂ ; dp = 3 mm	Strain of <i>Paracoccus denitrificans</i>	Reduction of COD from 5,000 to 109 mg/L under optimum condition; The degradation of IPA reached 98.3%.
Ismail et al. [172]	50	Furfural-laden wastewater	Natural polymers of guar gum (GG), agar agar (AA), and sodium alginate cross-linked with polyvinyl alcohol (PVA)	<i>Bacillus</i> cells	Removal efficiency of furfural was 100%, 100%, and 95% for the 1st, 2nd, and 3rd, cycles, respectively.
Kim et al. [173]	50	Synthetic wastewater with chemical oxygen demand (COD) averaging 513 mg/L	Granular activated carbon (GAC)	/	COD removals reached 99%.
Kwak et al. [174]	35	Low strength (60 mg/L TN) synthetic wastewater	Granular activated carbon; dp = 0.8-1 mm	/	Total nitrogen (TN) removal efficiency was over 82%.
Kwon et al. [175]	50	Synthetic wastewater with a COD of 300 mg /L	GAC particles; Dp = 0.84 mm	/	An overall removal efficiency of 82% of NH ₄ -N.
Oztemur et al. [176]	50	Synthetic wastewater	Silica; dp = 1-2 mm	/	COD oxidation and sulfate reduction efficiencies up to 98%
Patroescu et al. [21]	50	Low-pitched groundwater containing nitrates	Expanded clay granular; dp = 2-5 mm	/	The denitrification rate was between 3390-3867 g NO ₃ -N/m ³ /day in fluidized bed reactor.
Wang et al. [177]	38	Synthetic municipal wastewater	Activated carbon-coated polypropylene beads; dp = 3.0-3.5 mm	The dominant phyla were <i>Proteobacteria</i> , <i>Bacteroidetes</i> , and <i>Epsilonbacteraeota</i>	Total COD removal efficiencies of N 84% were achieved, concomitantly with complete nitrification. The overall nitrogen removal efficiencies were N75%.

To study the anaerobic post-treatment of wastewater, Kwak et al. [174] used the MFB membrane reactor (35 mm ID and 500 mm height) for low-strength ammonia wastewater treatment. Meanwhile, Oztemur et al. [176] reported the high sulfate reduction by their MFB membrane bioreactor, which consisted of a plexiglass column with 50 mm ID and 1250 mm

height. Such membrane reactors need no aeration requirement with less sludge production, but the membrane fouling remains a major issue [173]. As summarized in [Table 2.2](#), wastewater treatment is dependent on the specific microorganisms used for biodegradation or convert certain chemicals from the effluent. When combined with MFB reactor system, this would intensify the process of treating wastewater. To date, these miniaturized fluidized bed bioreactors have achieved convincing results in wastewater treatment, but its design procedure and operating conditions are too complex to standardize the wastewater treatment. The cultivation conditions (i.e., pH, temperature, growth medium, concentration, etc.) which differ for different cells or bacteria, could impact the wastewater treatment. For example, using a two-stage anaerobic/aerobic fluidized beds system (50 mm ID, 500 mm height) for the biodegradation of reactive blue 13, Lin et al. [178] obtained a maximum colour removal of 83.2% and COD removal of 90.7% was obtained at pH 7. Besides, another non-negligible issue is the long duration for cell cultivation and biodegradation: the cultivation period can last for several days and the degradation time can last for more than 300 hours in one wastewater treatment cycle [179, 180].

Bioproduction

One advantage of the MFB bioreactor is that it can control the processes for small-scale cell cultivation and fungal fermentation to obtain the desired biological products. This is desirable from the perspectives of parallelization, automation and cost reduction [181]. The production of biofuels (i.e., hydrogen, ethanol) is one of the typical applications of MFB bioreactor. Wu et al. [182] used a MFB bioreactor (27 mm ID and a height of 120 cm) to house immobilized anaerobic sludge for biohydrogen and bioethanol production. For H₂ production, the largest H₂ production rate of 59 mmol /h/L was observed with the sugar substrate of sucrose at the liquid velocity of 0.91 cm/s, while a H₂ yield of 1.04 mol mol hexose⁻¹ was achieved with glucose at the liquid velocity of 0.55 cm/s. Alternatively, Wu and co-workers demonstrated that the sugar

substrate of fructose led to the highest ethanol production rate of 378 mmol/h/L and yield of 0.65 mol mol hexose⁻¹ at the liquid velocity of 0.91 cm/s. Using an anaerobic fluidized bed reactor with expanded clay as support carrier and glucose as substrate, Cavalcantedeamorim et al. [183] demonstrated that hydrogen yield production and hydrogen production rate were linearly correlated with the hydraulic retention time (HRT). Furthermore, the authors compared two different support materials (polystyrene and expanded clay) for biohydrogen production with synthetic wastewater containing glucose (4000 mg/l). They concluded that the maximum hydrogen yield was 1.90 mol and 2.59 mol with the carrier of polystyrene and expanded clay, respectively, while the highest hydrogen production rates were 0.95 and 1.21 l/ h/ l for polystyrene and expanded clay, respectively [184]. They have also investigated other input parameters such as liquid velocity, temperatures and HRT on hydrogen production [185, 186]. It must be emphasized that minimum fluidization velocity presented a greater production of hydrogen, but they failed to give any explanation. From the point of hydrodynamics, it is plausible that minimum fluidization velocity can facilitate the fully expansion of the particle bed as well mitigate the solid agglomeration, thus enhancing the mass transfer rate for cell growth. Most importantly, the minimum fluidization velocity ensures lower shear force on cells, thus minimizing the cell damage and death.

Using the cell encapsulation as another cell immobilization method, Liu et al.[187] studied the production of natural pigment via the cultivation of encapsulated *Monascus purpureus*. They confirmed that encapsulated cells contained a higher cell density than free cells cultivation in flask, although a few cell leakages from encapsulation was observed. Another interesting study is the effect of different cultivation modes on product yields using the micro fluidized bed bioreactor. For instance, the different cultivation modes of gel-entrapped *Sphingomonas* sp. ZUTE03 was tested in the three-phase micro fluidized bed bioreactor to produce CoQ₁₀ [188], from which the CoQ₁₀ yield in conditions of single batch, feed of solid solanesol every 8 h

batch and feed of solid solanesol & PHB every 8 h was 43 mg/l, 171.52 mg/l and 441.65 mg/l, respectively.

Applications of MFB bioreactors in the bioengineering field have been reported elsewhere. Pereiro et al. [35] studied the magnetic MFB in combination with antibody-functionalized superparamagnetic beads to capture and detect infectious bacteria. Similarly, the microfluidic magnetic fluidized bed was also employed for DNA analysis [37]. In microfluidic chamber, the drag force between particles and wall effects are expected to overcome gravitational forces, therefore, the external forces such as magnetism can lead to a stable, steady-state fluidization process.

In summary, MFB bioreactor has several advantages for bioproduction applications, such as sufficient mass transfer, enhanced mixing effect and low shear stress. The high mass transfer and mixing rate ensure the medium and dissolved oxygen supply. Besides, the liquid/gas flows in the fluidized chamber result in lower hydrodynamic shear stress for cells, which mitigates the cell damage/death rate compared with stirred tank bioreactors. However, the long duration for cell cultivation through the immobilized cell fluidization may lead to the cell detachment from carriers or cell leakage from encapsulation. In the aerobic cultivation/fermentation, air provide oxygen in the form of bubbles, which could rupture in medium and influence cell morphology and cause cell death [189, 190]. Therefore, it is worthwhile optimizing the bubble velocity and size in the microfluidic system. Finally, as cells size and numbers are growing in the fluidized bed column, the liquid and/or gas flowrate should be continuously adjusted to maintain a desirable fluidization state. Often this may mean compromising on the final production yield and rate.

2.2.3 Conclusions and Prospect

In this chapter, the process intensification using micro-fluidized bed techniques have been discussed from the hydrodynamic properties of this miniaturized reactor. The discussions of

MFB applications have covered solid screening, chemical conversion, CO₂ capture, wastewater treatment and microbial processing. The miniaturized size enables the fast screening, controllable safety and low capital cost. Besides, the advantages of good mixing, excellent mass and heat transfer broaden the applications of MFB in traditional chemical engineering, as well as in environmental protection and bioengineering. Thus, MFB has been proved to be an effective preliminary screening tool to test its application in a safer, faster, cheaper and cleaner way.

However, the commercial applications of MFB are still in the initial stage with few documentations. One of the mature commercial products is the gas-solid MFB analytical device developed by Xu's group, which was used it for varieties of thermochemical gas-solid reactions as reviewed in this paper with more analytical details provided in a recent review paper from their group [191]. Recently, Samih et al. [192] proposed a MFB thermogravimetric analyzer for developing processes from complex feedstocks, which could be applied for coal gasification and other gasification processes development and design. Admittedly, the direct adoption of results obtained from MFB into commercial applications is limited by the inherent scale dependence of essential operation parameters [193]. For instance, the change of on parameter (e.g., bed size, partical size or density) with other parameters unchanged may lead to significantly different hydrodynamics. The widely applied method for fluidized bed scaling is to use the dimensionless numbers (e.g., Reynolds number, Froude number, gas/particle density ratio, sphericity and size distribution of the particle, etc.) for keeping the hydrodynamic similarity in different sizes of reactors [194], although the wall effects and particle interactions (which are significant in MFB but negligible in large-scale fluidized bed) make the scaling-up results impossibly consistent with those in MFB. Alternatively, advanced validating tools such as CFD simulation can assist to improve the scaling-up similarity. Finally, the promising method of using MFB for commercial-scale production is by combining numerous MFB in

parallel to enlarge the production rate while maintains the advantages of MFB. This can be exemplified by a novel Compact Micro Fluidized beds (CMFB, contains 100 micro fluidized beds) for CO₂ capture [161] and the micro-structured fluidized bed membrane reactors [195], but more studies on novel and effective MFB designs are expected to meet the demand of industrial production in future.

2.3 Fungal fermentation

Filamentous fungi are of great significance in biotechnological and bioprocessing industry to produce many primary and secondary metabolites including citric acid, lovastatin, lactic acid, carotene, and enzymes such as protease and laccase [196-198]. In this section, the fungi growth and pellet formation process were briefly reviewed. Besides, the reported parameters that affect the process of pelletization and bioproduction were also concluded. Finally, the advantages and challenges of fungal fermentation via the bioreactors have been addressed.

2.3.1 Pellet formation and growth

In submerged culture, fungi can grow either in dispersed mycelia or in the compact pellets surrounded with hypha structure. The mechanism of pellet formation is generally divided into two modes: coagulative and non-coagulative formation [199]. As shown in [Fig. 2.12](#), the coagulative type is achieved by agglomerating the spores and subsequently germinating hyphae to form the pellets. In contrast, the non-coagulative type starts with the swelling and germination of single spore before the aggregation of branches. In both two modes, the first stage of micro-morphological growth is dependent on the physico-chemical properties of the spores and hyphae, as well as on the cultivation conditions such as the pH and salinity of the growth medium and its rheological behaviour [200]. After the micro-morphological process, the next stage of macro-morphological growth involves the branching and extension of hyphae, which tend to interact and aggregate to form the pellets. The final stage, referred to fungal cell autolysis, is the process that pellets break up into the fragmented pieces, which are then served

as new source for next round pelletization for increasing the pellet biomass and inherent bioproduction.

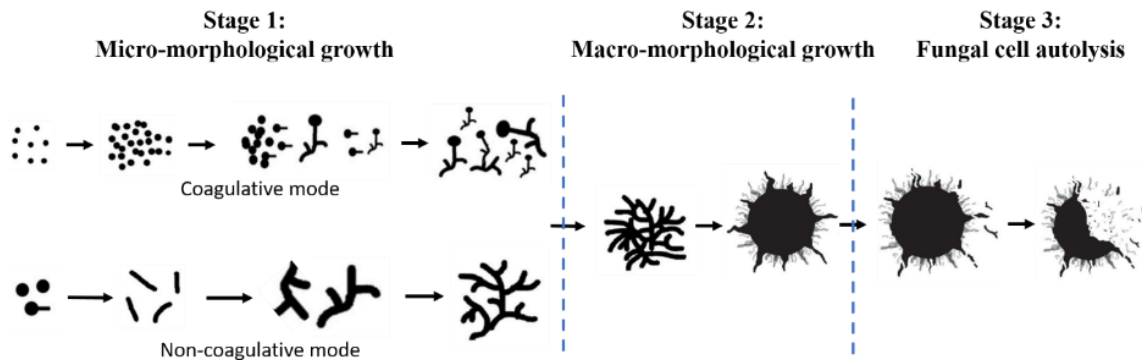


Fig. 2.12. Schematic of fungal growth and pelletization in different stages. Stage 1: Micro-morphological growth based on coagulative and non-coagulative mode, Stage 2: Macro-morphological growth with branching and extension of hyphae for pellet formation, Stage 3: fungal cell autolysis into fragmented species for next round pelletization.

The mature pellets are spherical, ellipsoidal or oval masses with the size ranging from several hundred micrometres to several millimetres, which is traditionally determined by means of image analysis [201, 202]. Relied on the staining of thin slices of *Penicillium chrysogenum* pellets with cresyl-violet, Wittier et al. [203] observed the different layer structures and distinguished the pellet into four different regions: (i) the first region corresponds to pellet centre, which presents a semi-anaerobic environment with very little amount of viable hyphae, (ii) the second region corresponds to the layer surrounding the central region with significant inhomogeneities in the pellet wall, (iii) a third region appears in hollow pellets, with hyphae showing clear signs of autolysis, and (iv) the fourth region corresponding to the external hairy zone whose thickness dependent on fermentation time. In this outer hairy region, the hyphae are viable and metabolically more active than in the other regions [204].

2.3.2 Factors on pellet growth

It is known that the parameters such as inoculum concentration and culture conditions largely affect pellet morphology, which in turn impact the productivity. For instance, the filamentous mycelia increase the viscosity of culture media, leading to the low mass transfer and mixing

effect. On the other hand, the pelleted fungi is challenged by the internal transport issues of substrates and products, which is depended on size and compactness of pellets [205]. Therefore, it is essential to study the effects of parameters including medium component, operating conditions on pellet growth for the purpose of improving the productivity.

The fungal inoculations include specific strain, inoculant concentration and age, etc. Fungi species determine the target product, while the inoculant concentration and age mean the biomass concentration of the fungi and its viability, respectively. It is reported that the high concentration of inoculum ensures the large number of biomass but it might lead to the formation of free mycelia instead of pellets, whilst the low level of inoculum (i.e. less than 10^8 spore/mL) promotes the pelletization process [206]. However, whether the free mycelia or the pellets have a better productivity must be associated to the fungal strains and other cultivation conditions.

Another important factor is the medium components, in which the substrates can either enhance or prevent the pellet formation to influence the fungal morphology. For instance, the carbon sources provided by lactose was reported to induce the *Aspergillus niger* grow into free mycelia, whereas the substrate of glucose led to the formation of pellets [207]. Additionally, the salinity of sodium chloride with high contraction was also reported to prevent the formation of pellets [208]. These descriptions are consistent with the medium components used by Bolker et al.[3], who used the glucose monohydrate (30 g/L) for carbon sources and a very low concentration of calcium chloride dihydrate (73.5 mg/L) in the medium for submerged culture of *N. niveo-tomentosa*. Besides the essential substrates, the supplement of precursors can also promote the final production, which was exemplified by the precursor of L-phenylalanine in improvement of raspberry ketone yields [3], although the effects of precursor on fungal morphology was unclear.

Other parameters are agitation and/or aeration forces from the bioreactor systems. The agitation system is widely used in the stirred fermenter to improve mass transfer rate but decrease the oxygen and heat gradients, while the aeration system is used for aerobic fermentation and can also minimise the pellet agglomeration by the bubble flows. The agitation system is reported to decrease the pellet size by shaving of hyphal elements at low agitation intensity and by breaking up the pellets at high agitation speed [209]. Rodriguez et al. [205] concluded that the fungal pellet diameter was up to 2300 μm with the agitation intensity of up to 300 rpm in the stirred tanks, while the more intense agitation speed (> 600 rpm) made the pellets of *Aspergillus terreus* smaller than 900 μm . Despite the reduction of pellet size, the total biomass productivity was not affected, which means the agitation system induce the compactness of pellets. In contrast, the aeration system is believed to increase the pellet size by the increased hyphal branching, so that the enlarged pellets become fluffy and hairy [209]. For instance, Krull et al. [210] stated that *Aspergillus niger* pellets were observed a much larger diameter with irregular shapes. In general, agitation effects are less severe than that from aeration system in terms of pellet growth and bioproduction.

2.3.3 Fungal fermentation in different reactors

Fungal fermentation in the bioreactors is generally divided into two forms: solid state fermentation (SSF) and submerged fermentation (SMF). Solid state fermentation is the microbial process occurred on wet solid materials under controlled conditions without the presence of running water or cultivation liquids, therefore the substrates must possess enough moisture to support growth and metabolism of micro-organism [211]. SSF is believed to stimulate the natural fungal fermentation on moist solids, thus developing the fermentation techniques in ancient time. On the other hand, SMF including static submerged culture and suspension culture are still the dominated fermentation methods for industrial-scale application, which is normally associated with the release of heat, CO_2 , and volatile compounds [212]. In

this section, attention is focus on the submerged fermentation techniques, as the fermentation of *Nidula niveo-tomentosa* and production of raspberry ketone in our project are conducted in the submerged cultivations.

Different bioreactors replied on external forces such as shaking incubator, agitation system and aeration system to suspend the fungal pellets, thus increasing the mass/heat transfer but minimizing the pellet settlement and agglomeration. During the suspended fermentation in bioreactors, fungi can grow in the form of free mycelia (freely dispersed filaments), clumps (aggregated but still dispersed) and pellets (denser, spherical aggregated forms), which is influenced by the operating conditions including gas flowrate, agitation speed, pH and substrates [204]. The simplest bioreactor is the Erlenmeyer flask, in which the fungi grow from mycelia into pellets and bioproduction are accumulated. To improve the yields, the flasks are kept in the incubator which provides the shaking system and temperature controller, during the fermentation.

Meanwhile, other bioreactor systems such as stirred-tank reactor (STR), panel bioreactor (PBR), continuous perfusion reactor and fluidized bed reactor (FBR) have also been used for submerged fermentation [213-215]. In general, STR improves the concentration gradient with low producibility and potential contamination due to frequent handling and sampling [216], but induces high shear stress from agitation system (i.e. stirred impellers) thus causing adverse effects on microorganisms, especially on shear-sensitive ones [217]. The photobioreactor (including vertical tubular photobioreactor, bubble column photobioreactor, airlift photobioreactor and flat panel photobioreactor) contains the enclosed, illuminated culture vessel for controlled cell growth and biomass production, which avoids water evaporation and environmental contaminants by using the humidify bottle for gases exchange [218]. Although PBR enhances light utilization by microalgae through photosynthesis, the high capital costs and energy consumption during operation must be taken into consideration [219, 220].

Continuous perfusion bioreactor relies on the highly porous microspheres/scaffolds to provide increased surface area for cell growth and proliferation [221]. The continuous perfusion of fresh or circulated medium promotes nutrients/oxygen transfer with less mechanical stress on cells, but the difficulty in harvesting and complexity of perfusion system (i.e., cell attachment) require further optimization. Similar to continuous perfusion reactor, the immobilization of cells on carriers is also required fluidized bed reactor system, which ensures the immobilized cells are fluidized by upward gas/liquid flows in fluidized bed bioreactor [222]. FBR improves mass/nutrients transfer and mixing effect with less shear force, but the cell sedimentation or elutriation may occur when the gas/liquid flowrate is too low or too high. Admittedly, it is somewhat difficult to compare the fungal fermentation or bioproduction by different bioreactor systems, which involves different growth conditions and parameters such as culture volume, agitation and aeration, mass transfer rate and shear considerations. Particularly, the different agitation and aeration systems have strong effects on fungal morphology and subsequent productivity. Krull et al. [210] pointed out that mycelial growth of filamentous fungi (i.e. *Aspergillus niger*) induced high viscosity of the cultivation media but low nutrient supply due to insufficient mixing, whilst the cultivation of fungal pellets presented Newtonian flow behaviour but limited nutrient transfer into inner core of the pellets. Compared to the aggregation of fungi affected by pH values, fungal morphology is dominantly determined by volumetric power input such as agitation and aeration [223]. More specifically, Taymaz-Nikerel et al. [224] confirmed that the aeration had a higher impact on fluffy pellets of *Escherichia coli*, but the higher agitation led to dense pellets with compact pellet surface. Therefore, to obtain an optimization of the production process, it is still worthwhile investigating the fermentation in different bioreactors and linking the fungal morphology to raspberry ketone production from the point of bioprocessing optimization.

2.4 Raspberry ketone production

Raspberry ketone (4-(4-hydroxyphenyl) butan-2-one; RK) is a well-known aroma component mainly existing in raspberries, although it is also observed in fruits such as cranberries, blackberries, grapes and other plants [7, 225]. Due to its distinct raspberry flavour, RK has been widely used in food industries and fragrance formulation (e.g., in aroma formulations of kiwi, cherry, strawberry) [7]. Meanwhile, raspberry ketone also attracts intense interest due to its lipid degradation and skin-lightening effects in mammalian metabolism, thus boosting its commercial values as healthcare products [6, 7]. However, the low natural abundance in raspberries (1-4 mg/kg raspberries) makes RK non-profitable for the commercial isolation. At present, the chemical synthesized RK has been proved to be simpler and more abundant than that from fruits extraction, but the various toxic by-products and environmental pollution resulted from the synthesis process render the use of such chemical methods [226, 227]. More importantly, based on the regulations of European Community, flavour compounds can only be identified as natural if the products are obtained either by physical processes (i.e. distillation and extraction of natural sources) or by enzymatic/microbial processes, which means the chemical synthetic RK is regarded as nature-identical product [228]. The difference in price of natural-derived RK (up to US\$ 3000/kg) and its chemical synthesized compound (less than US\$ 58/kg) is considerable, fostering the economic production of natural RK [7].

Natural raspberry ketone is initially identified and extracted from natural fruits and plants. For instance, Honkanen et al. [5] identified a total of 75 volatile components including raspberry ketone from fresh wild raspberries by combined gas chromatography-mass spectrometry. Using the same approach, the authors also detected RK from European and American cranberries but they failed to report the specific RK concentration or any extraction method [229]. Besides, Keng-Hong and Nishida [230] confirmed that *Bulbophyllum apertum* flower (Orchidaceae) could release RK to attract *Bactrocera* fruit flies. To measure RK content and

isolate it from fruits, Pabst et al. [225] used the XAD adsorption and subsequent methanol elution to obtain RK from raspberry fruit, which reported 2.2-2.8 mg raspberry compounds from 1.7 kg lyophilized raspberry fruits. More directly, Wang et al.[231] used 10 of raspberry samples purchased from local supermarket to determine the RK content ranging from 71.4-240.0 $\mu\text{g}/\text{kg}$ raspberry. Pedapudi et al. [232] characterized the maximum RK concentration exceeded 20 $\mu\text{g}/\text{g}$ fresh cells in the suspension cultures of raspberry cells (*Rubus idaeus*). It is obvious that the RK content in raspberry fruits is too low for commercial isolation, therefore, other approaches for high yields of natural RK production are required. In the fruit of raspberry (*Rubus idaeus*), the natural production of raspberry ketone initiates with the phenylpropanoid pathway, as shown in Fig. 2.13. Wang et al. [9] reported a heterologous pathway to produce raspberry ketone from p-coumaric acid, which extracted the candidate genes including CoA ligase (4CL), benzalacetone synthase (BAS), and raspberry ketone/zingerone synthase (RZS1) from plants and assembled these candidate genes into the host strain of *Escherichia coli*., achieving a final titer of 90.97 mg/l RK. Similarly, Lee et al. [7] assembled four heterologous genes, encoding phenylalanine/tyrosine ammonia lyase, cinnamate-4-hydroxylase, coumarate-CoA ligase and benzalacetone synthase in an industrial strain of *Saccharomyces cerevisiae* for the production of RK with the maximum concentration of 7.5 mg/L. Alternatively, Kosjek et al. [228] used the different lyophilized cells of *Rhodococcus spp* to perform the biocatalytic oxidation of 4-(p-hydroxyphenyl)butan-2-ol(rhododendrol) into 4-(p-hydroxyphenyl)butan-2-one (raspberry ketone), leading the substrate concentrations up to 500 g/L.

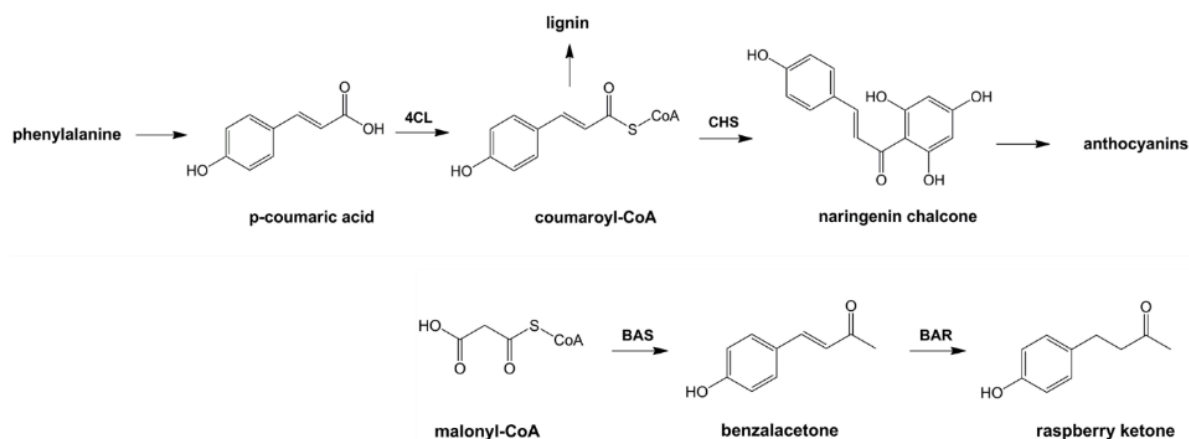


Fig. 2.13. Biosynthetic approach for raspberry ketone and anthocyanins. The biosynthesis of raspberry compounds starts from the coupling of p-coumaric acid to CoA by the 4CL enzyme. Afterwards, the coumaroyl-CoA is converted into raspberry ketone with the supply of malonyl-CoA.

Besides the isolation from natural fruits or bioconversion of natural precursors mentioned above, the fungal fermentation is another route for natural raspberry ketone production [233]. Ayer and Singer [234] initially identified RK from the metabolites of the bird's nest fungus *Nidula Niveo-Tomentosa*, leading to the development of RK production by *De novo* synthesis using the fungus *Nidula Niveo-Tomentosa*. Fischer et al. [13] screened various precursor substances and confirmed the precursors including L-Phenylalanine, phenyl pyruvate, phenyl propanoic acid, L-tyrosine, 4-hydroxyphenyl pyruvate, coumaric acid, 4-hydroxyphenyl propanoic acid, benzoic acid, hippuric acid, benzaldehyde, and 4hydroxy benzaldehyde promoted the synthesis of RK, while other precursors such as cinnamic acid, phenyl acetic acid, phenyl acetaldehyde, and 4-hydroxybenzoic acid methyl ester suppressed the growth of fungus *N. niveo-tomentosa* and raspberry compounds production. Meanwhile, Boker et al. [235] increased the raspberry compound yields to 200 mg/l by optimizing the media and supplementing the L-phenylalanine during the fermentation of the basidiomycete *Nidula niveo-tomentosa*.

2.5 Summaries

The development of MFB techniques have been reviewed from the hydrodynamic properties of this miniaturized reactor. The discussions of MFB applications have covered solid screening,

chemical conversion, CO₂ capture, wastewater treatment and microbial processing. The miniaturized size enables the fast screening, controllable safety and low capital cost. Besides, the advantages of good mixing, excellent mass and heat transfer broaden the applications of MFB in traditional chemical engineering, as well as in environmental protection and bioengineering. Thus, MFB has been proved to be an effective preliminary screening tool to test its application in a safer, faster, cheaper and cleaner way. However, the commercial applications of MFB are still in the initial stage with few documentations, more studies on novel and effective MFB designs are expected to meet the demand of industrial production in future.

The mechanism of pellet formation is generally divided into two modes: coagulative and non-coagulative formation. Both modes start from the first stage of micro-morphological growth, followed by the macro-morphological growth involves the branching and extension of hyphae, and reach the final stage of fungal cell autolysis. During fungal fermentation in bioreactors, the operating parameters of agitation and/or aeration systems strongly affect pellet morphology and subsequently fungal productivity. The agitation system is reported to decrease the pellet size by shaving of hyphal elements at low agitation intensity and by breaking up the pellets at high agitation speed, while the aeration system increases the pellet size by the increased hyphal branching to enlarge pellets become fluffy and hairy.

Raspberry ketone (4-(4-hydroxyphenyl) butan-2-one; RK) could be obtained either from natural fruits (e.g., raspberries, cranberries, blackberries) or chemical synthesis. However, the extraction from natural fruits is limited by the low abundance while the chemical synthesis may cause the problems such as toxic by-products and environmental pollution. The current methods of bioconversion of RK from natural precursors have achieved big progress. Alternatively, fungal fermentation of the *Nidula niveo-tomentosa* can directly produce RK, but most research are focused on flask culture, leading to the low production rates. Therefore, it is

important to explore and optimize the feasibility of submerged culture of *Nidula niveo-tomentosa* using other bioreactors such as STR and fluidized bed reactor, which may provide foundations for pilot scale and commercial-scale RK production in future.

Hence, this chapter reviewed the development of current research on micro-fluidized bed, fungal fermentation and raspberry ketone production. Most importantly, this chapter provides the theoretical supports to link the fluidized bed techniques with fungal fermentation together for the production of natural RK, which can not only broaden the development of fluidized bed but also explore the feasibility of improving RK yields by using novel bioreactor systems. In next chapter, the specific approaches to achieve the goals will be described.

Chapter 3 Approaches and methodologies

3.1 Introduction

This chapter described the methods for the design and fabrication of MFB, followed by the procedures of investigating the hydrodynamics in gas-liquid and gas-liquid-solid systems. Besides, the methodologies for fungal fermentation including the seed culture preparation, flask cultivation, liquid sampling, HPLC and YSI measurements were introduced. Finally, the experimental approaches to produce RK by submerged cultivation of *Nidula niveo-tomentosa* in different bench-scale bioreactors have been proposed.

3.2 Micro-fluidized bed techniques

Fluidized bed reactor is an established technology in chemical process industry due to its good mixing and high mass and heat transfer characteristics. In recent years, increasing attention has been paid to micro-fluidized bed reactors (MFBR), which reduce costs, decrease operation times, increase safety and intensify the engineering process [236]. However, there is no clearly defined distinction between micro and macro-fluidized beds. Whether the boundary should be asserted based on the 1 mm cross-sectional micro-fluidic context [17, 237] or on the wall effects related to volumetric effects (such as gravity) [19, 22] is still debatable. According to the previous studies, a fluidized bed can be regarded as “micro” when it shows apparent changes in hydrodynamic properties, although its hydraulic diameter could be up to 2-3 centimetres and the bed height reaches 5 cm [15, 18, 19]. In this section, the methodologies for fluidized bed design, fabrication and hydrodynamics characterization are presented.

3.2.1 Micro-fluidized bed design and fabrication

The use of additive manufacturing (also referred to as 3D printing technique) has been widely used for the fabrication of microfluidic devices [45, 238]. In this project, the 3D models of the miniaturized fluidized beds were created with the assist of CAD software (i.e., SketchUp). To minimise the visualization issues resulted from light refraction, the internal bed chamber is

cuboid shape instead of circular cross-section. In this project, fluidized beds with different dimensions of the cross-sectional area have been studied, shown in Fig. 3.1. On the one hand, the fluidized bed must be small enough to save the material as well as the time for fabrication. On the other hand, the tiny bed would fail to fluidize the particles due to big wall effect. Thus, the determination of final bed cross section area after many fluidization tests using fluidized beds with different dimensions is necessary, to balance the wall effect and the requirement of less resin. The bed height is limited to 15 cm because the building volume of Form2 printer is $145 \times 145 \times 165$ mm. However, the final height of fluidic devices can be extended by printing several parts and connecting them together. The entire fluidized bed was divided into upper part and lower part. The upper chamber is used for cell cultivation while the lower part is equipped with air and liquid inlets to provide oxygen and liquid broth for cell cultivation. Three types of distributors, namely bar-shape distributor, perforated plate distributor and mesh-particles distributor (discussed in Chapter 4), were designed with the aim to disrupt the big bubbles when the air flows through the fine tubes. At the top area of the column, the gas/liquid outlet is fitted with a mesh filter of 0.7 mm in gap size to remove liquid/gas and facilitate solid retention.

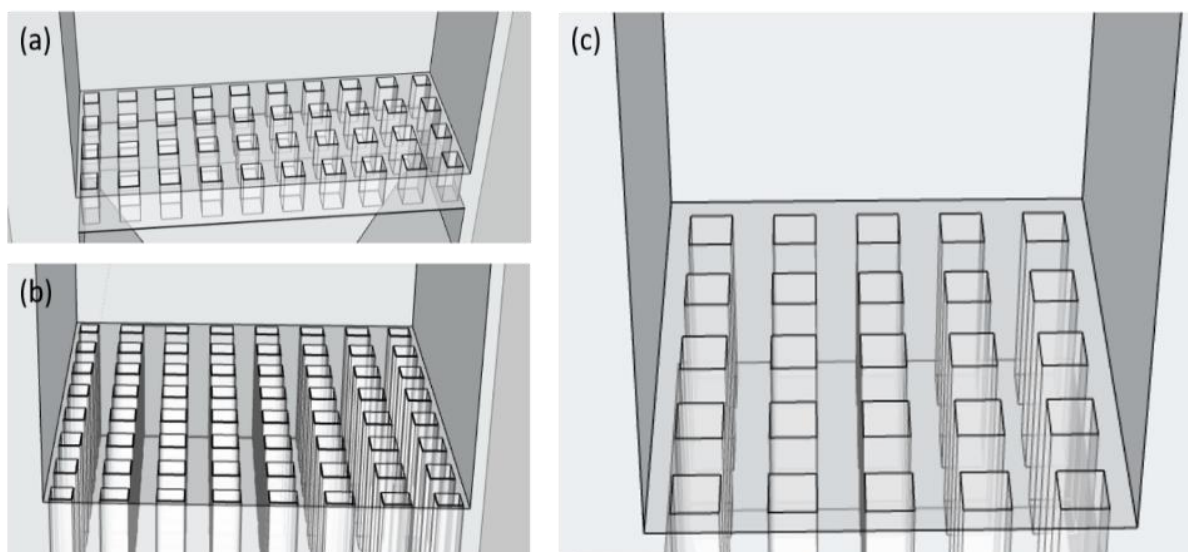


Fig. 3.1. Images of cross section of fluidized bed with different dimensions: (a) 7.5 mm \times 20 mm, (b) 10 mm \times 10 mm, (c) 15 mm \times 15 mm.

After the design of the fluidized bed models, the SketchUp files of fluidized beds were exported and converted into STL files which were read and pre-processed by the Form 2 SLA printer. The printing process and post-printing processes (post-washing and post-heating) was illustrated in Fig. 3.2a and Fig. 3.2b & c, respectively. During the printing process, the Form2 used a 405 nm UV laser (140 μ m spot size, 250 mW) to cure a translucent methyl acrylate based proprietary resin (FLGPCL02) comprising methyl acrylate monomer (55–75% w/w), methyl acrylate oligomers (35–40% w/w) and photoinitiator additives (10–15% w/w). Construction of each layer involved the laser scanning quickly through the resin tank according to the shape defined by the corresponding slice through the geometry, followed by the build platform being raised by the user-specified Z-axis resolution. The Form2 delivers a maximum XY (horizontal) resolution of 140 μ m and Z-axis (vertical) resolutions of 25–100 μ m; though 100 μ m produced the best surface quality of the designs.

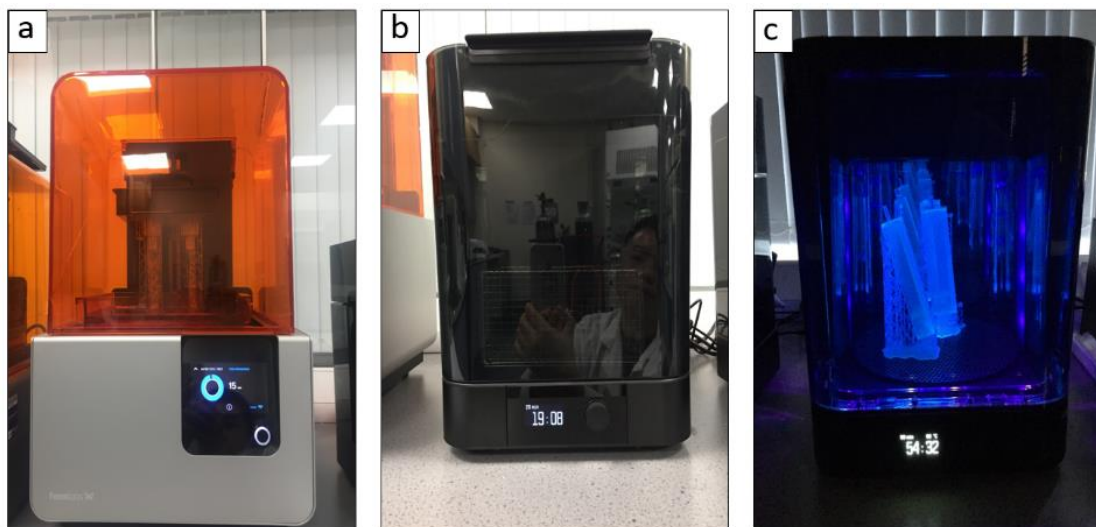


Fig. 3.2. Fluidized bed printing and post-printing process: (a) the fluid bed is printing by the Form 2 SLA printer, (b) post-washing process is to clean the surface of printed parts, (c) post-curing process is used to strengthen the inner bonds of the parts.

Afterwards, a post-printing process including post-washing and post-curing was to clean the surface of the printed-parts and improve the material properties. In the post-washing process, the printed part was firstly moved from 3D printer then placed in a basket filled with isopropyl

alcohol (IPA) inside the Form Wash machine. The washing machine was used to agitate the IPA to flow around the parts, aiming to clean the part surface. Finally, the post-curing process involved a heater and 13 LEDs to emit 405 nm light, which enhanced the formation of additional bonds inside the parts, making the part stronger and stiffer [239].

3.2.2 Image capture and processing

To measure the bubbles movement and particles fluidization performance in the micro-fluidized bed, the high-speed camera (acA640-750uc - Basler ace camera with 12 mm, f/1.8 Ci Series Fixed Focal Length Lens) combined with the Pylon Viewer were used, which access all the camera's parameters and control the camera's full functionality for desired image sequences, followed by the image analysis using Fiji ImageJ. Meanwhile, a backlighting system was used to improve the image analysis. For the bubble size and velocity characterization, the specific procedures were described in Section 3.2.3.1 liquid-gas-solid fluidization, as shown below.

3.2.3 Hydrodynamics investigation of the micro-fluidized bed

In this section, the hydrodynamic investigation of MFB was conducted on the bubble column and liquid-gas-solid fluidization. The liquid-gas system was intended to study bubbles morphology and movements arising from the effects of liquid velocity, gas velocity, gas orifice diameter. The liquid-gas-solid fluidization was aimed to: (1). explore the existence of surface force and wall effects in a small-scale fluidized bed; (2). characterize the pellets suspension and recirculation driven by liquid and/or gas flows.

The schematic diagram of the experimental setup for bubble column & liquid-gas-solid fluidization is shown in [Fig. 3.3](#). For the bubble column experiments, the study was focused on the bubbles' morphology and movement by gas flows without the involvement of solids. In liquid-solid/liquid-solid-gas fluidization systems, the fungal cells *Nidula niveo-tomentosa* were transferred from culture flask and then inoculated into the fluidized bed, followed by the step involving the pumping of liquid (ultrapure water or culture media) into the bioreactor by a

peristaltic pump (Watson Marlow 530U, US). First, the compressed air for the gas phase was firstly regulated by the pressure regulator (R07-200-RNEG, IMI Norgren, UK) and then adjusted to the desired flowrates using the gas rotameter (FL-3635G, Omega Engineering, UK). Images of pellets fluidization was recorded using a Basler acA640-750uc camera (751 fps, VGA) combined with a fixed focal length Lens (12 mm/F1.8 Lens, Edmund Optics Inc. USA), and was monitored using the Pylon Viewer software for off-line analysis.

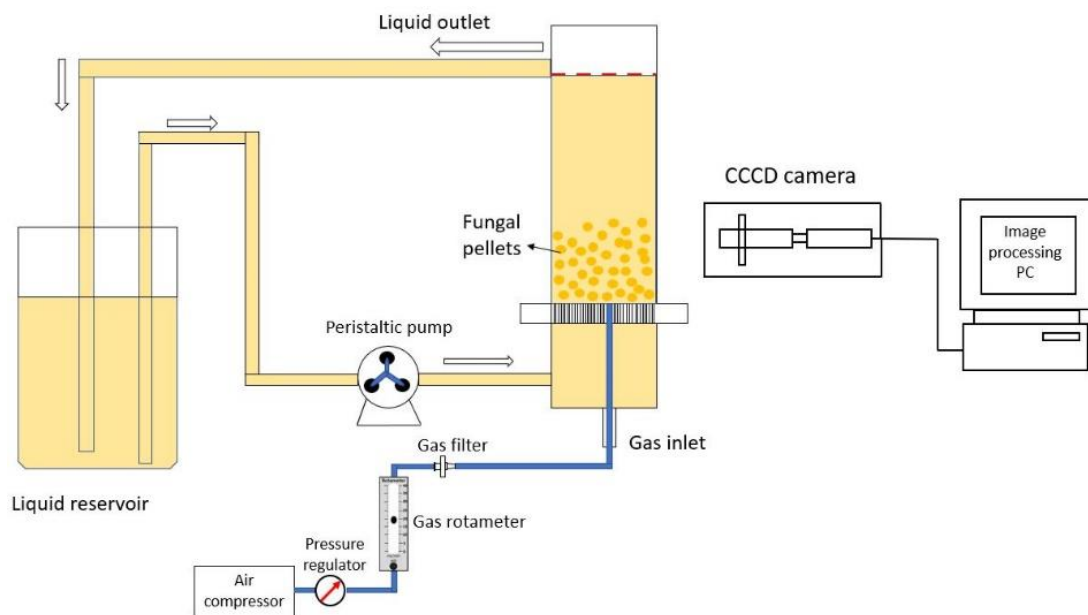


Fig. 3.3. Schematic diagram of the experimental setup for fungal pellets fluidization.

3.2.3.1 Liquid-gas-solid fluidization

For aerobic fermentation, the bubbles were generated when filtered air was pumped into bioreactors. The bubble flow was intended to provide oxygen and to enhance the mass transfer and mixing efficiency, as the bubbles could separate the agglomerated cells and detach the cells from bed walls. However, the bursting of the bubbles as well as bubbles-cells disengagement at the liquid surfaces have been reported to cause cell damage/death [63, 190]. Therefore, in this section the liquid-gas fluidization was focused on bubbles dynamics, to gain insights for controlling the bubbles control in the later part of the PhD work on aerobic fungal fermentation.

Bubble size

The bubble size measurement was conducted on images of the bubbles captured by the high-speed camera. In the calculation of the average bubble diameter, the volume-surface equation was applied to give more weights to the larger bubbles in the multi-bubble flows. The Sauter mean diameter equation is given as:

$$d_b = \frac{\sum d_i^3}{\sum d_i^2} \quad (3.1)$$

where d_i is the diameter of every single bubbles [33].

Bubble velocity

The bubbles rising paths resembled an upward spiral path, contrary to our expectation of a straight path. Therefore, the bubble velocities in the experiments refer to the vertical velocities. To characterize the bubble velocity, the function ‘Manual Tracking’ was applied. The operational principle for bubble velocity measurement is to record bubble’s displacement in Y direction (from bed bottle to the top liquid/gas interface) and the time for bubble’s movement. Here, the Y-displacement is the height of fluidized bed, while the time can be obtained based on the number of frames for bubble to move from bottom to top, as the high-speed camera takes images at the speed of 10 ms/frame (100 FPS).

Gas volume fraction

The gas volume fraction \mathcal{E}_G is a dimensionless quantity which is defined as the ratio of the gas volume to the volume of the column [240]. The measurement of \mathcal{E}_G is an effective method to predict the gas supply in reactor. In principle, the bubble size and velocity vary with liquid velocity, gas velocity and gas sparger diameter, and, consequently, this could result in the variation of \mathcal{E}_G . Here, the intent was to investigate gas volume fraction under the parameters of gas/liquid velocity, gas orifice diameters. Gas volume fraction \mathcal{E}_G was calculated using the equation below:

$$\varepsilon_G = \frac{\sum V_b}{V_C} \quad (3.2)$$

Where V_b is the volume of each bubble, V_c is the volume of bed column. The sum of bubble volume was obtained by timing the total numbers of bubble in the column with the average bubble volume, as the average bubble size has been calculated already. The column volume had a fixed value of 33.75 ml because the bed size has a cross section of 15×15 mm and a height of 150 mm.

3.2.3.2 Liquid-solid fluidization

This part reported a fluidization study of fungal pellets in the MFB was conducted. To investigate the hydrodynamic properties of fungal pellets in a liquid-solid and a liquid-solid-gas fluidized bed, the fungus species used in this work was *Nidula niveo-tomentosa* (Basidiomycota), which was supplied by Berger et al. at the University of Hannover [14]. The composition of the culture media is shown in [Table 3.1](#). To grow the seed culture, an agar-plug from the periphery of a 2-week-old agar plate (consist of 20 g/l malt extract and 15 g/l agarose) culture of the fungus was homogenized in a 100-ml Erlenmeyer flask containing 40 ml of culture media. The cells could grow in a MaxQ™ incubator (ThermoFisher Scientific, USA) with a rotational speed of 150 rpm at 24 °C for 4 weeks.

Table 3.1 Base culture media formulation for fungal cultivation.

Components in media	Concentration	Units
Glucose monohydrate	75	g/L
Peptone from soy	6	g/L
Potassium dihydrogen phosphate	2.5	g/L
magnesium sulphate	0.5	g/L
Yeast extract	1.5	g/L
Calcium chloride dihydrate	73.5	mg/L
Ultrapure water	Fill up to 1 L	

The pellets were subsequently transferred from the flask into the petri dishes for photographic image acquisition, with the use of a Scan 1200 (Interscience, France) colony counter ([Fig. 3.4a](#)).

Pellet size and sphericity was measured for these images using the ‘Analyze-Particles’ function

[241]. An example of the resulting pellet size distribution is shown in Fig. 3.4b. Pellet density was determined by dividing the weight of hydrated pellets by the corresponding volume. Pellet wet weight was determined by filtering the contents of the flask through a pre-weighed filter paper with a Buchner funnel. The volume of pellets was determined by measuring the volumetric displacement of ultrapure water in a measuring cylinder (ΔV). Ultrapure water and culture medium (components listed in Table 3.1) were used as the liquid phase, respectively, to characterize the effects of liquid properties (i.e. viscosity and density) on pellet fluidization.

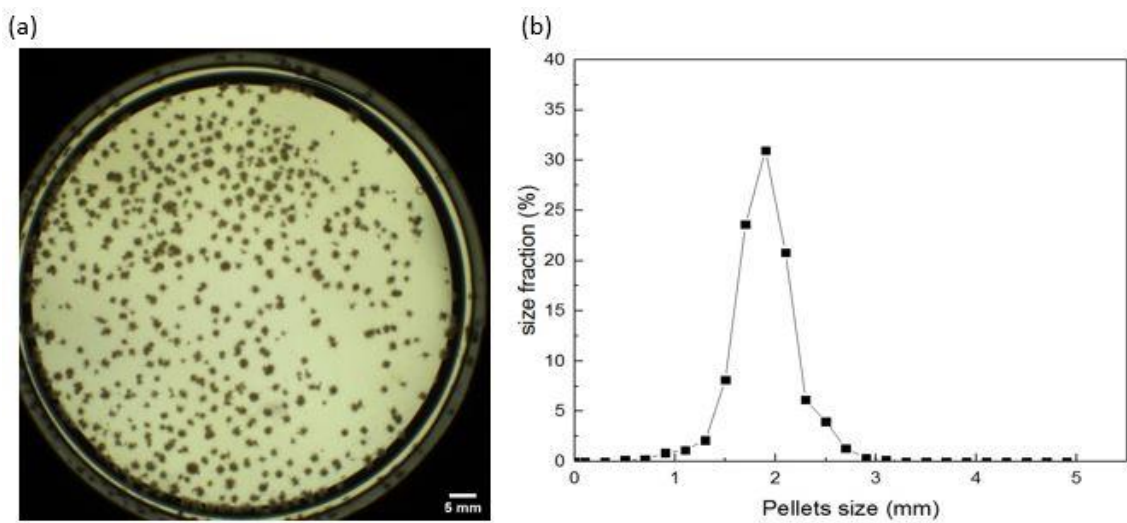


Fig. 3.4. (a) Image of fungal pellets after 4-week flask culture in 90 mm petri dish, (b) Corresponding size distribution obtained from 600 pellet samples.

3.3 Fungal fermentation

Fungal pellets are spherical, ellipsoidal or oval masses of intertwined hyphae with a size usually in the range of several hundred micrometres to several millimetres [201, 242]. Most fungal pellets contain a core of densely packed hyphae, surrounded to a large extent by a more annular dispersed or ‘hairy’ region that contains the radially growing portion of the hyphae [204]. The spherical shape and millimetre-scale size enable the immobilized fungal pellets to be cultured using a fluidized bed bioreactor. In this project, the specific fungi of *Nidula niveo-tomentosa* was initially cultivated using a traditional flask culture in a MaxQ™ 6000 incubator (ThermoFisher Scientific, USA) with the speed of 150 rpm and temperature of 24°C, to study

and optimize the cultivation media (i.e., glucose concentration, phenylalanine supply) as well as the cultivation conditions such as photo period time, age of pre-culture, for a high raspberry compounds production. The study of cultivation growth media and cultivation conditions was intended to be the preliminary experiments for the subsequent fungal fermentation using different bioreactors.

3.3.1 Microorganisms

The *Nidula niveo-tomentosa* strain (CBS strain 380.80) was provided courtesy of the group of Berger et al. [14]. For long-term storage and preservation, culture stocks of the strains were kept at -70 °C with 15% (V/V) glycerol. Seed culture was prepared by thawing 1 ml aliquot of frozen stock culture (0.5 ml strains and 0.5 ml of 30% glycerol) and inoculating it into 40 ml of culture medium.

3.3.2 Strain and Chemicals

The substrates for culture media were purchased from Sigma-Aldrich (Singapore), Merck (Darmstadt, Germany), Kento (Tokyo, Japan), 1st BASE (Gemini, Singapore) and BD (Miami, USA). The constituents of standard liquids for HPLC calibration, including raspberry ketone, rhododendrol and L-phenylalanine were supplied by Sigma-Aldrich (Shanghai, China). Solvents were purchased from VWR (Paris, France) and 1st BASE (Gemini, Singapore).

3.3.3 Cultivation medium preparation and characterization

The original culture medium was prepared based on the method reported by Andreas Boker, Manuela Fischer [3]. Specifically, the culture medium contained 75 g/l glucose monohydrate, 6 g/l soy peptone, 1.5 g/l yeast extract, 2.5 g/l KH₂SO₄, 0.5 g/l MgSO₄, 73.5 mg/l CaCl₂•H₂O. The seed culture was grown aerobically in 100 ml Erlenmeyer flask and kept in in a MaxQ™ 6000 incubator (ThermoFisher Scientific, USA) with the speed of 150 rpm at 24 °C. The cultivation period of seed culture was 14 days for fungi proliferation and pelletization, after which the content of seed culture was homogenized at the speed of 10,000 rpm for 1 minute

by the homogenizer device (T18 digital ULTRA-TURRAX[®], IKA, Germany). The homogenized seed culture was then used for fungal inoculum. To prevent contamination, all the flasks and culture media were autoclaved at 121 °C for 15-20 min before moving into biosafety cabinet (BSC) for further experiments.

To stimulate the RK production, 10% (v/v) of the filtered sterilization phenylalanine (110 mM) was added into fungi culture medium. At the same time, the cultures were irradiated using UV-A light with a photoperiod of 10 hours UV light and 14 hours dark. The blacklight UV tubes (F4T5BLB 352 mm × 6, SANKYO DENKI, Japan) were mounted on the top face of the incubator, or on a UV enclosure for bioreactors.

3.3.3.1 Density characterization

From the previous investigation, the pellets settled onto the bottom of flask during flask culture, because the pellets were denser than the cultivation media. The pellets were ideal for fluidization by upward liquid/gas flow (s) in fluidized bed reactors. However, the exact density value of the cultivation media remains unknown. Thus, experiments were performed to measure the density of media by mass-volume method.

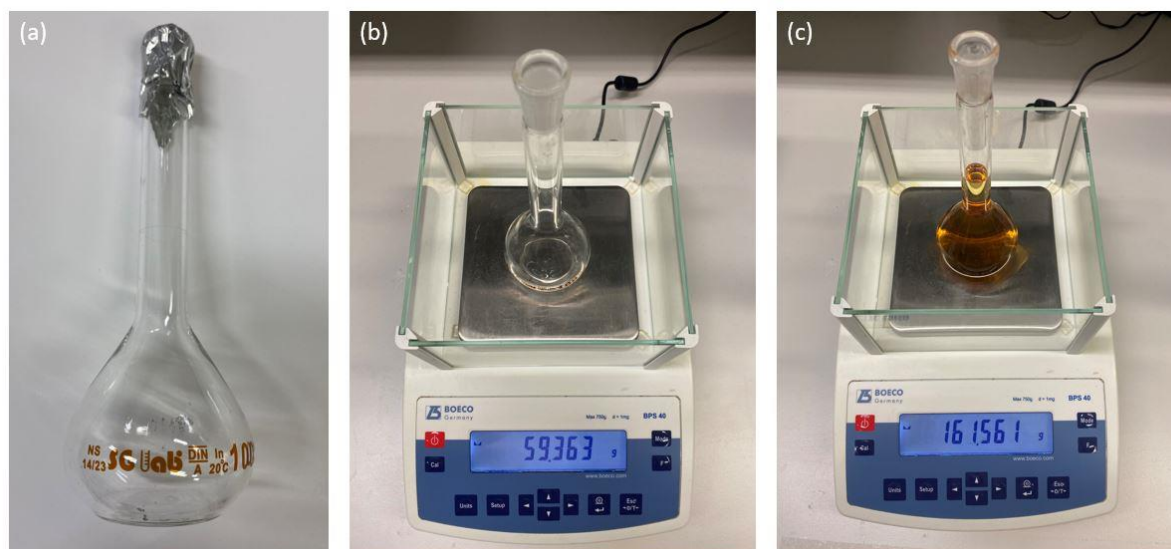


Fig. 3.5. Density measurement for cultivation media: (a) preparation of the clean and autoclaved volumetric flask, (b) weighing of the empty flask, (c) filling cultivation medium to the scale line and weighing the weight again.

As illustrated in Fig. 3.5, to measure the density of cultivation media, a clean and dry volumetric flask (NS 14/23, 100± ml, SG lab, Singapore) was firstly weighed using a standard precision balance (BOECO BPS 40, Germany) with the linearity error of ± 0.003g to get the weight of the empty volumetric flask, M_1 . Then the volumetric flask was filled with newly prepared and autoclaved cultivation media to the scale line (where the lowest part of concave liquid level was aligned with the scale line) and the flask was weighed (weight of the flask, M_2). Note, the above procedures were repeated at least three times, to minimize the experimental errors. The density of the cultivation media was calculated using:

$$\rho_{Media} = \frac{M_2 - M_1}{100} \quad (3.3)$$

3.3.3.2 Liquid viscosity characterization

Another key factor which could affect the particle fluidization performance is the liquid viscosity, which is related to the viscos stress in the deformation of the fluid. Therefore, the characterization of the viscosity of the cultivation medium is an effective way for fluidization analysis. In this experiment, the viscosity of the culture medium was measured using a digital viscometer (VISCOTM-895, ATAGO, Japan).

The first step involved the viscometer calibration using a refined mineral oil (standard liquid for calibrating viscometers, Nippon Grease Co., Ltd., Japan). The viscometer was set up according to the manual. Then the associated A1 spindle was screwed and immersed in the L Beaker with 100 mL calibration liquid inside (Fig. 3.6). The rotating speed of A1 spindle was set 250 rpm at room temperature (~22 °C), keyed in the corresponding viscosity value on the top screen of the viscometer after checking the viscosity computation table provided by the liquid calibration company. Finally, the calibrated value was recorded. For the viscosity measurement of the cultivation medium, the A1 spindle was used at the same condition (250 rpm, 22 °C) while L beaker was filled with 100 ml medium. The measurement button (on the

screen panel of the viscometer) was activated to determine the viscosity value for culture medium. The measurements were repeated three times to account for repeatability and to estimate of experimental errors.

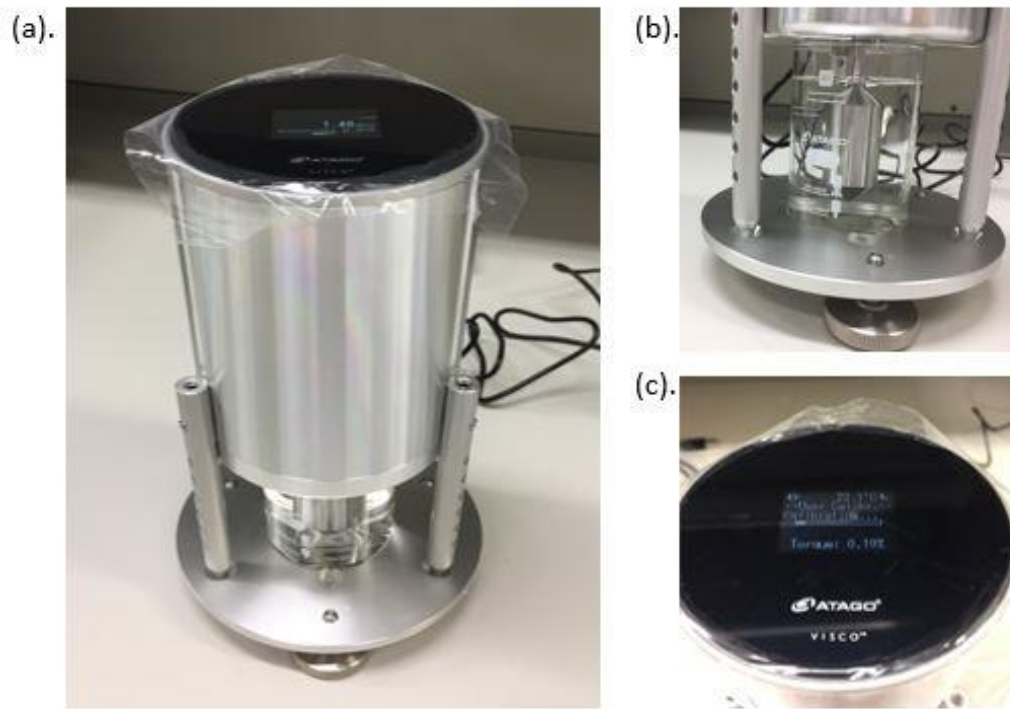


Fig. 3.6. Viscosity measurement for cultivation medium: (a) image of the VISCO™-895 digital viscometer, (b) A1 spindle with 100 ml calibrating liquid inside the L beaker for viscosity calibration, (c) digital screen on the top of viscometer shows the process of liquid viscosity measurement.

3.3.4 Preparation of seed culture and flask culture

The seed culture (also called ‘pre-culture’) was usually carried out in the cell cultivation or fungal fermentation to allow the cells recover from petri dish and proliferate exponentially [243]. Besides, the preparation of seed culture ensured that the inoculant could grow healthily, replicate well and decrease the variation of initial seeding density.

The fungal strains were initially maintained in petri dishes of the incubator with rotating speed of 150 rpm and temperature of 24 °C. To prevent contamination, all the procedures of seed culture preparation were performed in BSC. To begin with, 40 ml of fresh cultivation media was aliquoted into a 100 ml flask and capped immediately with white cork. Then, a sterilized straw was used to pick a 1 cm disk from the culture agar (consist of 20 g/l malt extract and 15

g/L agar powders) plate, and then transferred into the media flask by an autoclaved stick. Note, the disk was taken from edge where it is growing to maintain the bioactivity of strains. Finally, the homogenizer device (T18 digital ULTRA-TURRAX[®], IKA, Germany) was used to homogenize the content of the flask at the speed of 10,000 rpm for 1 minute. The well-mixed preculture was stored in incubator (150 rpm and 24 °C) for 2-week cultivation.

The inoculum for flask culture came from the seed culture which had been prepared 2 weeks in advance. To get the inoculum, the seed culture was homogenized by the homogenizer device (T18 digital ULTRA-TURRAX[®], IKA, Germany) at the speed of 10,000 rpm for 3 minutes, making pelleted fungus broken into free mycelia. Afterwards, 40 ml of fresh cultivation media and 4 ml 100 mM sterilized phenylalanine were subsequently aliquoted into a 100 ml flask and capped immediately with white cork. Finally, 4 ml of the homogenized seed culture was added into the flask. The prepared flask culture was then moved into incubator (150 rpm and 24°C) for 5-week cultivation.

3.3.5 Investigation of fungal pellets

Pellet's density, sphericity and size are three most significant impactors which determine the pellets fluidization, according to the Ergun equation [54]. Since fungal fermentation in this study is conducted by the means of pellets fluidization, pellet's density, sphericity and size will directly affect fluidization performance during fermentation and subsequent bioproduction. Therefore, the investigations of pellet size and density are essential for the optimization of the operating conditions in fluidized bed bioreactor.

3.3.5.1 Pellets size characterization

In this study, the pellet size was measured once a week along the 6-week flask cultivation, to get the pellet size weekly distribution. Specifically, the flasks were firstly taken out from the incubator (Fig. 3.7a). The pellets-media mixture was transferred from the flask culture into empty petri dishes (Fig. 3.7b) for imaging using Scan 1200 (Interscience, France). In Fig. 3.7c,

the photograph of the pellets in petri dishes were then processed using ImageJ to distinguish each pellet from the image [241]. Finally, the pellet size was automatically measured and displayed using ‘Analyse Particles’ function in ImageJ (Fig. 3.7d).

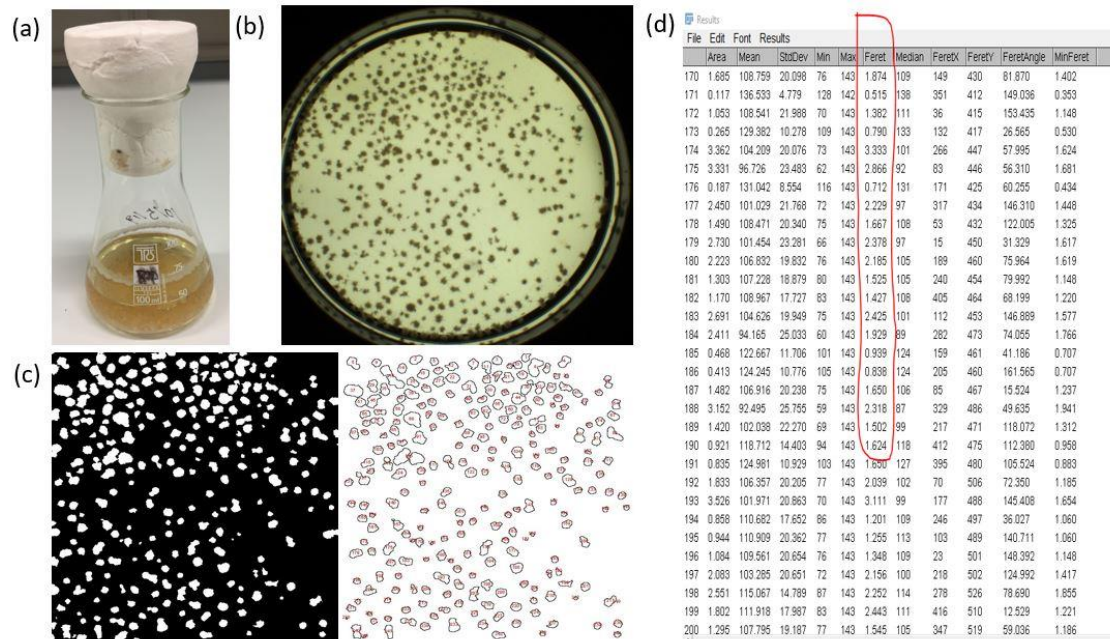


Fig. 3.7. Procedures for pellet size characterization: (a) take the flask culture from incubator, (b) transfer the pellets-media mixture from flask into petri dish for photograph using Scan 2000, (c) use ImageJ to process the photograph for size measurement, (c) use the function of Analyse Particles to get the results of each pellet’s diameter.

3.3.5.2 Pellets sphericity characterization

Pellet sphericity, regarded as part of pellet morphology, was associated with supply of nutrients, specially oxygen, and the ease of mixing of the broth [205]. Pellet sphericity is dependent on the fermentation conditions, such as agitation speed in stirred tank reactor, the gas flowrate and bubbles size in photo bioreactor and fluidized bed. In turn, knowing the pellet sphericity helps to reflect the effect of operating conditions of the ongoing fermenters, detailed discussions were given in **Chapter 4**.

The pellet sphericity characterization was also conducted using ImageJ. After an image of the pellets in petri dish was taken, the image was processed by ImageJ to distinguish each pellet. Next, the pellet sphericity was determined using the Shape Descriptors function under Set Measurements [244].

3.3.5.3 Density measurement

Pellet density was determined by dividing the pellet wet weight by its corresponding volume. Specifically, the fungal pellets were harvested from flask and then filtered using the Buchner funnel to remove the bulk of liquid. The pellets volume was determined by measuring the volumetric displacement of ultrapure water due to the pellets (ΔV).

3.3.6 Cultivation parameters for flask culture

3.3.6.1 Preservation and storage of fungi strains (agar plate VS freezer stock)

The fungal strains were initially kept in agar plate (consist of 20 g/L malt extract and 15 g/L agar powders) from generation II, which was maintained by serial subculture (Fig. 3.8a). To prepare the seed culture from agar plate, 1 cm plug of agar was isolated from the edge (where the culture was growing) to maintain the bioactivity of strains, then put into the flask containing 40 ml of fresh medium. Afterwards, the content of the flask was homogenized at the speed of 10,000 rpm for 1 minute. The well-mixed preculture was stored in the incubator (150 rpm and 24 °C) for cultivation over 2 weeks. Seed culture from freezer stock (Fig. 3.8b) was made by thawing one freezer stock of strains (0.5 ml strains and 0.5 ml of 30% autoclaved glycerol) and inoculating it into 40 ml of culture medium. Fig. 3.8c presented the samples of flask cultures which were prepared from either agar plate or freezer stick and cultivated in the incubator.

3.3.6.2 Fungal morphology (pellets VS mycelia)

In submerged cultivation, seed culture of *Nidula niveo-tomentosa* strains will grow in the form of pellets and produce raspberry ketone, but whether the pellets or free mycelia has a higher bioproductivity is still not clear. To compare the effect of fungal morphology on RK production, the free mycelia of fungi was obtained by homogenizing the flask content after two and three weeks of flask culture, respectively. The fungal growth and corresponding RK production were compared with those without homogenization during fermentation.

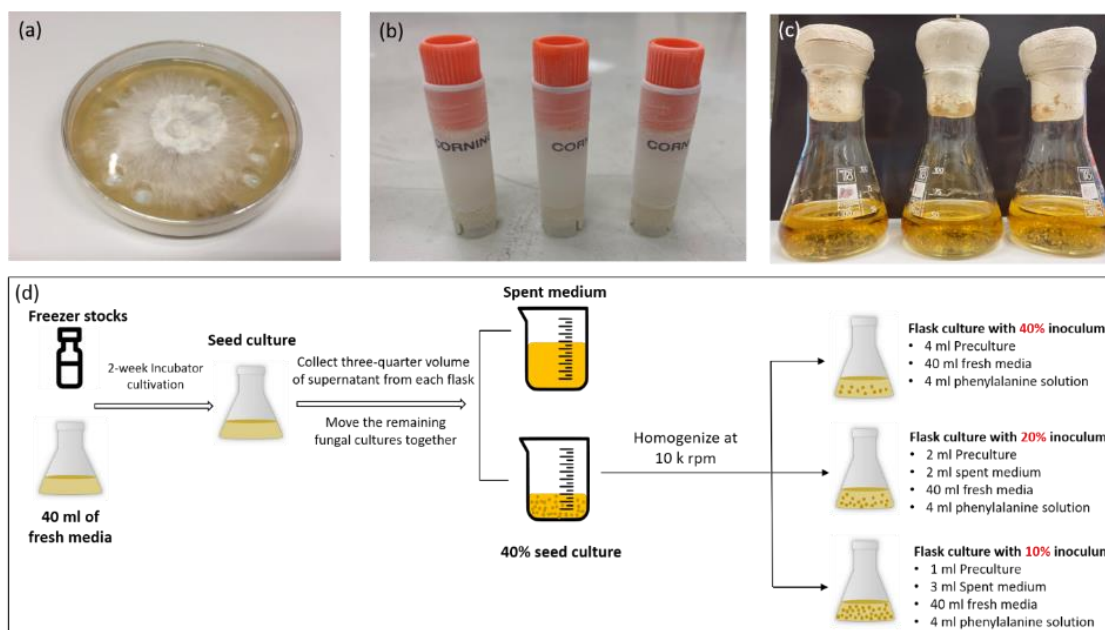


Fig. 3.8. (a) Agar plate for fungal strains storage, (b) Samples of freezer stocks kept in $-70\text{ }^{\circ}\text{C}$ fridge, (c) Images of well-prepared flask culture, (d) Schematic shows the procedure to prepare flask culture with inoculum concentration of 10%, 20% and 40%, respectively.

3.3.6.3 Cultivation parameters

Apart from the comparisons of fungi storage methods (agar plate VS freezer stock) and fungal morphology (pellets VS mycelia), this project also investigated the cultivation parameters at different levels, as listed in [Table. 3.2](#). Among the parameters, glucose is a fundamental substrate which not only provides carbon source but also promotes pellet formation [204]. Seed culture age and concentration determine the bioactivity and initial biomass of fungi cell, respectively. A detailed procedure to prepare seed culture with different concentration is illustrated in [Fig. 3.8d](#). In addition, phenylalanine (used as the precursor) and UV-A radiation, reported to promote RK production [13, 14], were investigated in this experiment. The goal of the parameter design is to identify the ideal level of each parameter, leading to the highest RK production.

3.3.7 Liquid sampling

The liquid sampling is aimed to analyse the fungal fermentation performance, which can be determined by the consumption of glucose and phenylalanine, production of raspberry ketone

and raspberry alcohol, and the PH variation of media during the fermentation. In the experiments, the liquid samplings were conducted twice a week for 5-week cultivation. Particularly, the concentrations of phenylalanine, raspberry ketone, raspberry alcohol were measured by high performance liquid chromatography (HPLC). Glucose concentration was measured through YSI Biochemistry Analyzer. The pH of the liquid samples was detected by pH meter.

Table. 3.2 Cultivation parameters and their corresponding levels.

Parameters	Level			
	1	2	3	4
A: Glucose concentration (g/l)	25	50	75	100
B: Preculture age (week)	1	2	3	-
C: Inoculum concentration (v/v)	10%	20%	40%	-
D: UV exposure time (hour per day)	0	10	17	24
E: Phenylalanine concentration (g/l)	0.5	1.5	2.5	-

3.3.7.1 HPLC analysis

The concentration of phenylalanine, RA and RK were measured by HPLC (1260 Infinity II, Agilent Technologies, USA). The configuration of HPLC is shown in [Fig. 3.9a](#). To perform the HPLC analysis, the procedures of liquid sampling preparation, HPLC standard liquid and column preparation were needed. The specific HPLC procedures and methods are described below:

Liquid sampling preparation

The liquid samples preparations prior to HPLC measurement involved six steps:

- (1). Three 10 ml plastic microcentrifuge tubes (for triplicates) were labelled RK1, RK2 and RK3, respectively.
- (2). The fermentation media was transferred from 3 flasks into the plastic tubes, respectively.
- (3). The media in the plastic tubes were subjected to centrifuging at 3000 RPM for 5 minutes using Eppendorf Centrifuge (Eppendorf 5810, Germany).

(4). The supernatant from each centrifuge tubes were transferred into different syringe. The supernatants were filtered using 45 μm filter (UNIFLO 25/0, 45 NYL, Whatman, UK) and the liquid was dispensed into HPLC glass vials (5182-0714, Agilent Technologies, USA).

(5). The HPLC glass vials were labelled with the use of the green stickers and kept in -20 C° fridge (Fig. 3.9b).

(6). Thaw the samples before analysis.

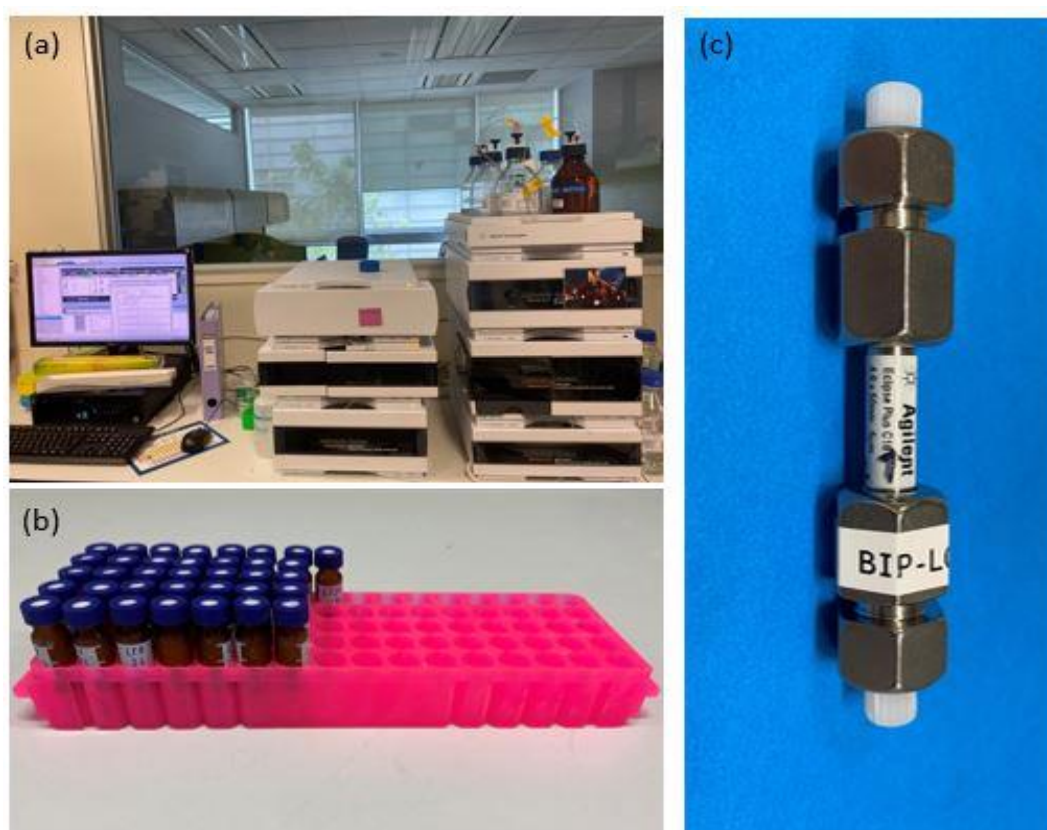


Fig. 3.9. (a) Configuration of the 1260 Infinity II HPLC, (b) Liquid samples are kept in HPLC glass vials in -20°C for long-term storage, (c) Image of ZORBAX Eclipse Plus C18 HPLC column for raspberry compounds detection.

HPLC procedures

There are two steps for HPLC measurements as given by following bullet points:

(1). Standard liquid preparation: Weigh 0.025 g of Raspberry Alcohol, Raspberry ketone and Phenylalanine Standard into a 25 mL volumetric flask and dilute to mark with water to give a 1 g/l stock and filter through 0.45 μm filter (Solution A). Dilute Solution A with media to

further give concentrations of 0.8, 0.6, 0.4, 0.2, 0.1 g/l and 50, 25, 12.5, 6.25, 3.125 and 1.56 mg/l solutions. The standard liquids were required to be filtered prior to injection for HPLC analysis and calibration.

(2). HPLC methods: Mobile phase A was the 0.1 M sodium acetate buffer whose pH was 4.66 adjusted by acetic acid, while mobile phase B was the pure methanol. The HPLC column (ZORBAX Eclipse Plus C18, Agilent Technologies, USA), shown in [Fig. 3.9c](#), was used at 35 °C with flow rate of 0.5 ml/min. Before the HPLC analysis, the column was eluted with 90% water and 10% methanol for 30 min and then flushed with 20% water and 80% methanol for another 30 minutes. Of each sample, 20 µl was injected for characterization with 9 minutes of HPLC running time. The wavelengths detected for phenylalanine is 257 nm; for raspberry ketone and alcohol, it is 280 nm. The details for the HPLC process are found in the manual of Agilent 1260 infinity quaternary LC [245].

3.3.7.2 Glucose measurement using YSI apparatus

The glucose concentration in media during the fungal fermentation were measured by YSI 2900 in [Fig. 3.10a](#), which can reflect the glucose consumption by comparing the initial and real-time glucose concentrations at different fermentation period. As the maximum glucose concentration of 25 g/l can be detected in YSI 2900, all the liquid samples were diluted with ultrapure water for 10 times (10% liquid samples + 90% ultrapure water) before glucose concentration measurements. It was noted that the measured glucose concentration in YSI was not the actual value of the samples, which were ten times bigger than the values displayed on YSI screen.

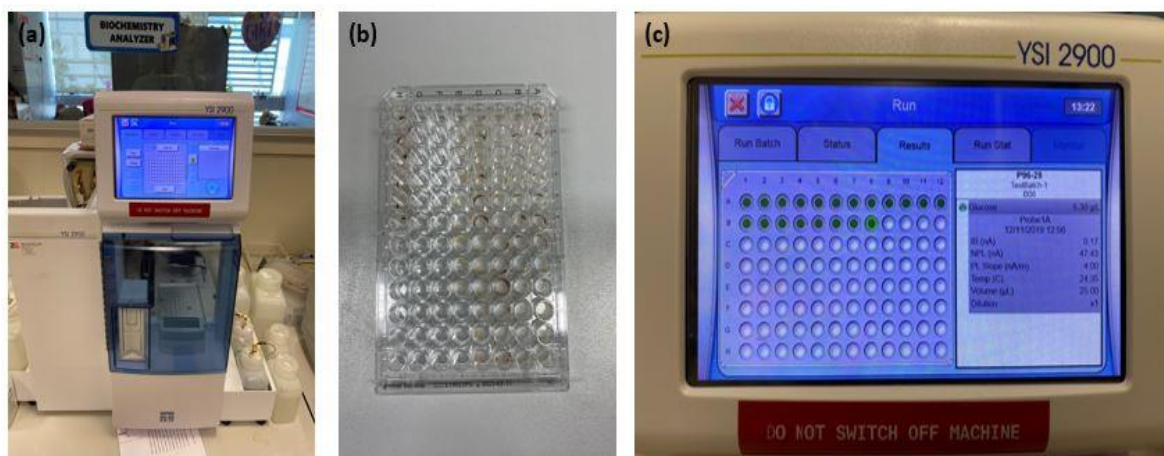


Fig. 3.10. (a) Configuration of the YSI 2900 Biochemistry Analyzers, (b) 96-well sample plate for loading samples, (c) The analysed results can be checked and displayed on the screen.

The liquid samples were diluted by ultrapure water first and then dispensed in 96-well plate (CELLSTAR, Greiner Bio-One 655180, Austria), which was inserted on the flexible sampling plate (Fig. 3.10b). Before the YSI analysis, the [Flush] button under Module 1 was pressed to wash the selected sample module with YSI 2357 buffer, until the current values of Biosensor probes were below 6 nA and stable. Then, the [Calibrate] button was selected for liquid calibration by using YSI 2776 standard D-Glucose (2.50 g/l). Finally, a [batch] was created, [glucose] was selected from Chemistries and the Run icon was pressed to start the glucose concentration measurement. The glucose concentration of the samples could be checked by touching the Results tab, as shown in Fig. 3.10c. The details for YSI operation are referred to the manual of YSI 2900 Series Biochemistry Analysers [246].

3.3.7.3 PH detection

The pH of liquid samples was measured twice a week, along with the liquid sampling for raspberry ketone and alcohol preparation. In this experiment, the pH was simply detected using pH meter (SevenCompact™, Ph/Ion meter S220, METTLER TOLEDO, US). The details for pH measurement are found in the manual of pH/Ion meter S220 [247].

3.3.8 Experimental setup

Three bench-scale bioreactors, namely stirred-tank bioreactor, photobioreactor and fluidized bed bioreactor used for the fungal fermentation and raspberry ketone production have been studied. The control study in terms of fermentation was the flask culture in a shaking incubator.

3.3.8.1 Flask culture

The fungi culture medium, comprising a 40 ml fresh medium (121 °C autoclave for 20 min), 4 ml (110 mM) phenylalanine (filter sterilization) and 4 ml of homogenized seed culture, was inoculated into a 100 ml Erlenmeyer flask. The flask culture was then cultivated in a MaxQ™ incubator (ThermoFisher Scientific, USA) with a rotational speed of 150 rpm at 24 °C for 5 weeks. On the top of incubator, the UV-A light with photoperiod of 10 h per day was applied.

3.3.8.2 Stirred-tank reactor (STR)

The lab-scale stirred tank reactor (Sartorius stedim, Germany) of 1 L capacity with the instrumentation necessary for *Nidula niveo-tomentosa* fermentation was used. In the reactor, 750 ml of culture medium was operated under batch conditions at room temperature. The agitation speed and aeration flowrate were maintained at 300 rpm and 0.15 VVM, respectively. The pH of the bioreactor was not controlled but monitored by the inline system. Similar to flask culture, the STR was also irradiated by the same UV-A light for 10 hours daily during the fermentation period.

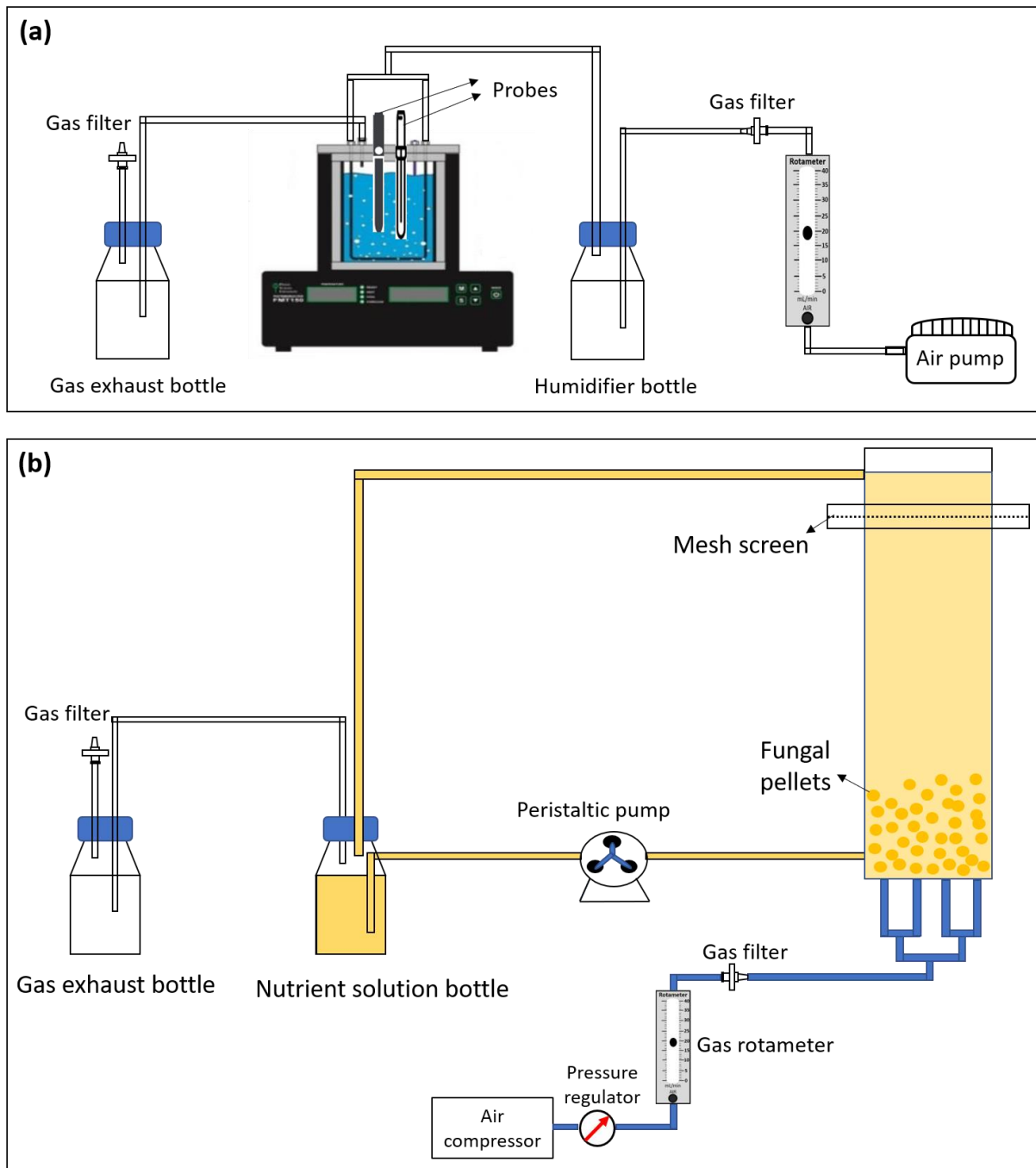


Fig. 3.11. Schematic diagram of the experimental setup: (a) panel bioreactor (PBR), (b) fluidized bed reactor (FBR).

3.3.8.3 Panel bioreactor (PBR)

Fungal fermentation using photobioreactor was carried out in an FMT 150/400 flat-panel bioreactor (PSI Photon system Instruments, Drasov, Czech Republic), in which 400 ml of fungi culture medium was cultivated, relying on the aeration system to provide mixing and air. In [Fig. 3.11a](#), the air source was firstly generated by the aeration pump (OTTO SA-2500, Taiwan),

maintained at a fixed gas flowrate of 0.15 v.v.m by a gas flowmeter (Dwyer Instruments, USA) and filtered using a 0.20 μm PTFE syringe filter (Sartorius, Singapore) before the air entered the humidifier bottle, which contained the autoclaved ultrapure water to prevent medium evaporation. Afterwards, the humidified air was delivered by tubing ($\text{\O} 6/3$ mm) through two headplate Luer connectors to reach a bottom-mounted stainless-steel U-tube sparger with aeration holes ($\text{\O} 1$ mm). To facilitate mixing, as an option, a magnetic stirrer with 35 mm long ($\text{\O} 6$ mm) teflon-coated magnetic controlled by the computer-controlled monitoring device was used to promote mixing and minimize dead zone. Finally, a gas exhausted bottle was integrated with gas filter to prevent environmental contamination before the exhaust of bubbles.

3.3.8.4 Fluidized bed reactor (FBR)

The schematic diagram of the experimental setup for liquid-solid & liquid-gas-solid fluidization system (1 L of effective volume) is shown in Fig. 3.11b. The lab-scale fluidized bed reactor comprised two sections: a) a lower section including liquid inlets on two sides, four bottom-mounted gas spargers ($\text{\O} 150 \mu\text{m} \times 4$) from bottom and a main column (5×5 cm in cross section, 20 cm in height); b) an upper headplate (5×5 cm in cross section, 5 cm in height) containing the gas/liquid outlet. The two sections were made of 3-mm thick quartz plates (Qudao Quartz Ltd., China), and connected via flat flange plates. Each plate featured a circular groove fitted with an O-ring rubber gasket (to prevent liquid/gas leakage). Between the two flange plates, a stainless-steel mesh screen with the aperture of 40 μm was inserted to prevent the pellet washout but discharge the medium during the pellet fluidization.

The seed culture of *Nidula niveo-tomentosa* were transferred from culture flask and then inoculated in the fluidized bed, followed by the step that medium culture was pumped into the bioreactor by a peristaltic pump (Watson Marlow 530U, US). The compressed air for gas phase was first regulated by pressure regulator (R07-200-RNEG, IMI Norgren, UK) and then adjusted to the same flowrates of 0.15 v.v.m using the gas rotameter (FL-3635G, Omega

Engineering, UK). To allow gas sparging, four ports of gas inlets on the bottom face were combined with the tight-fitting glass capillary tubing (CM Scientific, UK), with an outer and inner diameter of 3 mm and 150 μm , respectively. The capillary tubing was inserted from the gas outlet on the bottom, connecting to the manifold into the main column through the tight-fitting hole of the ports. Both liquid and gas phases were returned to the top outlet and flowed back to the nutrient bottles, so that the liquid phase could be circulated into the bioreactor while the gas phase will discharge out of the culture bottle to gas exhaust bottle.

3.4 Conclusions

This chapter has summarized the specific approaches to conduct the experiments including the design and fabrication of micro-fluidized bed design, hydrodynamics investigation of the multiphase fluidization systems, fungal fermentation steps (i.e., seed culture preparation and cultivation, fungal cultivation, liquid sampling, etc.). Therefore, this chapter provides details and procedure for fluidization and reactor experiments to enable feasibility studies and comparison of a novel RK fluidized bed bioreactor.

Chapter 4 Micro-fluidized bed design and hydrodynamics

4.1 Introduction

This chapter presents the development and study of micro-fluidized bed system starting from the screening of distributor and gas sparger for designing and improving the micro-fluidized bed performance. After determining the optimal distributor, the bubbles movement under the parameters of gas orifice size and liquid/gas flowrate were characterized, thus revealing the effects of these parameters on bubbles characteristics. Finally, the pellets fluidization study in both liquid-solid and liquid-solid-gas systems were investigated, which gave insights to the real pellet expansion, recirculation and agglomeration in the MFB. This chapter represents fundamental hydrodynamic study as necessary step for screening and validating the potential of fluidized bed reactor for future fungal fermentation and bioproduction.

4.2 Results and discussions

4.2.1 Micro-fluidized bed design and fabrication

In this section, 3 different distributor types were proposed, manufactured and analysed, for the purpose of selecting an optimal distributor to distribute liquid/gas flow for solid fluidization but also to keep the particles above the distributor plate. Afterwards, the gas sparger was equipped with the selected distributor to produce even smaller bubbles inside of the micro-fluidized bed.

4.2.1.1 Bed distributor design and selection

The gas/liquid distributor is an important component in a fluidized bed to evenly distribute the liquid/gas flow across the bed, thus promoting good mixing and mass transfer [248]. In this project, the distributor is not only used to distribute the liquid/gas flow uniformly, but also to keep the cell above the distributor to make sure the cells can be fluidized and suspended in the fluidic chamber. Therefore, the holes among the distributor for distributing flows must be smaller than the cells (1-2 mm at the beginning of cultivation). Inspired by the previous studies

[23], three different types of distributor (Bar-shape distributor, perforated plate distributor and mesh-particles distributor) were designed and their working performances are discussed in the following sub-sections.

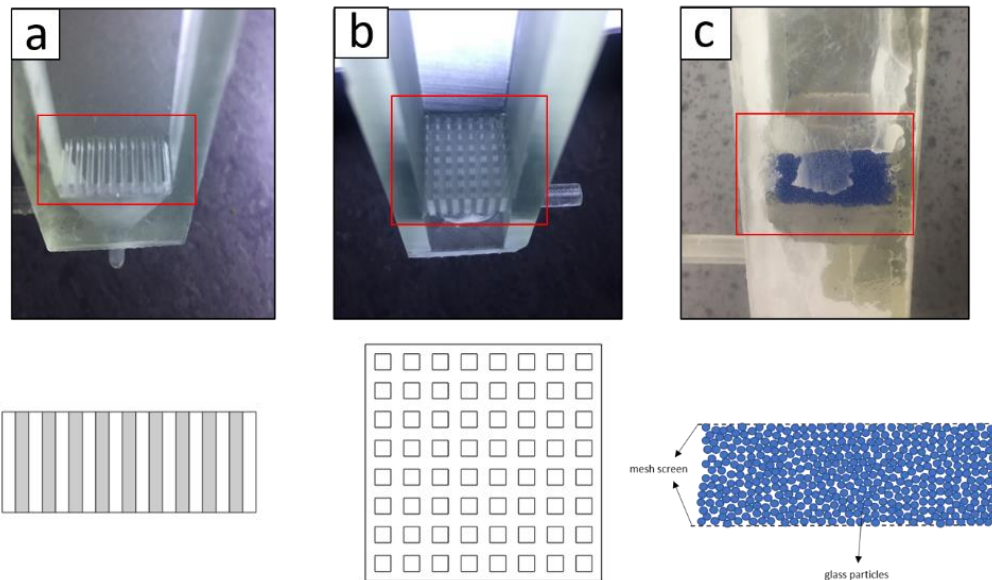


Fig. 4.1. Images of three different types of distributors: (a) bar-shape distributor, (b) perforated plate distributor, (c) mesh-particles distributor. Simple schematics of distributors are given below the actual images.

Bar-shape distributor

As shown in Fig. 4.1a, the bar-shaped distributor is a plate consisting of 9 smaller bars with a cross section of $1 \text{ mm} \times 7.5 \text{ mm}$ which were uniformly 3D-printed at 1 mm spacing. One of the advantages of the bar-shaped distributor is that the big gaps enable the bubbles to go through immediately thus decreasing the pressure drop between the two ends of the distributor. Besides, the 1 mm gaps width of the gas passages will also keep the cells above the distributor for fluidization.

Perforated plate distributor

A perforated plate type distributor (Fig. 4.1b), made up of uniformly placed 1 mm^2 square tubes on the rectangular plates ($15 \text{ mm} \times 15 \text{ mm}$ in cross section, 2 mm in thickness), largely decreases the air passages comparing with the bar-shaped distributor. The minimum size of each tube is limited with the resolution of the 3D printer and the printing resin being used. Here,

based on the Form2 SLA 3D printer and Form2 Clear ResinV4 we are using in the lab, the minimum size of the tube that can be printed successfully with minimal defects of around 1 mm. Compared with the bar-shape distributor, this perforated design has a lower open area which led to higher pressure drop but provides a more uniform distribution.

Mesh-particles distributor

The mesh-particles distributor is a sandwich-type distributor where the glass particles of 250 μm in diameter were filled and compacted between the two mesh-sheets with approximately 40 μm openings (Fig. 4.1c). To complete such a unique design, two layers of small channels around the column are created, then two mesh sheets with the suitable cross section are inserted into the small channels separately. Finally, the space between two mesh sheets is filled with particles. The porous structure of mesh-particle distributor is regarded as an effective approach to distributing liquids and gas and preventing the maldistribution of air. Besides, the tiny porosity should make the bubbles smaller, therefore decreasing the bubbles' diameter.

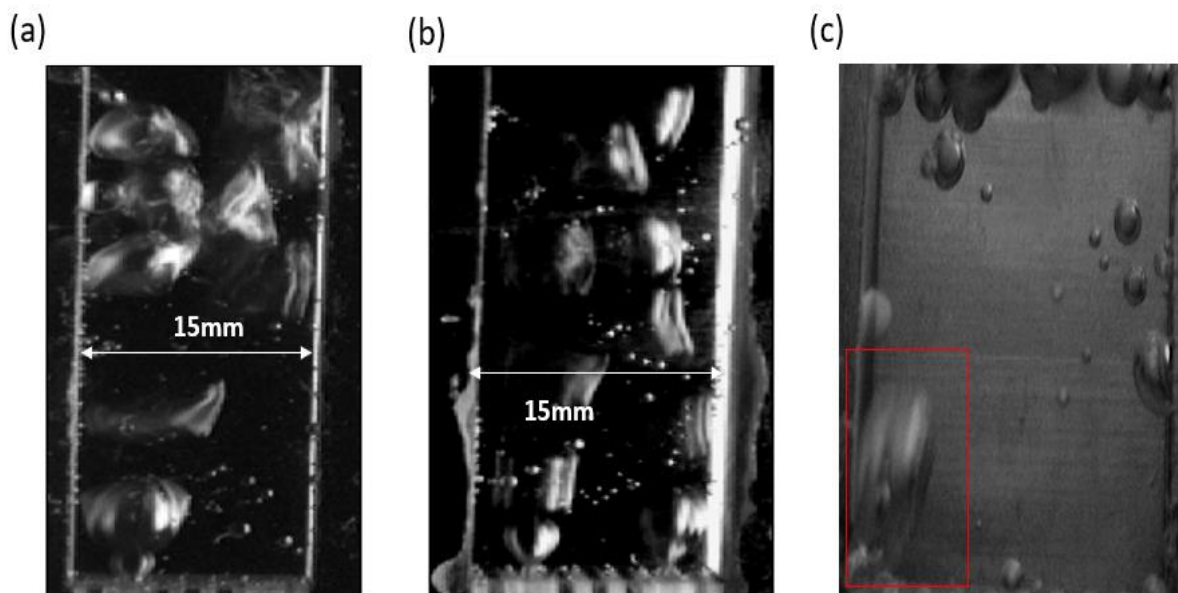


Fig. 4.2. Bubble morphologies in different distributors: (a) single bubbles of $>5\text{mm}$ in diameter in bar-shape distributor, (b) multiple bubble flows in perforated plate distributor, (c) single bubble flow goes through the left side of the mesh-particles distributor.

Evaluation of different distributors

In this project, we tested three different types of distributors that included bar-shaped distributor, perforated plate distributor, and mesh-particles distributor (Fig. 4.2). Although the bar-shaped distributor with big gaps enabled the bubbles to go through immediately, the big space among the distributor expectedly led to the big bubbles as bubble size is directly related to the size of gas sparger (the gaps between bars acts as gas sparger in this bar-shaped distributor). As shown in Fig. 4.2a, after passing through the distributor, bubbles tend to grow up because of liquid pressure, viscosity and bubble surface tension, resulting in the bubbles size up to 4-5 mm in diameter. Furthermore, the big bubbles will coalesce and interact with each other and easily rupture, likely causing cell damage and death. In Fig. 4.2b, multiple bubble flows with smaller bubbles size (3 mm in diameter) are observed when the flow rate of air and liquid is 0.5 mm/min and 1 mm/min, respectively. In this project, smaller bubbles mean a uniform bubbles flow and high liquid-gas mixing, which should be helpful to enhance the liquid-solid and gas mixing property when the cells (regarded as particles) are cultured in this fluidized bed bioreactor. In Fig. 4.2c, the bubbles are easier to go out of the distributor from the side of the mesh sheets, which means the maldistribution of design inherent to the manufacturing process. As the mesh sheet was manually fitted with a custom locking pin, it is very difficult to seal the space between the mesh sheets and the locking pin without disturbing particle packing. Another drawback of this design is the manually inserted mesh sheets and filled particles are unrepeatable and difficult to promise the quality and high standards, especially if some scale-up experiments are required in future.

To summarize, different types of distributors including bar-shaped distributor, perforated plate distributor and mesh-particles distributors have been tried and tested. Compared with bar-shaped distributor and mesh-particles distributor, the perforated plate distributor by 3D printing provided some promising results but the bubbles sizes were too big. Therefore, further studies

were conducted for gas sparger design to provide smaller bubbles. However, the results indicated that perforated plate design would provide good liquid distribution and was easy to 3D print so was kept as the base for the liquid distributor.

4.2.1.2 Hybrid distributor design

Based on the distributor design above, this part is aimed to design a suitable gas sparger for further improvements in resulting bubbles size, which was then combined with the perforated liquid distributor, thus enabling the co-current liquid/gas flow for the gas-liquid-solid fluidization system. As it is known, a high liquid-gas mixing efficiency is significant to enhance the oxygen dissolution and distribution in the liquid broth, thus ensuring the oxygen content required bioreactor for raspberry cell cultivation [249]. Furthermore, smaller bubbles flow will avoid the strong interaction between gas bubbles and reduce the bubbles coalesce phenomenon, thus decreasing the cell damage and death from bubbles rupture. To decrease the bubbles' sizes for the homogeneous flow, the capillary tubing (CM Scientific, UK) was used as the gas orifice, as the bubble size is directly proportional to the orifice size [250]. To study the effects of gas orifice size on bubbles, the capillary tubings with different inner diameters (50, 100 and 150 μm) were studied. To save the printing materials and reduce printing time, the micro-fluidized bed was divided into two parts: the fluidization column and the distributor part. The fluidization column is fixed and adaptable to the lower distributor part, while the distributor part contains the liquid distributor plate and gas sparger with different gas orifices.

In general, the micro-fluidized bed reactor comprised of two main sections, namely the lower (contains liquid/gas inlets and distribution plate) and upper (mainly bed column) sections. The entire reactor was designed using Google SketchUp, a 3D CAD modelling software similar to the approach used by the group [23]. Fig. 4.3a illustrated the lower section, which comprised of a square manifold (15 x 15 mm in cross section, 5 mm in height) with an 8 x 8 hole array (size of hole: 1 x 1 mm, square pitch with spacing of ~ 0.78 mm). The manifold served to

facilitate pellets suspension in the main column by channelling the liquid flowing from the inlet through the manifold into the main column. To allow gas sparging, a hole was designed at the centre of the distributor, to accommodate a tight-fitting glass capillary tubing (CM Scientific, UK), with the OD of 3 mm and ID ranging from 50 to 100 μm , respectively. The capillary tubing was inserted from the gas outlet on the bottom, connecting to the manifold into the main column through the tight-fitting hole (Fig. 4.3b). The upper section featured the main column for fungal pellet fluidization and a liquid/gas outlet, fitted with a mesh filter of 0.7 mm in gap size to remove liquid/gas and facilitate pellet retention (Fig. 4.3c). The bed column has a rectangular geometry, with a 150-mm column height and a 15 x 15 mm square cross section. The upper section was made of resin, fabricated by using a 3D printer (Form 2 SLA printer, Formlabs, USA) except for one vertical side, which was covered by a 3-mm thick Perspex sheet to facilitate visualization [23]. The upper and lower sections were connected via flat flange plates. Each plate featured a circular groove fitted with an O-ring rubber gasket (to prevent liquid/gas leakage) as well as 4 holes (for bolts).

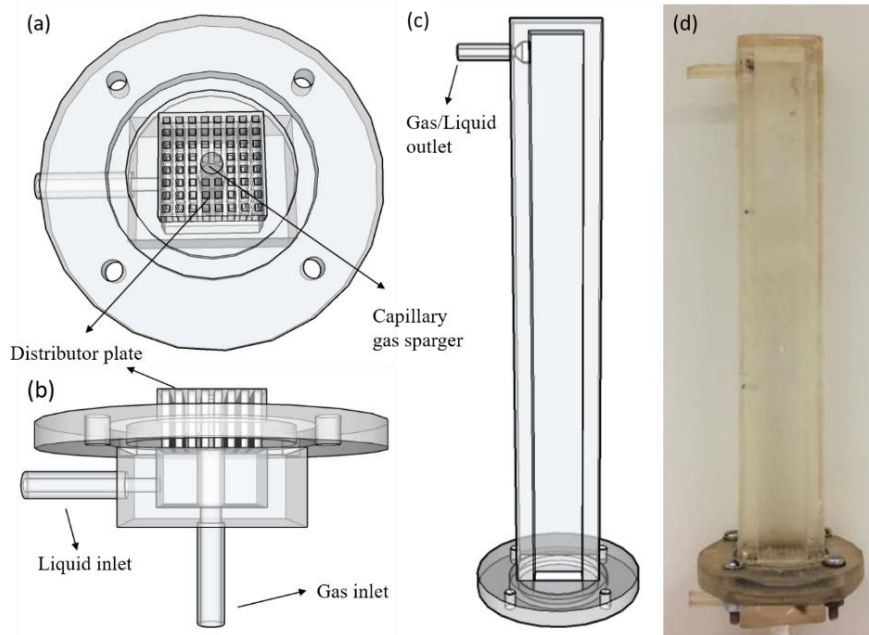


Fig. 4.3. Models of the fluidized bed: (a) top view of the lower part, (b) front view of the lower part showing the liquid inlet and gas inlet located at the left side and bottom, respectively, (c) CAD model of the main column, (d) image of the assembled 3D-printed fluidized bed.

4.2.2 Hydrodynamics investigation of the miniaturized fluidized bed

In this section, the liquid-gas, liquid-solid and liquid-solid-gas systems were investigated using the 3D-printed micro-fluidized bed described above. The liquid-gas system without the involvement of solids was used to explore the bubble properties including bubble size, velocity, bubble volume fraction, interfacial area as a function of liquid flowrate, gas flowrate, gas orifice size. The study of bubble properties was fundamentally important for the future fungal fermentation in the fluidized bed reactor, in which the bubbles not only help to suspend the pellets but also provide oxygen for fungi growth. The liquid-solid system was aimed to study pellet expansion, fluidization which revealed the different hydrodynamics between real fungal pellets and other solids (glass beads, polymers) used in literature. The liquid-solid-gas system imitated the real fungal cultivation status in the form of pellet fluidization by gas and/or liquid flows, thus presenting the effect of gas/liquid on fungal morphology.

4.2.2.1 Gas-liquid system

Bubble flow regimes

The representative images showing the gradual transitions of bubble flow regimes are presented in [Fig. 4.4](#). The different operation modes, design parameters and working fluids of the fluidized bed system would determine the gas flow regimes. Among these parameters, the bubble flow regimes are highly dependent on the bed size, gas sparger size and gas flowrate. For instance, Li et al. [33] identified three distinctive flow regimes including the dispersed bubble flow, the coalesced bubble flow and the slug flow in three-phase MFB of 0.8 mm ID with the increase of gas flowrate. The formation of slug flow in their study was mainly due to the narrow column, whose cross section could be fully occupied by the coalesced bubbles to form the gas slugs. However, no slug flow was observed in our study, because the bed column size of 15 mm in our MFB was much larger than the 0.8 mm ID in their design. In the relatively larger-diameter column, Besagni et al. [251] classified the bubble flow regimes into

homogenous bubble regime (including mono-dispersed homogeneous and poly-dispersed homogeneous), transition bubble regime and heterogeneous bubble regime, which well described the changes of bubble flows in our experiments. Here, the bubble flow regimes started from mono-dispersed homogeneous flow at a low gas flowrate (Fig. 4.4a) and turned into poly-dispersed homogeneous regime (Fig. 4.4b-d) with increasing gas flowrate. Regardless of whether it is mono-dispersed or poly-dispersed, the homogeneous regime means that discrete bubbles are uniformly distributed without coalescence [252]. Besides, the bubble density as well as bubble size in the homogeneous bubble regime increased linearly with gas flowrate, which is discussed in the following paragraphs. However, the continual increase of gas flowrate facilitated the emergence of coalesced bubbles, which remained discrete with uniform bubble size distribution (Fig. 4.4e). This discrete coalesced bubble flow is regarded as a transition bubble regime. At high gas flowrate, larger bubbles with wider size distribution are encountered but the distance between individual bubbles decreased [253]. More bubbles coalesced as they ascended to form the heterogeneous bubble regime, in which the coalesced bubbles were interspersed between the small ones [254], as shown in Fig. 4.4f. Apart from the gas flowrates, the gas orifices sizes can also influence the bubble flow regimes. In general, the smaller sparger size (i.e., 50 μm) needs a lower gas flowrate than 100 and 150 μm sparger to reach the transition point from mono-dispersed homogeneous flow to poly-dispersed homogeneous regime, and coalesced flow, because the single bubble flows were easier to be split into multi bubbles by the smaller orifice, forming the mono-dispersed homogeneous flow, further poly-dispersed homogeneous regime and final coalesced flow.

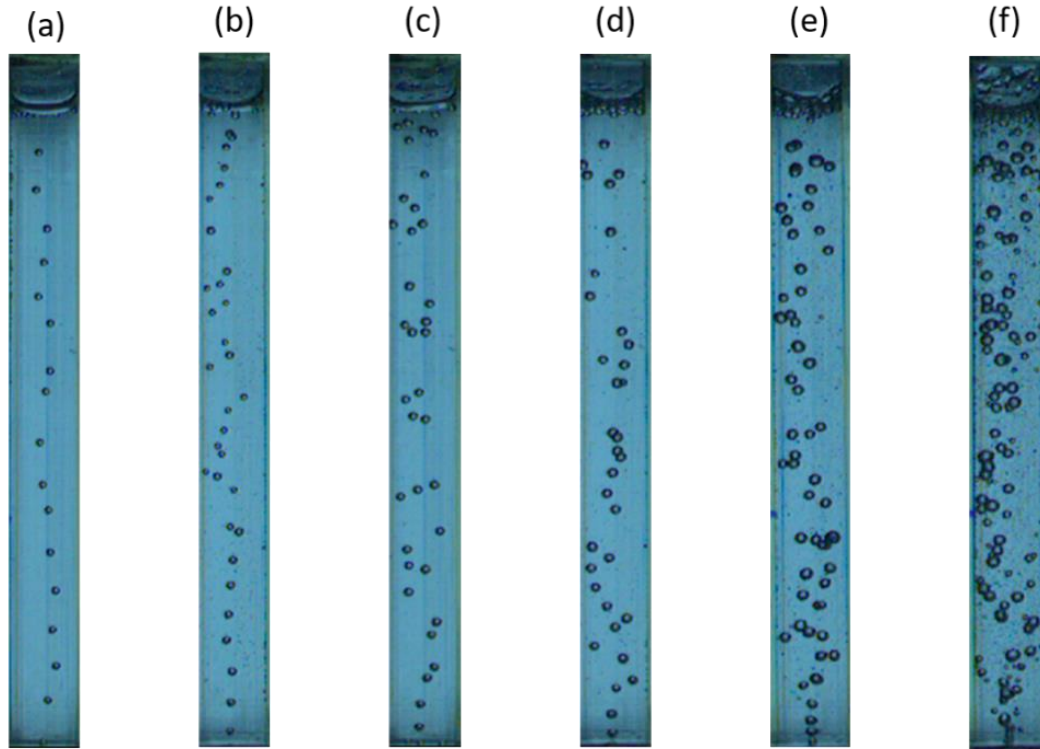


Fig. 4.4. Representative pictures of bubble flow regimes with the increase of gas flowrate but a static liquid flow. $d_G = 100 \mu\text{m}$. (a). $Q_G = 3.7 \text{ ml/min}$, (b). $Q_G = 5.4 \text{ ml/min}$, (c). $Q_G = 9.9 \text{ ml/min}$, (d). $Q_G = 15.5 \text{ ml/min}$, (e). $Q_G = 22.9 \text{ ml/min}$, (f). $Q_G = 32.7 \text{ ml/min}$. $d_B = 15 \text{ mm}$.

Bubble's size

Bubble size distributions (from dispersed bubble flows to coalesced bubble flows) under the parameters of gas sparger sizes, gas flowrates and liquid velocities were characterized as given in Fig. 4.5. Under the studied ranges of gas and liquid flowrates, bubble size distributions were 1.5 – 2.3 mm, 1.8 – 2.8 mm and 2.3 – 3.8 mm when gas orifice was 50, 100 and 150 μm , respectively. The results indicated that sparger size was a predominant factor to determine d_b , as larger gas orifices allow bigger bubbles' expansion and formation before they are detached from the gas nozzle [255]. Alternatively, it is noted that d_b increased with increasing gas flowrate, which was explained by the high gas flowrate for each sparger size, which introduced more gas in liquid column at a certain time to enhance the formation and expansion of bubbles. In contrast, d_b decreased with the increase of superficial liquid velocity, as the co-current liquid flow accelerated bubbles detachment, thus shortening the time for bubble' growth and expansion on the orifice face. However, the influence from liquid velocity on bubble size was

relatively insignificant, which could be reflected from the small descent slopes of curves, as shown in Fig. 4.5.

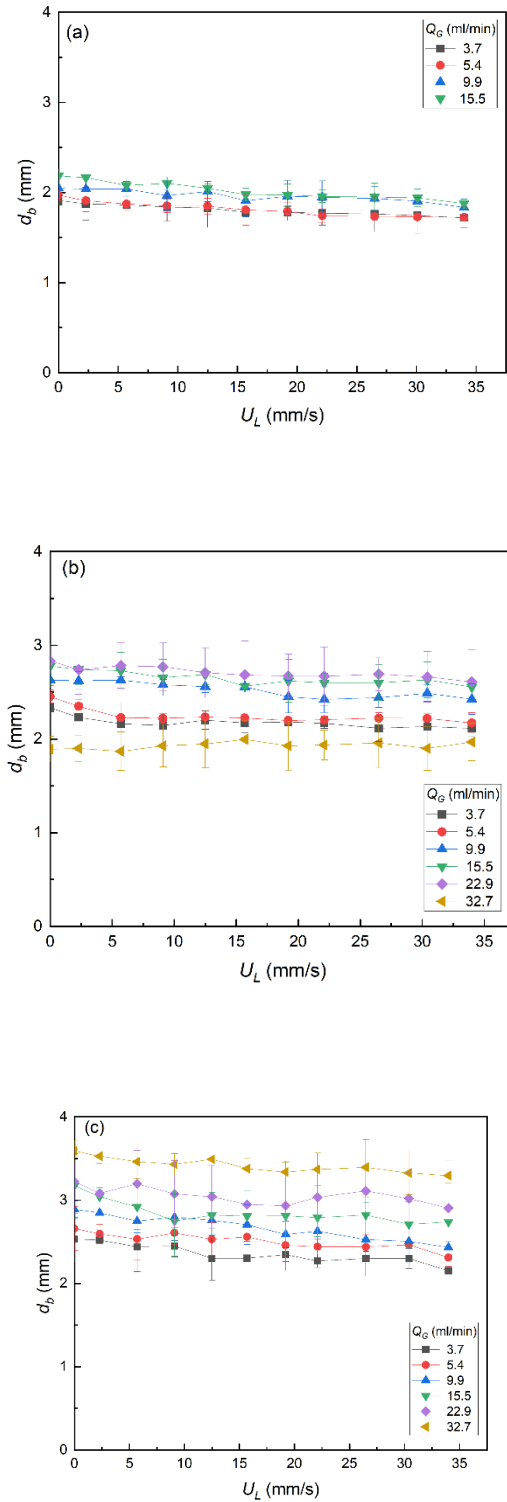


Fig. 4.5. The mean bubbles' size for different capillary sizes of (a) $d_G = 50 \mu\text{m}$, (b) $d_G = 100 \mu\text{m}$, (c) $d_G = 150 \mu\text{m}$ as a function of liquid velocity, U_L and gas flowrates, Q_G .

Therefore, all the operating parameters of gas orifice size, gas flowrate and superficial liquid velocity can impact bubble size distributions during the gas-liquid bubble column system. However, this section confirmed that the bubble size is primarily enhanced by the orifice diameter and gas flowrate [256], but also revealed that the co-current liquid flow could accelerate bubble detachment to inhibit bubble growth, but the effects from liquid flow is relatively lower.

Bubbles' velocity

For the range of studied gas and liquid flowrates, the values of bubble velocity, U_b varied from 1.46 to 1.86 m/s, 1.86 to 2.30 m/s and 1.91 to 2.36 m/s when gas orifice size was 50, 100 and 150 μm , respectively (Fig. 4.6). The increased bubble velocities with increasing gas orifices size indicated that micro-channels of the submerged orifice inhibited the bubble rising velocities. The kinetic energy of gas was regarded to be the same at a given gas flowrate, but the different orifice size resulted in the different energy consumption due to pressure drop when gas pass through the gas sparger tubing of different sizes [257]. The smaller orifice required a higher pressure drop and consumed more kinetic energy, thus leading to the lower bubbling velocity. Besides, the bubble velocity was observed to increase with the increase of gas flowrate, which was consistent with the previous literatures [258, 259].

Furthermore, it is obvious that the upward liquid flows can promote bubble rising velocity because of the co-current flows. However, this promotion from liquid flow was not drastic when the bubble regime changed from a homogenous a bubble regime to heterogeneous bubble regime at the high gas flowrates, indicating the importance of bubble regime transitions.

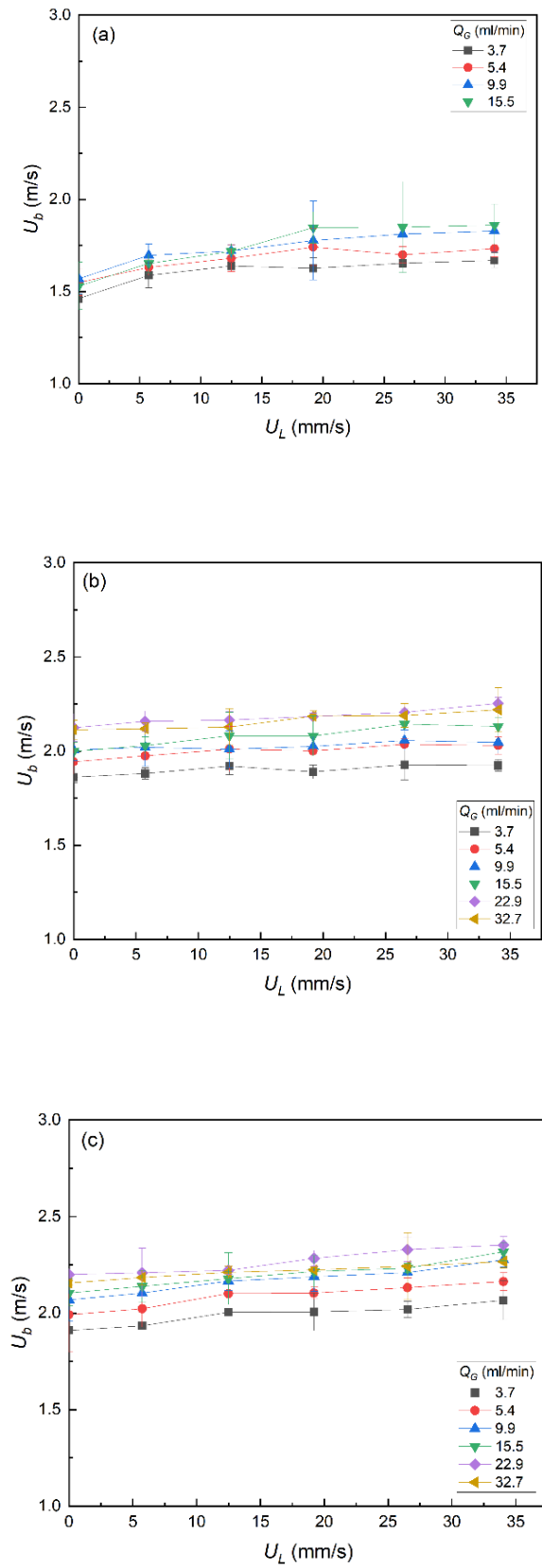


Fig. 4.6. Bubbles' velocity as a function of liquid velocity, U_L for the different gas flowrates, Q_G . Subfigures corresponds to the 3 different orifice sizes of (a) $d_G = 50 \mu\text{m}$, (b) $d_G = 100 \mu\text{m}$ and (c) $d_G = 150 \mu\text{m}$.

Gas volume fraction

Bubbles' volume fraction \mathcal{E}_G is the ratio of total bubbles volume to the bed volume, where the total bubbles volumes is not only related to the average bubble size but also the number of bubbles. The characterization of \mathcal{E}_G under parameters of different gas flowrate, liquid velocity and gas orifice size are illustrated in (Fig. 4.7). It is noticed that \mathcal{E}_G increased significantly with increasing of the gas flowrate, as high gas flowrate meant more gas pumped into the chamber per unit time to produce more bubbles. However, \mathcal{E}_G was observed to significantly increase when the high gas flowrate turned the homogenous flow regime into the heterogeneous regime (e.g., \mathcal{E}_G significantly increased when gas flowrate increased from 9.9 ml/min to 1.5 ml/min in Fig. 4.7a), where coalesced bubbles largely increased the total bubbles volume. The big error bars in heterogeneous bubble flow regimes suggested the existence of numbers of dispersed bubbles. On the other hand, the relatively horizontal curves of \mathcal{E}_G with the increase of liquid velocity indicated that the co-current liquid flow had no impact on \mathcal{E}_G , although its effects on bubble size and velocity have been confirmed.

Finally, at fixed gas and liquid flowrate, \mathcal{E}_G was observed to increase with increasing gas sparger size. A larger gas sparger can allow for the growth of bubble size, thus attributing to the higher \mathcal{E}_G . For instance, in the homogeneous flow regimes with 9.9 ml/min of gas flowrate and no liquid flow, \mathcal{E}_G reached 0.20%, 0.31% and 0.33% when gas sparger size was 50, 100 and 150 μm , respectively. Besides, the higher \mathcal{E}_G from the larger gas spargers were also witnessed in heterogeneous flow regime, as \mathcal{E}_G in conditions of 100 and 150 μm gas sparger was 0.53% - 0.57% and 0.71 % - 0.73% respectively, with the gas flowrate keeping at 32.7 ml/min (Fig. 4.7b & c). Therefore, this section has concluded that \mathcal{E}_G was increased with increasing the gas flowrate and the gas sparger size, but independent of liquid flows.

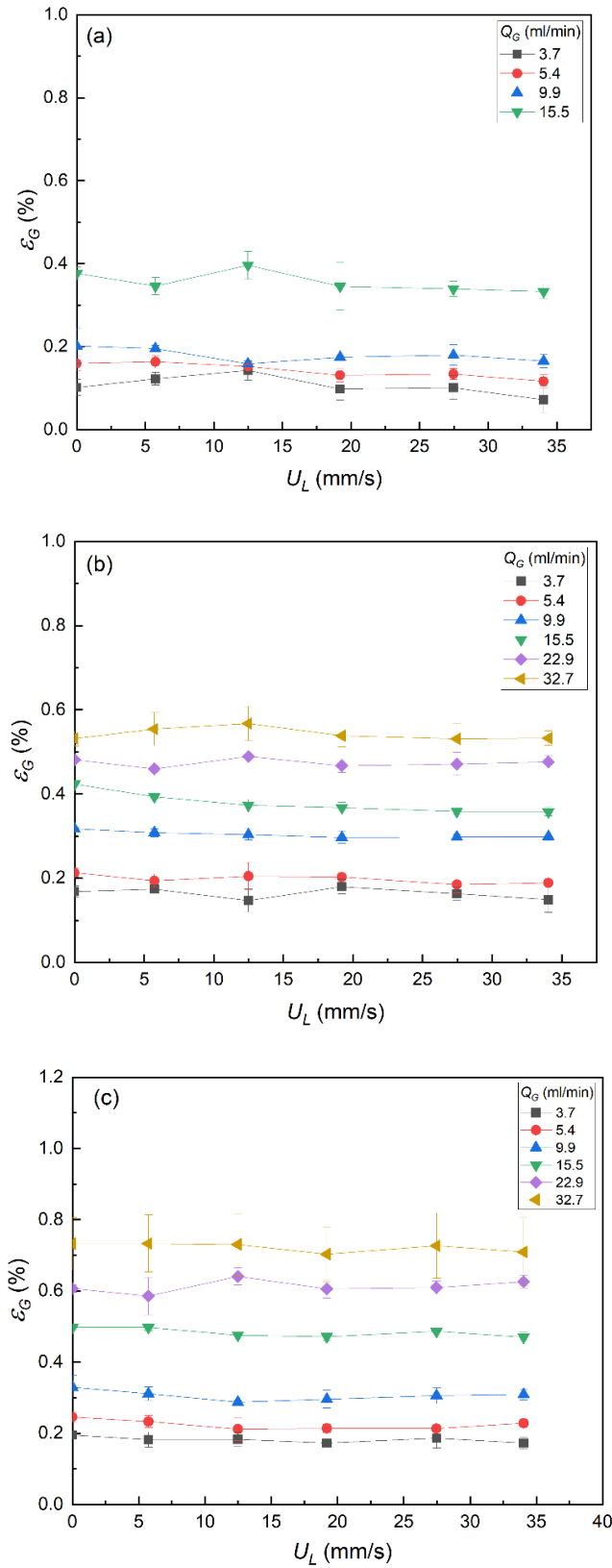


Fig. 4.7. Characterization of gas volume fraction, ϵ_G as a function of gas flowrate, Q_G and liquid velocity, U_L with different gas sparger sizes: (a) $d_G = 50 \mu\text{m}$, (b) $d_G = 100 \mu\text{m}$, (c) $d_G = 150 \mu\text{m}$.

4.2.2.2 Liquid-solid fluidization of pellets

In the liquid-solid micro-fluidization system, the hydrodynamic characteristics including bed voidage, minimum fluidization velocity, bed expansion were characterized through the fluidization of pellets in both ultrapure water and fresh medium. The pellet fluidization was measured from the recorded image series, which were then analysed by the software ImageJ.

Bed voidage determination

A significant parameter that affects the fluidization performance is initial bed voidage ε_0 , which is typically calculated as [59]:

$$\varepsilon_0 = 1 - \frac{m}{\rho_P H_0 A} \quad (4.1)$$

where H_0 , A , m and ρ_P represent the static bed height, internal bed cross-sectional area, mass and density of fungal pellets, respectively. The pellet density was measured to be 1.090 ± 0.094 g/cm³ after 4-week flask cultivation. Unlike other rigid particles such as glass beads or polymer spheres, the submerged cells can absorb liquid to enlarge pellet size and volume, thus altering bed voidage determination. To characterize the actual bed voidage, the ratio of pellet volume variation before and after filtration is obtained by:

$$R = \frac{\sum \frac{(d_P)^3}{(d'_P)^3}}{N} \quad (4.2)$$

where R is the ratio of pellets volume variation before and after filtration, d_P , d'_P and N present single pellet diameter before and after funnel filtration, and the number of pellets, respectively. The mean size of pellets was characterized to be 1.804 ± 0.548 mm in diameter and pellet sphericity was determined around 0.818 ± 0.123 using image analysis, after 4-week flask cultivation. It was observed that the volume of submerged pellets was 1.382 times bigger than that after filtration. Therefore, the actual pellets volume in bed should be $1.382 \times \frac{m}{\rho_P}$ and the newly revised equation was presented below:

$$\varepsilon_0 = 1 - \frac{1.382m}{\rho_p H_0 A} \quad (4.3)$$

Using Eq. (4.3) to calculate ε_0 for pellets with varied mass, it was found that ε_0 was 0.634, 0.618 and 0.577 when the filtered pellet mass used was 0.5 g, 1.0 g and 1.5 g, respectively. This finding seems to contradict previous studies that the static bed voidage was independent of particle mass [59]. Compression of pellets due to the increased weight of the fungal packed column is probably the main reason for this trend as the lowest value for voidage was observed for the highest mass [260].

The static bed voidage was observed to be higher than the expected value of 0.4 reported in literature [22, 33, 59]. The physical property of biological aggregates which are different from the rigid particles is the main reason for this difference. Smith et al. [261] reported that the bed voidage of settled yeast flocs was about 0.57, which is very close to the value of 0.577 here when 1.5 g of pellet were used. Unlike yeast flocs, the fungal pellets with branched external hyphae formed a gap between pellets, thus contributing to the larger voidage observed. Another possible reason for the higher observed voidages could be attributed to the wall-effect of the column, which is inevitable in micro-fluidized beds. For example, Kashani et al. [262] provided a curve for voidage as a function of bed-to-particle size inside square micro-channels albeit using solid microparticles. For the bed-to-particle ratio of 7.5 used in their study, it could be estimated that approximately 15% increase in voidage is expected. The percentage increase observed here was between 1% and 11% for different initial pellet mass while the maximum percentage increase from 0.57 to 0.634 was very similar to the prediction reported by Kashani et al. [262], notwithstanding the difference between the systems. Besides, the effects from the walls indeed are another contributor to the observed high values of voidage in our study, which could be confirmed by the lower density of fungal pellets near the walls of bed column especially during fluidization (Fig. 4.8).

Minimum fluidization velocity

Fig. 4.8 shows the snapshots of the flow regimes when 1 g of fungal pellets were fluidized in culture medium. With the increase of superficial liquid velocity, several flow regimes were observed starting from static bed, to expanded bed, followed by partially fluidized bed and fully fluidized bed. The descriptions for these four regimes are listed below:

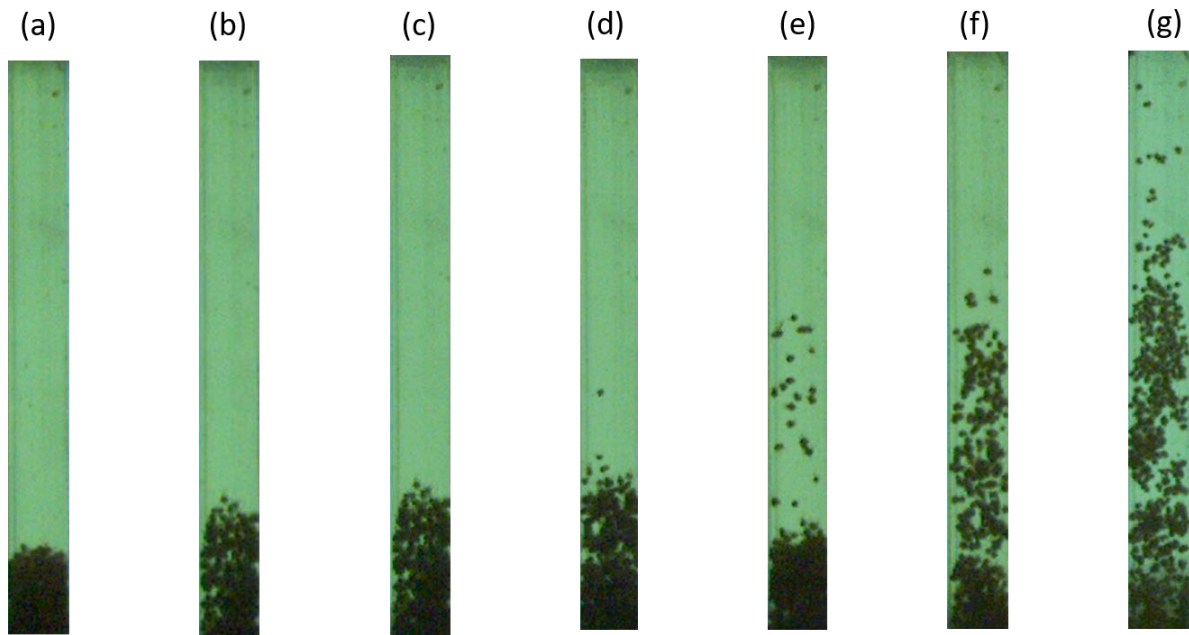


Fig. 4.8. Bed expansion with the increase of liquid velocity in medium culture using 1 g of pellets. (a) $U_L = 0$ mm/s; (b) $U_L = 1.242$ mm/s; (c) $U_L = 2.554$ mm/s; (d) $U_L = 3.866$ mm/s; (e) $U_L = 4.522$ mm/s; (f) $U_L = 5.718$ mm/s; (g) $U_L = 6.982$ mm/s. $d_B = 15$ mm.

- *Static bed.* The pellets settled on the bottom of the bed due to gravity. The height of the packed bed kept unchanged without any bed expansion when there was no liquid flow (Fig. 4.8a).
- *Expanded bed.* The pellet bed started to expand once liquid flow was supplied from the bottom of the bed. Bed height increased as the aggregative interaction between pellets became loose with the increase in liquid upward superficial velocity, although majority of filamentous pellets were still agglomerated together via their hyphae. (Fig. 4.8b-c).
- *Partially fluidized bed.* Part of the aggregated pellets were dispersed and fluidized along the column, as the continuously increasing liquid flow disengaged the filamentous links

between pellets. The numbers of dispersed pellets increased with increasing superficial liquid velocity, while the rest of pellets remained agglomerated and settled on the bottom of the column (Fig. 4.8e-f). Note that, this regime was not observed in defluidization experiments below.

- *Fully fluidized bed.* The whole bed became dispersed, and pellets were freely fluidized in the chamber, despite a few pellets remaining aggregated form during fluidization (Fig. 4.8g).

Classically, a packed bed containing rigid particles (i.e., glass beads) remains static until distinct expansion when superficial velocity reaches the minimum fluidization velocity U_{mf} . Therefore, the minimum fluidization velocity is obtained by linearly plotting the bed expansion ratio with superficial velocity, or by determining the velocity point that maintains constant pressure drop [58, 60, 263]. However, this linear plot of relative bed height as a function of superficial fluid velocity cannot accurately predict the U_{mf} for pellets bed expansion in our study. The main reason is that the pellet bed expanded gradually rather than remain static until instant fluidization. (Fig. 4.8b-d). Similar phenomenon was also reported by Smith et al. who observed gradual transition from packed bed to fluidized bed with the loose aggregates of flocs and pellets at a low liquid fluidization velocities during incipient fluidization [261]. In this experiment, based on the visual observation, $U_{mf, ex}$ was regarded as the liquid velocity which resulted in the expansion and detachment of the pellets bed from the base, with good overall fluidization.

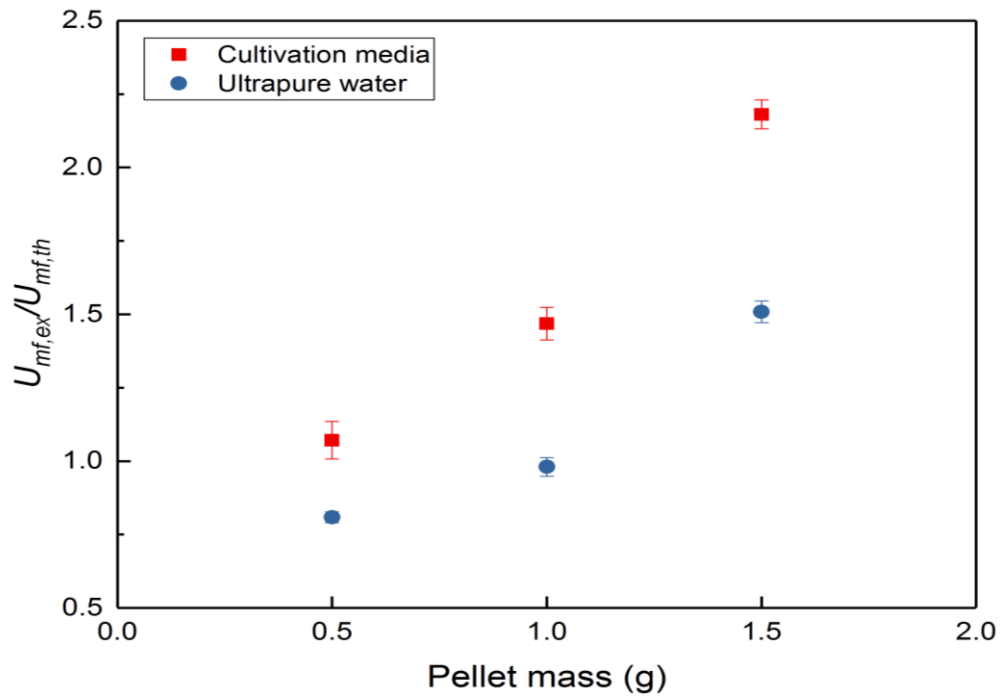


Fig. 4.9. Graph of the ratio of experimental $U_{mf, ex}$, to theoretical, $U_{mf, th}$, minimum fluidization velocity versus pellets mass in cultivation medium (squares) and ultrapure water (circles).

The experimental values of minimum fluidization velocities, $U_{mf, ex}$, were compared with the theoretical values, $U_{mf, th}$ (calculated by Ergun equation) [54] in Fig. 4.9, which presented a graph of the ratios of experimental minimum fluidization velocity $U_{mf, ex}$ to theoretical minimum fluidization velocity $U_{mf, th}$ versus pellet mass for two different media: cultivation medium and ultrapure water. It is noted that the $U_{mf, ex}/U_{mf, th}$ is approximately proportional to pellet mass in both growth medium and ultrapure medium. This could be due to two reasons: (1) $U_{mf, ex}$ increased with pellet mass, due to an increased fraction of agglomerated pellets, resulting in higher liquid flowrates required to achieve the complete fluidization; (2) $U_{mf, th}$ decreased with the initial bed voidage (based on the Ergun equation), which consequently decreased with the increase of pellet mass (described in Section 3.1.1). In addition, $U_{mf, ex}$ was obviously larger than $U_{mf, th}$ in culture medium, which is consistent with previous studies because of the significant wall effect of the miniaturized fluidized bed reactor [15, 19, 30]. However, the $U_{mf, ex}/U_{mf, th}$ was less than 1 in ultrapure water when pellet mass was below 1 g,

which indicates that $U_{mf, th}$ calculated by Ergun equation could not ideally reflect the correct ratio ($U_{mf, ex}/U_{mf, th} > 1$) when pellet mass was low.

Bed expansion study

In the experiments, the bed expansion ratio at a given superficial liquid velocity was defined as the ratio of the increase in bed height to the initial bed height, which was calculated by $(H - H_0)/H_0$. Bed expansion study is typically characterized through defluidization in order to avoid pressure overshoot and hysteresis effects [23, 32]. The defluidization process of the fungal pellet bed (from minimum fluidization state to static state) is illustrated in Fig. 4.10, where the top of pellets bed was flat and well defined, thus promoting the accuracy for the measurement for bed height expansion. Although the fluidization and defluidization process induced different fluidization regimes, the $U_{mf, ex}$ value of 6.69 ± 0.25 mm/s for 1 g pellets in culture medium, from either fluidization or defluidization experiments were actually very similar with little deviation.

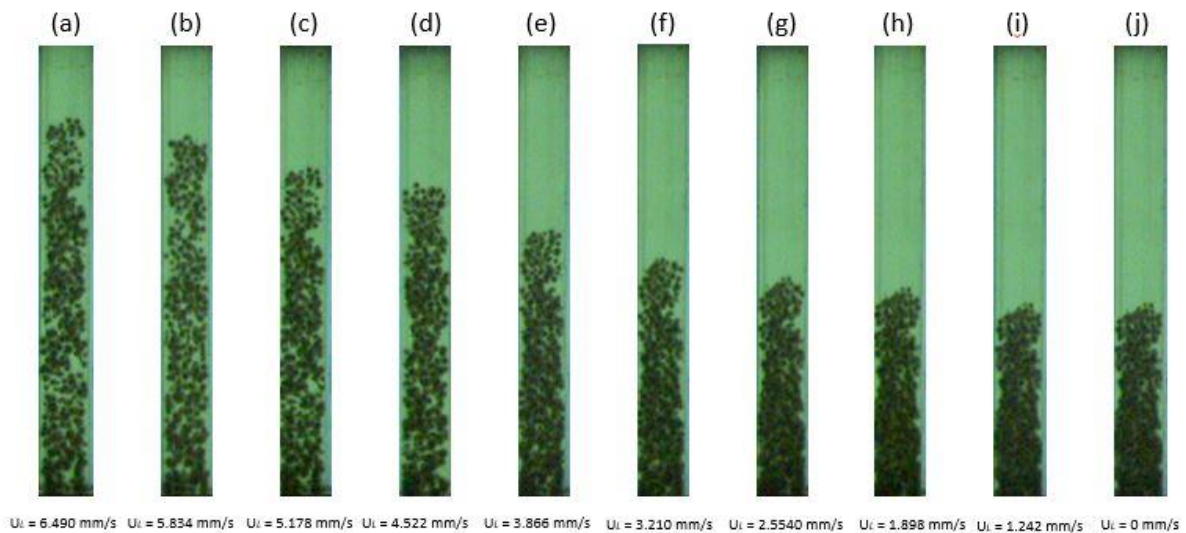


Fig. 4.10. Snapshots of pellets defluidization of 1 g pellets in cultivation medium. $d_B = 15$ mm.

The plots of pellet bed expansion ratio versus superficial liquid velocity based on the defluidization process (from the minimum fluidization state to the static packed bed state) presented in Fig. 4.11. The expansion curves showed linear behaviour against fluid velocity,

but there was an apparent change in the gradient at high liquid velocity when pellets mass was low (Fig. 4.11a & b). In Fig. 4.11a, the pellets were still agglomerated at low liquid velocity which led to a low expansion ratio rate of increase (i.e. expanded bed regime) in solid line A. Whereas at high liquid flow, a much higher expansion slope of solid line B was observed since the pellets became less agglomerated because of the lower interactive forces between pellets, as shown in Fig. 4.10b - d. The intercept between solid lines A and B reflected a significant change in bed expansion rate during defluidization, reflected from the sharp drop in expansion height illustrated in Fig. 4.10d and Fig. 4.10e. This can also be regarded as the point of transition from an expanded bed regime to a partially fluidized bed regime during the fluidization study in Fig. 4.8c - e. The bed expansion ratio 0.5 g of pellets in ultrapure water showed similar linear trends with a higher transition point between expanded bed regime to partially fluidized bed regime (Fig. 4.11a lines C & D).

Fig. 4.11b presents the expansion ratio when pellet mass was increased to 1.0 g. The slope transition with increasing liquid velocity was still apparent in both culture medium and ultrapure water, whilst the disparity of slope values between solid line A and B or dashed line C and D decreased compared with Fig. 4.11a where pellet mass was 0.5 g. It is clear for the water that this transition velocity decreased from 4.5 mm/s to 2.5 mm/s, but for cultivation media it occurred in both cases at around 3 mm/s. This could be explained by the different liquid viscosity between water and culture media, which influenced the bed expansion and transition of fluidization regime mentioned above. However, once pellets mass was increased to 1.5 g, this slope transition effect was not observed and the whole expansion ratio could be described by a linear relationship (Fig. 4.11c). One explanation for this could be the compaction and interaction of pellets. Lower mass of pellets meant lower height and less compacted pressure, so that bed height easily expanded with the increase of liquid velocity.

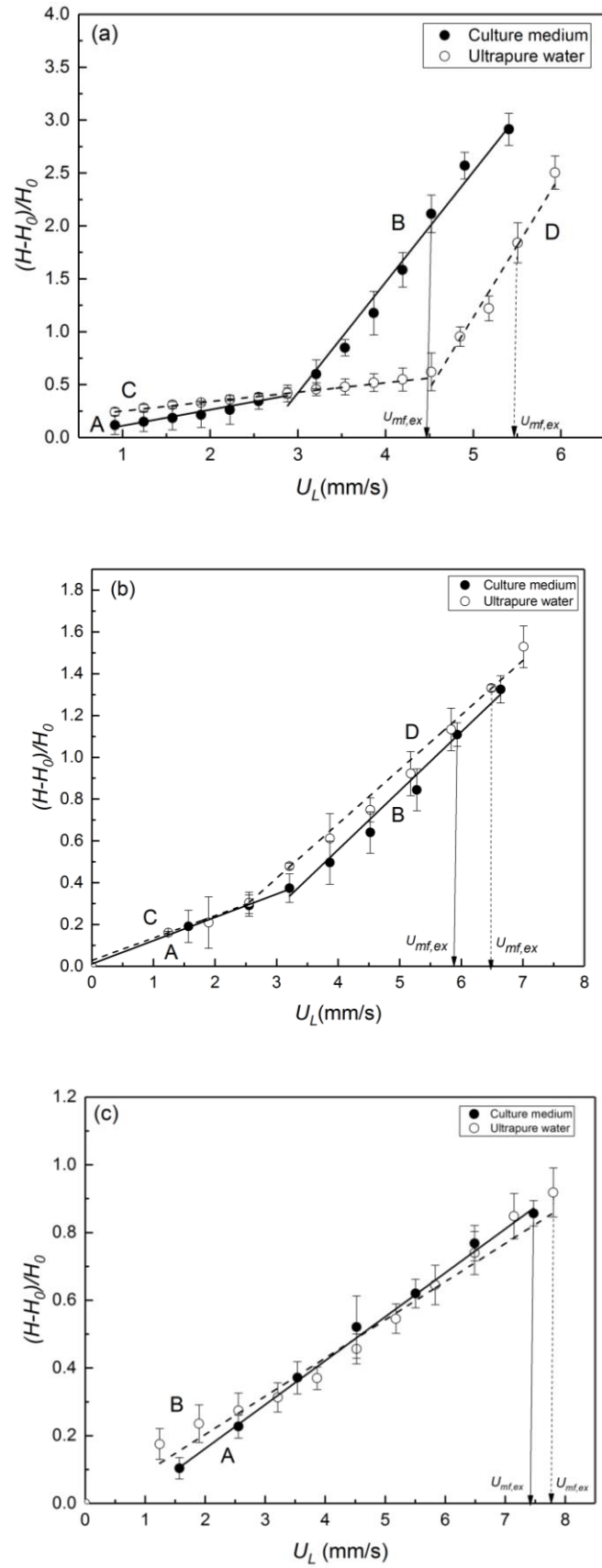


Fig. 4.11. Bed expansion studies of the fungal pellets in both cultivation medium and ultrapure water: (a) 0.5 g pellets, (b) 1.0 g pellets, (c) 1.5 g pellets.

While the expanded bed was suppressed by compaction pressure of pellets at higher pellet mass, the slope change was not obvious during liquid velocity increasing. Additionally, the friction forces between pellets might also contribute to a more linear relationship between $(H-H_0)/H_0$ versus U_L , so that the whole expansion ratio studied here could be fitted by a single linear regression. In fact, due to the significant expansion in the two bed regimes when 1.5 g of pellets were used (Fig. 4.11c), pellets were observed to elutriate from the column when fluid flowrate further increased, preventing experiments beyond the minimum fluidization velocities.

Based on the data in Fig. 4.11, the relationship between liquid superficial velocity U and bed voidage ε was plotted in log-log scale as shown in Fig. 4.12. The bed voidage was calculated from:

$$\varepsilon = 1 - (1 - \varepsilon_0) \frac{H_0}{H} \quad (4.4)$$

where H_0 and H are the static and measured bed height, respectively [59]. The packed bed voidage ε_0 was 0.634, 0.618 and 0.577 when pellet weights were 0.5 g, 1.0 g and 1.5 g, respectively (section 3.1.1). The logarithmic expansion curves were then described by the well-known Richardson-Zaki equation [49], expressed as:

$$U_L = U_t' \varepsilon^n = k U_t \varepsilon^n \quad (4.5)$$

where U_t is the single pellet settling velocity obtained from pellet settling experiments with the use of high-speed camera and n is the exponent to evaluate the logarithmic relationship between voidage and superficial liquid velocity. U_t' was the extrapolated terminal velocity obtained by extrapolating linear fitting curves to a voidage of unity, while k was the proportional coefficient of U_t' and U_t . Here, n was calculated from the function of terminal Reynolds number Re_t based on the original Richardson-Zaki correlations [264], while n' was the experimental determined value from the slope of the linear relationship in a log-log plot of the velocity vs voidage plots in Fig. 4.12 [48, 265].

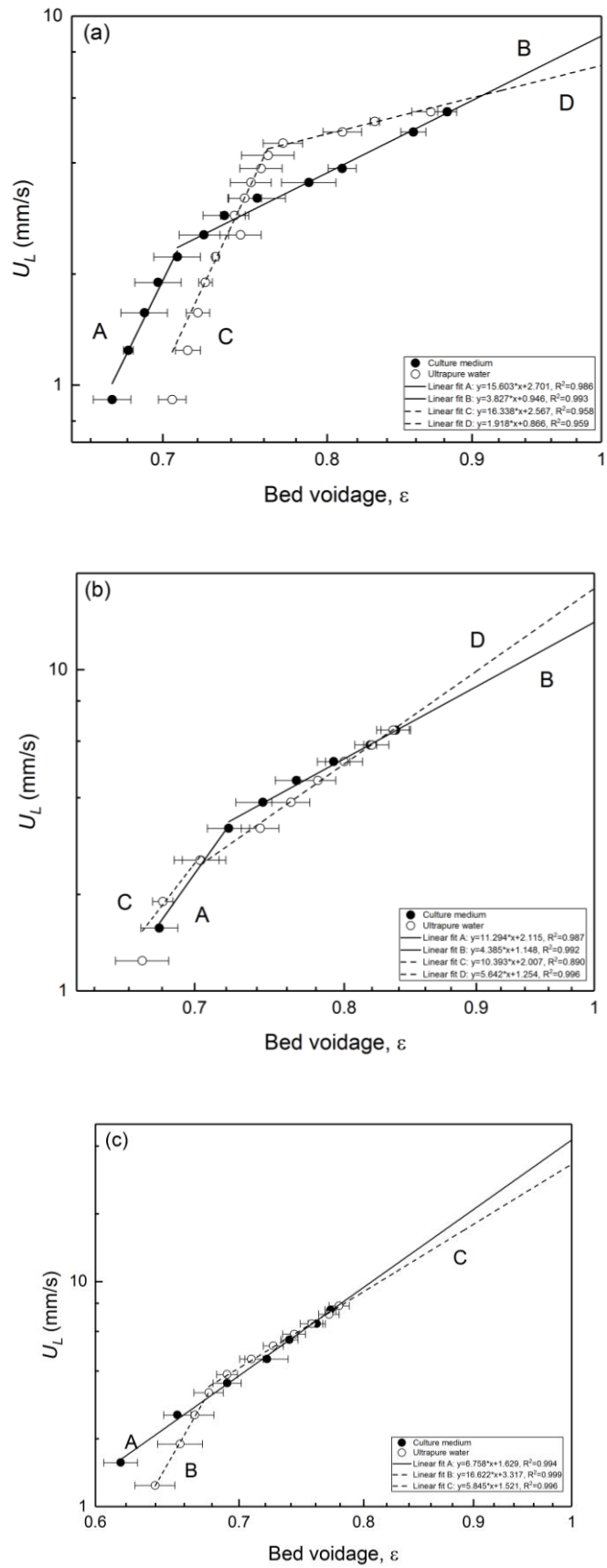


Fig. 4.12. Bed expansion characteristics with the parameters of liquid velocity and bed voidage: (a) 0.5 g pellets, (b) 1.0 g pellets, (c) 1.5 g pellets.

Fig. 4.12 illustrates the change of slopes from a larger slope to a smaller slope at high liquid velocity except the situation of 0.5 g pellets in cultivation medium (Fig. 4.12c), due to the different expansion efficiency between different bed regimes. In general, the slope changes were observed at the bed voidage of approximately 0.7 corresponding to the change in fluidization regime between extended bed and partially fluidized bed in both media and ultrapure water. The slope change was also reported by Smith et al. during the fluidization test using microbial aggregates of yeast flocs and filamentous pellets [261]. More specifically, we found the bed voidage values regarding the slope transition decreased with the increase of pellet mass in water.

Table 4.1 Calculated and extrapolated parameters of Richardson-Zaki equation.

Liquid phase	Pellet mass (g)	U_t (mm/s)	U_t' (mm/s)	Re_t	k	n	n'
Culture media	0.5		8.831	13.697	0.903	3.359	3.827
	1.0	9.780 ± 3.190	14.060		1.438		4.385
	1.5		42.560		4.352		6.758
Ultrapure water	0.5		7.345	35.230	0.375	3.081	1.918
	1.0	19.568 ± 4.064	17.949		0.917		5.642
	1.5		33.189		1.696		5.845

In the work presented here, the experimental values of n and k as well as extrapolated values are listed in Table 4.1. Both n and k in culture medium were larger than those in ultrapure water, indicating the effects of liquid density and viscosity on bed expansion. Compared the values of n from the single pellet settling experiments, the extrapolated n' was generally larger in both medium and water. These results were consistent with those reported by Di Felice [266] who pointed out that high values of n (3- 10) were commonly observed in biological fluidized liquid beds. Smith et al. [261] stated the n values could be larger than 10 with flocculent materials for solids phase, which was also confirmed in our study from the larger slopes when liquid velocity was low. For instance, in Fig. 4.12a, the slope of the fitted line A was 15.603 (above 10) at low liquid velocity but decreased to 3.827 at the terminal velocity. As commented above, the slope

transition is attributed to the fluidization bed regime change from expanded bed regime to partially and fully fluidized bed regime.

The typically lower values of k (less than 1) were observed when the pellets mass was low, which were consistent with the results reported by Naghib et al. who used the alginate beads as cell carrier for bed expansion study [265]. However, with the increase in pellet mass, the larger values of k (4.352 in medium and 1.696 in water) as well as the increased n' reflected the dominant effects of pellet agglomeration on bed fluidization. Regarding k values, Zivkovic et al. [32] argued that the higher values of the empirical constant was attributed largely to the wall effects and surface forces in micro-fluidized bed ($k = 1.70 \pm 0.35$ in their case).

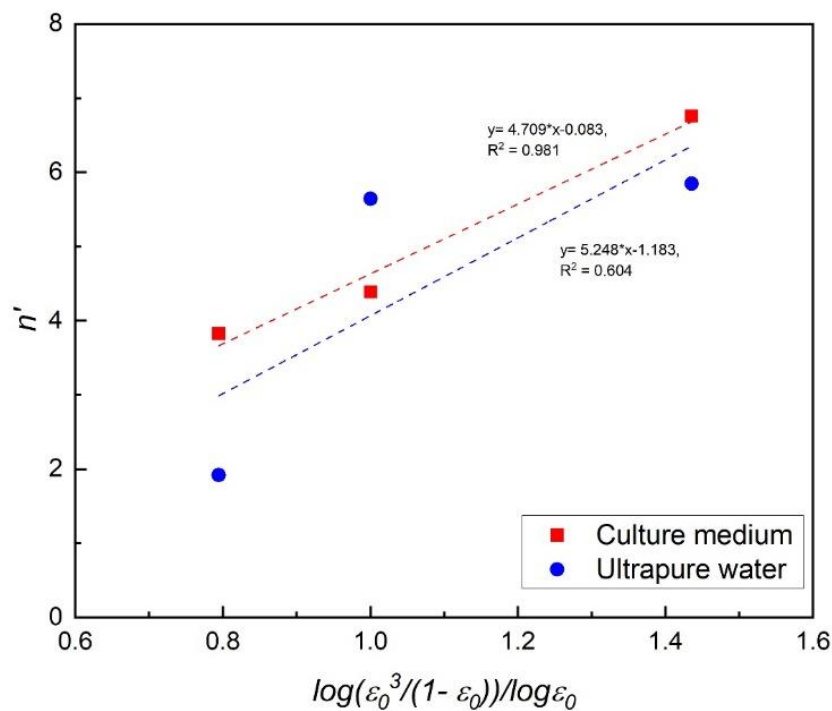


Fig. 4.13. Dependency of n' based on static bed voidage.

Considering the significant pellet agglomeration and rougher surface of pellets compared to that of soda lime glass microspheres used in previous reports, the much higher values of k here still seem reasonable. Kramer et al. [267] improved the Richardson-Zaki liquid-solid

fluidization model by characterizing the relationship between exponent of Richardson-Zaki equation and the static bed voidage with other parameters (i.e. particle Reynold terminal number). In their work they found that n' is function of $\frac{\log(\frac{\varepsilon_0^3}{1-\varepsilon_0})}{\log\varepsilon_0}$ in terms of dependence to the static bed voidage. Fig. 4.13 simply plots this relationship of n' versus above logarithmic equation for both fluids. The clear linear fitting in media means n' is highly depended on the static bed voidage, while ambiguous results in ultrapure water indicates the influences from other parameters which should be elucidated in further study.

Comparison of the terminal velocity obtained by experiments (U_t) and extrapolation (U_t'), it is obvious that both values of U_t and U_t' in culture media were smaller than those in water with different pellet mass. The U_t' ranged from 8.831 to 42.560 mm/s in culture and 7.345 to 33.189 mm/s in ultrapure water, respectively. These findings were generally in agreement with Smith et al.[261], who stated that the U_t values varied between 10 and 30 mm/s by regression analysis of the yeast flocs. They assumed the floc voidage had no remarkable effects on the U_t but failed to offer a satisfactory explanation. While our experiments clearly revealed the U_t' increased with pellets mass in both media and ultrapure water (Table 4.1), the increased pellets mass resulted in the decrease of static bed voidage due to the compression of pellets as mentioned above.

4.2.2.3 Gas-liquid-solid fluidization

Compared with liquid-solid reactors, the liquid-solid-gas reactors are more widely applied in cell cultivation and fungal fermentation. Aerobic fermentation needs gas supply to provide oxygen for cellular or fungal growth, while anaerobic cultivation requires no oxygen, but the anaerobic organisms may produce large number of gaseous products (such as CO₂ and biogas), in the form of bubbles. In this section, liquid-solid-gas fluidization of fungal pellets with the

parameters of gas flowrate, pellet biomass and liquid phase were studied, to identify pellet fluidization regimes as well as fluidization performance under different conditions.

Pellet fluidization by gas flow

In liquid-solid-gas fluidization, gas flows (in the form of bubbles) have more significant impact in pellet mixing, separation of aggregates and vorticity of fluidization than liquid flow. Therefore, this study is focused on the study of gas flowrate by changing the gas flowrate levels (9.9, 22.9 and 43.8 ml/min) but keeping the sparger size of 100 μm and the liquid phase static. Besides, both ultrapure water and culture medium were compared to distinguish their effects on the fluidization of fungal pellets with different biomass.

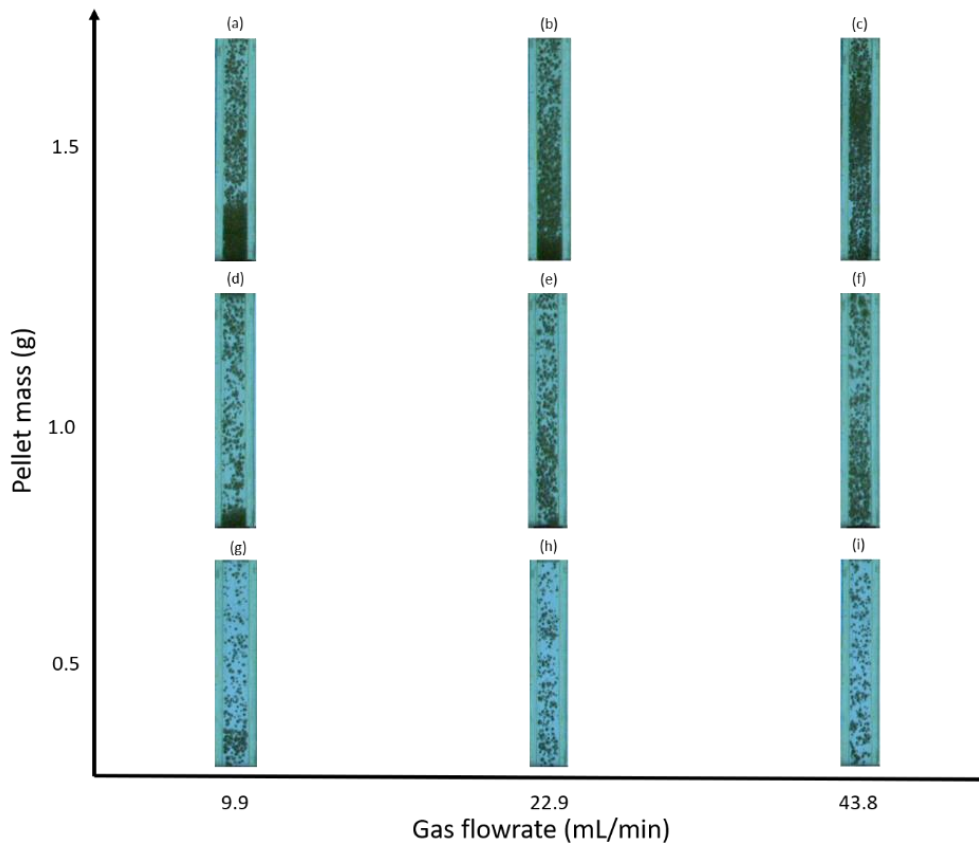


Fig. 4.14. Representative snapshots of different flow regimes with different gas flowrate and pellet biomass in ultrapure water. $d_B = 15$ mm.

Fig. 4.14 shows the representative images of the different flow regimes with the increasing of biomass and gas flowrate in ultrapure water, which were captured by high-speed camera (frame

rate: 100 fps; exposure time: 0.003 s). Based on the snapshots from the high-speed camera sequences, two different flow regimes were identified:

- Partially fluidized bed. Part of pellets accumulate on the bottom with rest of them freely fluidized on the upper part of column (Fig. 4.14a-d). This partially fluidization is attributed to the low gas flowrate which fails to suspend the whole bed. Instead, the bubble flow passes through the packed pellet bed and forms a channelling to continuously fluidize rest of pellets.
- Fully fluidized bed. Pellets were fully suspended and circulated by the single bubble flow, although clumps formed by pellet agglomeration were noticed. The fully fluidized bed regimes were illustrated in Fig. 4.14e-i.

At low biomass of 0.5 g pellets, all the pellets were fluidized with gas flowrates ranging from 9.9 to 43.8 ml/min, but more pellets were located on the lower part of column when gas flowrate was 9.9 ml/min. With the increase of gas flowrate, the distribution of pellets was more uniform along the column (Fig. 4.14h & i). When increasing the biomass to 1.0 g, partially fluidized bed appeared for low gas flowrate and transited into fully fluidized bed with increasing gas flowrate. Besides, more pellet clumps were observed with the increase of pellet mass regardless of the fluidization regimes. Although increasing the gas flowrate can significantly improve the pellet fluidization, the fluidization remained to be partially fluidized bed when biomass was 1.5 g at given gas flowrate range of 9.9 to 43.8 ml/min. On the other hand, Fig. 4.14a-c indicates the height of packed bed at bottom obviously decreased with increasing gas flowrate, thus confirming the improvement of fungi fluidization.

To characterize the influence of liquid phase on pellet fluidization, the ultrapure water was replaced by fresh medium but maintained the same conditions of pellet mass and gas flowrate.

Fig. 4.15 presents the snapshots of pellet fluidization in culture medium, which indicated the

similar transition of fluidization regimes from fully fluidized bed regimes were observed for low biomass and high gas flowrates but transitioning into partially fluidized bed with increasing of biomass at low gas flowrate. However, it is noted that pellets are easier to fluidize in culture medium than in water. For instance, at the same biomass of 1.0 g and gas flowrate of 9.9 ml/min, pellets were fully fluidized in medium (Fig. 4.15d) and partially fluidized in water (Fig. 4.14d). Besides, when increasing the biomass to 1.5 g, pellets were clearly stacked on the bottom of bed in water (Fig. 4.14a-c) while such packed-bed phenomenon was not identified in culture medium when gas flowrate was 22.9 ml/min and above. The better fluidization in culture media than in water is attributed to the higher density and viscosity of medium, which induced higher buoyancy to flow up the pellets and less pressure drop. The study of pellet fluidization, in the culture medium with gas supply, imitated the real fungal fermentation in the fluidized bed bioreactor where the pellets grow with the nutrient supply by culture medium and oxygen supply from bubble flows. The fully fluidization regimes initially confirmed the feasibility of using fluidized bed for fungal fermentation in future.

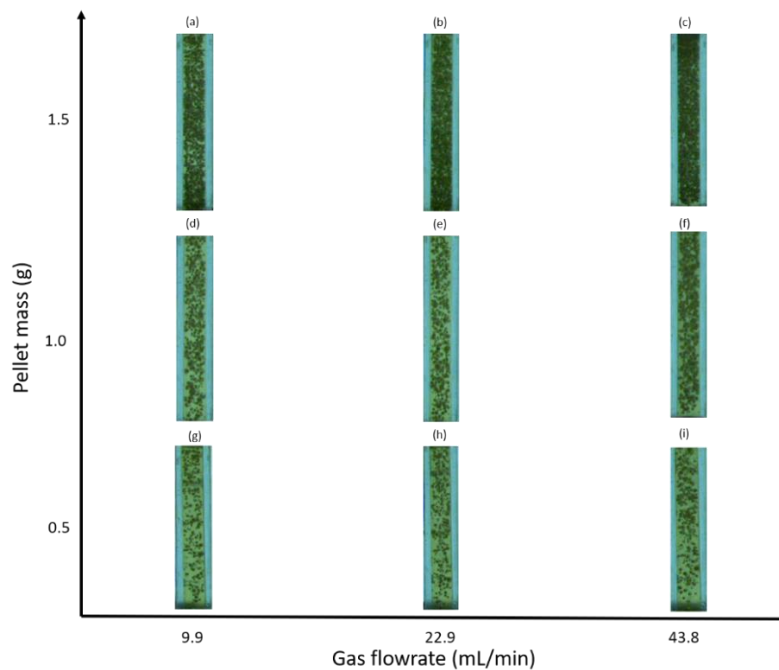


Fig. 4.15. Representative snapshots of different flow regimes with different gas flowrate and pellet biomass in medium. $d_B = 15$ mm.

Gas-liquid-solid fluidization regime maps

Characterization of the fluidization regime maps helps to identify the fluidization transition under different gas/liquid flow and particles properties, which is typically by plotting the dimensionless U_L^* vs d_P^* in liquid-solid bed or U_G^* vs d_P^* in gas-solid bed [268, 269]. Here, both liquid and gas flow are variable, but pellets have a fixed size and density. Besides, gas velocity U_G is hard to measure due to the gas pressure drop when gas passed through the capillary gas orifice. Thus, the pellet fluidization regime maps were plotted by using dimensionless liquid flowrate, Q_L^* and dimensionless gas flowrate, Q_G^* :

$$Q_L^* = Q_L \left(\frac{\rho_L^2}{\mu_L g \Delta \rho} \right)^{1/3} \quad (4.6)$$

$$Q_G^* = Q_G \left(\frac{\rho_G^2}{\mu_G g \Delta \rho} \right)^{1/3} \quad (4.7)$$

Three distinct fluidization regimes were observed in gas-liquid-solid fluidization with different liquid phase (ultrapure water and culture medium) and pellets mass (0.5 g, 1.0 g and 1.5 g):

Packed-bed regime: When gas/liquid flowrate is insufficient, pellets remain agglomerated and settle on the bottom, even though bed height is increased by gas/liquid flow.

Fluidization regime: Under certain liquid/gas flow rates, the pellets are well suspended and fluidized in the column.

Elutriation regime: When liquid/gas velocity is too high, pellets are floated to the top of column and washed out through the liquid/gas outlet.

Fig. 4.16 illustrates the fluidization regime maps for both ultrapure water and medium with different pellets weights. When pellets weight was 0.5 g, pellets bed could be fluidized only by gas flow or liquid flow (Fig. 4.16a) in both liquid phases, but the minimum Q_G^* (the intersection with X-axis) and minimum Q_L^* (the intersection with Y-axis) were smaller in the medium culture, which reflected the ease of fluidization in higher viscosity liquid. Furthermore,

the introduction of gas significantly promoted the fluidization performance, but the influence of gas was reduced with increase in the gas flow, as revealed in the fluidization curves, where Q_L^* decreased dramatically at the beginning with increasing gas flow.

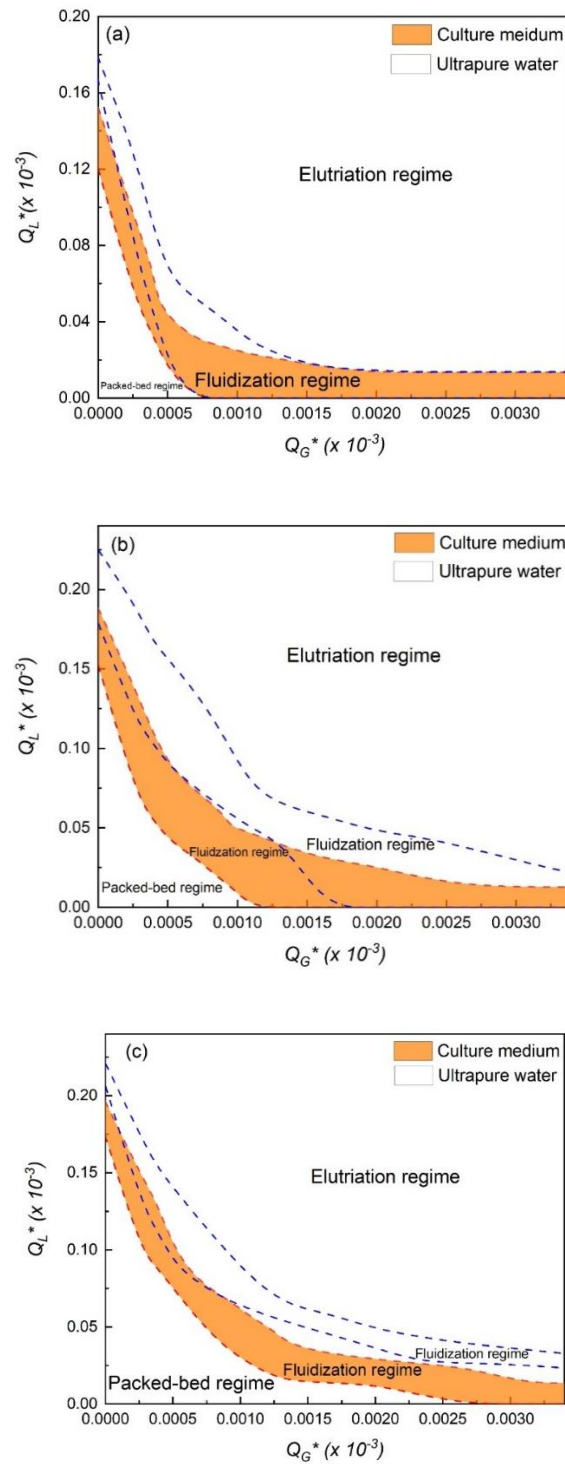


Fig. 4.16. Fluidization regime maps of fungi in both cultivation medium and ultrapure water: (a) 0.5 g pellets, (b) 1.0 g pellet, (c) 1.5 g pellets.

When the mass of pellets was increased from 0.5 g to 1.0 g and 1.5 g, both gas flow and liquid flowrate to fluidize pellets increased, regardless of the liquid phase. Additionally, the increase of pellets mass led to the area of fluidization regime decreased, because the high biomass inside the bed column resulted in the easier of pellet elutriation, which reflected by the gradually reduced fluidization regime areas from Fig. 4.16a to Fig. 4.16c. Therefore, a suitable weight of biomass is essential to not only maximum the production rate but also maintains the good fluidization. For instance, the 1g pellets with the H_0/D ratio of ~ 1 ensured a better fluidization but less elutriation than 1.5 g pellets with the H_0/D ratio of 1.34.

Pellet velocity analysis

Another phenomenon observed during the pellet fluidization experiments but not reflected in Fig. 4.16 is that compared with pellet fluidization in liquid-solid system, pellets in gas-liquid-solid system were transported faster and more chaotic with less aggregates. In order to validate this observation, the pellet velocities of 1.0 g pellets in medium during minimum fluidization in liquid-solid ($Q_L = 1.57$ ml/s) and gas-solid ($Q_G = 0.258$ ml/s) system, were quantitatively characterized using PIVlab tool from Matlab [270]. Fig. 4.17a & b present the snapshots from high-speed camera videos showing the direction and intensity of pellet movement by the green vectors. To improve the vector precision, the velocity vectors were validated by excluding the orange vectors which indicated the values interpolated by the software due to spurious or missing data points between image frames. The orderly green arrows clearly indicated the anti-clockwise fluidization of pellets by the liquid flow, while the pellets fluidization in gas-solid system was more chaotic and random. Pellet movement by gas flow were generally larger than by liquid flow, which could be confirmed by comparing the length of the green vectors, as shown in Fig. 4.17a & b, as well as the X and Y-Axis ranges in Fig. 4.17c & d. Specifically, the maximum pellet velocity in gas-solid fluidization was up to 10 mm/s while the maximum fluidization velocity in liquid-solid system was around 3 mm/s. Note, negative values of pellet

velocities only meant the moving direction is opposite to the default vector direction. Additionally, the velocity scatters were densely distributed in vertical direction for both liquid-solid and gas-liquid-solid system meaning that the axial velocities, v of pellets were generally higher than radial velocities, u as expected, because both the liquid flow and gas-liquid flow were supplied upward from the bottom of bed column. However, in the case of gas-liquid-solid fluidization there was also a significant spread in horizontal radial velocities, u , confirming the more chaotic motion of fungal pellets in this case.

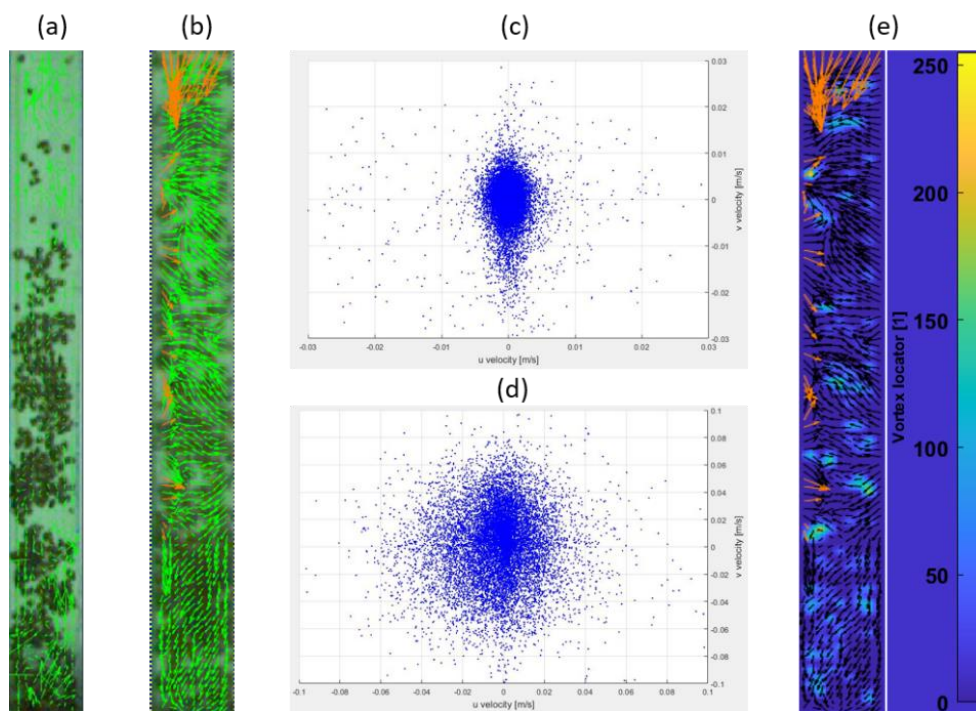


Fig. 4.17. Representative example of PIVlab analysis for 1 g pellets in medium: (a) mean velocity displays the pellet minimum fluidization by liquid flow, (b) mean velocity displays the pellet minimum fluidization by gas flow, (c) scatter plot showing the velocity distribution of 1 g pellets by liquid flow in medium, (d) scatter plot showing the velocity distribution of 1 g pellets by gas flow in medium, (e) display of the vortex locators with corresponding intensity for 1 g pellets by gas flow in medium.

Therefore, the more chaotic motion induced by the gas flow (in the form of bubbles) would in principle not only improve the mixing and mass transfer effect but would also inhibit the pellets agglomeration, while the high gas flow exerted higher shear force, which could lead to cell stress, damage and death [190, 271]. To deeply understand the effects of gas flow on pellet fluidization, this section investigated the pellet radial velocity, u and axial velocity, v with

different gas flowrate levels (9.9, 22.9 and 43.8 ml/min) and biomass levels (0.5, 1.0 and 1.5 g) in both static culture medium and ultrapure water.

- Radial velocity

Fig. 4.18a shows the mean radial velocities of pellet fluidization under certain fluidization conditions, which were obtained by PIVlab analysis of the image sequences (100fps, 6s). It is concluded that the mean radial velocity decreased with the increase of biomass but seemed to be independent of gas flowrate. The radial velocity decrease with increase of biomass was attributed to a greater number of pellets in column, which resulted in higher energy consumption to fluidize the pellets and more surface force between pellets. However, the gas flowrate had less effect on radial velocity. The bubble flow mainly suspended the pellets in the vertical direction along the column, while the radial movement of pellets was resulted from the vortexes in the gas-liquid-solid system. The vortexes were invisible but successfully identified by PIVlab tool illustrated in Fig. 4.17e. Besides, the surface force and drag force among the rough pellets could also induce the pellet radial movement. However, both vortexes and surface force were insignificant compared to the influence of vertical bubble flow, thus radial velocity was almost independent of gas flowrate. Regarding the liquid phase, the radial velocity was generally larger in culture medium than in ultrapure water, which again confirmed culture medium with higher density and viscosity is better for pellet fluidization.

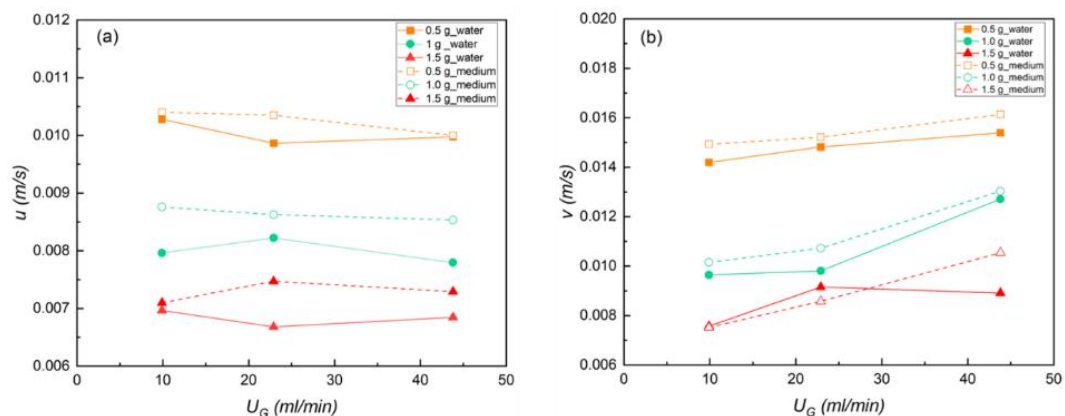


Fig. 4.18. (a) mean radial velocity of pellet fluidization at different conditions, (b) mean axial velocity of pellet fluidization at different conditions.

- Axial velocity

The mean axial velocity analysis of gas-liquid-solid fluidization is shown in [Fig. 4.18b](#). The axial velocity was decreased with the increase of pellet mass due to the increased pellet number and over all surface force, which was consistent with the relationship between radial velocity and biomass. Similarly, the culture medium resulted in higher mean axial velocity than water because of the higher density and viscosity. Different from the radial velocity, the axial velocity was observed to increase with the increase of gas flowrate, because the vertical bubble flow promoted the axial movement of pellets while the radial movement was caused by vortexes and surface force.

However, it is noted the axial velocity increased from 9.9 ml/min to 22.9 ml/min but decreased from 22.9 ml/min to 43.8 ml/min when biomass was 1.5 g in water, leading to the mean velocity in culture medium was lower than that in ultrapure water. Such a phenomenon was associated to the fluidization regimes. The fluidization regime was partially fluidized bed in water with gas flowrate ranging from 9.9 to 22.9 ml/min ([Fig. 4.14a & b](#)), which means only part of pellets were fluidized in water compared to the fully fluidized pellets in culture medium with same gas flowrate ranging from 9.9 to 22.9 ml/min ([Fig. 4.15a & b](#)). Therefore, lower energy consumption and less surface force in water led to faster pellet axial velocity in water. When increasing the gas flowrate to 43.8 ml/min, the fluidization regime in water was turned into fully fluidized bed ([Fig. 4.14c](#)). In the same fully fluidization regime, culture medium promoted pellet fluidization, reflected by the larger axial velocity in culture medium than in water when biomass was 1.5 g and gas flowrate was 43.8 ml/min, as shown in [Fig. 4.18b](#).

In summary, both radial and axial velocity decreased with increase of biomass at fixed gas flowrate, because the increased pellet mass causes more energy consumption and surface force thus suppressing the pellet movement. The main difference is that gas flowrate can only influence the axial velocity but has little effect on the radial velocity, as the radial velocity is

dominated by vortices and surface force while the axial velocity is determined by vertical bubble flow. Interestingly, the fluidization regime and liquid phase have also obviously influenced the axial velocity, because the partially fluidized bed with less fluidized pellets in water move faster than the fully fluidized bed with whole fluidized pellets in culture medium at same gas flowrate. Therefore, the optimization of concentration of pellets and gas flowrate is highly important in designing an ideal fluidized bed bioreactor for fungal fermentation in future, which not only maximizes the pellet concentration for higher bioproduction but also minimize the surface force to achieve a good fluidization state.

4.3 Conclusions

4.3.1 Fluidized bed design and fabrication

Currently different fluidized beds have been designed and fabricated by 3D printing technique. The optimization of the fluidized beds focused on obtaining homogeneous bubble flows when liquid and gas are pumped in. To make the bubbles smaller and more uniform, the perforated plate distributor was developed to break the bubbles, distribute liquid flows and support the particles above the distributor. The optimized fluidized bed enabled to produce homogeneous bubbles flow, which ensures the liquid-gas, liquid-gas-solid mixing efficiency and enhance the oxygen content inside the fluidic chambers, thus being selected for the final design. To allow gas sparging with smaller size, a hole was drilled at the centre of distributor, to accommodate a tight-fitting glass capillary tubing (CM Scientific, UK), with an outer diameter of 3 mm and 3 different inner diameters of 50, 100 and 150 μm . The capillary tubing was inserted from the gas outlet on the bottom, connecting to the manifold into the main column through the tight-fitting hole.

4.3.2 Hydrodynamics investigation of the miniaturized fluidized bed

4.3.2.1 Gas-liquid system

In this part, bubble flow regimes including mono-dispersed homogeneous regime, poly-dispersed homogeneous regime, transition bubble regime and heterogeneous bubble regime

were identified. Bubble size primarily increased with increasing orifice diameter and gas flowrate but slightly decreased with co-current liquid flow, which accelerated bubble detachment to inhibit bubble growth. Bubble velocity increase with the increase of gas flowrate as well as the upward liquid flow, but the promotion from liquid flow was insignificant in heterogeneous bubble regime. Gas volume fraction was increased with gas flowrate and gas sparger size but independent of liquid flowrate.

4.3.2.2 Liquid-solid and liquid-solid-gas system

In this part, fluidization of fungal pellets has been characterized using the 3D-printed miniaturized fluidized bed, which served as the preliminary exploration and optimization of the fluidized bed bioreactor for fungal fermentation and bioproduction. The main hydrodynamic characteristics of fungi fluidization are summarized as follows.

(1). The static bed voidage ε_0 of fungal pellets was 0.634, 0.618 and 0.577 when the pellet mass was 0.5 g, 1.0 g and 1.5 g, respectively. Compaction of pellets due to increase weight of packing might be the main reason for the trend as the lowest value of the voidage was observed for the highest mass. The values were larger than the conventional value of 0.4 as reported in previous studies. Unlike the micro spheres of glass beads and polymers used by other researchers, in this study, the fungal pellets and the hyphae on the surface of pellets enlarged the empty space between pellets, resulting in higher static bed voidage.

(2). Fluidization regimes in liquid-solid fluidization system have been observed and these regimes corresponded to static bed, expanded bed, partially fluidized bed, and fully fluidized bed. Because of the agglomeration effect of fungal cells, the pellets were not able to directly change from packed bed to fluidized bed during fluidization at low liquid velocity. However, the bed was observed to expand gradually with inter-connected branching filaments throughout the whole bed when the liquid velocity was low. As liquid velocity increased, the fungal pellets gradually became dispersed and fluidized, reached the fully fluidized bed regime when all the

pellets were fluidized along the column by the high liquid flowrate. The increased minimum fluidization velocity with increasing pellet mass also confirmed the influence of the interconnected hyphae on fluidization performance.

(3). Fungal pellets could be fluidized by only gas flow or liquid flow in both ultrapure water and cultivation medium when pellets mass was low (0.5 g). Liquid fluidization velocity and minimum gas fluidization velocity in culture medium were lower than those in ultrapure water, which indicated that the higher viscosity and density in liquid could have promoted the pellets fluidization. This finding was also observed when increasing pellets mass to 1.0 g and above, as the pellets could only be fluidized by gas flow in culture medium rather than in ultrapure water. Bubble flow was observed to not only enhance the mixing effect and mass transfer but also decreased the pellets aggregation, thus promoting the fungi fluidization.

The pellets fluidization study has confirmed that pellets can be well fluidized in liquid-solid and liquid-solid gas systems. The different fluidization regime maps established in this study will be used as a guideline to control the liquid and/or gas flowrates, to optimize pellets fluidization and bioproduction for the fungal fermentation in future studies. In next chapter, the investigation of fungal fermentation in flask culture is explored to lay a solid foundation to determine the optimal cultivation parameters, which could be used for further experiments of fungal fermentation in bioreactor systems.

Chapter 5 Investigation of cultivation parameters for fungal fermentation

5.1 Introduction

Raspberry ketone (4-(4-hydroxyphenyl) butan-2-one; RK) has been widely used not only in food industries and fragrance formulation (i.e., in aroma formulations of kiwi, cherry, strawberry) but also for healthcare products due to its lipid degradation and skin-lightening effects [6, 225]. However, the low abundance in natural fruits such as raspberries, cranberries, blackberries, grapes make the extraction of RK non-profitable. Cost-wise, the price of fruits-derived RK can be as high as US\$ 3000/kg [7]. Although chemical synthesis provides the alternative pathway to enlarge the yields of RK, the chemical synthetic compound is regarded as nature-identical product which can cost as low as US\$ 58/kg [226, 227]. Therefore, the natural production of RK with higher yields has been the subject of study in recent years.

In fact, in addition to the physical processes (i.e. distillation and extraction of natural sources), flavour compounds obtained by enzymatic/microbial processes can also be identified as natural based on the European Community regulations [228]. Hence, many researchers have attempted to improve the natural production of RK using biochemical and bioengineering methods. For instance, Wang et al. [9] reported a heterologous pathway to produce RK from p-coumaric acid, which extracted the candidate genes including CoA ligase (4CL), benzalacetone synthase (BAS), and RK/zingerone synthase (RZS1) from plants and assembled these candidate genes into the host strain of *Escherichia coli.*, achieving a final titer of 90.97 mg/l RK. Similarly, Lee et al. [7] assembled four heterologous genes, encoding phenylalanine/tyrosine ammonia lyase, cinnamate-4-hydroxylase, coumarate-CoA ligase and benzalacetone synthase in an industrial strain of *Saccharomyces cerevisiae* for the production of RK with the maximum concentration of 7.5 mg/l. Alternatively, Kosjek et al. [228] used the different lyophilized cells of

Rhodococcus spp to perform the biocatalytic oxidation of 4-(p-hydroxyphenyl) butan-2-ol (rhododendrol) into 4-(p-hydroxyphenyl) butan-2-one (RK), leading the substrate concentrations up to 500 g/l. However, the above microbial processes involving the gene edition are too complex for industrial applications. Alternatively, the fungal fermentation of specific fungi is a promising route to directly produce natural RK [233]. For instance, Ayer and Singer [234] initially identified RK from the metabolites of the bird's nest fungus *Nidula Niveo-Tomentosa*, accelerating the development of RK production by *De novo* synthesis using the fungus *Nidula Niveo-Tomentosa*. Fischer et al. [13] screened various precursor substances and confirmed the precursors including L-phenylalanine, phenyl pyruvate, phenyl propanoic acid, L-tyrosine, 4-hydroxyphenyl pyruvate, coumaric acid, 4-hydroxyphenyl propanoic acid, benzoic acid, hippuric acid, benzaldehyde and 4hydroxy benzaldehyde promoted the synthesis of RK, while other precursors such as cinnamic acid, phenyl acetic acid, phenyl acetaldehyde, and 4-hydroxybenzoic acid methyl ester suppressed the growth of fungus *N. niveo-tomentosa* and raspberry compounds production. Meanwhile, Boker et al. [235] increased the raspberry compound (RC, ketone + alcohol) yields to 200 mg/l by optimizing the media and supplementing the L-phenylalanine during the fermentation of the basidiomycete *Nidula niveo-tomentosa*. Taupp et al. [14] reported that 10 hours/day of the UV-A radiation could stimulate the growth and synthesis of RK from submerged culture of *Nidula niveo-tomentosa*, although the optimal value of exposure time and radiation intensity was unclear. Thus, the research on fungal fermentation using *Nidula niveo-tomentosa* for RK production is still in the initial stage. The key factors (i.e., substrate components, seed culture age and inoculum, precursor selection and operating conditions) which strongly affect fungal growth and bioproduction, have been underestimated and remained unexplored.

In this study, *Nidula niveo-tomentosa* was retained to study fungal growth and RK production. The present systematic study will provide additional information by investigating the

cultivation parameters including fungal preservation methods, fungal morphology, glucose and phenylalanine concentration, UV exposure time, preculture concentration and age (described in Chapter 3). By filling this knowledge gap, the experimental investigation can give new insights to the optimization for RK production and future scale-up production.

5.2 Results and discussions

5.2.1 Glucose concentration

The culture medium components, especially the carbon source, are key factors for the pellet growth. Compared to lactose as the carbon source which leads to the growth of free mycelia, glucose was reported to promote the pelletization process [272]. Boker et al. [235] proposed 30 g/L of glucose in their culture medium for *Nidula niveo-tomentosa* fermentation, but whether a glucose concentration higher or lower than 30 g/l enables higher RK accumulation is unclear. Thus, glucose concentration levels ranging from 25 g/l to 100 g/l were studied in this section.

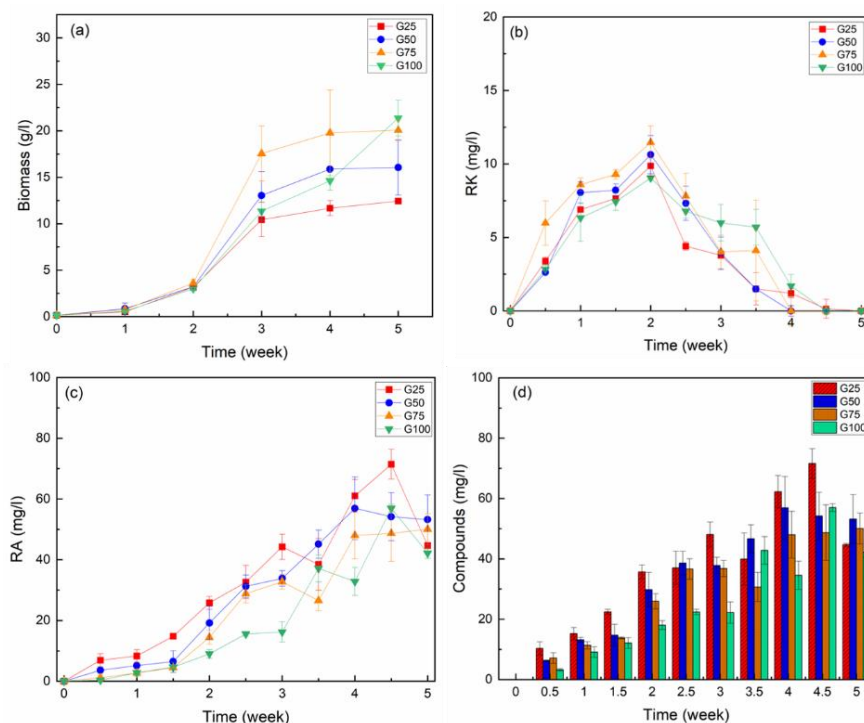


Fig. 5.1. Study of glucose concentrations on fungal growth and bioproduction: (a) time-course profiles of biomass dry weight, (b) RK curves during 5-weeks fermentation, (c) RA production during fermentation, (d) RC accumulation during the fermentation. Other cultivation parameters: 2 weeks old of preculture, 10% of inoculum concentration, 10h/d of UV-A exposition, 1.5 g/l of phenylalanine.

The biomass growths and raspberry production during a 5-week flask culture study are presented in Fig. 5.1. Specifically, the biomass curves in Fig. 5.1a indicate that there was an initial lag phase of two weeks where the pellets grew slowly to adjust to the new cultivation conditions, followed by a more rapid log phase growth from the third week. The biomass concentration entered a stationary phase in the last 2 weeks. The final biomass concentration was proportional to the initial glucose concentration up to 75 g/l glucose concentration. Both G75 and G100 produced a final biomass of 20 g/l. Therefore, it is concluded that the higher glucose concentration promoted pellet growth, up to a glucose concentration of 75 g/l, because higher glucose concentration may lead to substrate stress on fungus.

The RK production trend Fig. 5.1b shows that RK reached its maximum value in the second week of culture and then started to decrease towards the end of the fermentation period. There was no major difference between the RK values at different glucose concentrations, suggesting that the glucose concentration does not largely affect the RK productivity. Nevertheless, the rank of peak RK concentrations which was $G75 > G50 > G25 > G100$ indicated that 75 g/l glucose concentration exhibited better facilitation than others, while the 100g/l glucose inhibited RK production despite its promotional effect on pellet growth. On the other hand, the decrease of RK from week-2 is not attributed to low RK production rate but to higher conversion of RK to RA conversion, which was confirmed by Zorn et al. [273] who used a label study to elucidate the formation of RK by *Nidula niveo-tomentosa*. The converted RA was continuously accumulated during the fermentation, illustrated in Fig. 5.1c.

Unlike the RK concentration order, the RA concentration order of $G25 > G50 > G75 > G100$ suggested that glucose limitation generally enhanced the RK-to-RA conversion. Namely, more RK was consumed and transformed into RA in low glucose conditions, which was reflected by the low RK concentration in Fig. 5.1b and higher RA concentration in Fig. 5.1c for G25 and G50. Finally, the accumulation of RC in Fig. 5.1d indicated the final compounds concentrations

between different glucose concentration conditions were insignificant. In other words, glucose concentration in cultivation medium only affects the RK-to-RA conversion but has little impact on the titre of compounds. From the perspective of RK production, the optimal glucose concentration of 75 g/l is recommended. Such a glucose concentration was also used in our following studies.

5.2.2 Freezer stock VS agar plate

To determine a fungi preservation method for high bioproduction, the flask culture inoculated by the seed culture prepared through agar plate and freezer stock were compared. Fig. 5.2 presented the biomass growth and raspberry production in 4-week flask culture, in which the preculture was prepared by agar plate and freezer stock, respectively. Fig. 5.2a showed that the initial biomass concentration at week-0 from petri dish (0.147 g/l) was 44% higher than that from glycerol stock (0.102 g/l). The much higher biomass concentration from petri dish at week-0 was due to the manual operation that an agar plug was picked from the edge of fungal colony for seed culture preparation, which was difficult to quantitatively maintain the seed culture biomass. Although the initial biomass concentration was different, the difference between agar plate and freezer stock became insignificant after 1 week of fermentation, considering the error bars. Similarly, the RK production from agar plate and freezer stock was close during the fermentation, as maximum RK concentration from agar plate and freezer stock was 7.468 ± 1.189 and 7.736 ± 1.930 mg/l, respectively (Fig. 5.2b). On the other hand, raspberry alcohol produced from agar plate was observed to be 50% higher than that from freezer stock by the end of fermentation (Fig. 5.2c), which was attributed to the higher titre of compounds (RC, raspberry ketone + alcohol). Besides, the seed culture was directly swabbed from the edge of fungi colony in petri dish, while the fungi stocks from freezer stock were required to be thawed and revived before seed culture preparation, leading to a late lag phase. In other words, the flask culture from agar plate grows faster than those in freezer stock, leading

to more compounds production. However, the raspberry ketone concentration was independent of preservation methods, as RK was continuously converted into RA due to metabolic activity, which only resulted in more compounds accumulation (Fig. 5.2d).

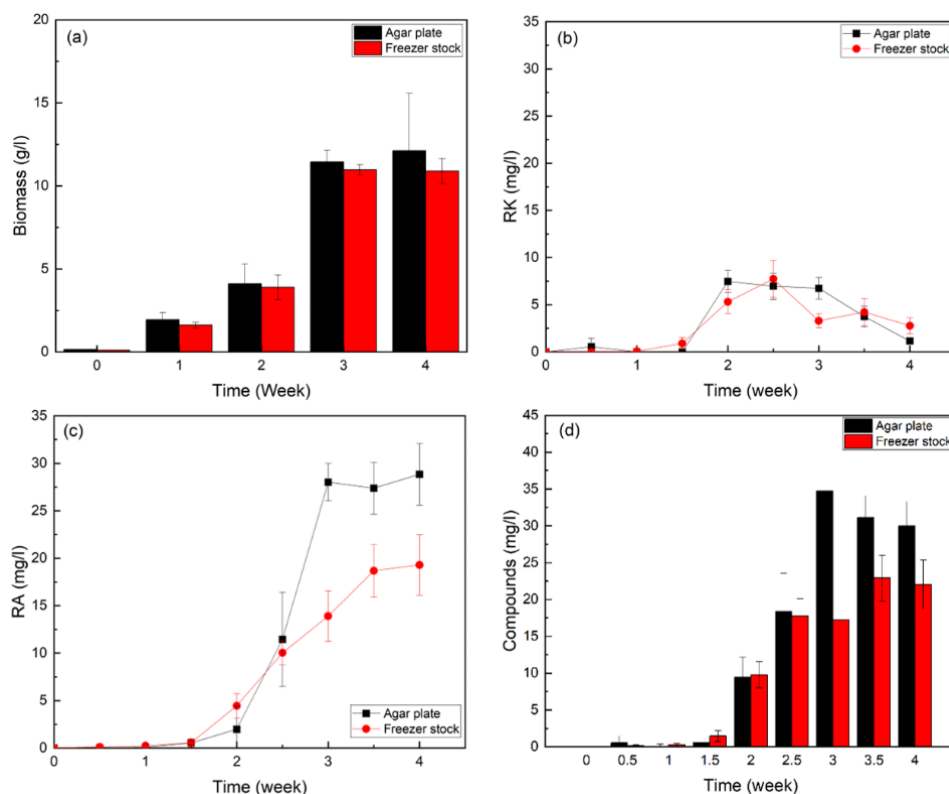


Fig. 5.2. Comparison of the seed culture type on fungal growth and bioproduction: (a) Time-course profiles of biomass dry weight, (b) RK curves during 4-week fermentation, (c) RA production during fermentation, (d) RC accumulation during the fermentation. Other cultivation parameters: 75g/l of glucose concentration, 2 weeks old of preculture, 10% of inoculum concentration, 10h/d of UV-A exposition, 1.5 g/l of phenylalanine concentration.

From the point of view of RK production, both methods can maintain the fungal bioactivity and lead to the same level of RK concentration. However, the preservation of fungi strains by agar plate means the continues subcultures at the interval of every 2-3 months, which is a time-consuming and repeated labour work. More importantly, the continuous subculture may change the physiological and molecular characteristics of fungi and increase the contamination rate during subculture transfer [274-276]. Instead, frozen glycerol stocks described in this section achieved the similar inactivation of metabolism and promised a longer storage periods [277]. Thus, freezer stocks are recommended for the preservation of the commercially and academically important fungi (*Nidula Niveo-tomentosa*) for long-term use. Such a preservation method will be also applied to prepare seed cultures in the following sections.

5.2.3 Seed culture age

Seed culture age determines the inoculum concentration as well as fungi viability. The seed culture age of *Nidula niveo-tomentosa* reported for RK production was 2 weeks old [3, 278], but whether a shorter or longer seed culture period facilitates RK production is unknown. In this section, three levels of seed culture age with cultivation time of 1 week (W1), 2 weeks (W2) and 3 weeks (W3), were prepared to determine the optimal seed culture age for promoting RK concentration. The biggest influence of seed culture age was that the flask culture was inoculated with older preculture led to more fungi strains, which was reflected by the overall biomass growth (Fig. 5.3a). For instance, the initial inoculum concentration of W1, W2, and W3 was 0.173, 0.269 and 0.445 g/l, respectively. The higher biomass concentration led to higher peaks of raspberry ketone as well as compounds accumulation, as the maximum RK and compounds concentration was determined by the initial biomass concentration, as shown in Fig. 5.3b & c.

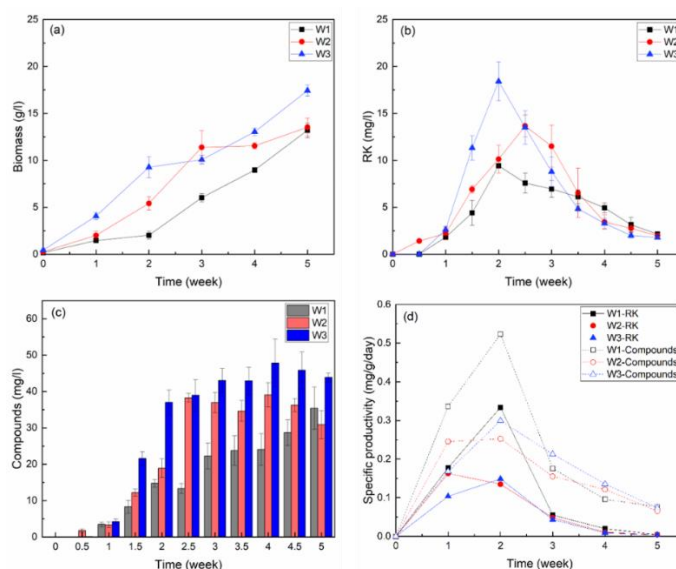


Fig. 5.3. Effects of the seed culture age on fungal growth and bioproduction: (a) biomass growth curves, (b) RK curves during 5-week fermentation, (c) RC accumulation during flask culture, (d) specific productivities for RA and RC. Other cultivation parameters: 75g/l of glucose concentration, 10% of inoculum concentration, 10h/d of UV-A exposition, 1.5 g/l of phenylalanine concentration.

However, it was noted that the final biomass concentration as well as compounds concentration of W1 and W2 reached the same level, which revealed that initial inoculum concentration was

not the only factor to influence fungal growth. Here, the specific productivity (Q_p) was used to evaluate fungi ability to produce RK over the full duration of flask culture [279]. Specific productivity (Q_p) was determined as shown below.

$$Q_p = \frac{\text{Accumulation of prouct}}{\text{Biomass concentration} \times \text{Time}} \quad (5.1)$$

Fig. 5.3d illustrates the specific productivities for RK and compounds at each week during 4-week long flask cultures. The results indicate that the Q_p for both RK and compounds increased to a maximum after two weeks, followed by a continual decrease to the end of fermentation. Such a trend was consistent with the RK production profiles, which means the highest fungal viability and productivity appeared after two weeks cultivation. Additionally, compared to the Q_p from the conditions of W2 and W3, W1 was observed the highest Q_p of both RK and compounds, suggesting the 1-week-old seed culture exhibited the biggest fungi activity. Therefore, the higher bioactivity of W1 seed culture promises an efficient biomass growth and bioproduction, leading its final biomass and compounds concentration to reach the same level as W2, although W1 had the lowest initial inoculum concentration. Based on the study of seed culture age, it is concluded that the seed culture age not only determines the initial inoculum concentration but also affects fungi productivity. The older seed culture has higher biomass concentration due to longer cultivation time, while the younger seed culture is proved to be more viable and efficient for fungi growth and production. However, the biomass concentration in a young seed culture is lower and thus the RK titre yield will be lower.

5.2.4 Inoculum concentration

Based on the study of seed culture age above, it is noticed that the older seed culture produced more raspberry ketone because the older preculture contained more fungi due to longer preculture time. In this section, three levels inoculum concentration (10%, 20% and 40%) with the same seed culture age of 2 weeks. The results indicated that biomass concentration was

related to the seed culture concentration (Fig. 5.4a), as higher seed culture concentration means that more fungi can grow into pellets leading to higher biomass. Consequently, the more fungi improve the bioproduction (Fig. 5.4b-d). However, the higher seed culture concentration required more nutrients for fungal growth, which was reflected from the glucose consumption in Fig. 5.4e. The glucose concentration curves based on the YSI results clearly show that the glucose consumption was dependent on the seed culture concentration. Therefore, it is concluded that higher preculture concentration with more inoculants in flask requires more nutrients for fungal biomass growth, which consequently produce more bioproducts.

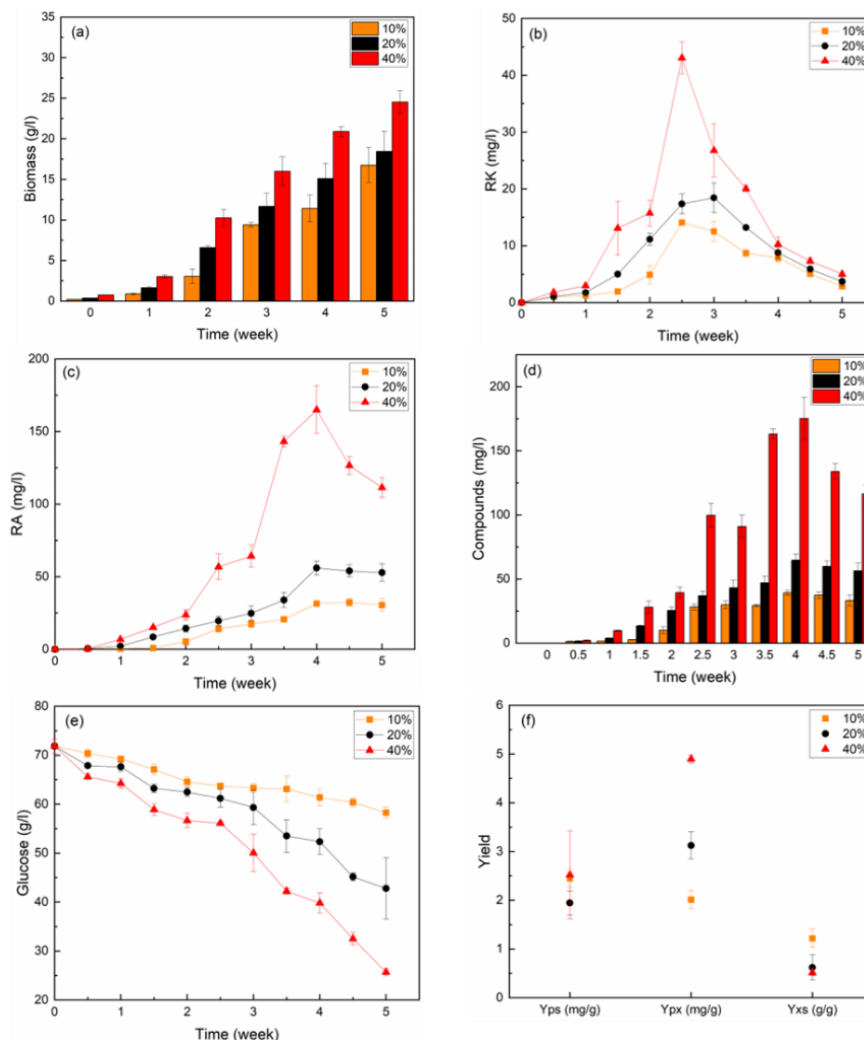


Fig. 5.4. Study of seed culture concentration on 5-week fungal growth and bioproduction: (a) biomass concentration profiles, (b) RK curves, (c) RA curves, (d) RC accumulation during flask culture, (e) glucose consumption during fungal fermentation, (f) average yield coefficients Y_{Xs} (gram dry weight per gram substrate), Y_{Ps} (gram product per gram substrate) and Y_{Px} (gram product per gram dry weight) during batch fermentations. Other cultivation parameters: 75g/l of glucose concentration, 2 weeks old of preculture, 10h/d of UV-A exposition, 1.5 g/l of phenylalanine concentration.

However, it is still unclear whether the RK formation is more dependent on fungal growth or on the nutrient consumption. Thus, Fig. 5.4f summarized the average yield coefficients of Y_{XS} (g dry weight g substrate⁻¹), Y_{PS} (g product g substrate⁻¹) and Y_{PX} (g product g dry weight⁻¹) over 5-week fermentations [280]. The results emphasized that the high seed culture resulted in higher yields of Y_{PS} and Y_{PX} but lower yield of Y_{XS} . Regarding the production of RK, Y_{PX} was generally higher than Y_{PS} in each level of seed culture concentration. In other words, it is believed that RK production is higher regarding the biomass concentration rather than glucose consumption. This is because the RK production is directly depended on biomass concentration, which determines the number of fungi involved in bioproduction. Note, the substrate of glucose is not only used for fungal growth but also for metabolism activities including the RK production, which means that the overall glucose consumption is not the direct factor to evaluate the yield of RK [281].

5.2.5 UV radiation time

Ultraviolet (UV) irradiation is a typical method to enhance the bioproduction in biotechnology [282, 283]. UV-A radiation on *Nidula Niveo-tomentosa* has also been reported to stimulate the fungal growth and synthesis of raspberry ketone, but the optimal UV exposure times was still unknown [14]. In this section, four different UV-A exposition time of 0 hour per day (UV-0), 10 hours per day (UV-10), 17 hours per day (UV-17) and 24 hours per day (UV-24) were investigated to determine the optimal UV radiation time for RK production. Fig. 5.5a shows that the biomass growth in dark conditions (UV-0) were approximately half lower than those with UV exposition in the third week of fermentation. This was consistent with the results from Taupp et al. [14], who reported the biomass of the culture exposed with 10h UV-A per day nearly 2 times more than that cultivated in dark condition at day-13. They explained the higher biomass with UV-A radiation was due to the growth-related enzymes of the citric cycle, which were identified as a response to irradiation with UV-A. However, in our study, the final

biomass concentration in conditions of different UV radiation times reached the same level from the fourth week of fermentation. In other words, the UV radiation might only affect the fungal growth in the first 3 weeks, as the growth rate was limited for all after 4 weeks. Besides, it is also observed that the biomass concentration of UV-17 and UV-24 were lower than UV-10 in the first 2 weeks but reached the same level by the end of fermentation, suggesting the UV radiation time of 10 hours might only induce stress on biomass growth in the initial stage. It is assumed that increased cell density could lead to shading of UV light, hence UV effect per cell is reduced, but more work is required to confirm this assumption.

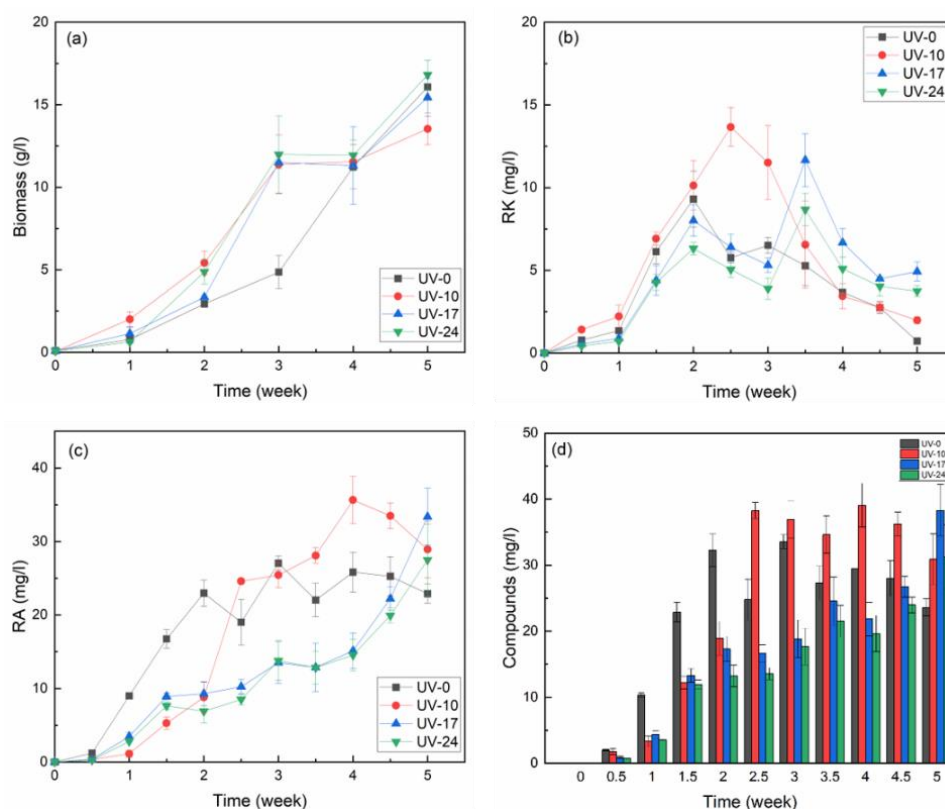


Fig. 5.5. Effects of UV-A exposition time on fungal growth and bioproduction: (a) biomass growth curves, (b) RK curves during 5-week fermentation, (c) RA curves during flask culture, (d) RC accumulation during 5-week fermentation. Other cultivation parameters: 75g/l of glucose concentration, 2 weeks old of preculture, 10% of inoculum concentration, 1.5 g/l of phenylalanine concentration.

The synthesis of RK in UV-0 and UV-10 peaked at around week-2 with the maximum concentration of 9.303 ± 1.698 mg/l and 13.663 ± 1.175 mg/l, respectively (Fig. 5.5b). The different RK concentrations between UV-0 and UV-10 at the peak points indicated the

enhancement effect of UV exposition for RK synthesis. In addition, the RK concentration in the condition with longer UV radiation of 17 and 24 hours were lower than that in UV-10, confirming the stress of long-time UV exposition. This stress seemed to decrease with the increase of fermentation time due to the potential light-regulation ability of fungi, as the second peaks appeared at week-3.5 for both UV-17 and UV-24. However, the stress increased with increasing the UV period. For instance, the second peak for UV-24 was lower than that of UV-17, revealing the 24 hours UV radiation suppressed RK synthesis when UV exposure time increased beyond 17 hours. Noteworthily, the second RK peak of UV-17 almost reached the maximum RK of UV-10, which not only confirmed the light-regulation ability of fungi but also indicated the UV radiation time of 10 or 17 hours had little impacts on RK production, as the UV-period of 10 and 17 hours was comparable. The little difference of 10 or 17h UV periods on fungal bioproduction could be confirmed by the similar values of maximum RA (Fig. 5.5c) and RC concentration (Fig. 5.5d) between UV-10 and UV-17. In this section, by studying the UV-A radiation time, it is confirmed the enhancement of UV exposition on fungal fermentation compared to dark condition. However, it is also noticed the light stress of long-time UV exposure on RK production from UV-17 and UV-24, although the stress can decrease due to the potential light-regulation ability of fungi. Thus, the 10h per day of UV radiation (UV-10) which could improve RK synthesis but cause less light-stress for fungi is recommended for submerged culture of *Nidula niveo-tomentosa*.

5.2.6 Phenylalanine concentration

Phenylalanine is known as the precursor for RK synthesis, but the optimal phenylalanine concentration for submerged cultivation of *Nidula niveo-tomentosa* is unclear. Here, three different phenylalanine concentration 0.5, 1.5 and 2.5g/l were used to investigate the effects of phenylalanine on fungal fermentation, thus determining an optimal concentration for RK production. The results in Fig. 5.6a shows the highest biomass concentration was observed in

the condition of 0.5 g/l initial phenylalanine concentration, which indicated the possibility that high phenylalanine concentration may induce growth-related stress. Previous experimental evidence revealed the oxidative stress of phenylalanine on hippocampus and rats [284]. Besides, the intermediate 2-phenylethanol (PEA) produced from phenylalanine is confirmed to reduce yeast growth and viability [285]. However, there is no direct evidence to support the stress of phenylalanine on fungal growth. Our experiments spotted this stress effects on fungi biomass, but further investigations are required to confirm the findings.

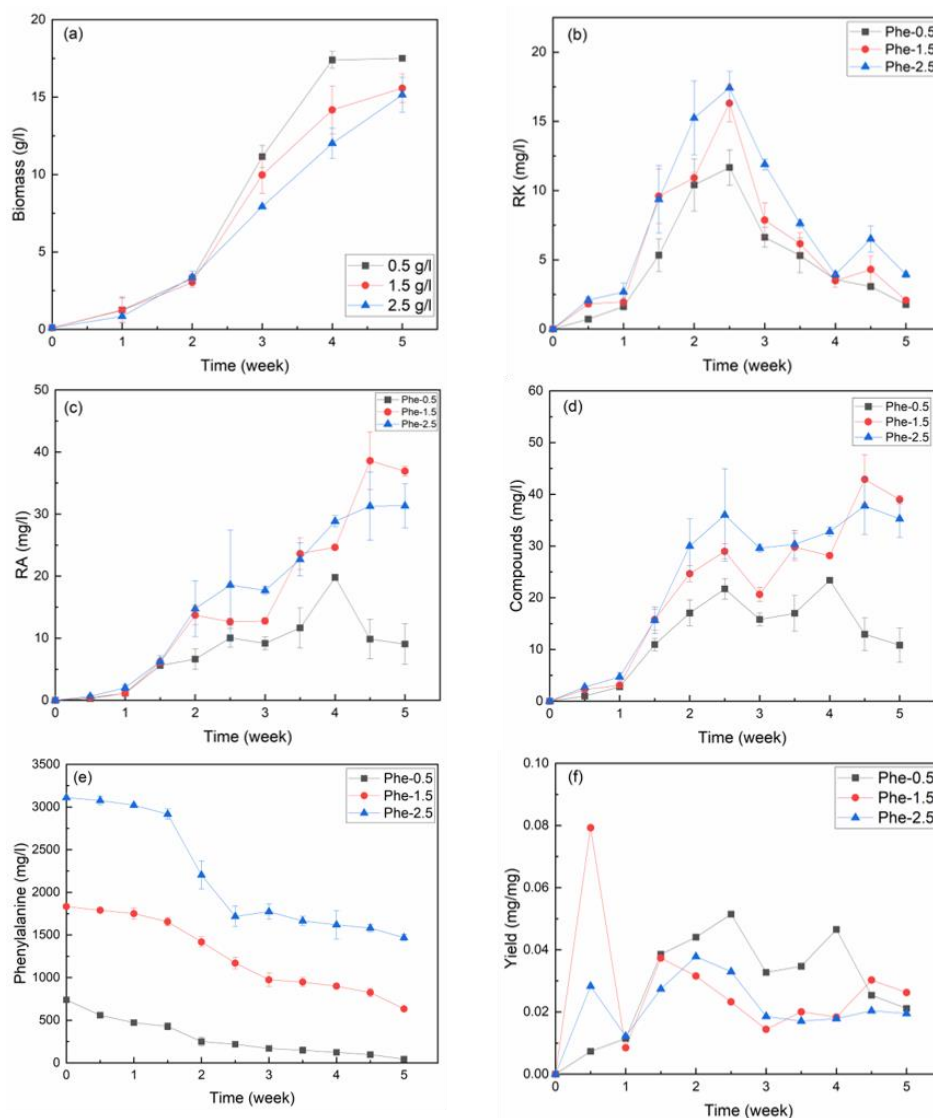


Fig. 5.6. Study of phenylalanine concentration on fungal fermentation: (a) Biomass concentration curves, (b) RK curves during 5-week fermentation, (c) RA curves in 5-week fermentation, (d) RC accumulation during flask culture, (e) phenylalanine consumption during fungal fermentation, (f) average yield coefficients YPS (gram compounds produced per gram phenylalanine consumed). Other cultivation parameters: 75g/l of glucose concentration, 2 weeks old of preculture, 10% of inoculum concentration, 10h/d of UV-A exposition.

Unlike its impacts on biomass, higher phenylalanine was observed to improve the RK, RA and subsequent compounds production, as shown in Fig. 5.6b-d. That is explained by the precursor activity of phenylalanine. The natural production of RK initiates with the phenylpropanoid pathway, which converts phenylalanine into p-coumaric acid, followed by the condensation reactions between coumaroyl-CoA and malonyl-CoA for the conversion of p-coumaric to RK [7, 286]. It is expected that more of the precursor phenylalanine in culture can lead to a higher concentration of RK, which is subsequently converted into RA. Fig. 5.6e illustrates that more phenylalanine was consumed in conditions of Phe-2.5 and Phe-1.5 than that in Phe-0.5, leading to the higher RK, RA and compounds concentration in conditions of Phe-2.5 and Phe-1.5 than that in Phe-0.5. Notwithstanding, highest yielding rate was from the condition of Phe-0.5, as shown in Fig. 5.6f, because the biosynthesis process of RK from phenylalanine produces many intermediates and unknown metabolite by-products [278]. Thus, a higher phenylalanine concentration improved the bioproduction of RK, but the yielding rate decreased with increasing phenylalanine concentration.

5.2.7 Pellet morphology

Although the fungal pellets are easier to handle in bioreactor processing, it is unknown whether the pellets or filamentous fungi of *Nidula niveo-tomentosa* have a better productivity for RK. In this section, both the fungal pellets and mycelia fungi were investigated from the point of view of RK production. The mycelia fungi were prepared by homogenizing the whole content of flask at week-2 (H2) or week-3 (H3) during the 5-week flask fermentation, so that the pellets were broken into small mycelia again during the fermentation. The inoculum in control flasks without homogenization (NH) were allowed to directly grow into compact mature pellets.

Fig. 5.7 presents the photographic images of fungi samples after 5-week flask culture, which were captured by a Scan1200 (Interscience, France) colony counter [287]. The fungi in the flask culture without homogenization were spherical pellets composed of dense core region

and extended hairy region (Fig. 5.7a). The fungi with homogenization consisted of both smaller pellets and mycelia, as the homogenizer broke the mature pellets into tiny fragments which continued to form new pellets or aggregated mycelia. It is noted that bigger pellets with less mycelia in H2 were identified, because the fungi in H2 were homogenised at week-2 and had another 3 weeks for growth. Smaller pellets with more mycelia were presented in H3 as H3 were homogenised at week-3 which had less time for pellet formation and expansion.

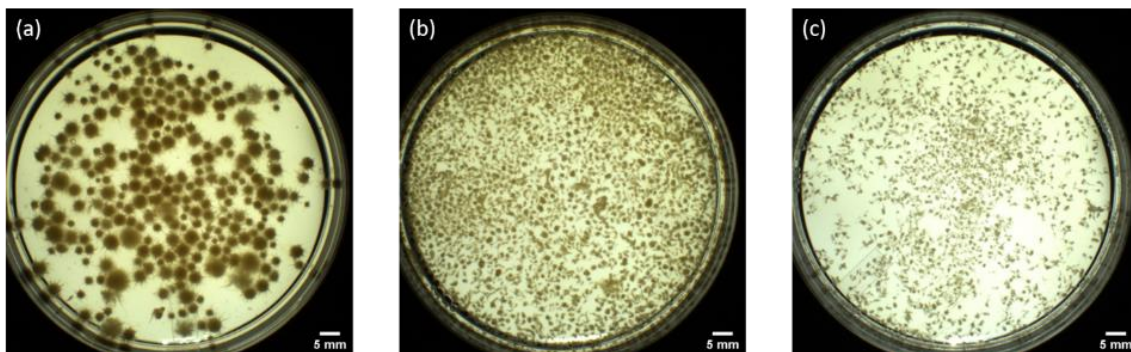


Fig. 5.7. Images of Fungal samples after 5-week flask fermentation: (a) no homogenization during flask culture, (b) homogenization of the flask at week-2 (Homogenization-2), (3) homogenization of the flask content at week-3 (Homogenization-3). Other cultivation parameters: 75g/l of glucose concentration, 2 weeks old of preculture, 10% of inoculum concentration, 10h/d of UV-A exposition, 1.5 g/l of phenylalanine concentration.

Fig. 5.8a suggests the homogenization during flask culture had little effect on biomass growth, as the final biomass from three groups all achieved 15 g/l. Thus, it is concluded that fungal biomass of *Nidula niveo-tomentosa* is independent of fungal morphology. In contrast, the fungal morphology strongly influenced the synthesis of RK (Fig. 5.8b). Compared to the peak RK concentration of ~15g/l for NH at week-2, peaks for H2 and H3 was up to 25 g/l at week-3 and week-4.5, respectively. The maximum RK for H2 and H3 seemed to appear after one week of the homogenization. Besides, much high RA and raspberry compounds were also observed in H2 and H3, which confirmed that homogenization promotes RK production. In other words, mycelial fungi morphology led to a higher RK productivity than pellet morphology fungi under equivalent cultivation conditions. The main issue with fungal pellet morphology is the low internal transport of nutrient and product, which limits the further

growth of pellets as well the RK production [288]. Besides, the nutrient limitation in central region of pellets were reported to cause the autolysis, which can also decrease both cellular metabolism and product synthesis [289, 290]. Instead, the filamentous fungi with a larger hairy region can promote the substrate absorption and product release. Finally, maximum values of RK, RA and compounds between H2 and H3 were all close, indicating the homogenization time at week-2 or week-3 was insignificant to affect the raspberry bioproduction.

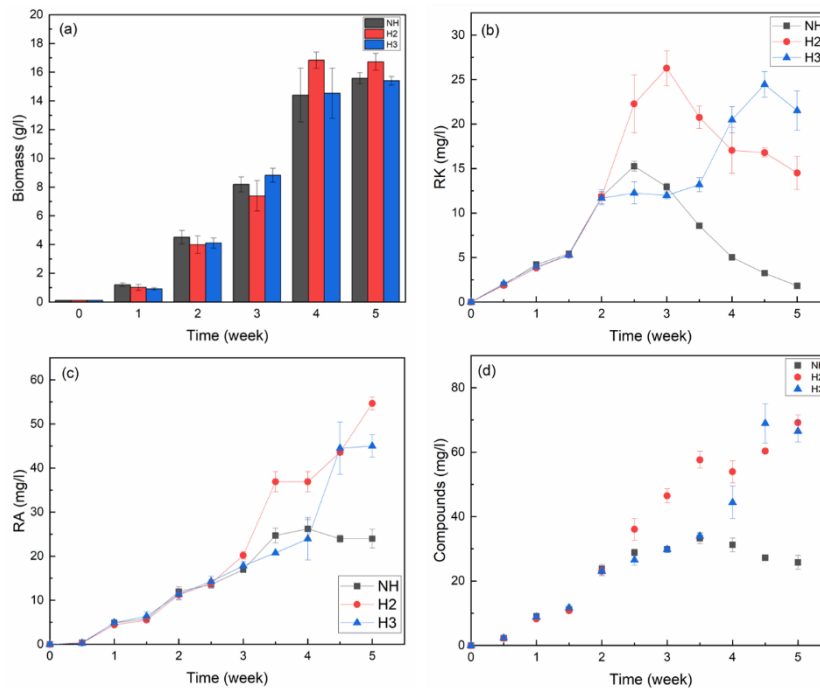


Fig. 5.8. Effects of fungal morphology on fungal growth and bioproduction: (a) biomass concentrations, (b) RK curves during 5-week fermentation, (c) RA curves during flask culture, (d) RC accumulation during 5-week fermentation.

Based on the selected strains as well as the target bioproducts, selection of the appropriate morphology type from the mycelium, clump, and pellet for a given biotechnological process is of great significance. In this section, the free mycelial *Nidula Niveo-tomentosa* has been proved to improve the RK production in flask culture, although fungal pellets have the advantages of harvest ease and low broth viscosity [199]. However, the excessive growth of free mycelia provokes the operation problems. For instance, the mycelia were reported to aggregate and attach in the baffles of Stirred-tank bioreactor to form the dead zone. Thus, it is important to

optimize the bioprocessing and bioreactor design based on the selected microorganisms and targeted bioproducts.

5.2.8 Optimized conditions

Based on the investigations of the cultivation parameters, the optimal conditions for flask culture have been identified, as listed in [Table 5.1](#). This section intends to achieve the maximum RK synthesis by combining the optimized factors together. Besides, the cultivation time is also extended from the normal period of 5 weeks to 6 weeks because the maximum RK only appears after 5 weeks of flask culture under the optimized conditions. [Fig. 5.9a](#) indicates that the biomass growth started from week-0 (1.36 g/l) to week-1 (3.82 g/l) during the lag phase, followed by the log phase until week-4 (30.92 g/l) before it entered a stationary phase (week-4 to week-5) and finally the decline phase (week-5 to week-6). Therefore, 6 weeks fermentation time is enough for fungal growth. On the other hand, the glucose consumption, based on the YSI measurement, indicates that 75 g/l glucose in fresh media is sufficient for the optimal fungal fermentation. Notably, the initial glucose concentration of less than 75 g/l was due to the dilution effect from the addition of 10% seed culture and 10% phenylalanine solution.

Table 5.1 Optimal parameters for improving RK synthesis in flask culture.

Optimized conditions	
Glucose concentration (g/l)	75
Fungi preservation method	Freezer stock
Seed culture age (week)	3
Inoculum concentration	40%, ~1.36 g/l
UV-A radiation time (hour per day)	10
Phenylalanine concentration (g/l)	2.5
Fungal morphology	Free mycelia (Homogenization at 10K rpm for 3 min)

[Fig. 5.9b](#) presents the bioproduction of RK, RA and compounds under the optimized conditions in 6-week fermentation. The synthesis of RK peaked around 154.35 mg/l at week-4, which not only suggested that the maximum RK was largely improved but also indicated its production

was extended to week-4 before declining, compared to the normal peak at week-2 under non-optimized conditions. The increased RK is attributed to the high initial inoculum concentration (40%) as well as other optimal parameters such as UV radiation time, phenylalanine, glucose concentration, etc. For instance, 10 hours per day of UV exposure can promote the pellet production compared to the dark condition, and induced less stress compared to the 17 and 24 hours exposure time. Compared to the compact fungal pellets, the fungi with mycelia morphology (due to homogenization) containing a hairy region enhance the nutrient absorption and product release. Besides, the optimal phenylalanine (2.5 g/l) and glucose concentration (75 g/l) were also observed to improve RK production. The extended peak time was mainly due to the homogenization at week-2, which broke the pellets into small mycelia and resulted in the new growth of fungi. Meanwhile, the production of RA (converted from RK) had a similar trend to RK, which peaked at week-4 and gradually decreased. The reduction of RA suggested RA was converted into other unknown metabolites during the flask culture. The titre of compounds (RK + RA) reached 365.1 mg/l, indicating the maximum productivity of *Nidula Niveo-tomentosa* under optimized conditions.

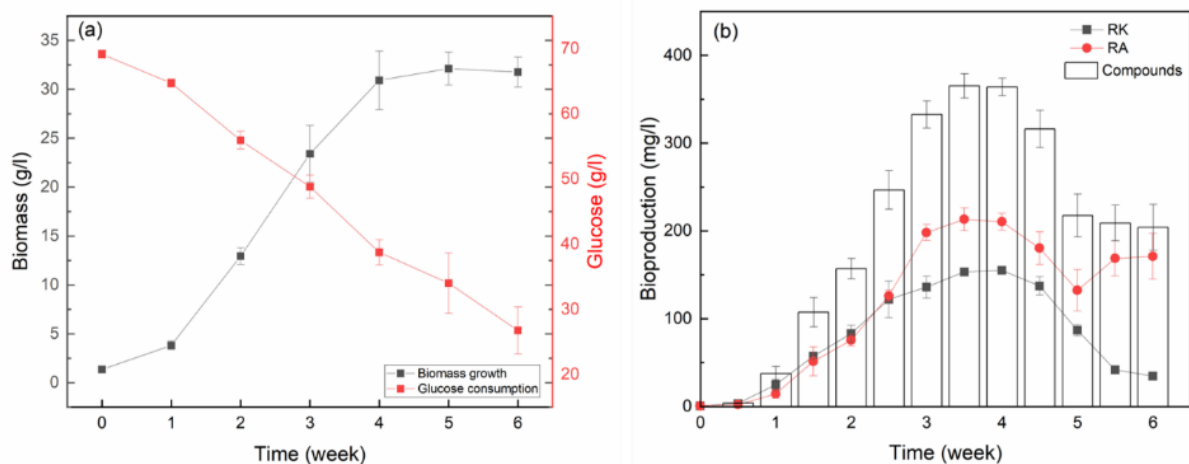


Fig. 5.9. Fungal fermentation under optimized conditions: (a) biomass growth and glucose consumption, (b) bioproduction.

5.3 Conclusions

This chapter has characterized and identified the optimal cultivation parameters for improved RK production by *Nidula niveo-tomentosa*. The optimal cultivation conditions are: 75 g/l of glucose concentration, freezer stock method for fungi preservation, seed culture age of 3 weeks and initial concentration of 40%, 10 h/day of UV-A radiation, 2.5 g/l of phenylalanine concentration of 2.5 g/l and free mycelia fungal morphology. It is concluded that a suitable glucose and phenylalanine concentration can not only maintain the substrates supply but also reduce substrate stress. UV-A radiation has little effect on biomass growth but can effectively stimulate the synthesis of RK. Besides, a younger seed culture resulted in higher specific productivity, but older seed culture led to higher RK production due to its higher inoculum concentration. Compared to fungal pellets, the mycelial morphology enhanced RK production as the mycelia fungi promoted nutrients intake and bioproducts transportation. Finally, a maximum RK value of 154.35 mg/l was obtained by combining the optimal parameters together, which is the highest ever reported for the RK production by submerged culture of *Nidula niveo-tomentosa*, demonstrating the potential of fungal fermentation in the production of natural raspberry ketone. Besides, this chapter is also the basis for the next chapter study of fungal fermentation in bioreactor systems.

Chapter 6 Comparison of RK production in different bench-scale bioreactors

6.1 Introduction

The filamentous fungus *Nidula niveo-tomentosa* produces a natural phenolic compound known as raspberry ketone (RK), which is widely used in the food and healthcare industry. The scale-up of RK fermentation requires an understanding of the relationship between pellet morphology and bioreactor systems. In this study, pellet morphology and raspberry ketone production were investigated in different lab-scale bioreactor systems including flask culture, stirred-tank reactor (STR), panel bioreactor (PBR) and fluidized bed reactor (FBR). The effects of main operating parameters, such as conventional agitation (300 rpm) in STR, and aeration (0.15 V.V.M) in STR, PBR and FBR were linked to pellet size and sphericity, final biomass concentration, RK and compounds production. The resulting fungal morphologies with corresponding RK productions are of fundamental importance for selecting and optimizing the suitable fungal morphology for a given biotechnological process and the scale up of RK production in future.

6.2 Results and discussions

6.2.1 Pellet morphology

[Fig. 6.1](#) presents the fungi morphology from different bioreactors after 4 weeks of fermentation. Typically, fungal pellets are formed from free mycelia [20], but the final fungal morphology and corresponding production rate depends on specific cultivation systems. Here, fungi cultured in flasks grew into compact pellets surrounded by hyphae, which exhibited the smallest size (2.27 ± 0.48 mm), but highest sphericity (0.88 ± 0.06) compared to those grown in other bioreactors ([Fig. 6.1a](#) & e). Interestingly, while the fungal pellets in the STR were also compact pellets similar to flask culture, they showed an elliptical nature, (3.16 ± 1.80 mm in diameter, 0.16 ± 0.18 mm in sphericity), and lacked a hyphal fringe ([Fig. 6.1b](#)). Thus, impeller-

based agitation (300 rpm) of the STR had more impact on pellet sphericity than pellets size. Fig. 6.1c and Fig. 6.1d indicate the pellets morphologies in PBR and FBR, respectively. Both PBR and FBR had a gas flowrate of 0.15 v.v.m to suspend the pellets, while in the PBR a magnetic mixer was used to mitigate the dead zone. Therefore, the main difference between PBR and FBR was mechanical stress from magnetic stirrer, causing pellets breakage in PBR (Fig. 6.1c), which was overcome in the FBR by improved gas delivery. Furthermore, the continuous bubbles rupture on the upper liquid-gas interface inside the PBR can also be attributed to pellets fragmentation [190, 271], while in the FBR bubbles could pass through a mesh screen before reaching the surface, separating pellets from this disturbance. As a result, as can be seen in Figure 2c-d, the FBR showed noticeable increase in pellet diameter (7.49 ± 1.83 mm) and sphericity (0.83 ± 0.08), compared to the pellets in PBR (4.43 ± 1.35 mm in diameter, 0.75 ± 0.10 in sphericity). Therefore, by using improved upward flow and minimal bubble disturbance, the FBR represents an improved design compared to the PBR, overcoming the need for magnetic stirring and avoid bubble rupture disturbance, thereby maintaining pellet integrity.

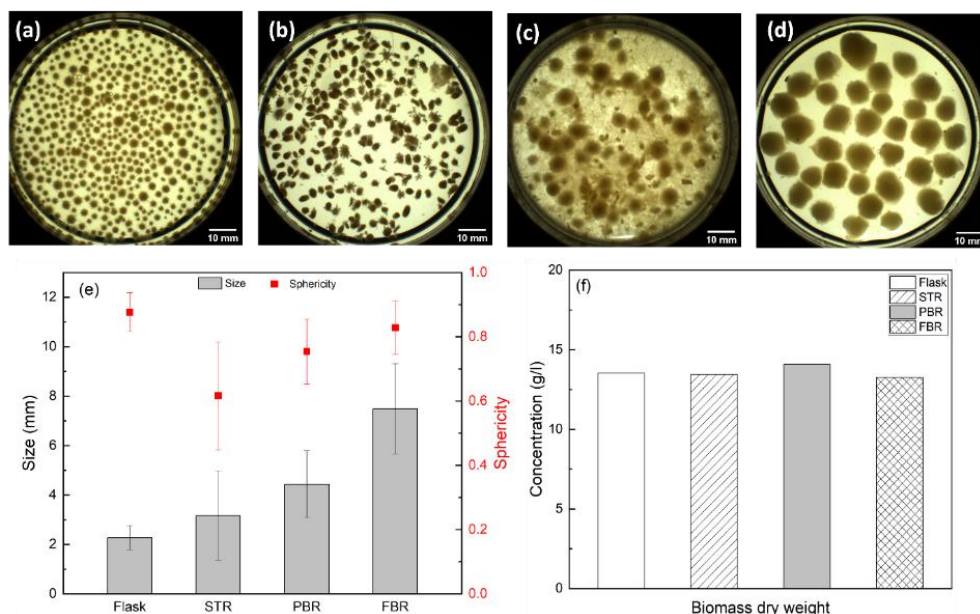


Fig. 6.1. Images of pellet samples after 5-weeks fermentations in (a) flask culture, (b) stirred-tank reactor (STR), (c) panel bioreactor (PBR) and (d) fluidized bed reactor (FBR), (e) pellet size and sphericity after 5-week fermentation from different bioreactors, (f) biomass concentrations of fungal cells after 5-weeks fermentation in different bioreactors.

In general, both aeration and agitation approaches of the bioreactor designs in STR, PBR and FBR strongly affects pellet morphology by changing pellet size as well as sphericity. To understand the pellet morphology mechanisms under different bioreactor systems, Fig. 6.2 illustrates this morphological variation from hirsute spherical pellets in flask culture to shaved elliptical pellets in the STR, and both fragmented pellet fragments and complete floccose pellets in PBR and FBR, respectively. In our experiments, the agitation system in STR sheared the outer pellet hirsute zone and changed spherical pellets into elliptical spores of high compactness.

On the other hand, aeration-based mixing systems had little effect on pellet sphericity and allowed loosened the interactions of hyphae, thus encouraging expanded pellets. It is known that the fungal pellets could be formed from either a single spore (non-coagulative), aggregates of spores (coagulative) or agglomerated hyphae [204]. The continuous bubble flows in both PBR and FBR not only expanded the pellets, but also tended to break the hyphal aggregates, resulting in floccose pellets with larger pellet size. The fragmentation of floccose pellets in PBR was attributed to the magnetic stir bar, leading to the disrupted nature visible in Fig. 6.1c. Thus, these findings are congruent with those reported above, confirming that aeration-based mixing led to larger, floccose pellets spherical in shape, while stirred agitation encouraged the formation of compact smooth pellets with an elliptical shape.

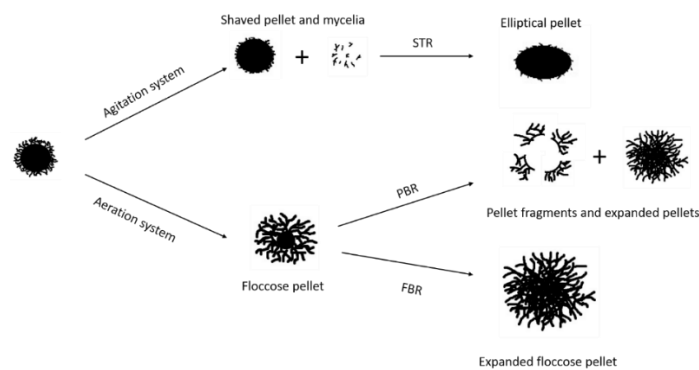


Fig. 6.2. Schematic diagram of pellet morphology changes in different bioreactors. STR: stirred-tank reactor, PBR: panel bioreactor, FBR: fluidized bed reactor.

6.2.2 Pellet biomass

It is interesting to note that despite differences in morphology, total biomass is largely unchanged regardless of cultivation system. As can be seen in Fig. 6.1f, after 4 weeks fermentation, the final dry weight reached 13.5, 13.4, 14.1 and 13.3 g/l in the flask culture, STR, PBR and FBR respectively, suggesting under mixing conditions of 300 rpm agitation speed or 0.15 v.v.m gas flowrate, no comparable differences can be observed on biomass growth, and the consistency of final yields suggests that there was no limitation in terms of dissolved oxygen or substrate availability. In future, a more comprehensive study on rate of fungal biomass growth under more aggressive agitation/aeration conditions can be explored to confirm the relationship between fungal biomass and dissolved oxygen. What this work shows is that fungal pellet morphology differs substantially between gas-mixed systems and those employing impellers, with gas mixing giving rise to expanded, low-density floccose pellets in comparison to dense smooth pellets under mechanical mixing.

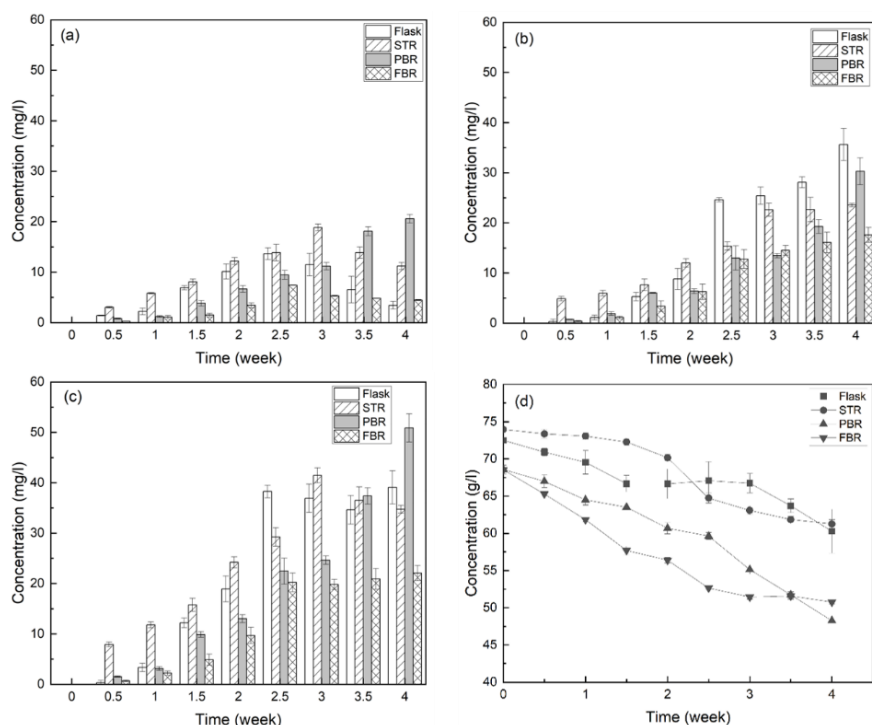


Fig. 6.3. Bioproduction and substrate consumption during 4 weeks of fungal fermentation. (a) Graph of raspberry ketone concentration versus time, (b) Graph of raspberry alcohol versus time, (c) Graph of total raspberry compounds concentration versus time, (d) Graph of glucose consumption concentration versus time to illustrate glucose consumption. STR: stirred-tank reactor, PBR: panel bioreactor, FBR: fluidized bed reactor.

6.2.3 Production of RK and RA

In this study, RK was the target product produced by submerged cultivation of *Nidula niveotomentosa*. Importantly, if the bioreactor design affects pellet morphology, the effect of these changes on RK production is merited. However, RK is an intermediary metabolite, which is subsequently fermented to RA, and thus a holistic assessment of both RK and RA (i.e., total raspberry compounds, RC) needs to be considered to fully understand the fermentation, and relevant titres, yields, and productivities are shown in [Table 6.1](#).

Table 6.1 Various yield values at endpoint in different bioreactors using glucose as substrate.

Yields	Flask	STR	PBR	FBR
Time endpoint (week)	2.5	3	4	2.5
RK (mg/l)	13.67	18.86	20.59	7.44
RA (mg/l)	24.61	22.61	30.30	12.78
RC (mg/l)	38.28	41.47	50.89	20.22
RC $Y_{P/S}$ (mg/g)	7.07	3.81	2.51	1.27
RC Vol. productivity (mg l⁻¹ day⁻¹)	2.19	1.97	1.82	1.16
RK selectivity	0.36	0.45	0.40	0.37

It can be seen that the highest titres for RK and RC were achieved by the PBR (RK=20.59 mg/l, RC= 50.89 mg/l), followed by the STR (RK=18.86 mg/l, RC= 41.47 mg/l), Flask (RK=13.67 mg/l, RC=38.28 mg/l) and FBR (RK=7.44 mg/l, RC=20.22 mg/l). As can be seen in [Fig. 6.3a](#), the maximum values for each treatment for both RK and RC were achieved simultaneously. What can also be seen is that the time to reach these values (i.e., endpoint) varied with treatment as well, wherein the flask experiments and FBR reached endpoint after 2.5 weeks, while STR stabilized at 3 weeks, with PBR showing steady production over the 4-week fermentation. Thus, while a maximum titre of 50.8 ± 2.8 mg/l of raspberry compounds (ketone and alcohol) was achieved by the PBR, maximal volumetric productivity calculated from time to endpoint was achieved by Flask (2.19 mg l⁻¹ day⁻¹), followed by STR (1.97 mg l⁻¹ day⁻¹), PBR (1.82 mg l⁻¹ day⁻¹), and FBR (1.16 mg l⁻¹ day⁻¹).

Finally, the glucose concentration profiles in Fig. 6.3d illustrated that more glucose was consumed by the floccose pellets in FBR and PBR compared to those compact pellets in flasks and STR. It should be noted there was continued decreasing glucose concentration in PBR and FBR until the end of the experiment, suggesting that RK production is not directly to glucose consumption, as it is a secondary metabolite. For instance, in the case of the flask, STR, and FBR treatment glucose consumption continued past RC endpoint. Therefore, while it is apparent that floccose pellets (in FBR and PBR) can consume more glucose, this consumption is not necessarily linked to bioproduction of the target compounds or finalized biomass.

6.2.4 Effects of pellet morphology and suspension stages

As demonstrated above, different reactor designs have clear effects on pellet morphology, and these changes in morphology in turn affect reactor performance. It is interesting to note that while the flask treatment showed the lowest titre and selectivity, it also showed the highest $Y_{P/S}$ and volumetric productivity with values of 7.07 mg/g and 2.19 ml l⁻¹ day⁻¹, respectively, shown in Table 6.1. The highest $Y_{P/S}$ was mainly due to the lowest glucose consumption, again demonstrating the independence of RC production from glucose consumption. The high productivity suggests that this form of mixing is positive for increasing the rates of RC formation. Similar to the flask treatment, STR pellets were small and compact, and showed faster rates of productivity (1.97 mg l⁻¹ day⁻¹), compared to the PBR treatment (1.82 mg l⁻¹ day⁻¹) which led to larger expanded pellets. Thus, it could be that the more vigorous mixing such as in the flask culture and STR promotes rates of production, which could be a direct impact of mixing, or the formation of smaller pellets, which could both increase mass transfer phenomena. It may equally be possible these smaller pellets and more rapid mixing may also facilitate more exposure to UV light bombardment, which is a requisite for RK formation.

Notably, the PBR required additional magnetic stirring in its design that caused pellet breakage and more turbid conditions (Fig. 6.1c). Conversely, the FBR approach generates large,

unbroken pellets, showing substantially different pellet morphology from both the flask and STR, which may aid in UV light penetrance. However, the FBR treatment performance suffered from poor pellet suspension instead of pellet compactness. Fungal pellets were observed to be fully fluidized and homogeneously suspended by the bubble flows in first two weeks, during which time the inoculated seed culture grew into pellets. From week 3, as pellets became enlarged and more hirsute, this led to insufficient upward flow from aeration, resulting in partial pellet agglomeration and sedimentation, while some pellets remained in suspension by the bubble flow. The cause for this sedimentation was because of a fixed aeration rate of 0.15 v.v.m, which was maintained to remain consistent with other reactor designs, and this flowrate became insufficient to fluidize the pellets which increased in both biomass and size. This insufficiency of aeration was more obvious in week-4 when all the pellets were settled on the bottom of column, forming a packed bed. This obviously caused a concurrent decrease in RC production, which plateaued after the RK concentration decreased from week-3 to week-4 in FBR was due to the poor mass and oxygen transfer in partially fluidized bed and packed bed regimes. It may be possible to overcome this pellet agglomeration with dynamic aeration however and achieve results similar or even improved results in comparison to a PBR design.

6.2.5 Selectivity: Raspberry Ketone vs. Raspberry Alcohol

RK and RA selectivity, as defined as the fraction of a given product over total product (e.g. [raspberry ketone] / [raspberry compounds]) during the RK-to-RA transition process in different bioreactors. Fig. 6.4 shows the graphs of the selectivity of the respective RK and RA versus time. From previous literature, the increase of RA concentration was due to the biotransformation from RK, as Zorn et al. [278] used the labeling study of ^{13}C -labeled L-phenylalanine and $[1-^{13}\text{C}]$ glucose as supplementary to detect the biotransformation from RK into RA in submerged cultivation of *Nidula niveo-tomentosa*. Their findings could also be used to explain the RK concentration change in Fig. 6.3a. It can be observed that in the flask culture

study, the proportion of RK sharply increases, followed by a strong constant decline, with a concomitant increase in RA distribution, that leads to lower selectivity (0.36). Conversely, both STR and PBR do not show a rapid transition to raspberry alcohol, showing relatively stable values after an initial rise (Fig. 6.4b). Interestingly, while the STR shows similar productivity compared to the flask culture, STR shows a stronger selectivity for RK at endpoint (i.e., 0.45). Conversely, PBR shows more consistent but lower selectivity (i.e., 0.40), matching the slower steady production of raspberry compounds observed with this system. The FBR showed selectivity of 0.37, likely due to insufficient airflow and subsequent pellet settling, as described above. It is possible that the STR and PBR showed better selectivity compared to the flask culture because the increased dissolved oxygen delivered by active aeration could favour RK over RA, but this mechanism requires further investigation.

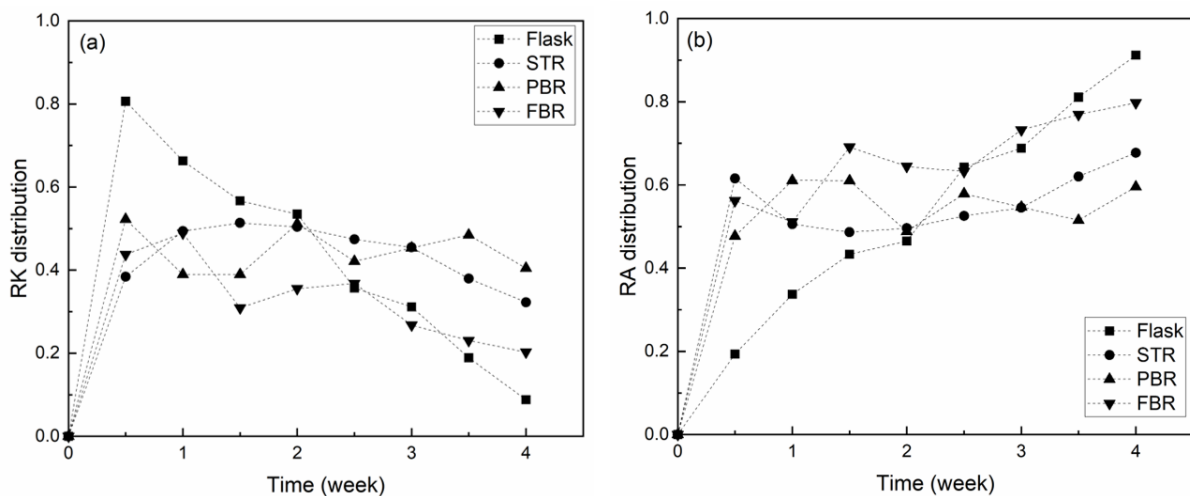


Fig. 6.4. Selectivity of RK and RA in RK-to-RA transition: (a) graph of RK distribution versus time, (b) graph of RA distribution versus time. STR: stirred-tank reactor, PBR: photobioreactor, FBR: fluidized bed reactor.

6.2.6 Challenges and prospects

It is noted that any preference in fungal morphology depends on species and targeted products. To date, the literature on RK production by *Nidula-Niveo tomentosa* were mainly conducted in flask culture. The present study compared the effects of different bioreactor systems on fungal morphology, which was linked to its bioproduction. The results indicated that the filamentous

morphology is more appropriate for long-term fermentation, as fungal fragments in PBR resulted in the continual RK increase during 4-week fermentation, while RK production in flask culture and STR rapidly accumulated within 3 weeks, thus saving fermentation time, which could have significant ramifications in operation costs. Excessive growth of free mycelia represents operational problems. For instance, the mycelia were observed to aggregate and attach in the baffles of STR, form the dead zone in vessel corners of PBR in our experiments. Other issues such as fouling of the fermenter probes, growth back along nutrient feed and sampling lines, efficiency decrease due to increased viscosity and limited mass transfer were reported by other researchers [198, 199].

Regarding the fluidized bed reactor, the main novelty is effective mixing without external application such as shaking bed or agitated impellers. Although the fungal pellets in FBR were also floccose, the decrease of RK was attributed to pellets settlement at given aeration rate from the 3rd week of fermentation. Fungal pellets were cultivated in the form of pellet fluidization by gas and/or liquid flows, in which gas flow not only expanded pellets but also provided the dissolved oxygen whilst liquid flow promoted the mass transfer and broth circulation. The main limitation of fluidized bed bioreactor, however, is that the fixed gas flowrate of 0.15 v.v.m could only maintain the fully fluidization in first 2-week of fermentation. With continual pellet size increase and biomass growth, the fully fluidized pellets gradually turned into partially fluidized bed and packed bed in the end, which accounted for RK increase in first two-week and reduction in final two-weeks. Therefore, further improvements to RK production with a FBR system could be achieved by a dynamic management of gas/liquid flowrate to avoid pellet settlement as well as pellet wash out, thus achieving a stable fluidization stage. It may be possible that this system could potentially surpass the limitations of other systems by contribution significantly more oxygen and mixing, while avoiding pellet disruption.

6.3 Conclusions

The results indicated that both agitation and aeration system influenced the pellet morphology and subsequent bioproduction instead of biomass concentration. The agitation system in STR had less effect on pellet size but changed pellet shape, while the aeration system in PBR and FBR enlarged pellet size by making pellets expanded and floccose. The higher titres of raspberry ketone (20.59 mg/l) and compounds (50.89 mg/l) were from an airlift type panel bioreactor during four weeks fermentation due to the floccose pellets and filamentous fungi, but higher volumetric productivity ($1.97 \text{ mg l}^{-1} \text{ day}^{-1}$) in STR compared to PBR ($1.82 \text{ mg l}^{-1} \text{ day}^{-1}$) suggested the compact pellets due to intensive agitation mixing led to the fast cumulation of raspberry compounds regardless of the slightly lower titres (18.86 mg/l of RK, 41.47 mg/l of RC). This study provides an experimental basis on optimizing raspberry ketone production and industrial scale-up in future.

Chapter 7 Fungal fermentation using bench-scale fluidized bed reactor

7.1 Introduction

Raspberry ketone (RK) has high commercial values in the food and healthcare industries. The research on RK production has been increasing dramatically in recent years, but mainly conducted in the flask culture with the limitations of low mass transfer, little oxygen supply and difficulties in scale-up for industrial production. On the other hand, the fluidized bed has been commonly used as a type of reactors in chemical and process industries with the advantages of minimum diffusional resistance, good heat/mass transfer and relatively low energy consumption [1]. In terms of bioengineering and bioprocessing fields, cell cultivation in the fluidized bed bioreactor is achieved in the form of cells fluidization by liquid/gas flow, thus ensuring the sufficient mass transfer rate but low shear stress compared to other types of bioreactors (e.g., stirred-tank reactor, photobioreactor, membrane bioreactor). Typically, to fluidize the microorganisms of micro-scale size and much lower density than water, the cell immobilization technologies (i.e., attachment, entrapment, self-aggregation, containment) were developed to enhance cell stability in continuous fluidization conditions [11, 12]. However, the long-term cell cultivation through the immobilized cell fluidization currently suffers from the cell detachment from carriers or cell leakage from encapsulation [12, 291]. In contrast, the fungus of *Nidula niveo-tomentosa* grow from free mycelia to mature pellets with up to centimetres-scale size and higher density than water, which means the fungal pellets can be directly fluidized and cultivated in fluidized bed bioreactor without the use of cell immobilization technologies.

In this chapter, the fungal fermentation using bench-scale fluidized bed bioreactor (described in **Chapter 3**) for RK production has been systematically investigated based on the parameters

including gas flowrate, gas sparger size, fluidization regimes. These parameters can significantly influence the hydrodynamics and operating performance of the reactor, thus determining the yield of bioproduction. By applying the fluidized bed reactor in fungal fermentation, this work is used as the early-stage screening for RK production, which addresses the development of fluidized bed techniques and gives insights to industrial scale-up in future.

7.2 Results & discussions

7.2.1 Gas flowrates

Gas flowrate is a key factor affecting bubble size and velocity to impact pellets fluidization. In these experiments, the gas sparger size was kept at 0.15 mm and the liquid flowrate was fixed at 0.25 ml/s to maintain the culture medium circulation. Meanwhile, different gas flowrates of 0.15, 0.3 and 0.45 v.v.m were studied with the gas sparger size of 0.15 mm. Fig. 7.1 shows the snapshots of fluidization regimes changes during the 4-week fungal fermentation in the condition of 0.15 v.v.m gas flowrate. Three different fluidization regimes were identified:

- *Fluidization bed regime*: Pellets were fully fluidized by the bubble flows in the first 2 weeks (Fig. 7.1 a & b).
- *Partially fluidized bed regime*: Part of the pellets were fluidized while rest of them agglomerated and settled on bottom of bed column in week 2-3 (Fig. 7.1 c).
- *Packed bed regime*: All the pellets were agglomerated and accumulated on bottom with bubble flows forming channelings through the pellets in the fourth week (Fig. 7.1 d).

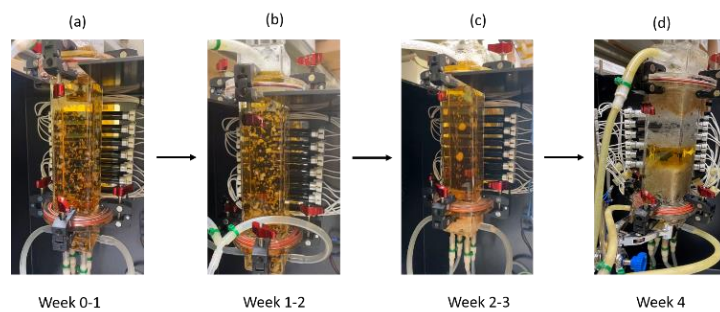


Fig. 7.1. Fluidization regimes showing the change of pellet fluidization during 4-week of fermentation. $Q_G = 0.15$ v.v.m, $d_G = 0.15$ mm. $d_B = 50$ mm.

The fluidization regimes changed from fluidized bed regimes to partially fluidized bed regimes and eventual packed bed regimes which was attributed to the pellet growth and biomass accumulation at low fluid flowrate. Namely, the initial fungi inoculum was small with low biomass weight, which was easily fluidized by the gas flows. The continued fermentation enables the free mycelia fungi (in the week - 0) to grow into mature fungal pellets (in week 1-2) with the increase of pellet numbers and weights. However, the long-term gas sparging seemed to make the pellets fluffy and hairy resulting in pellet agglomeration. The insufficient gas flowrates (0.15 – 0.45 v.v.m) failed to fluidize the big clumps, leading to the aggregated pellet settling on the bottom, forming the partially fluidized bed in week-3 and finally packed bed in week4.

Besides the effects of gas flowrates on fluidization regimes, the influences on biomass concentration were studied. As shown in [Fig. 7.2a](#), the final biomass dry weight increased to 13.3, 18.1 and 14.8 g/l with the gas flowrate of 0.15, 0.30 and 0.45 v.v.m, respectively. The lowest biomass growth in the experiments with 0.15 v.v.m was because the low gas flowrate led to the early pellets' sedimentation due to the insufficient gas flow. However, the biomass in the experiments with 0.45 v.v.m gas flowrate was lower than that in 0.30 v.v.m indicated that the much higher gas flow might cause strong shear stress on pellet growth, as higher gas flowrate led to more pellet breakage into fragments. Besides, the much higher gas flowrate was observed to wash out the fungal cells, which were attached to the top mesh screen and formed the dead zone. Therefore, an optimal gas flowrate is important to not only mitigate pellet sedimentation, but also decrease potential pellet elutriation [45].

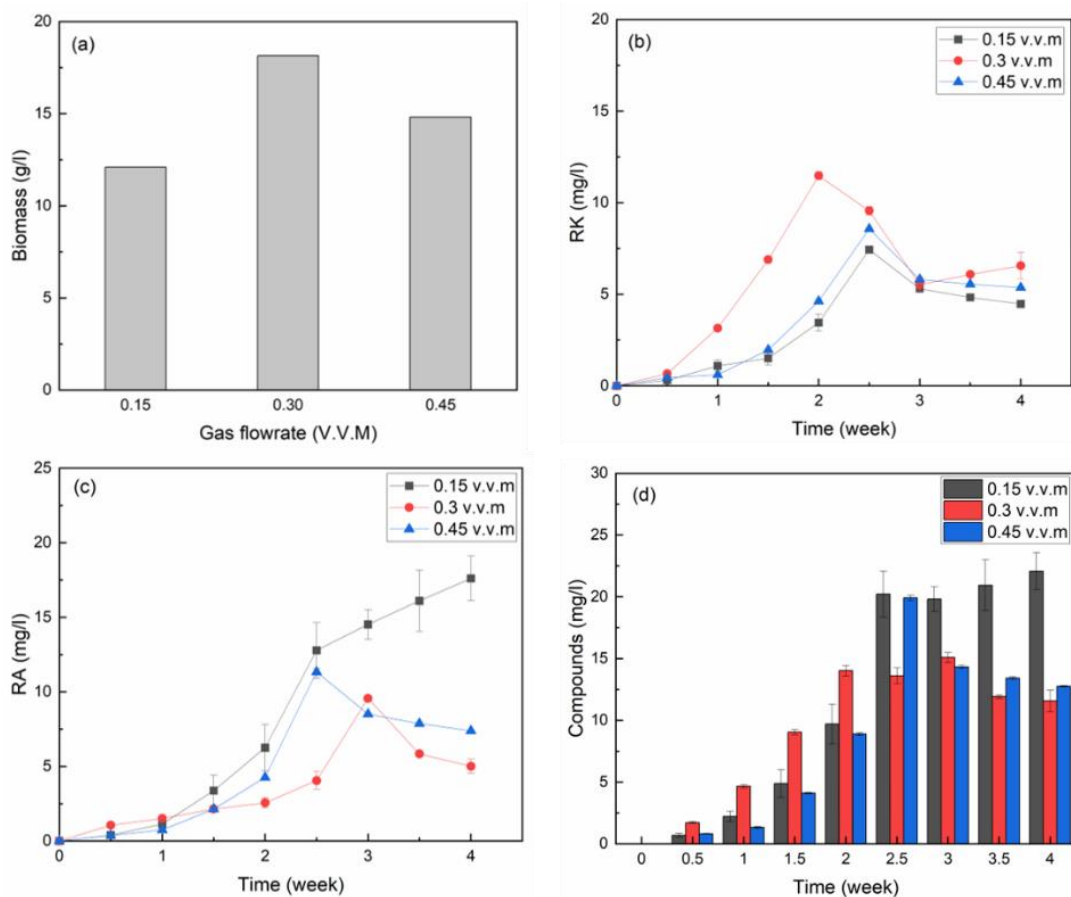


Fig. 7.2. Study of gas flowrates on fungal growth and bioproduction: (a) final biomass dry weights under different gas flowrates, (b) raspberry ketone curves during 4-weeks fermentation, (c) raspberry alcohol production during fermentation, (d) raspberry compounds accumulation during the fermentation.

The curves of RK production are presented in Fig. 7.2b, in which the RK concentration increased from 0 in week-0 to the maximum at around week-2 before their reductions. Specifically, highest detected RK concentration was for the experiments using gas flowrate of 0.3 v.v.m than in other conditions in the first 2 weeks. This can be explained that both the early pellet sedimentation at lower gas flowrate and severe pellet elutriation at higher gas flowrate reduce the production. However, the final RK concentrations were relatively close, as RK was rapidly consumed due to the poor mixing and oxygen supply in the packed bed regime occurring in all the cases in the final week of the experiments. The low mass transfer and poor gas supply led to the accumulation of RA, as oxygen is believed to delay the RK-to-RA conversion. In other words, poor gas supply will result in more RK reduction but high RA accumulation, which could be confirmed by Fig. 7.2c that the highest RA concentration was

from the condition of the lowest gas flowrate of 0.15 v.v.m. It is noticed that a slightly RA reduction for the conditions of 0.30 and 0.45 v.v.m at the end of fermentation, indicating other bioconversions involving RK and/or RA conversions were taken place at relatively higher gas flowrates, leading to compounds accumulation in 0.15 v.v.m was much higher than that in higher gas flowrate conditions (Fig. 7.2d). In summary, the fixed gas flowrate ranging from 0.15 to 0.45 v.v.m with 0.15 mm gas sparger ID cannot provide the complete pellet fluidization throughout the 4-week fermentation due to the small bubble size and increased pellet biomass. The optimal gas flowrate of 0.30 v.v.m not only showed higher mass transfer and gas supply compared to 0.15 v.v.m gas flow but also mitigated pellet elutriation compared to higher gas flowrate, thus leading to higher biomass accumulation and RK synthesis.

7.2.2 Gas sparger size

To study the parameter of gas sparger size (0.15 mm, 0.8 mm and 1.2 mm ID, respectively), gas flowrate was kept at 0.3 v.v.m and liquid flowrate at 0.25 ml/s. The bubble size increased with increasing gas sparger size [292], while the bubble flow numbers were observed to decrease with increasing gas orifice size. This was attributed to the reduction of gas force, as the increase of gas orifice increased gas/liquid contact area but decreased gas pressure, bubbles cannot form and detach when gas pressure around the gas nozzle was lower than the liquid pressure. In this study, the bubble flow numbers were 4, 3 and 1 when gas orifice size was 0.15, 0.8 and 1.2 mm, respectively, although the FBR was equipped with 4 gas spargers. The fluidization regime with 0.15 mm sparger started from the fully fluidized bed in the first two weeks, followed by the partially fluidized bed in the third week and the packed bed in the last week, while the fluidization regime remained in the fully fluidized regime with 0.8 mm and 1.2 mm gas sparger size during the whole 4-week fermentation experiments. The main difference of the fully fluidized regimes between using 0.8 mm and 1.2 mm gas sparger was that less pellet agglomeration formed for the condition of 0.8 mm sparger size, where 3 bubble

flows promoted pellet mixing to mitigate pellet clumps. The biomass growth in Fig. 7.3a shows higher biomass concentration was achieved using 0.15 mm ID sparger, in which the partially fluidized bed in week-3 and packed bed in week-4 avoided pellet elutriation compared to the throughout fully fluidized bed regime when using 0.8 mm and 1.2 mm gas spargers.

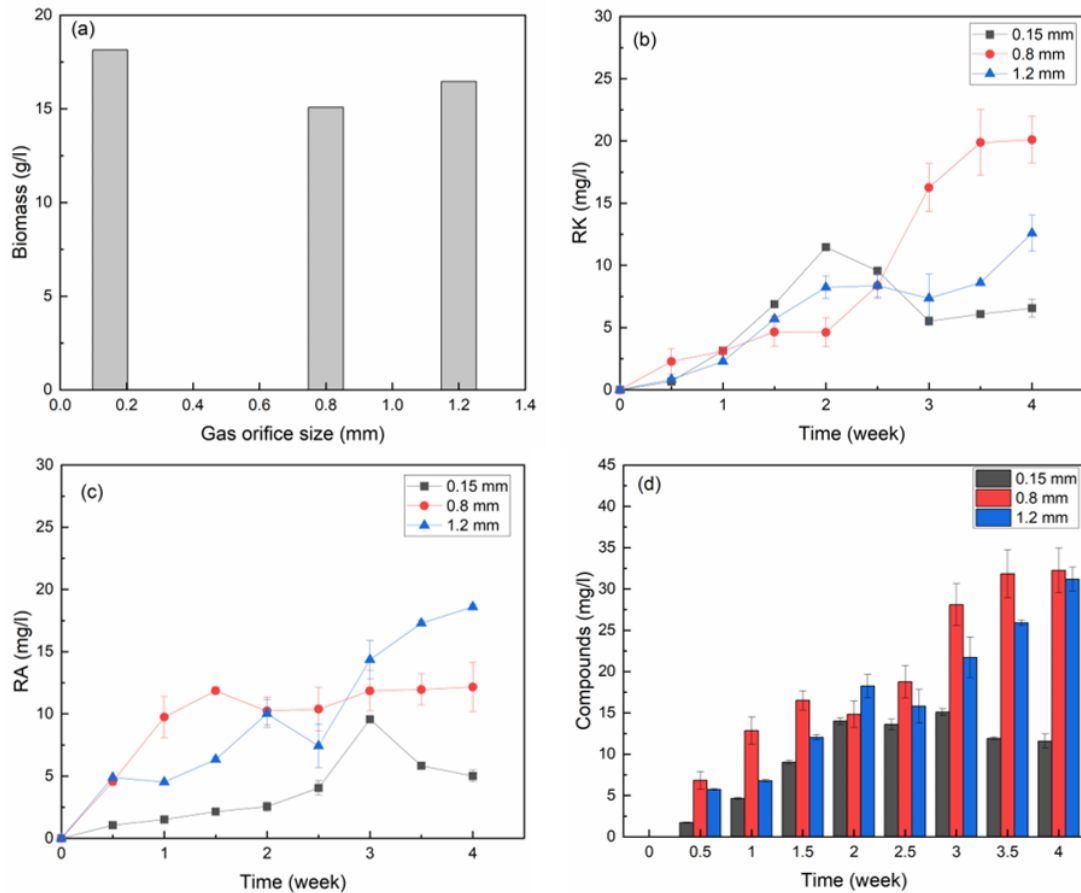


Fig. 7.3. Effects of gas sparger size on fungal growth and bioproduction: (a) final biomass dry weights under different gas orifice sizes, (b) raspberry ketone curves during 4-weeks fermentation, (c) raspberry alcohol production during fermentation, (d) raspberry compounds accumulation during the fermentation.

The RK synthesis in Fig. 7.3b indicates that RK increased in the first two weeks and then gradually decreased for 0.15 mm gas sparger, while in the case of 0.8 mm and 1.2 mm spargers RK kept increasing during the whole 4 weeks of fermentations. The decrease of RK in the case of 0.15 mm sparger was due to the gradual pellet sedimentation from the second week of fermentation. Instead, the continuously increased RK concentration with larger gas spargers can be attributed to the good mass transfer and gas supply in the fully fluidized bed. On the other hand, the higher RK concentration in the case of 0.8 mm sparger than that in 1.2 mm

sparger revealed that the more efficient pellet mixing with less aggregation by 3 bubble flows could enhance RK production. For RA conversions, higher RA was from 0.8 mm and 1.2 mm spargers with the fully fluidized bed regime than from the packed bed regime presented in the 0.15 mm sparger situation, which confirmed the intensification of mass transfer and gas supply due to good pellet fluidization. However, the highest RA was from 1.2 mm sparger and not from 0.8 mm sparger, which was inconsistent with the results in RK production as shown in [Fig. 7.3c](#). One possible explanation is that the one bubble flow in the fluidized bed with 1.2 mm sparger induced poor gas and oxygen compared to the three bubble flows of 0.8 mm gas sparger. It was reported that the low dissolved oxygen promoted RK-to-RA conversion [7]. Despite the difference in RK and RA concentration, the compound concentrations between the conditions of 0.8 mm and 1.2 mm spargers were similar ([Fig. 7.3d](#)). Therefore, the number of bubble flows can only alter RK and RA yields but has little effect on overall raspberry compounds. Thus, by studying the effects of gas sparger size, it is concluded that the fully pellet fluidization regime with more bubble flows is a good strategy to promote mass transfer and gas supply for higher RK synthesis, although the fully fluidized bed regime will not alter overall fungal productivity.

7.2.3 Minimum fluidization operation using increasing gas flowrate

Based on the study of gas flowrates and sparger size, the results indicated that the fully fluidization is important to promise sufficient mass transfer and gas supply, thus improving fungal production. In this section, the continually increased gas flowrate with different gas orifice sizes was applied, thus ensuring the fungal pellets whose biomass kept increasing during fermentation could be fully fluidized. Besides, to avoid pellet elutriation, the gas flowrate was adjusted accordingly to maintain the condition just above to the minimum fluidization of pellets [22, 48]. [Fig. 7.4](#) presents the snapshots of pellet fluidization performance under minimum fluidization operations by the end of fermentation with different gas orifice size. In previous

studies with the fixed gas flowrate of 0.3 v.v.m, pellet fluidization regime changed from fully packed bed to partially fluidized bed and final packed bed regime when gas sparger size was 0.15mm with fungi growth. Here no packed bed was observed with increasing gas flowrate in the case of 0.15 mm sparger, which exhibited the enhancement of gas flow on pellet fluidization. Yet, the continually increased gas flowrate was unable to maintain the complete pellet fluidization by the end of fermentation, as a small number of pellets aggregated and attached on the corner of the bed wall (Fig. 7.4a). The inevitable pellet aggregation and attachment on the bed wall means that the smaller bubbles generated from the spargers of 0.15 mm ID were too small to completely suspend pellets in the fluidized state. When gas orifice size was increased to 0.8 mm and 1.2 mm, the whole pellets were successfully suspended by the bubble flows (Fig. 7.4b & c). Besides, compared to the fixed gas flowrate of 0.3 v.v.m, the minimum fluidization state due to continually increased gas flowrates led to fewer pellet aggregations. The specific gas flowrates values which support pellet fluidization were plotted in Fig. 7.5a. Higher gas velocities were required for smaller sparger sizes starting from day 5 when pellets were formed, the overall gas flowrate for the smallest gas spargers was higher throughout the whole experiments. The difference between 0.8 mm and 1.2 mm spargers were much smaller and up to day 21/22 (week 3) slightly higher velocities were needed for 0.8 mm to maintain fluidization, indicating that the bigger bubbles due to bigger gas sparger promoted pellet fluidization. However, in the final week (7-8 days) this was reversed and slightly lower velocities were needed for 0.8 mm sparger, because the 3 bubble flows in case of 0.8 mm spargers presented better mixing and fluidization properties than 1 bubble flow in the case of 1.2 mm sparger size, especially in situations where pellets are bigger, floccose and partially agglomerated.

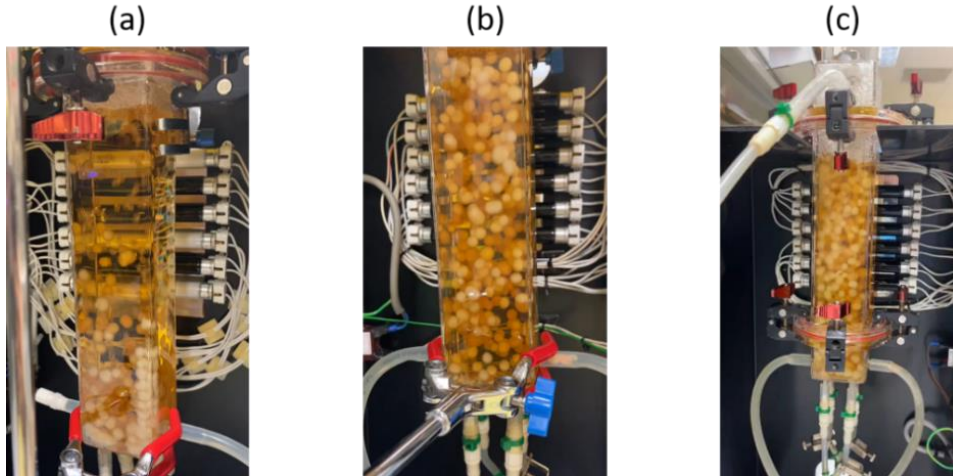


Fig. 7.4. Snapshots of fungal fermentation in last week under minimum fluidization regime by increased gas flowrate with different gas orifice size. (a). 0.15 mm gas sparger; (b). 0.8 mm gas sparger; (c). 1.2 mm gas sparger. $d_B = 50$ mm.

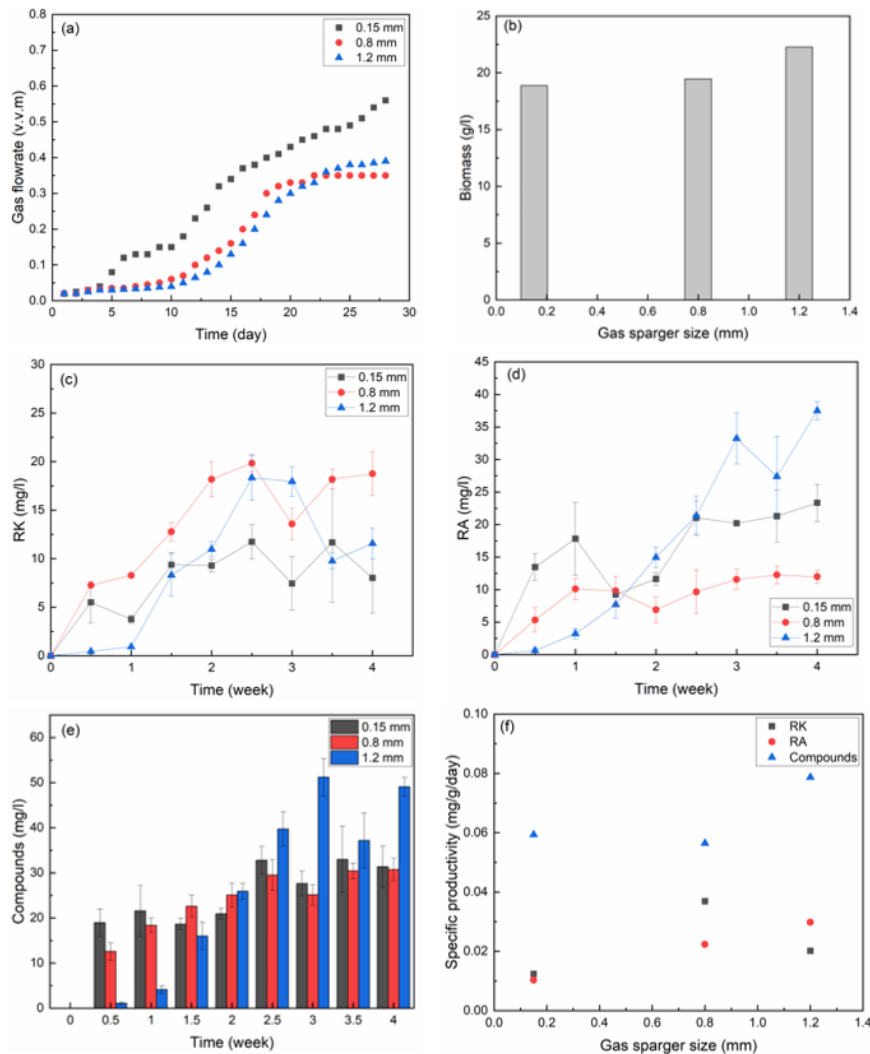


Fig. 7.5. Study of the minimum fluidization state operations with different gas orifice sizes on fungal fermentation: (a) Profiles of minimum gas flowrates to fluidize pellets during the fermentations, (b) final biomass dry weights for each gas sparger size under minimum fluidization condition, (c) RK concentration profiles for each gas sparger size under minimum fluidization condition, (d) RA conversions for each gas sparger size under minimum fluidization condition, (e) RC accumulation for each gas sparger size under minimum fluidization condition, (f) average specific productivities for RK, RA and compounds under minimum fluidization state.

Fig. 7.5b shows the final biomass dry weights of fungal pellets for different gas sparger sizes operating under a minimum fluidization state. The close values of biomass dry weights indicated the gas orifice size had little effects on fungal growth if pellets could be well fluidized. In contrast, the different RK curves exhibited the impact of different gas sparger sizes on fungal production. Fig. 7.5c presents the RK concentration profiles for 0.15 mm and 0.8 mm gas spargers increased to the maximums in the first two weeks and then maintained the maximal values until the end of fermentation, which suggested that the fully fluidization regime could promote RK synthesis due to sufficient pellet mixing. However, a slight RK reduction was observed in the case of 1.2 mm sparger although the pellets were fully fluidized. The RK reduction might be explained by the gas supply with 1.2 mm spargers in the FBR, where only one bubble flow was spouted due to low gas pressure with larger spargers. The dissolved oxygen in FBR with only one bubble flow was much lower than that with multiple bubble flows. Therefore, it is highly recommended to not only maintain a fully fluidization regime to improve mass transfer but also introduce more bubble flows to increase dissolved oxygen. The low dissolved oxygen supply in FBR with one bubble flow could be confirmed by the RA production in Fig. 7.5d, in which the highest RA concentration was from the 1.2 mm gas sparger condition, because the high RA concentration was obtained due to the RK-to-RA conversion at low oxygen supply. Meanwhile, similar compounds concentration for both 0.15 mm and 0.8-mm spargers but larger compounds in 1.2 mm spargers demonstrated the unknown bioconversions involving the consumption of RK and RA when dissolved oxygen is sufficient during the fermentation (Fig. 7.5e).

Finally, the results of specific productivity for RK, RA and compounds for 3 different gas spargers are plotted in Fig. 7.5f. The highest specific productivity of RK was achieved using 0.8 mm gas sparger, while the 1.2 mm gas sparger resulted in the highest specific productivities of RA and raspberry compounds. As described above, the fully fluidization state with multiple

bubbles flows in the case of 0.8 mm gas spargers not only promoted mass transfer but also promised oxygen supply, leading to higher RK productivity. However, the one bubble flow with 1.2 mm gas spargers caused low oxygen supply, which suppressed RK production but enhanced the RK-to-RA conversion. In summary, by studying the fluidization stages under different gas sparger sizes, it is concluded that the fully fluidization regime can provide good mass transfer and subsequent fungal growth, but the higher dissolved oxygen due to multiple gas flows is another important factor to improve RK synthesis.

7.2.4 Optimized conditions

This section adopted the optimal cultivation conditions based on the flask cultures (described in Chapter 5) and the optimized operating parameters from fluidized bed reactor system study described above, to investigate and maximize the RK concentration in FBR. The details of the adopted cultivation conditions are listed in [Table 7.1](#). For instance, the gas orifice size of 0.8 mm was used for multiple bubbles flows, thus improving dissolved oxygen. The gradually increased gas flowrate was used to maintain a minimum fluidization stage which promised the fully fluidization regime with less pellet elutriation.

Table 7.1 Details of the optimal cultivation parameter adopted in fluidized bed reactor system.

Optimized conditions		
Cultivation parameters	Glucose concentration (g/l)	75
	Fungi preservation method	Freezer stock
	Seed culture age (week)	2
	Inoculum concentration	40%, ~1.36 g/l
	UV-A radiation time (hour per day)	10
	Phenylalanine concentration (g/l)	2.5
Operating parameters	Gas orifice size (mm)	0.8
	Gas flowrate	Continually increasing to maintain minimum fluidization stage
	Liquid flowrate (ml/s)	~0.24

However, under the optimal fluidization conditions, fungal fermentation in FBR exhibited very different fluidization behaviours to the ones described above. At the beginning of the

fermentation, the homogenized inoculum (in the form of free mycelia) was partially agglomerated due to high inoculum concentration, the aggregation of free mycelia increased with the fermentation from Day 1 to Day 3 (Fig. 7.6a & b). Note, the nutrient recirculation was supplied after Day 3, which allowed the pellet formation in the first three days since they were inoculated in FBR. With the recirculation of culture medium from Day 3, the liquid-solid-gas FBR enabled to fully fluidize the fungal pellets with minimum pellet aggregation (Fig. 7.6c). This fully fluidized bed regime turned into a partially fluidized bed regime with the growth of fungal pellets, which grew into bigger pellets during fungal fermentation (Fig. 7.6d). Besides, due to the interaction between bubbles, pellets became more floccose and caused more pellets aggregation in the form of clumps. The big fungal clumps sedimented on the bottom were in a packed bed regime, while the rest of the dispersed pellets suspended by gas flows were in the fluidized bed regime. Furthermore, the packed bed regime increased but the fluidized bed regime decreased with the further formation of pellet clumps, which could be reflected by the increased height of packed bed while at the same time of fluidized pellets decreased, as can be seen in Fig. 7.6c to Fig. 7.6f. The further influence of bubble movements with increased gas flowrates was observed to cause pellet breakage into free mycelia, which accelerated pellet agglomeration and subsequent sedimentation, leading to the fully packed bed regime operation as shown in Fig. 7.6g. In the packed bed regime, the gas flows could pass through the porous space of the packed pellets, forming the gas channels. Nevertheless, the voidage of packed pellets decreased under gravity, which meant the porous pellets bed became more compact. The compact pellets bed would block the gas channels, thereby resulting in gas accumulation under the pellets bed. The accumulated gas could float the pellets bed to the top of the bed column and terminate the fermentation, which occurred on Day 17 of our experiments, as illustrated in Fig. 7.6h.

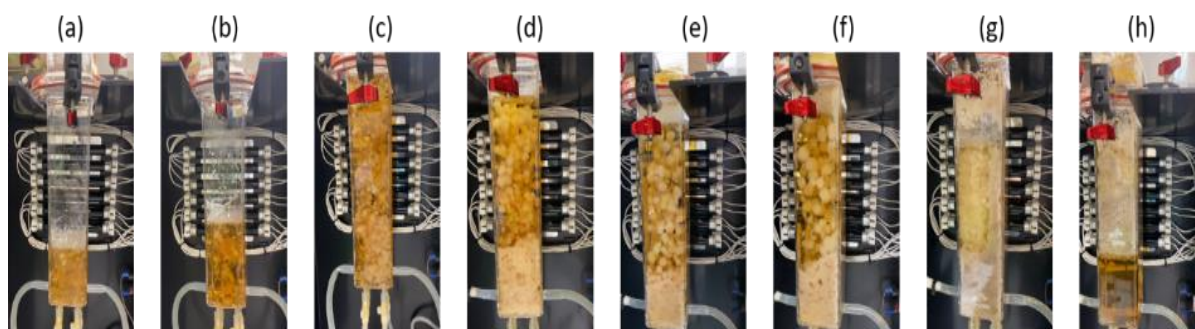


Fig. 7.6. Snapshots show fungal fluidization regimes changes under optimized cultivation conditions during fungal fermentation: (a) Day 1, (b) Day 3, (c) Day 5, (d) Day 7, (e) Day 10, (f) Day 13, (g) Day 15, (h) Day 17. $d_B = 50$ mm.

During 17 days of fermentation under optimal cultivation conditions, the final biomass dry weight increased up to 28.7 g/l, which increased by 56 % compared to the normal value of ~18 g/l in previous FBR studies. Meanwhile, the phenylalanine concentration decreased from ~2500 g/l to 85 mg/l, glucose was consumed up to 67.6%. The fast increase of biomass dry weight with largely consumed nutrients and precursors indicated the adopted cultivation conditions were an effective strategy for fungal growth. More importantly, the drastic increase of RK concentration confirmed the optimal parameters are better for RK synthesis in FBR, as illustrated in Fig. 7.7.

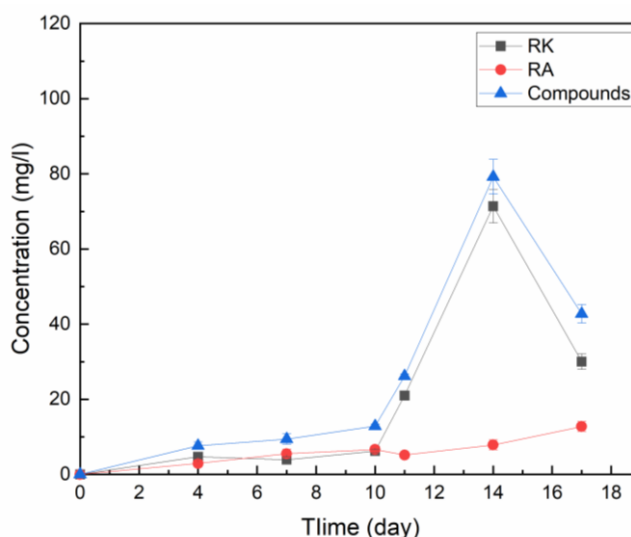


Fig. 7.7. Bioproduction of RK, RA and compounds in FBR under optimized cultivation parameters.

The RK curves increased from day 1 to the maximum value of 71.4 mg/l at day 14, followed by the RK decrease. The increase of RK concentration in the first two weeks was due to the

good fluidization performance with sufficient dissolved oxygen supply, while its reduction occurred at day 14 corresponding to the fluidization regime transition point when partially fluidized bed regime was turned into the packed bed regime (Fig. 7.6f & g). Both mass transfer and gas supply in packed bed regime was limited for RK production. Compared to the maximum values of less than 20 mg/l in the conditions of fixed gas flowrates and gas sparger sizes (Fig. 7.2b & Fig. 7.3b), the optimized conditions led to the 4-fold higher RK production, indicating the importance and effectiveness of optimizing the operating conditions in FBR. However, in **Chapter 5** the maximum RK in the flasks culture with optimized cultivation parameters reached 154.35 mg/l, which is twice higher than the RK production using FBR in the optimized operating conditions. This was mainly due to the difference of pellet morphology, as free mycelial fungi in flasks promoted nutrient intake and product release, but they could result in aggregation and/or elutriation in FBR and subsequently cause a low RK production.

On the other hand, the RA concentration maintained at a very low level in fully and partially fluidized bed regime, which also indicated the suppressed RK-to-RA conversions due to sufficient gas supply. RA started to grow up only when the packed bed regime formed on Day 14. Finally, the compounds curve was highly consistent with that of RK, showing the RK synthesis rather than RA conversion was the predominant bioactivity under optimized FBR fermentation conditions.

7.3 Conclusion

In this chapter, the effects of operating parameters in FBR such as gas flowrate, gas orifice size and pellet fluidization states on fungal fermentation and its bioproduction were systematically investigated in the FBR system. The results indicated that the smaller gas orifice size led to higher gas pressure, which allowed the multiple bubble flows to sparge from gas inlets to improve gas supply. However, the tiny gas sparger size limited bubble size, as the smaller bubbles was insufficient to suspend pellets and caused pellet sedimentation, thus hindering RK

synthesis. The gas flowrate was another key parameter, as a higher gas flowrate promoted the mass transfer and gas supply but also decreased pellet agglomeration, thus enhancing RK production. However, the high gas flowrate may cause pellet elutriation and subsequently lower the efficiency of fungal fermentation. Therefore, the optimization of both gas flowrate and gas orifice size is important for fungal fermentation in FBR. Finally, by adopting the optimal parameters of cultivation based on flask culture and FBR studies, a maximum RK concentration of 71.4 mg/l was achieved. This demonstrated a 14-fold increase in RK compared to the reported values of around 5 mg/l by submerged flask culture of *Nidula nevio-tomentosa* in the literatures [3, 10], thus confirming the effectiveness of the optimized cultivation conditions. Besides, the good performance of FBR in RK production also exhibited the huge potential of FBR system for future industrial-scale fungal fermentation.

Chapter 8 Conclusions and future work

8.1 Conclusions

RK is an expensive ingredient widely used food flavour and healthcare industry, but the low production of natural RK limits its development. Therefore, the overall objective of this study is to evaluate and optimize the production of raspberry ketone (RK) by the *Nidula niveo-tomentosa* fungus in a fluidized bed reactor system. Four specific aims were implemented to guide the objective: (I). Design and prototyping of a novel micro-fluidized bed (MFB) by 3D-printing technique; (II). Evaluating the performance of the MFB by studying the liquid-gas and liquid-solid-gas hydrodynamic characteristics; (III). Investigating the cultivation parameters and comparing the performance of different bioreactors for fungal fermentation and production; (IV). Investigating the bench-scale fluidized bed reactor for fungal fermentation and raspberry ketone production.

In the following sections, the main research outcomes from this project are summarized:

8.1.1 Micro-fluidized bed techniques

8.1.1.1 MFB design and fabrication

A prototype of the MFB has been produced with the following main features. The MFB comprises of two main sections: the lower section containing liquid/gas inlets and distribution plate and upper bed column section. In general, the lower section is a square manifold (15 x 15 mm in cross section, 5 mm in height) with an 8 x 8 hole array (size of hole: 1 x 1 mm), which is used for the liquid distributor. Meanwhile, the single gas sparger is a hole drilled at the centre of distributor, to accommodate a tight-fitting glass capillary tubing (CM Scientific, UK) with ~ 3 mm OD and micrometre-scale ID. The upper and lower sections are assembled by the flat flange plates, which featured a circular groove fitted with an O-ring rubber gasket (to prevent liquid/gas leakage) as well as 4 holes (for bolts).

8.1.1.2 Liquid-gas systems

When running fluid through the MFB, bubble flow regimes including mono-dispersed homogeneous regime, poly-dispersed homogeneous regime, transition bubble regime and heterogeneous bubble regime were identified. It was observed that bubble size primarily increased with increasing orifice diameter and gas flowrate but slightly decreased with co-current liquid flow, which accelerated bubble detachment to inhibit bubble growth. Bubble velocity increased with the increase of gas flowrate as well as the upward liquid flow, but the increase from liquid flow was insignificant in heterogeneous bubble regime. Gas volume fraction was increased with gas flowrate and decreased with gas sparger size. However, gas volume fraction did not change with increasing liquid flowrate.

8.1.1.3 Pellet fluidizations

Using the following pellet mass of 0.5 g, 1.0 g and 1.5 g, the corresponding static bed voidage ϵ_0 of fungal pellets was characterized to be 0.634, 0.618 and 0.577, respectively. Compaction of pellets due to increase weight of packing might be the main reason for the trend as the lowest value of the voidage was observed for the highest mass. The values were larger than the conventional value of 0.4 as reported in previous studies. The fungal pellets and the hyphae on the surface of pellets enlarged the empty space between pellets, resulting in higher static bed voidage.

Fluidization regimes in liquid-solid fluidization system have been observed and these regimes corresponded to static bed, expanded bed, partially fluidized bed and fully fluidized bed. Because of the agglomeration effect of fungal cells, the pellet-filled packed bed could not be transformed into a fluidized bed during the fluidization process. However, the bed was observed to expand and inter-connected branching filaments appeared throughout the whole bed when the liquid velocity was low. As the liquid velocity increased, the fungal pellets were gradually dispersed and fluidized, reached the fully fluidized bed regime where all the pellets

were fluidized along the column by the high liquid flowrate. The increased minimum fluidization velocity with increasing pellet mass also confirmed the influence of the interconnected hyphae on fluidization performance.

In the process of gas-liquid-solid fluidization, the fluidization regime maps revealed changes in the packed-bed regime, fluidization regime and elutriation regime with increasing liquid/gas flowrate. It was noticed that gas flow could promote pellet fluidization as well as reduce the pellet aggregation. With the use of PIVlab, both radial and axial velocity were observed to decrease with increasing biomass at given gas flowrate. Axial velocity was influenced by the vertical gas flow, while radial velocity was independent of gas flow but dominated by vortices and pellet surface force.

8.1.2 Fungal fermentation study

8.1.2.1 Optimization of cultivation parameters for flask culture

A suitable glucose and phenylalanine concentration can not only promise the substrates supply but also reduce substrates stress. UV-A radiation has little effects on biomass growth but can stimulate the synthesis of RK, but the long exposition time could inhibit RK production. Besides, a younger seed culture presented higher specific productivity, but the older seed culture led to higher RK production due to higher inoculum concentration in old seed culture. Compared to fungal pellets, the mycelial fungi enhanced RK production as the mycelia is easier for nutrients intake and bioproducts transportation. By optimizing the cultivation parameters in flask culture, the maximum yield of RK achieved was 154.35 mg/l. This demonstrated the great potential of the fungal fermentation of *Nidula niveo-tomentosa* in production of natural RK.

8.1.2.2 Fungal fermentation using different bench-top bioreactors

In this study, the pellet morphology and RK production were investigated in the following lab-scale bioreactor systems, namely flask culture, stirred-tank reactor (STR), photobioreactor

(PBR) and fluidized bed reactor (FBR). The effects of main operating parameters including agitation speed (300 rpm) in STR, and aeration (0.15 V.V.M) in STR, PBR and FBR were related to the pellet size and sphericity, final biomass concentration, RK and compounds production. The results indicated that the agitation system in STR altered pellet shape but had little influence on pellet size. However, the aeration system in PBR and FBR enlarged pellet size and resulted in floccose pellets. Yet, the different bioreactors had no significant impact on fungal biomass. RK rapidly increased to maximum values in flask and STR within 3 weeks before its decrease, while ketone in PBR and FBR continued to increase during the fermentation period, indicating the floccose pellets were better for long-term fermentation than compact pellets. The highest yield of RK (26.8 mg/L) and an overall compound (57.4 mg/L) were observed in PBR, suggesting the floccose pellets from these filamentous fungi promote RK production.

8.1.2.3 Fungal fermentation using bench-scale fluidized bed reactor

The fungal fermentation and its bioproduction was systematically investigated in the FBR system. The result indicated that the operating parameters in FBR such as gas flowrate, gas orifice size and pellet fluidization regimes can strongly affect RK production. The gas flow not only expanded the fungal pellets to improve the mixing effects but also provided the dissolved oxygen for fungal growth. The size of gas spargers regulated bubble size. Overall, this helped to control the fluidization performance by bubble flows. A good pellet fluidization regime avoided pellet sedimentation or elutriation, thus maintaining a good fluidization stage and subsequent RK productivity. By adopting the optimal parameters of cultivation based on flask culture and FBR studies, a maximum RK concentration of 71.4 mg/l was achieved, which confirmed the effectiveness of the optimized cultivation conditions. Besides, the good results also exhibited the huge potential of FBR system for future industrial-scale fungal fermentation.

8.2 Future work

The pellets fluidization study conducted in MFB showed that pellets could be well fluidized in the liquid-solid and liquid-solid gas systems. This suggests the potential of fungal fermentation using fluidized bed bioreactors. As a proof-of-concept, the MFB was fabricated primarily from resin using a benchtop 3D printer. Unfortunately, the resin-based MFB was not suitable for autoclaving as it could not withstand high temperatures. Therefore, it is anticipated that future developmental study of FBR made from more robust materials (i.e., quartz, steel) can meet the demands of autoclave, but the prices of these materials might be another issue.

In addition, the main limit of pellets fluidization study is that pellets used in the experiments had a fixed biomass and uniform size around 2mm while in real fungal fermentation pellets can grow up with bigger size and more biomass. Thus, continuous adjustment of gas/liquid flowrate is required to maintain a good fluidization state in real long-term fungal fermentation. Besides, a systematic study of optimizing the fluidized bed geometry (i.e., column size and height) will be the alternative research direction in future.

The characterization of the effects of cultivation parameters' impacts on RK production in flask cultures have identified the optimal values of glucose and phenylalanine concentration, UV exposure time, seed culture preservation, concentration and age for maximizing the RK yield. The combinations of the optimal parameters enabled the maximum RK concentration to reach 154.4 mg/l. However, the RK-to-RA conversion during fungal fermentation would also consume a proportion of the produced RK. Therefore, it is important to find more effective methods that can minimize the RK consumption. One of the promising approaches is to use the ISPR method which can absorb the RK from cultivation medium and extracts it in the downstream processes, thus avoiding the consumption of RK and obtaining the purified products. Therefore, further study of the ISPR method as well as other potential methods will be conducted to explore how these could improve the RK production from fungal fermentation.

The fungal fermentation and its bioproduction was systematically investigated in the FBR system. The result indicated that the operating parameters in FBR such as gas flowrate, gas orifice size and pellet fluidization regimes can strongly affect the RK production. The smaller gas orifice size induces higher gas pressure, which allows the multiple bubble flows to sparge from gas inlets to improve gas supply. However, the tiny gas sparger size resulted in small bubble size, which were unable to suspend pellets and caused pellet sedimentation. Consequently, this hindered the RK synthesis. The gas flowrate is another key parameter affecting RK production. It is observed that higher gas flowrate can promote mass transfer and decrease pellet agglomeration; higher mass transfer and gas supply, and lower pellet agglomeration could enhance RK production. However, the high gas flowrate may cause pellet elutriation and reduce the efficiency of fungal fermentation. Therefore, it is envisaged that the optimization of gas flowrate and gas orifice size of fluidized bed reactor for fungal fermentation are important topics for future studies.

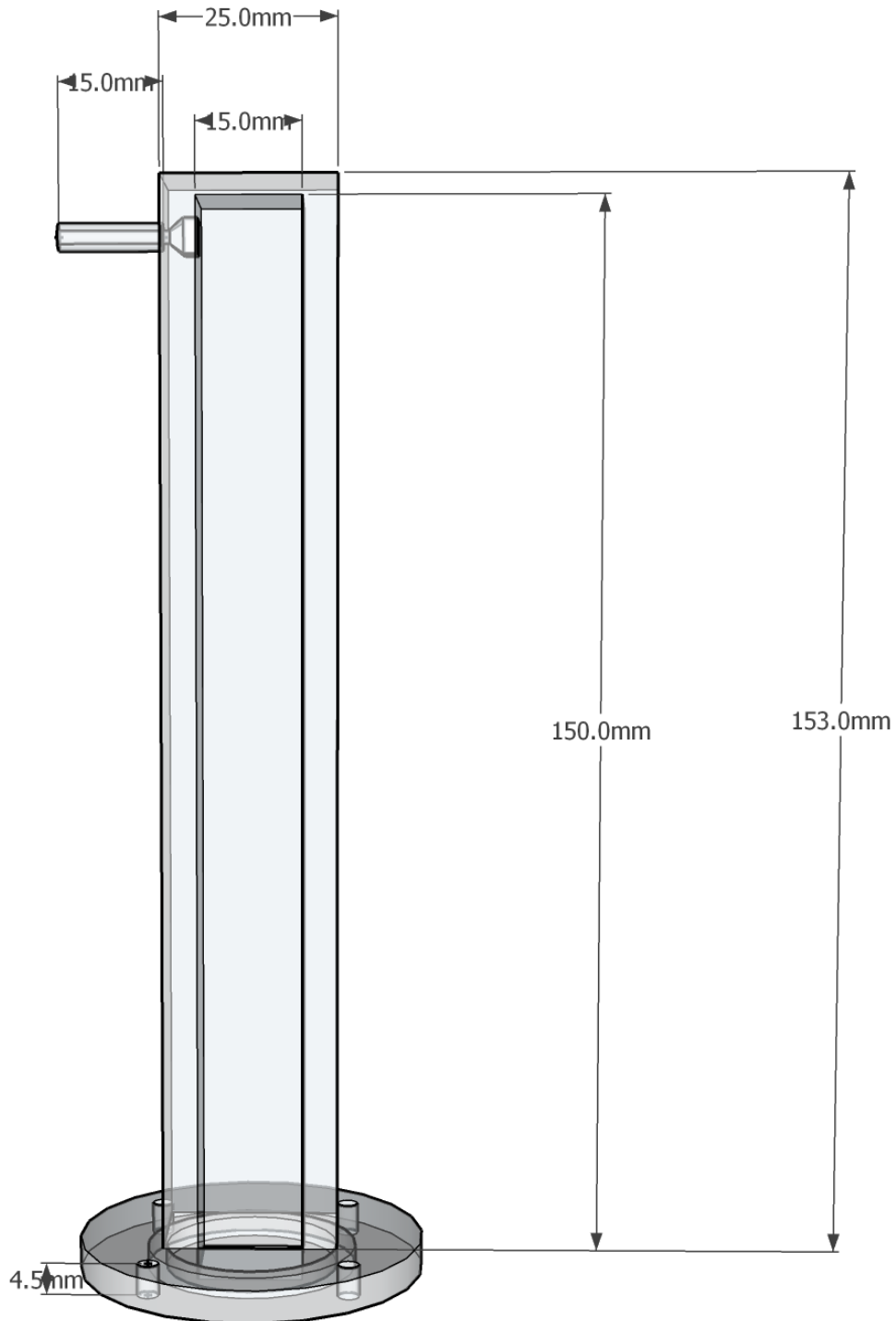
Finally, the bench-scale fluidized bed reactor identified the successful fungal fermentation and good RK production, which indicates the potential of using FBR for industrial RK production. Atypical method of using small-scale reactors for industrial production is by putting many small reactors in parallel to boost the yield of target products. However, to achieve the large scale-up, there are still many things to do. For instance, the automotive adjustment of gas/liquid flow are required to maintain the good fluidization state, otherwise, fungal pellets could be settled on bottom or elutriated to the top of reactor. Besides, an effective RK extraction method is also highly important, which can continuously collect the RK from the bioreactor, thus minimizing the substrate inhibition. Therefore, it is believed that the scale-up production of RK can be successful if the associated techniques could be reached.

Appendices

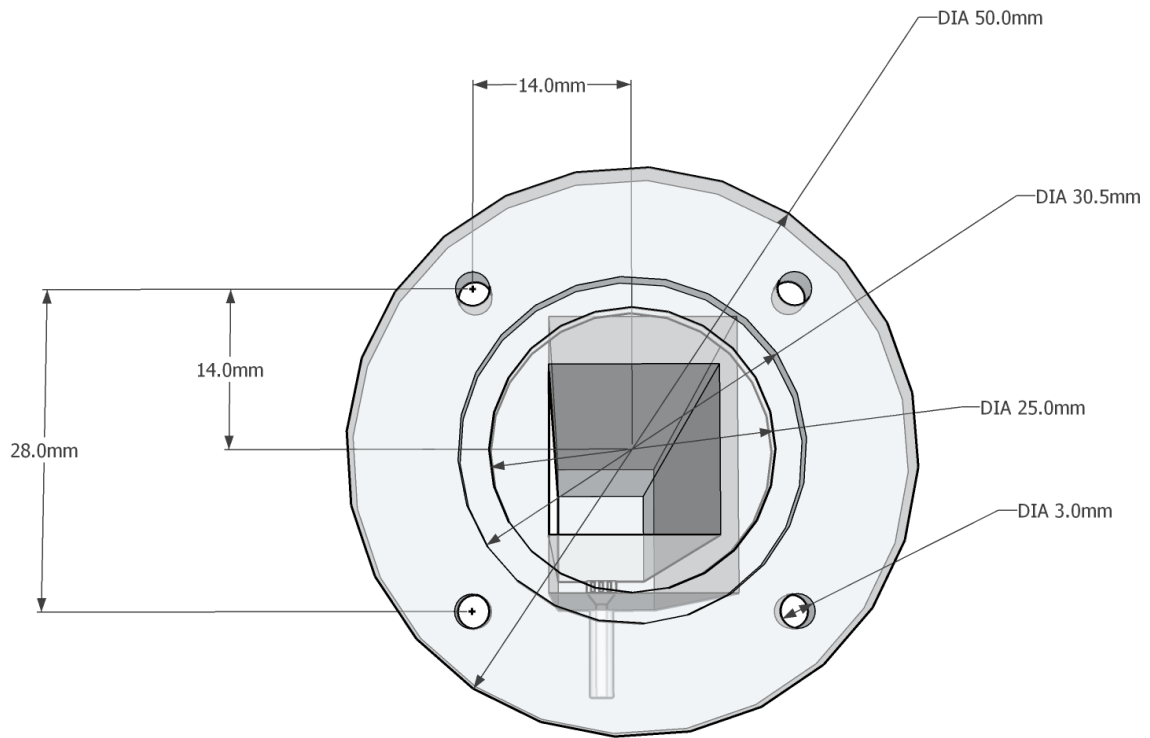
Appendix A: Micro-fluidized bed geometry with dimensions

A.1. Upper part

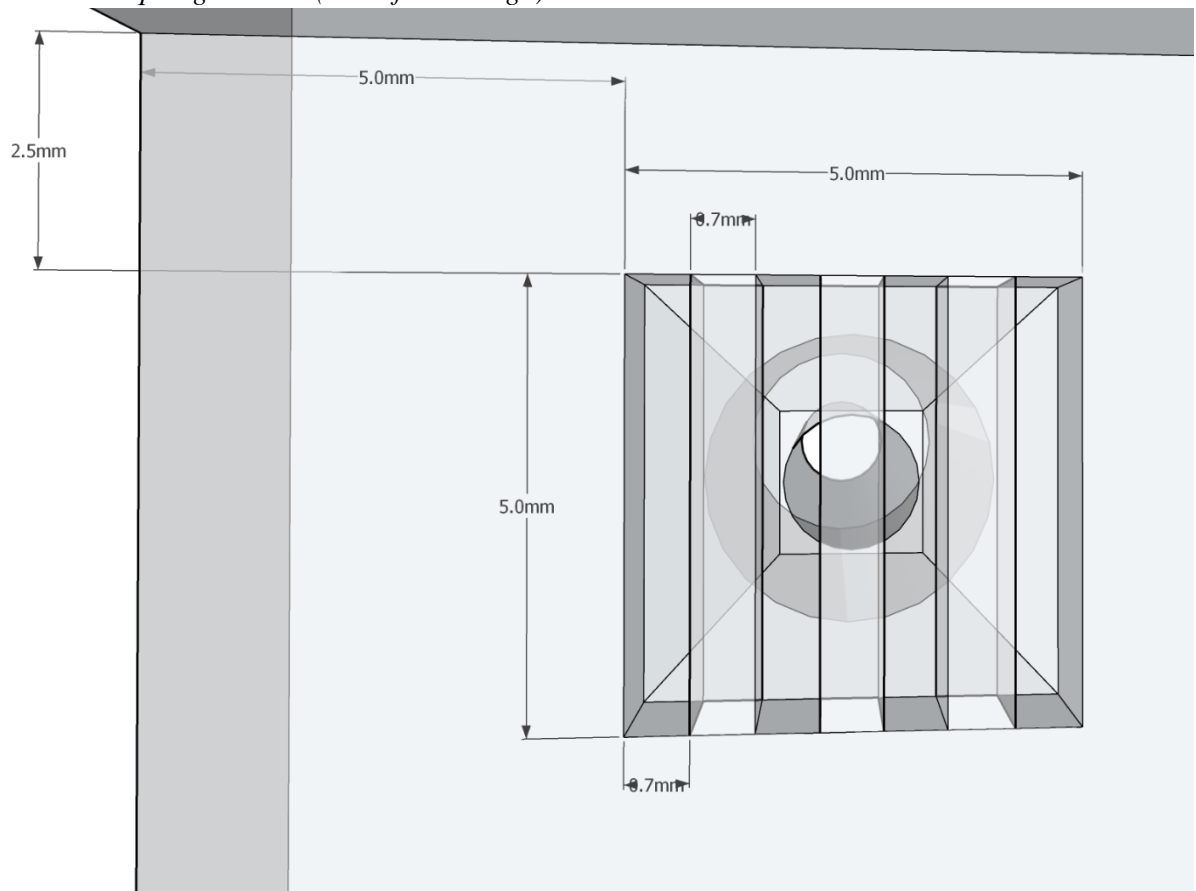
A.1.1 Front view



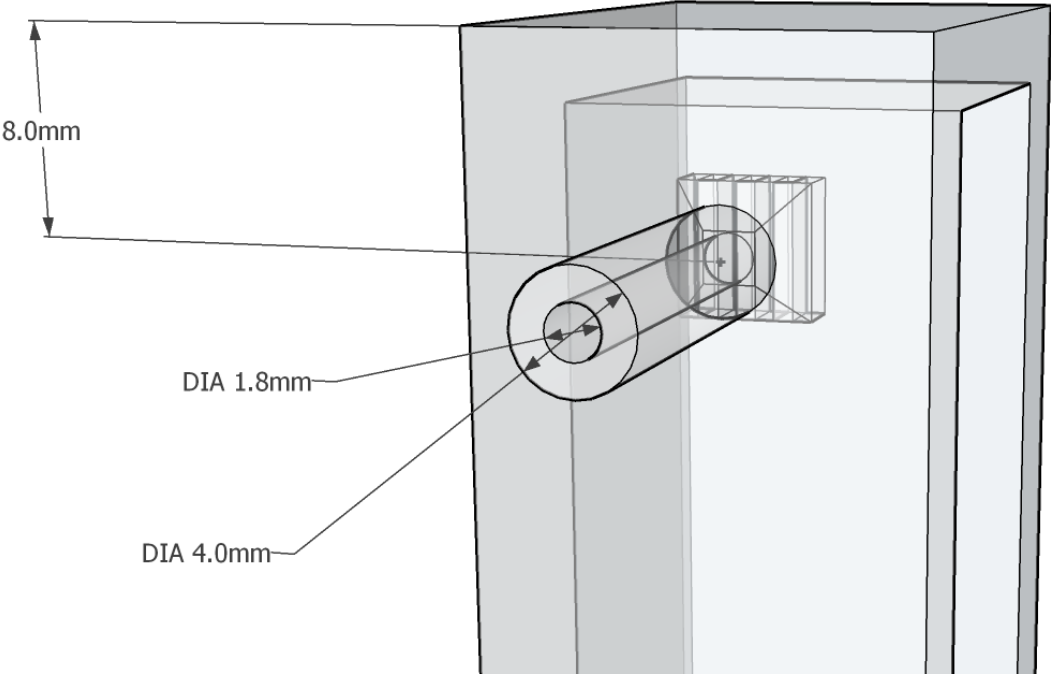
A.1.2 Bottom view



A.1.3 Zoomed liquid/gas outlet (inner filter design)



A.1.4 Zoomed liquid/gas outlet (outer design)



Appendix B: Experimental calibration

B.1 OMEGA-FL3635G gas flowmeter calibration

Omega FL-3635G	
SCALE	Flowrate (mL/min)
0	0
5	3.7
10	5.4
15	7.3
20	9.9
25	12.6
30	15.5
35	19
40	22.9
45	27.9
50	32.7
55	38.1
60	43.8
65	48.7

B.2 WASTON MARLOW 530U Peristaltic Pump

Speed (rpm)	Liquid flowrate(mL/S)			Average (mL/S)
	1st	2nd	3rd	
0	0	0	0	0.000
10	0.858369	0.765432	0.762631	0.795
20	1.651528	1.539119	1.569859	1.587
30	2.40668	2.329275	2.288218	2.341
40	3.204524	3.077816	3.019324	3.101
50	3.946102	3.824092	3.905447	3.892
60	4.695305	4.60251	4.628737	4.642
70	5.425056	5.321508	5.365854	5.371
80	6.103764	6.147935	6.111111	6.121
90	6.969027	6.79803	6.79702	6.855
100	7.654432	7.456979	7.458292	7.523
110	8.405797	8.262911	8.221797	8.297
120	8.890926	8.959538	8.959538	8.937
130	9.838998	9.68661	9.718173	9.748
140	10.58632	10.47619	10.59863	10.554
150	11.34328	11.0687	11.02204	11.145
160	12.07224	11.90253	10.84906	11.608
170	12.75761	12.64706	12.64822	12.684
180	13.5006	13.49134	13.65762	13.550
190	14.1339	14.2006	14.02672	14.120
200	14.88095	15.02392	14.90196	14.936
210	15.73276	15.58164	15.57692	15.630
220	16.42129	16.46919	16.21359	16.368



B.3 Liquid viscosity measurement by ATAGO VISCO™-985 viscometer

Liquid	Spindle	Beaker (mL)	speed (rpm)	Viscosity (mPa.S)	Average (mPa.S)	STDEV
Ultrapure water	A1	100	250	1.39	1.38	0.015
				1.36		
				1.38		
25 g/L Glucose	A1	100	250	1.45	1.49	0.040
				1.49		
				1.53		
50 g/L Glucose	A1	100	250	1.77	1.78	0.012
				1.77		
				1.79		
75 g/L Glucose	A1	100	250	1.85	1.87	0.020
				1.89		
				1.87		
100 g/L Glucose	A1	100	250	1.91	1.93	0.025
				1.93		
				1.96		

References

1. Miller, C.O., A.J.I. Logwinuk, and E. Chemistry, *Fluidization Studies of Solid Particles*. 1951. **43**(5): p. 1220-1226.
2. Potic, B., et al., *Fluidization with hot compressed water in micro-reactors*. Chemical Engineering Science, 2005. **60**(22): p. 5982-5990.
3. Andreas Boker, Manuela Fischer, and R.G. Berger, *Raspberry Ketone from Submerged Cultured Cells of the Basidiomycete *Nidula niveo-tomentosa**. Biotechnology Progress, 2001. **17**: p. 568-572.
4. Tsai, Y.C., et al., *Heme oxygenase-1 mediates anti-adipogenesis effect of raspberry ketone in 3T3-L1 cells*. Phytomedicine, 2017. **31**: p. 11-17.
5. Erkki Honkanen, Tapani Pyysalo, and T. Hirvi, *The Aroma of Finnish Wild Raspberries, *Rubus idaeus*, L.* Zeitschrift für Lebensmittel-Untersuchung und -Forschung, 1980: p. 180-182.
6. Sekizuka, M., *Effect of a Dietary Supplement Containing Raspberry Ketone on Cytochrome P450 3A Activity*. Pharmaceutica Analytica Acta, 2014. **05**(06).
7. Lee, D., et al., *Heterologous production of raspberry ketone in the wine yeast *Saccharomyces cerevisiae* via pathway engineering and synthetic enzyme fusion*. Microb Cell Fact, 2016. **15**: p. 49.
8. Seshu Pedapudi, C.-K.C., Henrik Pedersen, *Production and Elicitation of Benzalacetone and the Raspberry Ketone in Cell Suspension Cultures of *Rubus idaeus**. Biotechnology Progress, 2000. **16**: p. 346-349.
9. Wang, C., P. Zheng, and P. Chen, *Construction of synthetic pathways for raspberry ketone production in engineered *Escherichia coli**. Appl Microbiol Biotechnol, 2019. **103**(9): p. 3715-3725.
10. Beekwilder, J., et al., *Microbial production of natural raspberry ketone*. Biotechnol J, 2007. **2**(10): p. 1270-9.
11. Kourkoutas, Y., et al., *Immobilization technologies and support materials suitable in alcohol beverages production: a review*. Food Microbiology, 2004. **21**(4): p. 377-397.
12. Sekoai, P.T., et al., *Microbial cell immobilization in biohydrogen production: a short overview*. Crit Rev Biotechnol, 2018. **38**(2): p. 157-171.
13. Fischer, M., A. Böker, and R.G. Berger, *Fungal Formation of Raspberry Ketone Differs from the Pathway in Plant Cell Culture*. Food Biotechnology, 2001. **15**(3): p. 147-155.
14. Taupp, D.E., et al., *Stress response of *Nidula niveo-tomentosa* to UV-A light*. Mycologia, 2008. **100**(4): p. 529-38.
15. Zivkovic, V. and M.J. Biggs, *On importance of surface forces in a microfluidic fluidized bed*. Chemical Engineering Science, 2015. **126**: p. 143-149.
16. Wang, F. and L.-S. Fan, *Gas-Solid Fluidization in Mini- and Micro-channels*. Industrial & Engineering Chemistry Research, 2011. **50**(8): p. 4741-4751.
17. Gunther, A. and K.F. Jensen, *Multiphase microfluidics: from flow characteristics to chemical and materials synthesis*. Lab Chip, 2006. **6**(12): p. 1487-503.
18. Geng, S., et al., *Conditioning micro fluidized bed for maximal approach of gas plug flow*. Chemical Engineering Journal, 2018. **351**: p. 110-118.
19. Liu, X., G. Xu, and S. Gao, *Micro fluidized beds: Wall effect and operability*. Chemical Engineering Journal, 2008. **137**(2): p. 302-307.
20. Banerjee, A. and A.K. Ghoshal, *Biodegradation of real petroleum wastewater by immobilized hyper phenol-tolerant strains of *Bacillus cereus* in a fluidized bed bioreactor*. 3 Biotech, 2016. **6**(2): p. 137.
21. Patroescu, V.I., et al., *Nitrate removal from groundwater by denitrification in fixed and fluidized bed biofilm reactors*. 2019.

22. do Nascimento, O.L., D.A. Reay, and V. Zivkovic, *Influence of surface forces and wall effects on the minimum fluidization velocity of liquid-solid micro-fluidized beds*. Powder Technology, 2016. **304**: p. 55-62.
23. McDonough, J.R., et al., *Fluidization in small-scale gas-solid 3D-printed fluidized beds*. Chemical Engineering Science, 2019. **200**: p. 294-309.
24. van Eck, N.J. and L. Waltman. *VOS: A New Method for Visualizing Similarities Between Objects*. in *Advances in Data Analysis*. 2007. Berlin, Heidelberg: Springer Berlin Heidelberg.
25. Scott, D.S. and J. Piskorz, *The flash pyrolysis of aspen-poplar wood*. The Canadian Journal of Chemical Engineering, 1982. **60**(5): p. 666-674.
26. Scott, D.S. and J. Piskorz, *The continuous flash pyrolysis of biomass*. The Canadian Journal of Chemical Engineering, 1984. **62**(3): p. 404-412.
27. Funazukuri, T., R.R. Hudgins, and P.L. Silveston, *Product distribution in pyrolysis of cellulose in a microfluidized bed*. Journal of Analytical and Applied Pyrolysis, 1986. **9**(2): p. 139-158.
28. Effendi, A., et al., *Steam reforming of a clean model biogas over Ni/Al₂O₃ in fluidized- and fixed-bed reactors*. Catalysis Today, 2002. **77**(3): p. 181-189.
29. Effendi, A., et al., *Characterisation of carbon deposits on Ni/SiO₂ in the reforming of CH₄-CO₂ using fixed- and fluidised-bed reactors*. Catalysis Communications, 2003. **4**(4): p. 203-207.
30. Rao, A., et al., *The effect of column diameter and bed height on minimum fluidization velocity*. AIChE Journal, 2010: p. NA-NA.
31. Xu, G., *Micro fluidized bed reaction kinetic analyzer*, A project application submitted to Chinese Academy of Sciences, C.N.I.P.A. (CNIPA), Editor. 2005: China.
32. Zivkovic, V., M.J. Biggs, and Z.T. Alwahabi, *Experimental study of a liquid fluidization in a microfluidic channel*. AIChE Journal, 2013. **59**(2): p. 361-364.
33. Li, X., M. Liu, and Y. Li, *Bed expansion and multi-bubble behavior of gas-liquid-solid micro-fluidized beds in sub-millimeter capillary*. Chemical Engineering Journal, 2017. **328**: p. 1122-1138.
34. Li, Y., M. Liu, and X. Li, *Flow regimes in gas-liquid-solid mini-fluidized beds with single gas orifice*. Powder Technology, 2018. **333**: p. 293-303.
35. Pereira, I., et al., *A new microfluidic approach for the one-step capture, amplification and label-free quantification of bacteria from raw samples*. Chem Sci, 2017. **8**(2): p. 1329-1336.
36. Pereira, I., et al., *Magnetic fluidized bed for solid phase extraction in microfluidic systems*. Lab Chip, 2017. **17**(9): p. 1603-1615.
37. Hernandez-Neuta, I., et al., *Microfluidic magnetic fluidized bed for DNA analysis in continuous flow mode*. Biosens Bioelectron, 2017. **102**: p. 531-539.
38. Zivkovic, V., M.N. Kashani, and M.J. Biggs, *Experimental and theoretical study of a micro-fluidized bed*. 2013. p. 93-96.
39. Becker, H. and C. Gartner, *Polymer microfabrication technologies for microfluidic systems*. Anal Bioanal Chem, 2008. **390**(1): p. 89-111.
40. do Nascimento, O.L., D.A. Reay, and V. Zivkovic, *Solid Circulating Velocity Measurement in a Liquid-Solid Micro-Circulating Fluidised Bed*. Processes, 2020. **8**(9): p. 1159.
41. Macdonald, N.P., et al., *Comparing Microfluidic Performance of Three-Dimensional (3D) Printing Platforms*. Anal Chem, 2017. **89**(7): p. 3858-3866.
42. Lu, Y., et al., *Minimum fluidization velocities for supercritical water fluidized bed within the range of 633–693K and 23–27MPa*. International Journal of Multiphase Flow, 2013. **49**: p. 78-82.
43. Yu, J., et al., *Kinetics and mechanism of solid reactions in a micro fluidized bed reactor*. AIChE Journal, 2010. **56**(11): p. 2905-2912.
44. Pang, F., et al., *Study on the influence of oxygen-containing groups on the performance of Ni/AC catalysts in methanol vapor-phase carbonylation*. Chemical Engineering Journal, 2016. **293**: p. 129-138.

45. Zhang, Y., et al., *Fluidization of fungal pellets in a 3D-printed micro-fluidized bed*. Chemical Engineering Science, 2021. **236**.
46. Zeng, X., et al., *Behavior and Kinetics of Drying, Pyrolysis, Gasification, and Combustion Tested by a Microfluidized Bed Reaction Analyzer for the Staged-Gasification Process*. Energy & Fuels, 2020. **34**(2): p. 2553-2565.
47. Han, Z., et al., *State-of-the-art hydrodynamics of gas-solid micro fluidized beds*. Chemical Engineering Science, 2021. **232**.
48. Li, X., M. Liu, and Y. Li, *Hydrodynamic behavior of liquid–solid micro-fluidized beds determined from bed expansion*. Particuology, 2017.
49. J.F. Richardson and W.N. Zaki, *The sedimentation of a suspension of uniform spheres under conditions of viscous flow*. Chemical Engineering Science, 1954. **3**(2): p. 65-73.
50. Kunii. Daizo and L. Octave, *Fluidization engineering*. 2nd ed. 2013: Elsevier. 491.
51. Clark O. Miller and A.K. Logwinuk, *Fluidization Studies of Solid Particles*. Industrial & Engineering Chemistry, 1951. **43**(5): p. 1220-1226.
52. Leva, M., *Fluidization*. 1959, New York; Toronto; London: McGraw-Hill.
53. Wen, C.Y. and Y.H. Yu, *Mechanics of Fluidization*. The Chemical Engineering Progress Symposium Series, 1966. **162**: p. 100-111.
54. Ergun, S., *Fluid flow through packed columns*. Chemical Engineering Process, 1952. **48**: p. 89-94.
55. Yates, J.G., *Effects of temperature and pressure on gas-solid fluidization*. Chemical Engineering Science, 1996. **51**(2): p. 167-205.
56. Choi, Y.S., S.J. Kim, and D. Kim, *A Semi-empirical Correlation for Pressure Drop in Packed Beds of Spherical Particles*. Transport in Porous Media, 2008.
57. Li, L. and W. Ma, *Experimental Study on the Effective Particle Diameter of a Packed Bed with Non-Spherical Particles*. Transport in Porous Media, 2011. **89**(1): p. 35-48.
58. Doroodchi, E., et al., *Fluidisation and packed bed behaviour in capillary tubes*. Powder Technology, 2012. **223**: p. 131-136.
59. Tang, C., M. Liu, and Y. Li, *Experimental investigation of hydrodynamics of liquid–solid mini-fluidized beds*. Particuology, 2016. **27**: p. 102-109.
60. Guo, Q.J., Y.Q. Xu, and X.H. Yue, *Fluidization Characteristics in Micro-Fluidized Beds of Various Inner Diameters*. Chemical Engineering & Technology, 2009. **32**(12): p. 1992-1999.
61. Chen, Y., *The influence of surface hydrophobicity in fluidization of ultrafine Al₂O₃ particles*. Chemical Engineering and Processing: Process Intensification, 2016. **110**: p. 21-29.
62. Vanni, F., et al., *Effects of reducing the reactor diameter on the fluidization of a very dense powder*. Powder Technology, 2015. **277**: p. 268-274.
63. Ma, N., et al., *Quantitative studies of cell-bubble interactions and cell damage at different pluronic F-68 and cell concentrations*. Biotechnology Progress, 2004. **20**(4): p. 1182-1191.
64. Zivkovic, V., N. Ridge, and M.J. Biggs, *Experimental study of efficient mixing in a micro-fluidized bed*. Applied Thermal Engineering, 2017. **127**: p. 1642-1649.
65. Mao, Z. and C. Yang, *Micro-mixing in chemical reactors: A perspective*. Chinese Journal of Chemical Engineering, 2017. **25**(4): p. 381-390.
66. McDonough, J.R., et al., *Micromixing in oscillatory baffled flows*. Chemical Engineering Journal, 2019. **361**: p. 508-518.
67. Hartge, E.U., K. Luecke, and J. Werther, *The role of mixing in the performance of CFB reactors*. Chemical Engineering Science, 1999. **54**(22): p. 5393-5407.
68. Doroodchi, E., et al., *Liquid–liquid mixing using micro-fluidised beds*. Chemical Engineering Research and Design, 2013. **91**(11): p. 2235-2242.
69. Derksen, J.J., *Scalar mixing with fixed and fluidized particles in micro-reactors*. Chemical Engineering Research and Design, 2009. **87**(4): p. 550-556.

70. Shabanian, J. and J. Chaouki, *Fluidization characteristics of a bubbling gas–solid fluidized bed at high temperature in the presence of interparticle forces*. Chemical Engineering Journal, 2016. **288**: p. 344-358.
71. Menéndez, M., et al., *Experimental methods in chemical engineering: Reactors—fluidized beds*. The Canadian Journal of Chemical Engineering, 2019. **97**(9): p. 2383-2394.
72. Geldart, D.J.P.t., *Types of gas fluidization*. Powder technology, 1973. **7**(5): p. 285-292.
73. Wang, J., et al., *Review of (gas)-liquid-solid circulating fluidized beds as biochemical and environmental reactors*. Chemical Engineering Journal, 2019.
74. Zhang, Y., B. Jin, and W. Zhong, *Experiment on particle mixing in flat-bottom spout–fluid bed*. Chemical Engineering and Processing: Process Intensification, 2009. **48**(1): p. 126-134.
75. Wu, G., et al., *Mixing Characteristics of Binary Mixture with Biomass in a Gas-Solid Rectangular Fluidized Bed*. Energies, 2019. **12**(10).
76. Wang, F., et al., *Distinctive Hydrodynamics of a Micro Fluidized Bed and Its Application to Gas–Solid Reaction Analysis*. Energy & Fuels, 2017. **32**(4): p. 4096-4106.
77. Kulkarni, A.V., S.V. Badgandi, and J.B. Joshi, *Design of ring and spider type spargers for bubble column reactor: Experimental measurements and CFD simulation of flow and weeping*. Chemical Engineering Research and Design, 2009. **87**(12): p. 1612-1630.
78. Odeleye, A.O.O., et al., *On the use of 3D-printed flow distributors to control particle movement in a fluidized bed*. Chemical Engineering Research and Design, 2018. **140**: p. 194-204.
79. McDonough, J.R., et al., *Miniaturisation of the toroidal fluidization concept using 3D printing*. Chemical Engineering Research and Design, 2020.
80. Goksen G. Yaralioglu, et al., *Ultrasonic Mixing in Microfluidic Channels Using Integrated Transducers*. Analytical Chemistry, 2004. **76**(13): p. 3694-3698.
81. Jr-HungTsai and LiweiLin, *Active microfluidic mixer and gas bubble filter driven by thermal bubble micropump*. Sensors and Actuators A: Physical, 2002. **97–98**(1): p. 665-671.
82. Lee, S.H., et al., *Effective mixing in a microfluidic chip using magnetic particles*. Lab Chip, 2009. **9**(3): p. 479-82.
83. Karimi, F., et al., *Multiscale characterization of nanoparticles in a magnetically assisted fluidized bed*. Particuology, 2020. **51**: p. 64-71.
84. Chen, H., et al., *Effect of mixing state of binary particles on bubble behavior in 2D fluidized bed*. Chemical Engineering Communications, 2018. **205**(8): p. 1119-1128.
85. Ballesteros, R.L., J.P. Riba, and J.P. Couderc, *Dissolution of non spherical particles in solid-liquid fluidization*. Chemical Engineering Science, 1982. **37**(11): p. 1639-1644.
86. Fan, L.-T., Y.-C. Yang, and C.-Y. Wen, *Mass transfer in semifluidized beds for solid-liquid system*. AIChE Journal, 1960. **6**(3): p. 482-487.
87. Arters, D.C. and L.-S. Fan, *Solid-liquid mass transfer in a gas-liquid-solid fluidized bed*¹¹*This paper was presented at the 1984 Annual Meeting of the American Institute of Chemical Engineers, 25-30 November*. Chemical Engineering Science, 1986. **41**(1): p. 107-115.
88. Upadhyay, S.N. and G. Tripathi, *Liquid-phase mass transfer in fixed and fluidized beds of large particles*. Journal of Chemical & Engineering Data, 1975. **20**(1): p. 20-26.
89. Boskovic-Vragolovic, N., D. Brzic, and Z. Grbavcic, *Mass transfer between a fluid and an immersed object in liquid-solid packed and fluidized beds*. Journal of the Serbian Chemical Society, 2005. **70**(11): p. 1373-1379.
90. Kalaga, D.V., et al., *Particle-liquid mass transfer in solid–liquid fluidized beds*. Chemical Engineering Journal, 2014. **245**: p. 323-341.
91. Koloini, T., M. Sopčič, and M. Žumer, *Mass transfer in liquid-fluidized beds at low reynolds numbers*. Chemical Engineering Science, 1977. **32**(6): p. 637-641.
92. Livingston, A.G. and J.B. Noble, *Mass transfer in liquid—solid fluidized beds of ion exchange resins at low Reynolds numbers*. Chemical Engineering Science, 1993. **48**(6): p. 1174-1178.

93. Rahmant, K. and M. Streat, *Mass transfer in liquid fluidized beds of ion exchange particles*. Chemical Engineering Science, 1981. **36**(2): p. 293-300.
94. Chavan, P.V., D.V. Kalaga, and J.B. Joshi, *Solid-Liquid Circulating Multistage Fluidized Bed: Hydrodynamic Study*. Industrial & Engineering Chemistry Research, 2009. **48**(9): p. 4592-4602.
95. Frossling, N., *Über die Verdunstung fallender Tropfen*. Beitr. Geophys. Gerlands, 1938. **52**: p. 170-216.
96. Scala, F., *Particle-fluid mass transfer in multiparticle systems at low Reynolds numbers*. Chemical Engineering Science, 2013. **91**: p. 90-101.
97. McCune, L.K. and R.H. Wilhelm, *Mass and Momentum Transfer in a Solid-Liquid System*. Industrial & Engineering Chemistry, 1949. **41**(6): p. 1124-1134.
98. Dwivedi, P.N. and S.N. Upadhyay, *Particle-Fluid Mass Transfer in Fixed and Fluidized Beds*. Industrial & Engineering Chemistry Process Design and Development, 1977. **16**(2): p. 157-165.
99. Yang, Z., M. Liu, and C. Lin, *Photocatalytic activity and scale-up effect in liquid-solid mini-fluidized bed reactor*. Chemical Engineering Journal, 2016. **291**: p. 254-268.
100. Arters, D.C. and L.-S. Fan, *Experimental methods and correlation of solid-liquid mass transfer in fluidized beds*. Chemical Engineering Science, 1990. **45**(4): p. 965-975.
101. Li, J., et al., *A two-stage reduction process for the production of high-purity ultrafine Ni particles in a micro-fluidized bed reactor*. Particuology, 2015. **19**: p. 27-34.
102. Liu, H., et al., *Experimental study on the fluidization behaviors of the superfine particles*. Chemical Engineering Journal, 2015. **262**: p. 579-587.
103. Li, J., et al., *Self-agglomeration mechanism of iron nanoparticles in a fluidized bed*. Chemical Engineering Science, 2018. **177**: p. 455-463.
104. Zhong, Y., et al., *Defluidization behavior of iron powders at elevated temperature: Influence of fluidizing gas and particle adhesion*. Powder Technology, 2012. **230**: p. 225-231.
105. Lin, Y.H., Z.C. Guo, and H.Q. Tang, *Iron ore reduction in a small fluidized bed*. Revue de Métallurgie, 2013. **110**(4): p. 265-273.
106. Barde, A.A., J.F. Klausner, and R. Mei, *Solid state reaction kinetics of iron oxide reduction using hydrogen as a reducing agent*. International Journal of Hydrogen Energy, 2016. **41**(24): p. 10103-10119.
107. He, K., Z. Zheng, and Z. Chen, *Multistep reduction kinetics of Fe₃O₄ to Fe with CO in a micro fluidized bed reaction analyzer*. Powder Technology, 2020. **360**: p. 1227-1236.
108. Li, J., et al., *Decoupling reduction-sulfurization synthesis of inorganic fullerene-like WS₂ nanoparticles in a particulate fluidized bed*. Chemical Engineering Journal, 2014. **249**: p. 54-62.
109. Li, J., G. Luo, and F. Wei, *Efficient production of Mg₂Si in a fluidized-bed reactor*. Powder Technology, 2012. **229**: p. 152-161.
110. Rosenkranz, K., et al., *Encapsulation of irregularly shaped solid forms of proteins in a high-pressure fluidized bed*. The Journal of Supercritical Fluids, 2008. **46**(3): p. 351-357.
111. Burggraef, A., et al., *Process analytical tools for monitoring, understanding, and control of pharmaceutical fluidized bed granulation: A review*. Eur J Pharm Biopharm, 2013. **83**(1): p. 2-15.
112. Hu, X., J. Cunningham, and D. Winstead, *Understanding and predicting bed humidity in fluidized bed granulation*. J Pharm Sci, 2008. **97**(4): p. 1564-77.
113. Guignon, B., A. Duquenoy, and E.D. Dumoulin, *Fluid Bed Encapsulation of Particles: Principles and Practice*. Drying Technology, 2002. **20**(2): p. 419-447.
114. Tsutsumi, A., et al., *A novel fluidized-bed coating of fine particles by rapid expansion of supercritical fluid solutions*. Powder Technology, 1995. **85**(3): p. 275-278.
115. Schreiber, R., et al., *Fluidized bed coating at supercritical fluid conditions*. The Journal of Supercritical Fluids, 2002. **24**(2): p. 137-151.

116. Rodríguez-Rojo, S., J. Marienfeld, and M.J. Cocero, *RESS process in coating applications in a high pressure fluidized bed environment: Bottom and top spray experiments*. Chemical Engineering Journal, 2008. **144**(3): p. 531-539.
117. Leeke, G.A., et al., *Application of nano-particle coatings to carrier particles using an integrated fluidized bed supercritical fluid precipitation process*. The Journal of Supercritical Fluids, 2014. **91**: p. 7-14.
118. Nienow, A.W. and D.J. Cheesman, *The Effect of Shape on the Mixing and Segregation of Large Particles in a Gas-Fluidised Bed of Small Ones*, in *Fluidization*, J.R. Grace and J.M. Matsen, Editors. 1980, Springer US: Boston, MA. p. 373-380.
119. Chen, J.L.-P. and D.L. Keairns, *Particle segregation in a fluidized bed*. The Canadian Journal of Chemical Engineering, 1975. **53**(4): p. 395-402.
120. Taek Woon Hong and D.H. Lee, *Effect of particle size distribution on mixing and segregation in a gas-solid fluidized bed with binary system*. International Journal of Engineering Research & Science, 2018. **4**(3): p. 2395-6992.
121. Nienow, A., N. Naimer, and T. Chiba, *Studies of segregation/mixing in fluidised beds of different size particles*. Chemical Engineering Communications, 1987. **62**(1-6): p. 53-66.
122. Feng, Y.Q. and A.B. Yu, *Effect of Bed Thickness on the Segregation Behavior of Particle Mixtures in a Gas Fluidized Bed*. Industrial & Engineering Chemistry Research, 2010. **49**(7): p. 3459-3468.
123. Wu, S.Y. and J. Baeyens, *Segregation by size difference in gas fluidized beds*. Powder Technology, 1998. **98**(2): p. 139-150.
124. Girimonte, R., B. Formisani, and V. Vivacqua, *The relationship between fluidization velocity and segregation in two-component gas fluidized beds: Density- or size-segregating mixtures*. Chemical Engineering Journal, 2018. **335**: p. 63-73.
125. Zhang, Y., et al., *Systematic Investigation of Particle Segregation in Binary Fluidized Beds with and without Multilayer Horizontal Baffles*. Industrial & Engineering Chemistry Research, 2012. **51**(13): p. 5022-5036.
126. Damartzis, T. and A. Zabaniotou, *Thermochemical conversion of biomass to second generation biofuels through integrated process design—A review*. Renewable and Sustainable Energy Reviews, 2011. **15**(1): p. 366-378.
127. Fouilland, T., J.R. Grace, and N. Ellis, *Recent advances in fluidized bed technology in biomass processes*. Biofuels, 2014. **1**(3): p. 409-433.
128. Boffito, D.C., G. Blanco Manrique, and G.S. Patience, *One step cracking/transesterification of vegetable oil: Reaction–regeneration cycles in a capillary fluidized bed*. Energy Conversion and Management, 2015. **103**: p. 958-964.
129. Edake, M., et al., *Catalytic glycerol hydrogenolysis to 1,3-propanediol in a gas–solid fluidized bed*. RSC Advances, 2017. **7**(7): p. 3853-3860.
130. Boffito, D.C., et al., *Biofuel synthesis in a capillary fluidized bed*. Catalysis Today, 2014. **237**: p. 13-17.
131. Guo, F., et al., *Catalytic decomposition of biomass tar compound by calcined coal gangue: A kinetic study*. International Journal of Hydrogen Energy, 2016. **41**(31): p. 13380-13389.
132. Jia, L., et al., *On-line analysis of primary tars from biomass pyrolysis by single photoionization mass spectrometry: Experiments and detailed modelling*. Chemical Engineering Journal, 2017. **313**: p. 270-282.
133. Jia, L., et al., *Fast Pyrolysis in a Microfluidized Bed Reactor: Effect of Biomass Properties and Operating Conditions on Volatiles Composition as Analyzed by Online Single Photoionization Mass Spectrometry*. Energy & Fuels, 2015. **29**(11): p. 7364-7374.
134. Gao, W., et al., *Kinetic modeling of pyrolysis of three Iranian waste oils in a micro-fluidized bed*. Petroleum Science and Technology, 2017. **35**(2): p. 183-189.
135. Mao, Y., et al., *Fast co-pyrolysis of biomass and lignite in a micro fluidized bed reactor analyzer*. Bioresour Technol, 2015. **181**: p. 155-62.

136. Yu, J., et al., *Biomass pyrolysis in a micro-fluidized bed reactor: Characterization and kinetics*. Chemical Engineering Journal, 2011. **168**(2): p. 839-847.
137. Umeki, K., et al., *High temperature steam-only gasification of woody biomass*. Applied Energy, 2010. **87**(3): p. 791-798.
138. Liu, H., et al., *High-Temperature Gasification Reactivity with Steam of Coal Chars Derived under Various Pyrolysis Conditions in a Fluidized Bed†*. Energy & Fuels, 2010. **24**(1): p. 68-75.
139. Zeng, X., et al., *Characterization of Char Gasification in a Micro Fluidized Bed Reaction Analyzer*. Energy & Fuels, 2014. **28**(3): p. 1838-1845.
140. Zeng, X., et al., *Fluidized Bed Two-Stage Gasification Process for Clean Fuel Gas Production from Herb Residue: Fundamentals and Demonstration*. Energy & Fuels, 2016. **30**(9): p. 7277-7283.
141. Wang, F., et al., *Isothermal Gasification of in Situ/ex Situ Coal Char with CO₂ in a Micro Fluidized Bed Reaction Analyzer*. Energy & Fuels, 2015. **29**(8): p. 4795-4802.
142. Wang, F., et al., *Characterization of coal char gasification with steam in a micro-fluidized bed reaction analyzer*. Fuel Processing Technology, 2016. **141**: p. 2-8.
143. Zhang, Y., et al., *Reactivity and kinetics for steam gasification of petroleum coke blended with black liquor in a micro fluidized bed*. Applied Energy, 2015. **160**: p. 820-828.
144. Zhang, Y., et al., *Characteristics and Kinetics of Coked Catalyst Regeneration via Steam Gasification in a Micro Fluidized Bed*. Industrial & Engineering Chemistry Research, 2014. **53**(15): p. 6316-6324.
145. Cortazar, M., et al., *Experimental study and modeling of biomass char gasification kinetics in a novel thermogravimetric flow reactor*. Chemical Engineering Journal, 2020. **396**.
146. Zeng, X., et al., *High-temperature drying behavior and kinetics of lignite tested by the micro fluidization analytical method*. Fuel, 2019. **253**: p. 180-188.
147. Li, Y., et al., *Measuring the fast oxidation kinetics of a manganese oxygen carrier using microfluidized bed thermogravimetric analysis*. Chemical Engineering Journal, 2020. **385**.
148. Chen, L., et al., *NO Reduction and Emission Characteristics of Coal/Char Mixtures in a Microfluidized Bed Reaction Analyzer*. Energy & Fuels, 2018. **33**(1): p. 276-286.
149. Song, Y., et al., *Reduction of NO over biomass tar in micro-fluidized bed*. Fuel Processing Technology, 2014. **118**: p. 270-277.
150. Latifi, M. and J. Chaouki, *A novel induction heating fluidized bed reactor: Its design and applications in high temperature screening tests with solid feedstocks and prediction of defluidization state*. AIChE Journal, 2015. **61**(5): p. 1507-1523.
151. Boot-Handford, M.E., et al., *Carbon capture and storage update*. Energy Environ. Sci., 2014. **7**(1): p. 130-189.
152. Fang, F., Z.-S. Li, and N.-S. Cai, *Experiment and Modeling of CO₂ Capture from Flue Gases at High Temperature in a Fluidized Bed Reactor with Ca-Based Sorbents*. Energy & Fuels, 2009. **23**(1): p. 207-216.
153. Fang, F., Z.-s. Li, and N.-s. Cai, *CO₂ capture from flue gases using a fluidized bed reactor with limestone*. Korean Journal of Chemical Engineering, 2010. **26**(5): p. 1414-1421.
154. Li, Y., et al., *CaO carbonation kinetics determined using micro-fluidized bed thermogravimetric analysis*. Fuel, 2020. **264**.
155. Yu, J., et al., *Kinetics and mechanism of direct reaction between CO₂ and Ca(OH)₂ in micro fluidized bed*. Environ Sci Technol, 2013. **47**(13): p. 7514-20.
156. Shen, T., et al., *Design of micro interconnected fluidized bed for oxygen carrier evaluation*. International Journal of Greenhouse Gas Control, 2019. **90**.
157. Adanez, J., et al., *Progress in Chemical-Looping Combustion and Reforming technologies*. Progress in Energy and Combustion Science, 2012. **38**(2): p. 215-282.
158. Raganati, F., P. Ammendola, and R. Chirone, *CO₂ adsorption on fine activated carbon in a sound assisted fluidized bed: Effect of sound intensity and frequency, CO₂ partial pressure and fluidization velocity*. Applied Energy, 2014. **113**: p. 1269-1282.

159. Raganati, F., P. Ammendola, and R. Chirone, *CO₂ capture performances of fine solid sorbents in a sound-assisted fluidized bed*. Powder Technology, 2014. **268**: p. 347-356.
160. Raganati, F., et al., *CO₂ capture performance of HKUST-1 in a sound assisted fluidized bed*. Chemical Engineering Journal, 2014. **239**: p. 75-86.
161. Li, X., et al., *Numerical and experimental study of a novel compact micro fluidized beds reactor for CO₂ capture in HVAC*. Energy and Buildings, 2017. **135**: p. 128-136.
162. Alfe, M., et al., *Magnetite loaded carbon fine particles as low-cost CO₂ adsorbent in a sound assisted fluidized bed*. Proceedings of the Combustion Institute, 2015. **35**(3): p. 2801-2809.
163. Hornbostel, K., et al., *Packed and fluidized bed absorber modeling for carbon capture with micro-encapsulated sodium carbonate solution*. Applied Energy, 2019. **235**: p. 1192-1204.
164. Bello, M.M., A.A. Abdul Raman, and M. Purushothaman, *Applications of fluidized bed reactors in wastewater treatment – A review of the major design and operational parameters*. Journal of Cleaner Production, 2017. **141**: p. 1492-1514.
165. Chowdhury, N., et al., *A Novel Liquid-Solid Circulating Fluidized-Bed Bioreactor for Biological Nutrient Removal from Municipal Wastewater*. 2009. **32**(3): p. 364-372.
166. Kuyukina, M.S., et al., *Petroleum-contaminated water treatment in a fluidized-bed bioreactor with immobilized Rhodococcus cells*. International Biodeterioration & Biodegradation, 2009. **63**(4): p. 427-432.
167. Kuyukina, M.S., et al., *Oilfield wastewater biotreatment in a fluidized-bed bioreactor using co-immobilized Rhodococcus cultures*. Journal of Environmental Chemical Engineering, 2017. **5**(1): p. 1252-1260.
168. Qiu, L., et al., *Formaldehyde biodegradation by immobilized Methylobacterium sp. XJLW cells in a three-phase fluidized bed reactor*. Bioprocess Biosyst Eng, 2014. **37**(7): p. 1377-84.
169. Ballesteros, F.C., et al., *Removal of nickel by homogeneous granulation in a fluidized-bed reactor*. Chemosphere, 2016. **164**: p. 59-67.
170. Chen, W.-H., et al., *Treatment of campus domestic wastewater using ambient-temperature anaerobic fluidized membrane bioreactors with zeolites as carriers*. International Biodeterioration & Biodegradation, 2019. **136**: p. 49-54.
171. Geng, Y., et al., *Isopropanol biodegradation by immobilized Paracoccus denitrificans in a three-phase fluidized bed reactor*. Prep Biochem Biotechnol, 2016. **46**(8): p. 747-754.
172. Ismail, Z.Z. and H.A. Khudhair, *Novel application of immobilized Bacillus cells for biotreatment of furfural-laden wastewater*.
173. Kim, J., et al., *Anaerobic Fluidized Bed Membrane Bioreactor for Wastewater Treatment*. Environmental Science & Technology, 2011. **45**(2): p. 576-581.
174. Kwak, W., et al., *Influence of hydraulic retention time and temperature on the performance of an anaerobic ammonium oxidation fluidized bed membrane bioreactor for low-strength ammonia wastewater treatment*. Chemical Engineering Journal, 2020. **386**.
175. Kwon, D., et al., *Feasibility of the highly-permselective forward osmosis membrane process for the post-treatment of the anaerobic fluidized bed bioreactor effluent*. Desalination, 2020. **485**.
176. Oztemur, G., et al., *Fluidized bed membrane bioreactor achieves high sulfate reduction and filtration performances at moderate temperatures*. Chemosphere, 2020. **252**.
177. Wang, H., et al., *Performance and bacterial community structure of a novel inverse fluidized bed bioreactor (IFBBR) treating synthetic municipal wastewater*. Sci Total Environ, 2020. **718**: p. 137288.
178. Lin, J., et al., *Biodegradation of Reactive blue 13 in a two-stage anaerobic/aerobic fluidized beds system with a Pseudomonas sp. isolate*. Bioresour Technol, 2010. **101**(1): p. 34-40.
179. González, G., et al., *Biodegradation of phenolic industrial wastewater in a fluidized bed bioreactor with immobilized cells of Pseudomonas putida*. Bioresource Technology, 2001. **80**(2): p. 137-142.

180. Zou, G., et al., *High rate autotrophic denitrification in fluidized-bed biofilm reactors*. Chemical Engineering Journal, 2016. **284**: p. 1287-1294.
181. Kumar, S., C. Wittmann, and E. Heinzle, *Minibioreactors*. Biotechnology Letters, 2004. **26**: p. 1-10.
182. Wu, K.-J., C.-F. Chang, and J.-S. Chang, *Simultaneous production of biohydrogen and bioethanol with fluidized-bed and packed-bed bioreactors containing immobilized anaerobic sludge*. Process Biochemistry, 2007. **42**(7): p. 1165-1171.
183. Cavalcantedeamorim, E., et al., *Anaerobic fluidized bed reactor with expanded clay as support for hydrogen production through dark fermentation of glucose*. International Journal of Hydrogen Energy, 2009. **34**(2): p. 783-790.
184. Barros, A.R., et al., *Biohydrogen production in anaerobic fluidized bed reactors: Effect of support material and hydraulic retention time*. International Journal of Hydrogen Energy, 2010. **35**(8): p. 3379-3388.
185. dos Reis, C.M. and E.L. Silva, *Effect of upflow velocity and hydraulic retention time in anaerobic fluidized-bed reactors used for hydrogen production*. Chemical Engineering Journal, 2011. **172**(1): p. 28-36.
186. Ferreira, T.B., et al., *Selection of metabolic pathways for continuous hydrogen production under thermophilic and mesophilic temperature conditions in anaerobic fluidized bed reactors*. International Journal of Hydrogen Energy, 2018. **43**(41): p. 18908-18917.
187. Liu, J., Y. Ren, and S. Yao, *Repeated-batch Cultivation of Encapsulated Monascus purpureus by Polyelectrolyte Complex for Natural Pigment Production*. Chinese Journal of Chemical Engineering, 2010. **18**(6): p. 1013-1017.
188. Qiu, L., et al., *Coenzyme Q(10) production by immobilized Sphingomonas sp. ZUTE03 via a conversion-extraction coupled process in a three-phase fluidized bed reactor*. Enzyme Microb Technol, 2012. **50**(2): p. 137-42.
189. Trinh, K., et al., *Quantification of damage to suspended insect cells as a result of bubble rupture*. Biotechnology and Bioengineering, 1994. **43**(1): p. 37-45.
190. Walls, P.L.L., et al., *Quantifying the potential for bursting bubbles to damage suspended cells*. Sci Rep, 2017. **7**(1): p. 15102.
191. Han, Z., et al., *Characteristics of gas-solid micro fluidized beds for thermochemical reaction analysis*. Carbon Resources Conversion, 2020. **3**: p. 203-218.
192. Samih, S., et al., *From complex feedstocks to new processes: The role of the newly developed micro-reactors*. Chemical Engineering and Processing - Process Intensification, 2018. **131**: p. 92-105.
193. Rüdüsüli, M., et al., *Scale-up of bubbling fluidized bed reactors — A review*. Powder Technology, 2012. **217**: p. 21-38.
194. Glicksman, L.R., *Scaling relationships for fluidized beds*. Chemical Engineering Science, 1984. **39**(9): p. 1373-1379.
195. Dang, N.T.Y., F. Gallucci, and M. van Sint Annaland, *Micro-structured fluidized bed membrane reactors: Solids circulation and densified zones distribution*. Chemical Engineering Journal, 2014. **239**: p. 42-52.
196. Cabaleiro, D.R., et al., *Comparison between the protease production ability of ligninolytic fungi cultivated in solid state media*. Process Biochemistry, 2002. **37**(9): p. 1017-1023.
197. Nanou, K., T. Roukas, and E. Papadakis, *Improved production of carotenoids from synthetic medium by Blakeslea trispora in a bubble column reactor*. Biochemical Engineering Journal, 2012. **67**: p. 203-207.
198. Moreira, M.T., et al., *Control of pellet morphology of filamentous fungi in fluidized bed bioreactors by means of a pulsing flow. Application to Aspergillus niger and Phanerochaete chrysosporium*. Enzyme and Microbial Technology, 1996. **19**(4): p. 261-266.
199. Zhang, J. and J. Zhang, *The filamentous fungal pellet and forces driving its formation*. Crit Rev Biotechnol, 2016. **36**(6): p. 1066-1077.

200. Grimm, L.H., et al., *Influence of mechanical stress and surface interaction on the aggregation of Aspergillus niger conidia*. Biotechnol Bioeng, 2005. **92**(7): p. 879-88.
201. Cui, Y.Q., et al., *Modeling and measurements of fungal growth and morphology in submerged fermentations*. 1998. **60**(2): p. 216-229.
202. Kües, U., M.J.C.T.i.B. Rühl, and Pharmacy, *Automated image analysis to observe pellet morphology in liquid cultures of filamentous fungi such as the basidiomycete Coprinopsis cinerea*. 2009. **3**(3): p. 241-253.
203. Wittier, R., et al., *Investigations of oxygen transfer into Penicillium chrysogenum pellets by microprobe measurements*. 1986. **28**(7): p. 1024-1036.
204. Espinosa-Ortiz, E.J., et al., *Fungal pelleted reactors in wastewater treatment: Applications and perspectives*. Chemical Engineering Journal, 2016. **283**: p. 553-571.
205. Rodríguez Porcel, E.M., et al., *Effects of pellet morphology on broth rheology in fermentations of Aspergillus terreus*. Biochemical Engineering Journal, 2005. **26**(2-3): p. 139-144.
206. Papagianni, M. and M. Moo-Young, *Protease secretion in glucoamylase producer Aspergillus niger cultures: fungal morphology and inoculum effects*. Process Biochemistry, 2002. **37**(11): p. 1271-1278.
207. Réczey, K., et al., *Mycelia-associated β -galactosidase activity in microbial pellets of Aspergillus and Penicillium strains*. 1992. **38**(3): p. 393-397.
208. Wucherpennig, T., T. Hestler, and R. Krull, *Morphology engineering - Osmolality and its effect on Aspergillus niger morphology and productivity*. Microbial Cell Factories, 2011. **10**(1): p. 58.
209. Veiter, L., V. Rajamanickam, and C. Herwig, *The filamentous fungal pellet-relationship between morphology and productivity*. Appl Microbiol Biotechnol, 2018. **102**(7): p. 2997-3006.
210. Krull, R., et al., *Morphology of Filamentous Fungi: Linking Cellular Biology to Process Engineering Using Aspergillus niger*, in *Biosystems Engineering II: Linking Cellular Networks and Bioprocesses*, C. Wittmann and R. Krull, Editors. 2010, Springer Berlin Heidelberg: Berlin, Heidelberg. p. 1-21.
211. Pandey, A., *Solid-state fermentation*. Biochemical Engineering Journal, 2003. **13**(2): p. 81-84.
212. Carboué, Q., et al., *Solid state fermentation pilot-scaled plug flow bioreactor, using partial least square regression to predict the residence time in a semicontinuous process*. Biochemical Engineering Journal, 2019. **149**.
213. Merten, O.-W., et al., *Comparison of Different Bioreactor Systems for the Production of High Titer Retroviral Vectors*. 2001. **17**(2): p. 326-335.
214. Nuutila, A.M., L. Toivonen, and V. Kauppinen, *Bioreactor studies on hairy root cultures of Catharanthus roseus: Comparison of three bioreactor types*. Biotechnology Techniques, 1994. **8**(1): p. 61-66.
215. Takayama, S. and M. Akita, *The types of bioreactors used for shoots and embryos*. Plant Cell, Tissue and Organ Culture, 1994. **39**(2): p. 147-156.
216. Kowalczyk, M., et al., *Process challenges relating to hematopoietic stem cell cultivation in bioreactors*. J Ind Microbiol Biotechnol, 2011. **38**(7): p. 761-7.
217. Papoutsakis, E.T., *Fluid-mechanical damage of animal cells in bioreactors*. Trends in Biotechnology, 1991. **9**(1): p. 427-437.
218. Singh, R.N. and S. Sharma, *Development of suitable photobioreactor for algae production – A review*. Renewable and Sustainable Energy Reviews, 2012. **16**(4): p. 2347-2353.
219. Wang, B., C.Q. Lan, and M. Horsman, *Closed photobioreactors for production of microalgal biomasses*. Biotechnol Adv, 2012. **30**(4): p. 904-12.
220. Zijffers, J.W., et al., *Design process of an area-efficient photobioreactor*. Mar Biotechnol (NY), 2008. **10**(4): p. 404-15.

221. Zhao, F. and T. Ma, *Perfusion bioreactor system for human mesenchymal stem cell tissue engineering: dynamic cell seeding and construct development*. Biotechnol Bioeng, 2005. **91**(4): p. 482-93.
222. Davison, B.H. and J.E. Thompson, *Continuous direct solvent extraction of butanol in a fermenting fluidized-bed bioreactor with immobilized Clostridium acetobutylicum*. Applied Biochemistry and Biotechnology, 1993. **39**(1): p. 415-426.
223. Nasution, U., et al., *Generating short-term kinetic responses of primary metabolism of Penicillium chrysogenum through glucose perturbation in the bioscope mini reactor*. Metab Eng, 2006. **8**(5): p. 395-405.
224. Taymaz-Nikerel, H., et al., *Development and application of a differential method for reliable metabolome analysis in Escherichia coli*. Anal Biochem, 2009. **386**(1): p. 9-19.
225. Pabst, A., et al., *Phenylbutan-2-one β -D-glucosides from raspberry fruit*. Phytochemistry, 1990. **29**(12): p. 3853-3858.
226. Bandarenko, M. and V. Kovalenko, *Synthesis of Raspberry and Ginger Ketones by Nickel Boride-catalyzed Hydrogenation of 4-Arylbut-3-en-2-ones*. Zeitschrift für Naturforschung B, 2014. **69**(8): p. 885-888.
227. Bareño, V., et al., *An Acetal Acylation Methodology for Producing Diversity of Trihalomethyl-1,3-dielectrophiles and 1,2-Azole Derivatives*. Journal of the Brazilian Chemical Society, 2020.
228. Kosjek, B., et al., *Efficient production of raspberry ketone via 'green' biocatalytic oxidation*. Tetrahedron, 2003. **59**(48): p. 9517-9521.
229. Hirvi, T., E. Honkanen, and T. Pyysalo, *The aroma of cranberries*. Zeitschrift für Lebensmittel-Untersuchung und Forschung, 1981. **172**(5): p. 365-367.
230. Keng-Hong, T. and R. Nishida, *Synomone or kairomone?--Bulbophyllum apertum flower releases raspberry ketone to attract Bactrocera fruit flies*. J Chem Ecol, 2005. **31**(3): p. 497-507.
231. Wang, L., et al. *Determination of raspberry ketone in raspberry by high performance liquid chromatography tandem mass spectrometry*. in *Proceedings 2011 International Conference on Human Health and Biomedical Engineering*. 2011.
232. Pedapudi, S., C.K. Chin, and H. Pedersen, *Production and elicitation of benzalacetone and the raspberry ketone in cell suspension cultures of Rubus idaeus*. Biotechnol Prog, 2000. **16**(3): p. 346-9.
233. Serra, S., C. Fuganti, and E. Brenna, *Biocatalytic preparation of natural flavours and fragrances*. Trends Biotechnol, 2005. **23**(4): p. 193-8.
234. Ayer, W.A. and P.P. Singer, *Phenolic metabolites of the bird's nest fungus Nidula niveo-tomentosa*. Phytochemistry, 1980. **19**(12): p. 2717-2721.
235. Böker, A., M. Fischer, and R.G. Berger, *Raspberry ketone from submerged cultured cells of the basidiomycete Nidula niveo-tomentosa*. Biotechnol Prog, 2001. **17**(3): p. 568-72.
236. Wang, H., et al., *A review of process intensification applied to solids handling*. Chemical Engineering and Processing: Process Intensification, 2017. **118**: p. 78-107.
237. Hartman, R.L. and K.F. Jensen, *Microchemical systems for continuous-flow synthesis*. Lab Chip, 2009. **9**(17): p. 2495-507.
238. McDonough, J.R., *A perspective on the current and future roles of additive manufacturing in process engineering, with an emphasis on heat transfer*. Thermal Science and Engineering Progress, 2020. **19**.
239. Formlabs. *Form Wash + Form Cure: Post-Processing Designed for the Form 2*. 2018 May 1, 2018]; Available from: <https://www.goprint3d.co.uk/form-wash.html>.
240. Sardeshpande, M.V., S. Harinarayan, and V.V. Ranade, *Void fraction measurement using electrical capacitance tomography and high speed photography*. Chemical Engineering Research and Design, 2015. **94**: p. 1-11.
241. Schneider, C.A., W.S. Rasband, and K.W. Eliceiri, *NIH Image to ImageJ: 25 years of image analysis*. Nature methods, 2012. **9**(7): p. 671-675.

242. Braun, S. and S.E. Vecht-Lifshitz, *Mycelial morphology and metabolite production*. Trends in Biotechnology, 1991. **9**(2): p. 63-68.
243. Castano-Izquierdo, H., et al., *Pre-culture period of mesenchymal stem cells in osteogenic media influences their in vivo bone forming potential*. J Biomed Mater Res A, 2007. **82**(1): p. 129-38.
244. Takashimizu, Y. and M. Iiyoshi, *New parameter of roundness R: circularity corrected by aspect ratio*. Progress in Earth and Planetary Science, 2016. **3**(1).
245. LC, A.I.Q. *System Manual and Quick Reference*. December 9, 2019]; Available from: https://www.agilent.com/cs/library/usermanuals/public/G1311-90300_QuaternarySystem_ebook.pdf.
246. Series, Y. *YSI 2900 Series Biochemistry Analyzers Operations and Maintenance Manual*. December 29, 2019]; Available from: <https://www.ysi.com/File%20Library/Documents/Manuals/YSI-2900-Series-Manual.pdf>.
247. TOLEDO, M. *SevenCompact™ pH/Ion meter S220*. 49.
248. Wormsbecker, M., T.S. Pugsley, and H. Tanfara, *The influence of distributor design on fluidized bed dryer hydrodynamics*. 2007.
249. Leonard, C., et al., *Bubble column reactors for high pressures and high temperatures operation*. Chemical Engineering Research and Design, 2015. **100**: p. 391-421.
250. Ribeiro Jr., C.P. and P.L.C. Lage, *Experimental study on bubble size distributions in a direct-contact evaporator*. Brazilian Journal of Chemical Engineering, 2004. **21**: p. 69-81.
251. Besagni, G., et al., *Experimental investigation on the influence of ethanol on bubble column hydrodynamics*. Chemical Engineering Research and Design, 2016. **112**: p. 1-15.
252. Kaji, M., et al., *Behaviours of bubble formation from a bottom porous nozzle bath*. Proceedings of the Fifth ExHFT, 2001: p. 1503-1508.
253. Zhang, J.P., et al., *Flow regime identification in gas-liquid flow and three-phase fluidized beds*. Chemical Engineering Science, 1997. **52**(21): p. 3979-3992.
254. Sharaf, S., et al., *Global and local hydrodynamics of bubble columns – Effect of gas distributor*. Chemical Engineering Journal, 2016. **288**: p. 489-504.
255. Ramakrishnan, S., R. Kumar, and N.R. Kuloor, *Studies in bubble formation—I bubble formation under constant flow conditions*. Chemical Engineering Science, 1969. **24**(4): p. 731-747.
256. Kulkarni, A.A. and J.B. Joshi, *Bubble Formation and Bubble Rise Velocity in Gas-Liquid Systems: A Review*. Industrial & Engineering Chemistry Research, 2005. **44**(16): p. 5873-5931.
257. Zivkovic, V., et al., *A pressure drop correlation for low Reynolds number Newtonian flows through a rectangular orifice in a similarly shaped micro-channel*. Chemical Engineering Research and Design, 2013. **91**(1): p. 1-6.
258. Whitehead, A.B., D.C. Dent, and G.N. Bhat, *Fluidisation studies in large gas-solid systems Part I: Bubble rise rates*. Powder Technology, 1967. **1**(3): p. 143-148.
259. Whitehead, A.B., D.C. Dent, and A.D. Young, *Fluidisation studies in large gas-solid systems Part II: The effect of distributor design and solid properties on fluidisation quality*. Powder Technology, 1967. **1**(3): p. 149-156.
260. Kogej, A., B. Likozar, and A. Pavko, *Lead Biosorption by Self-Immobilized Rhizopus nigricans Pellets in a Laboratory Scale Packed Bed Column: Mathematical Model and Experiment*. Food Technology and Biotechnology, 2010. **48**(3): p. 344-351.
261. Smith, E.L., A. James, and M. Fidgett. *Fluidization of microbial aggregates in tower fermenters*. in *Fluidization*. 1978. Trinity College, Cambridge, England: Combride University Press.
262. Navvab Kashani, M., et al., *A new method for reconstruction of the structure of micro-packed beds of spherical particles from desktop X-ray microtomography images. Part A. Initial*

- structure generation and porosity determination*. Chemical Engineering Science, 2016. **146**: p. 337-345.
263. Besagni, G., et al., *Computational Fluid-Dynamic modeling of the pseudo-homogeneous flow regime in large-scale bubble columns*. Chemical Engineering Science, 2017. **160**: p. 144-160.
264. Richardson, J.F. and W.N. Zaki, *Sedimentation and fluidisation: Part I*. Chemical Engineering Research and Design, 1997. **75**: p. S82-S100.
265. Naghib, S.D., et al., *Expansion properties of alginate beads as cell carrier in the fluidized bed bioartificial liver*. Powder Technology, 2017. **316**: p. 711-717.
266. Di Felice, R., *Hydrodynamics of liquid fluidisation*. Chemical Engineering Science, 1995. **50**(8): p. 1213-1245.
267. Kramer, O.J.I., et al., *Improvement of the Richardson-Zaki liquid-solid fluidisation model on the basis of hydraulics*. Powder Technology, 2019. **343**: p. 465-478.
268. Grace, J.R., *Contacting modes and behaviour classification of gas—solid and other two-phase suspensions*. The Canadian Journal of Chemical Engineering, 1986. **64**(3): p. 353-363.
269. do Nascimento, O.L., David Reay, and V. Zivkovic, *Study of Transitional Velocities of Solid–Liquid Micro-circulating Fluidized Beds by Visual Observation*. Journal of chemical engineering of Japan, 2018. **51**(4): p. 349-355.
270. Thielicke, W. and E.J. Stamhuis, *PIVlab – Towards User-friendly, Affordable and Accurate Digital Particle Image Velocimetry in MATLAB*. Journal of Open Research Software, 2014. **2**.
271. Ningning Ma, e.J.C., John G. Auninü s, Weichang Zhou, and L. Xie, *Quantitative Studies of Cell-Bubble Interactions and Cell Damage at Different Pluronic F-68 and Cell Concentrations*. Biotechnology Progress, 2004. **20**(4): p. 1183-1191.
272. Réczey, K., et al., *Mycelia-associated β -galactosidase activity in microbial pellets of *Aspergillus* and *Penicillium* strains*. Applied Microbiology and Biotechnology, 1992. **38**(3): p. 393-397.
273. Baillie, R.C., *Behavior of individual particles in a fluidized bed*. Retrospective Theses and Dissertations, 1965. **4027**.
274. Kitamoto, Y., et al., *A new method for the preservation of fungus stock cultures by deep-freezing*. Mycoscience, 2002. **43**(2): p. 143-149.
275. Jadhav, S.K., J.S. Paul, and K.L. Tiwari, *Long Term Preservation of Commercial Important Fungi in Glycerol at 4°C*. International Journal of Biological Chemistry, 2015. **9**(2): p. 79-85.
276. Ehinger, M.O., et al., *Significant genetic and phenotypic changes arising from clonal growth of a single spore of an arbuscular mycorrhizal fungus over multiple generations*. New Phytol, 2012. **196**(3): p. 853-61.
277. Carmichael, J.W., *Frozen Storage for Stock Cultures of Fungi*. Mycologia, 1956. **48**(3): p. 378-381.
278. Zorn, H., M. Fischer-Zorn, and R.G. Berger, *A labeling study to elucidate the biosynthesis of 4-(4-hydroxyphenyl)-butan-2-one (raspberry ketone) by *Nidula niveo-tomentosa**. Appl Environ Microbiol, 2003. **69**(1): p. 367-72.
279. Meleady, P., et al., *Sustained productivity in recombinant Chinese Hamster Ovary (CHO) cell lines: proteome analysis of the molecular basis for a process-related phenotype*. BMC Biotechnology, 2011. **11**(1): p. 78.
280. Zwicker, N., et al., *Optimization of fermentation conditions for the production of ethylene-diamine-disuccinic acid by *Amycolatopsis orientalis**. Journal of Industrial Microbiology and Biotechnology, 1997. **19**(4): p. 280-285.
281. Mori, T., et al., *Effects of Glucose Concentration on Ethanol Fermentation of White-Rot Fungus *Phanerochaete sordida* YK-624 Under Aerobic Conditions*. Curr Microbiol, 2019. **76**(3): p. 263-269.
282. Vu, V.H., T.A. Pham, and K. Kim, *Improvement of fungal cellulase production by mutation and optimization of solid state fermentation*. Mycobiology, 2011. **39**(1): p. 20-5.

283. Ho, H. and K. Ho, *Fungal Strain Improvement of Aspergillus brasiliensis for Overproduction of Xylanase in Submerged Fermentation through UV Irradiation and Chemicals Mutagenesis*. Journal of Advances in Biology & Biotechnology, 2015. **3**(3): p. 117-131.
284. Fernandes, C.G., et al., *Experimental Evidence that Phenylalanine Provokes Oxidative Stress in Hippocampus and Cerebral Cortex of Developing Rats*. Cellular and Molecular Neurobiology, 2009. **30**(2): p. 317-326.
285. Eshkol, N., et al., *Production of 2-phenylethanol from L-phenylalanine by a stress tolerant Saccharomyces cerevisiae strain*. J Appl Microbiol, 2009. **106**(2): p. 534-42.
286. Milke, L., M. Mutz, and J. Marienhagen, *Synthesis of the character impact compound raspberry ketone and additional flavoring phenylbutanoids of biotechnological interest with Corynebacterium glutamicum*. Microb Cell Fact, 2020. **19**(1): p. 92.
287. Zhang, Y., et al., *Fluidization of fungal pellets in a 3D-printed micro-fluidized bed*. Chemical Engineering Science, 2021.
288. Dynesen, J. and J. Nielsen, *Surface hydrophobicity of Aspergillus nidulans conidiospores and its role in pellet formation*. Biotechnol Prog, 2003. **19**(3): p. 1049-52.
289. Phillips, D.H., *Oxygen transfer into mycelial pellets*. 1966. **8**(3): p. 456-460.
290. Elmayergi, H., J.M. Scharer, and M. Moo-Young, *Effects of polymer additives on fermentation parameters in a culture of A. niger*. 1973. **15**(5): p. 845-859.
291. Park, J.K. and H.N. Chang, *Microencapsulation of microbial cells*. Biotechnology Advances, 2000. **18**(4): p. 303-319.
292. Islam, M.T., et al., *Effect of orifice size and bond number on bubble formation characteristics: A CFD study*. The Canadian Journal of Chemical Engineering, 2015. **93**(10): p. 1869-1879.